THE STEREOCHEMISTRY OF Cu^{2+} OXYSALT MINERALS: AN *AB INITIO* MOLECULAR-ORBITAL APPROACH

BY

PETER C. BURNS

A Thesis
Submitted to the Faculty of Graduate Studies
in Partial Fulfilment of the Requirements
for the Degree of

DOCTOR OF PHILOSOPHY

Department of Geological Sciences
University of Manitoba
Winnipeg, Manitoba

ISBN 0-315-92261-3

Name Peter Carman Burns

Dissertation Abstracts International is arranged by broad, general subject categories. Please select the one subject which most nearly describes the content of your dissertation. Enter the corresponding four-digit code in the spaces provided.

Mineralogy
SUBJECT TERM

0411
SUBJECT CODE

U·M·I

Subject Categories

THE HUMANITIES AND SOCIAL SCIENCES

COMMUNICATIONS AND THE ARTS
Architecture 0729
Art History 0377
Cinema 0900
Dance 0378
Fine Arts 0357
Information Science 0723
Journalism 0391
Library Science 0399
Mass Communications 0708
Music 0413
Speech Communication 0459
Theater 0465

EDUCATION
General 0515
Administration 0514
Adult and Continuing 0516
Agricultural 0517
Art 0273
Bilingual and Multicultural 0282
Business 0688
Community College 0275
Curriculum and Instruction 0727
Early Childhood 0518
Elementary 0524
Finance 0277
Guidance and Counseling 0519
Health 0680
Higher 0745
History of 0520
Home Economics 0278
Industrial 0521
Language and Literature 0279
Mathematics 0280
Music 0522
Philosophy of 0998
Physical 0523
Psychology 0525
Reading 0535
Religious 0527
Sciences 0714
Secondary 0533
Social Sciences 0534
Sociology of 0340
Special 0529
Teacher Training 0530
Technology 0710
Tests and Measurements 0288
Vocational 0747

LANGUAGE, LITERATURE AND LINGUISTICS
Language
- General 0679
- Ancient 0289
- Linguistics 0290
- Modern 0291

Literature
- General 0401
- Classical 0294
- Comparative 0295
- Medieval 0297
- Modern 0298
- African 0316
- American 0591
- Asian 0305
- Canadian (English) 0352
- Canadian (French) 0355
- English 0593
- Germanic 0311
- Latin American 0312
- Middle Eastern 0315
- Romance 0313
- Slavic and East European 0314

PHILOSOPHY, RELIGION AND THEOLOGY
Philosophy 0422
Religion
- General 0318
- Biblical Studies 0321
- Clergy 0319
- History of 0320
- Philosophy of 0322

Theology 0469

SOCIAL SCIENCES
American Studies 0323
Anthropology
- Archaeology 0324
- Cultural 0326
- Physical 0327

Business Administration
- General 0310
- Accounting 0272
- Banking 0770
- Management 0454
- Marketing 0338

Canadian Studies 0385
Economics
- General 0501
- Agricultural 0503
- Commerce-Business 0505
- Finance 0508
- History 0509
- Labor 0510
- Theory 0511

Folklore 0358
Geography 0366
Gerontology 0351
History
- General 0578
- Ancient 0579
- Medieval 0581
- Modern 0582
- Black 0328
- African 0331
- Asia, Australia and Oceania 0332
- Canadian 0334
- European 0335
- Latin American 0336
- Middle Eastern 0333
- United States 0337

History of Science 0585
Law 0398
Political Science
- General 0615
- International Law and Relations 0616
- Public Administration 0617

Recreation 0814
Social Work 0452
Sociology
- General 0626
- Criminology and Penology 0627
- Demography 0938
- Ethnic and Racial Studies 0631
- Individual and Family Studies 0628
- Industrial and Labor Relations 0629
- Public and Social Welfare 0630
- Social Structure and Development 0700
- Theory and Methods 0344

Transportation 0709
Urban and Regional Planning 0999
Women's Studies 0453

THE SCIENCES AND ENGINEERING

BIOLOGICAL SCIENCES
Agriculture
- General 0473
- Agronomy 0285
- Animal Culture and Nutrition 0475
- Animal Pathology 0476
- Food Science and Technology 0359
- Forestry and Wildlife 0478
- Plant Culture 0479
- Plant Pathology 0480
- Plant Physiology 0817
- Range Management 0777
- Wood Technology 0746

Biology
- General 0306
- Anatomy 0287
- Biostatistics 0308
- Botany 0309
- Cell 0379
- Ecology 0329
- Entomology 0353
- Genetics 0369
- Limnology 0793
- Microbiology 0410
- Molecular 0307
- Neuroscience 0317
- Oceanography 0416
- Physiology 0433
- Radiation 0821
- Veterinary Science 0778
- Zoology 0472

Biophysics
- General 0786
- Medical 0760

EARTH SCIENCES
Biogeochemistry 0425
Geochemistry 0996
Geodesy 0370
Geology 0372
Geophysics 0373
Hydrology 0388
Mineralogy 0411
Paleobotany 0345
Paleoecology 0426
Paleontology 0418
Paleozoology 0985
Palynology 0427
Physical Geography 0368
Physical Oceanography 0415

HEALTH AND ENVIRONMENTAL SCIENCES
Environmental Sciences 0768
Health Sciences
- General 0566
- Audiology 0300
- Chemotherapy 0992
- Dentistry 0567
- Education 0350
- Hospital Management 0769
- Human Development 0758
- Immunology 0982
- Medicine and Surgery 0564
- Mental Health 0347
- Nursing 0569
- Nutrition 0570
- Obstetrics and Gynecology 0380
- Occupational Health and Therapy 0354
- Ophthalmology 0381
- Pathology 0571
- Pharmacology 0419
- Pharmacy 0572
- Physical Therapy 0382
- Public Health 0573
- Radiology 0574
- Recreation 0575
- Speech Pathology 0460
- Toxicology 0383

Home Economics 0386

PHYSICAL SCIENCES
Pure Sciences
Chemistry
- General 0485
- Agricultural 0749
- Analytical 0486
- Biochemistry 0487
- Inorganic 0488
- Nuclear 0738
- Organic 0490
- Pharmaceutical 0491
- Physical 0494
- Polymer 0495
- Radiation 0754

Mathematics 0405
Physics
- General 0605
- Acoustics 0986
- Astronomy and Astrophysics 0606
- Atmospheric Science 0608
- Atomic 0748
- Electronics and Electricity 0607
- Elementary Particles and High Energy 0798
- Fluid and Plasma 0759
- Molecular 0609
- Nuclear 0610
- Optics 0752
- Radiation 0756
- Solid State 0611

Statistics 0463

Applied Sciences
Applied Mechanics 0346
Computer Science 0984
Engineering
- General 0537
- Aerospace 0538
- Agricultural 0539
- Automotive 0540
- Biomedical 0541
- Chemical 0542
- Civil 0543
- Electronics and Electrical 0544
- Heat and Thermodynamics 0348
- Hydraulic 0545
- Industrial 0546
- Marine 0547
- Materials Science 0794
- Mechanical 0548
- Metallurgy 0743
- Mining 0551
- Nuclear 0552
- Packaging 0549
- Petroleum 0765
- Sanitary and Municipal 0554
- System Science 0790

Geotechnology 0428
Operations Research 0796
Plastics Technology 0795
Textile Technology 0994

PSYCHOLOGY
General 0621
Behavioral 0384
Clinical 0622
Developmental 0620
Experimental 0623
Industrial 0624
Personality 0625
Physiological 0989
Psychobiology 0349
Psychometrics 0632
Social 0451

Nom _____

Dissertation Abstracts International est organisé en catégories de sujets. Veuillez s.v.p. choisir le sujet qui décrit le mieux votre thèse et inscrivez le code numérique approprié dans l'espace réservé ci-dessous.

_____ ☐☐☐ U·M·I

SUJET — CODE DE SUJET

Catégories par sujets

HUMANITÉS ET SCIENCES SOCIALES

COMMUNICATIONS ET LES ARTS
Architecture 0729
Beaux-arts 0357
Bibliothéconomie 0399
Cinéma 0900
Communication verbale 0459
Communications 0708
Danse 0378
Histoire de l'art 0377
Journalisme 0391
Musique 0413
Sciences de l'information 0723
Théâtre 0465

ÉDUCATION
Généralités 515
Administration 0514
Art 0273
Collèges communautaires 0275
Commerce 0688
Économie domestique 0278
Éducation permanente 0516
Éducation préscolaire 0518
Éducation sanitaire 0680
Enseignement agricole 0517
Enseignement bilingue et multiculturel 0282
Enseignement industriel 0521
Enseignement primaire. 0524
Enseignement professionnel 0747
Enseignement religieux 0527
Enseignement secondaire 0533
Enseignement spécial 0529
Enseignement supérieur 0745
Évaluation 0288
Finances 0277
Formation des enseignants 0530
Histoire de l'éducation 0520
Langues et littérature 0279
Lecture 0535
Mathématiques 0280
Musique 0522
Orientation et consultation 0519
Philosophie de l'éducation 0998
Physique 0523
Programmes d'études et enseignement 0727
Psychologie 0525
Sciences 0714
Sciences sociales 0534
Sociologie de l'éducation 0340
Technologie 0710

LANGUE, LITTÉRATURE ET LINGUISTIQUE
Langues
- Généralités 0679
- Anciennes 0289
- Linguistique 0290
- Modernes 0291

Littérature
- Généralités 0401
- Anciennes 0294
- Comparée 0295
- Médiévale 0297
- Moderne 0298
- Africaine 0316
- Américaine 0591
- Anglaise 0593
- Asiatique 0305
- Canadienne (Anglaise) 0352
- Canadienne (Française) 0355
- Germanique 0311
- Latino-américaine 0312
- Moyen-orientale 0315
- Romane 0313
- Slave et est-européenne 0314

PHILOSOPHIE, RELIGION ET THÉOLOGIE
Philosophie 0422
Religion
- Généralités 0318
- Clergé 0319
- Études bibliques 0321
- Histoire des religions 0320
- Philosophie de la religion 0322

Théologie 0469

SCIENCES SOCIALES
Anthropologie
- Archéologie 0324
- Culturelle 0326
- Physique 0327

Droit 0398
Économie
- Généralités 0501
- Commerce-Affaires 0505
- Économie agricole 0503
- Économie du travail 0510
- Finances 0508
- Histoire 0509
- Théorie 0511

Études américaines 0323
Études canadiennes 0385
Études féministes 0453
Folklore 0358
Géographie 0366
Gérontologie 0351
Gestion des affaires
- Généralités 0310
- Administration 0454
- Banques 0770
- Comptabilité 0272
- Marketing 0338

Histoire
- Histoire générale 0578
- Ancienne 0579
- Médiévale 0581
- Moderne 0582
- Histoire des noirs 0328
- Africaine 0331
- Canadienne 0334
- États-Unis 0337
- Européenne 0335
- Moyen-orientale 0333
- Latino-américaine 0336
- Asie, Australie et Océanie 0332

Histoire des sciences 0585
Loisirs 0814
Planification urbaine et régionale 0999
Science politique
- Généralités 0615
- Administration publique 0617
- Droit et relations internationales 0616

Sociologie
- Généralités 0626
- Aide et bien-être social 0630
- Criminologie et établissements pénitentiaires 0627
- Démographie 0938
- Études de l' individu et de la famille 0628
- Études des relations interethniques et des relations raciales 0631
- Structure et développement social 0700
- Théorie et méthodes. 0344
- Travail et relations industrielles 0629

Transports 0709
Travail social 0452

SCIENCES ET INGÉNIERIE

SCIENCES BIOLOGIQUES
Agriculture
- Généralités 0473
- Agronomie. 0285
- Alimentation et technologie alimentaire 0359
- Culture 0479
- Élevage et alimentation 0475
- Exploitation des pâturages 0777
- Pathologie animale 0476
- Pathologie végétale 0480
- Physiologie végétale 0817
- Sylviculture et faune 0478
- Technologie du bois 0746

Biologie
- Généralités 0306
- Anatomie 0287
- Biologie (Statistiques) 0308
- Biologie moléculaire 0307
- Botanique 0309
- Cellule 0379
- Écologie 0329
- Entomologie 0353
- Génétique 0369
- Limnologie 0793
- Microbiologie 0410
- Neurologie 0317
- Océanographie 0416
- Physiologie 0433
- Radiation 0821
- Science vétérinaire 0778
- Zoologie 0472

Biophysique
- Généralités 0786
- Medicale 0760

SCIENCES DE LA TERRE
Biogéochimie 0425
Géochimie 0996
Géodésie 0370
Géographie physique 0368
Géologie 0372
Géophysique 0373
Hydrologie 0388
Minéralogie 0411
Océanographie physique 0415
Paléobotanique 0345
Paléoécologie 0426
Paléontologie 0418
Paléozoologie 0985
Palynologie 0427

SCIENCES DE LA SANTÉ ET DE L'ENVIRONNEMENT
Économie domestique 0386
Sciences de l'environnement 0768
Sciences de la santé
- Généralités 0566
- Administration des hôpitaux 0769
- Alimentation et nutrition 0570
- Audiologie 0300
- Chimiothérapie 0992
- Dentisterie 0567
- Développement humain 0758
- Enseignement 0350
- Immunologie 0982
- Loisirs 0575
- Médecine du travail et thérapie 0354
- Médecine et chirurgie 0564
- Obstétrique et gynécologie 0380
- Ophtalmologie 0381
- Orthophonie 0460
- Pathologie 0571
- Pharmacie 0572
- Pharmacologie 0419
- Physiothérapie 0382
- Radiologie 0574
- Santé mentale 0347
- Santé publique 0573
- Soins infirmiers 0569
- Toxicologie 0383

SCIENCES PHYSIQUES
Sciences Pures
Chimie
- Généralités 0485
- Biochimie 487
- Chimie agricole 0749
- Chimie analytique 0486
- Chimie minérale 0488
- Chimie nucléaire 0738
- Chimie organique 0490
- Chimie pharmaceutique 0491
- Physique 0494
- PolymÈres 0495
- Radiation 0754

Mathématiques 0405
Physique
- Généralités 0605
- Acoustique 0986
- Astronomie et astrophysique 0606
- Électronique et électricité 0607
- Fluides et plasma 0759
- Météorologie 0608
- Optique 0752
- Particules (Physique nucléaire) 0798
- Physique atomique 0748
- Physique de l'état solide 0611
- Physique moléculaire 0609
- Physique nucléaire 0610
- Radiation 0756

Statistiques 0463

Sciences Appliqués Et Technologie
Informatique 0984
Ingénierie
- Généralités 0537
- Agricole 0539
- Automobile 0540
- Biomédicale 0541
- Chaleur et thermodynamique 0348
- Conditionnement (Emballage) 0549
- Génie aérospatial 0538
- Génie chimique 0542
- Génie civil 0543
- Génie électronique et électrique 0544
- Génie industriel 0546
- Génie mécanique 0548
- Génie nucléaire 0552
- Ingénierie des systèmes 0790
- Mécanique navale 0547
- Métallurgie 0743
- Science des matériaux 0794
- Technique du pétrole 0765
- Technique minière 0551
- Techniques sanitaires et municipales 0554
- Technologie hydraulique 0545

Mécanique appliquée 0346
Géotechnologie 0428
Matières plastiques (Technologie) 0795
Recherche opérationnelle 0796
Textiles et tissus (Technologie) 0794

PSYCHOLOGIE
Généralités 0621
Personnalité 0625
Psychobiologie 0349
Psychologie clinique 0622
Psychologie du comportement 0384
Psychologie du développement 0620
Psychologie expérimentale 0623
Psychologie industrielle 0624
Psychologie physiologique 0989
Psychologie sociale 0451
Psychométrie 0632

THE STEREOCHEMISTRY OF Cu^{2+} OXYSALT MINERALS:

AN *AB INITIO* MOLECULAR-ORBITAL APPROACH

BY

PETER C. BURNS

A Thesis submitted to the Faculty of Graduate Studies of the University of Manitoba in partial fulfillment of the requirements of the degree of

DOCTOR OF PHILOSOPHY

I hereby declare that I am the sole author of this thesis. I authorize the University of Manitoba to lend this thesis to other institutions or individuals for the purpose of scholarly research.

Peter C. Burns

I further authorize the University of Manitoba to reproduce this thesis by photocopying or by other means, in total or in part, at the request of other institutions or individuals for the purpose of scholarly research.

Peter C. Burns

ABSTRACT

Divalent-copper oxysalt minerals show a myriad of atomic arrangements which are often not isostructural with analogous non-Cu^{2+} oxysalt minerals. This structural diversity is due at least in part to the variability of Cu^{2+} coordination polyhedra; octahedral, square-pyramidal, triangular-bipyramidal and square-planar $Cu^{2+}\phi_n$ polyhedra ($\phi = O^{2-}$, OH^-, H_2O) occur in Cu^{2+} oxysalt minerals. The most common coordination geometry is octahedral, which is invariably distorted from holosymmetric octahedral symmetry. The distortion is due to the Jahn-Teller effect associated with the energetically degenerate electronic state of the d^9 cation in an octahedral ligand field. The octahedral distortion usually takes the form of a (4+2)-distortion (4 short equatorial bonds and 2 long apical bonds). Only a few cases of (2+4)-distorted octahedra have been reported, and at least some of these may result from the dynamic Jahn-Teller effect.

Ab initio Hartree-Fock MO (molecular-orbital) calculations were used to predict the geometries and energetics of the various $Cu^{2+}\phi_6$ coordination polyhedra. The calculations were successful in predicting the nature of the distortion of the $Cu^{2+}\phi_6$ octahedron, and a potential-energy function was derived for $Cu^{2+}\phi_6$ octahedra. The function was used to calculate Cu^{2+} oxysalt mineral structures *via* structure-energy minimization, and is transferable between structures.

Many $Cu^{2+}\phi_n$ polyhedra in Cu^{2+} oxysalt minerals represent members of structural pathways between the ideal geometries. Hartree-Fock MO calculations were used to predict the geometries and energetics of these structural pathways.

Mixed-ligand $Cu^{2+}\Phi_6$ octahedra ($\Phi = O^{2-}$, OH^-, H_2O and Cl^-) in Cu^{2+}

oxysalt minerals have been classified according to their distortion geometry. All such octahedra are (4+2)-distorted by the pseudo-Jahn-Teller effect, and the Cl^- ligands show a strong preference for the apical octahedral positions, as predicted by Hartree-Fock MO calculations.

The effect of Cu^{2+} substitution into non-Cu^{2+} structures was examined by synthesizing perovskite and rutile-structure $K(M_{1-x}Cu_x^{2+})F_3$ and $(M_{1-x}Cu_x^{2+})F_2$ (M = Zn, Mg, Ni) series. Phase transitions occur in each series, and mark the onset of the cooperative Jahn-Teller effect which is caused by electron-phonon coupling. X-ray powder diffraction and Rietveld structure refinements were used to characterize the structural changes and MF_6 octahedral bond-length variations across the phase transitions in each series. The phase transition in each series marks the onset of the cooperative Jahn-Teller effect.

This work has shown that much of the stereochemical variation in Cu^{2+} oxysalt minerals can be quantitatively predicted by *ab initio* MO theory, and is due specifically to the Jahn-Teller effect.

ACKNOWLEDGEMENTS

This work was supported by the Natural Sciences and Engineering Research Council of Canada in the form of a Post-Graduate Fellowship to the author. The University of Manitoba provided support in the form of a Duff-Roblin Fellowship and The J.S. Lightcap Award. The International Centre for Diffraction Data (ICDD) supported this work with the 1993 Crystallography Scholarship to the author.

It would not have been possible to complete this work without the continued support of my wife, Tammy. The moral support given by my parents is greatly appreciated.

Mr. Neil Ball provided expert technical assistance in the X-ray diffraction laboratories. Inspirational discussions with Dr. Mati Raudsepp and Mr. Mark Cooper kept me going through the slow periods.

Dr. Frank C. Hawthorne supervised this thesis research, and provided ample encouragement and inspiration, while at the same time leaving me free to pursue my own ideas.

I recognize the excellent and inspirational teaching of Dr. Lowell T. Trembath (1936-1993), who stimulated my interest in Mineralogy when I was an undergraduate student at the University of New Brunswick. If it were not for Dr. Trembath's dedication to teaching, I would not have pursued studies in Mineralogy.

TABLE OF CONTENTS

ABSTRACT iv

ACKNOWLEDGEMENTS vi

LIST OF FIGURES xvii

LIST OF TABLES xxiv

1. INTRODUCTION 1

1.1 Cu^{2+} Oxysalt Minerals 1

1.2 Outline of the Thesis 9

1.3 Conventions used in this Thesis 16

2. THE JAHN-TELLER EFFECT AND $Cu^{2+}\phi_6$ ($\phi = O^{2-}$, OH^-, H_2O) OCTAHEDRA IN Cu^{2+} OXYSALT MINERALS 18

2.1 Cu^{2+} Octahedra in Cu^{2+} Oxysalt Minerals 18

2.2 Jahn-Teller Theory 18

2.2.1 Screening Arguments 18

2.3 The Dynamic Jahn-Teller Effect 21

2.3.1 Variable-Temperature Structure Refinement 21

2.3.2 Vibronic Coupling and the Jahn-Teller Effect 22

2.4 Static Jahn-Teller Effects and the Cooperative Jahn-Teller Effect 29

2.4.1 Static Jahn-Teller Effects 29

2.4.2 Cooperative Jahn-Teller Effects 29

2.5 $Cu^{2+}\phi_6$ Geometries in Cu^{2+} Oxysalt Minerals 30

2.5.1 General Features of $Cu^{2+}\phi_6$ Octahedral Geometries 30

2.5.2 Examination of (4+2)-Distorted $Cu^{2+}\phi_6$ Octahedral Geometries 34

2.5.3 Holosymmetric $Cu^{2+}\phi_6$ Octahedra in Cu^{2+} Oxysalt Minerals 37

2.5.4 Occurrences of (2+4)-Distorted $Cu^{2+}\phi_6$ Octahedra in Cu^{2+} Oxysalt Minerals 43

2.5.5 Occurrences of (2+2+2)-Distorted $Cu^{2+}\phi_6$ Octahedra in Cu^{2+} Oxysalt Minerals 58

2.6 The Dynamic Jahn-Teller Effect Revisited 62

2.7 Possible Dynamic Jahn-Teller Effects in Minerals 68

2.8 Recognition of Dynamic Jahn-Teller $Cu^{2+}\phi_6$ Octahedra in Minerals 68

2.8.1 Variable-Temperature Crystallography 68

2.8.2 Anisotropic-Displacement Parameters 69

2.8.3 Electron-Spin-Resonance Spectroscopy 70

2.9 Possible Dynamic $Cu^{2+}\phi_6$ Octahedra in Minerals 71

2.9.1 A Dynamic (2+2+2)-Distorted $Cu^{2+}\phi_6$ Octahedron in Cyanochroite 71

2.9.2 Dynamic $Cu^{2+}\phi_6$ Octahedra in the Structures of Bayldonite, Volborthite and $KCu_3^{2+}(OH)_2[(AsO_4)H(AsO_4)]$ 72

2.10 Discussion 86

3. MOLECULAR-ORBITAL METHODS 89

3.1 The Molecular-Orbital Method as Applied to Minerals 89

3.2 Molecular-Orbital Models 90

3.3 The Born-Oppenheimer Approximation 91

3.4 The Hartree-Fock Method 91

3.5 Basis-Set Selection 94

3.6 Post-Hartree-Fock Methods 96

4. *AB INITIO* MOLECULAR-ORBITAL CALCULATIONS FOR $Cu^{2+}\phi_6$ OCTAHEDRA 99

4.1 Introduction 99

4.2 Previous Work 100

4.3 Molecular-Orbital Calculations: $Cu^{2+}\phi_6$ Geometries 100

4.4 Discussion of Results 102

4.5 Post-Hartree-Fock Calculations for $[Cu^{2+}(OH)_6]^{4-}$ Clusters 105

4.6 Summary 107

5. AN *AB INITIO* POTENTIAL-ENERGY FUNCTION FOR $Cu^{2+}\phi_6$ OCTAHEDRA 109

5.1 Introduction 109

5.2 Computational Methods of Structure-Energy Minimization . . . 110

5.2.1 Non-Bonded Energy 111

5.2.2 Potential Forms for Bonding Interactions 111

5.2.3 Methods of Energy Minimization 113

5.3 Calculation of a Potential-Energy Surface for $[Cu^{2+}(OH)_6]^{4-}$ . . . 114

5.4 Fitting a Potential-Energy Function to the *Ab Initio* Potential-Energy Surface 117

6. CALCULATION OF Cu^{2+} OXYSALT MINERAL STRUCTURES USING THE *AB INITIO* $^{[6]}Cu^{2+}$-ϕ POTENTIAL FUNCTION 120

6.1 Implementation of the Potential 120

6.2 Determination of Optimal Potential-Energy Parameters 121

6.2.1 Tenorite ($Cu^{2+}O$): Structure-Energy Minimization 122

6.2.2 Chalcocyanite ($Cu^{2+}SO_4$): Structure-Energy Minimization 126

6.2.3 Bonnatite ($Cu^{2+}SO_4 \cdot 3H_2O$): Structure-Energy Minimization 126

6.2.4 Lindgrenite $[Cu_3^{2+}(MoO_4)_2(OH)_2]$: Structure-Energy Minimization 131

6.2.5 Optimal r°_{ap}, r°_{eq} and C Parameters for Maximum Transferability of the $Cu^{2+}\phi_6$ Potential 140

6.3 Discussion 140

7. *AB INITIO* MOLECULAR-ORBITAL INVESTIGATIONS OF FIVE-COORDINATED Cu^{2+} CLUSTERS 143

7.1 $Cu^{2+}\phi_5$ Geometries in Cu^{2+} Oxysalt Minerals 143

7.2 Molecular-Orbital Calculations for $Cu^{2+}\phi_5$ Polyhedra 147

7.3 Possible Explanations of Why Square-Pyramids Seem to be Favoured Over Triangular-Bipyramids 149

8. COORDINATION GEOMETRY STRUCTURAL PATHWAYS IN Cu^{2+} OXYSALT MINERALS 152

8.1 Introduction 152

8.2 Structural Pathways in Cu^{2+} Oxysalt Minerals 152

8.2.1 (4+2)-Octahedral <---> Square-Pyramidal 154

8.2.2 (4+2)-Octahedral <---> Triangular-Bipyramidal 154

8.2.3 (4+2)-Octahedral <---> Square-Planar 159

8.2.4 Square-Pyramidal <---> Square-Planar 159

8.2.5 Square-Pyramidal <---> Triangular-Bipyramidal 163

8.2.6 Triangular-Bipyramidal <---> Square-Planar 163

8.3 *Ab Initio* Hartree-Fock Molecular-Orbital Examination of Structural Pathways Between ($Cu^{2+}\phi_n$) Coordination Geometries 163

8.3.1 (4+2)-Octahedral <---> Square-Pyramidal 166

8.3.2 (4+2)-Octahedral <---> Triangular-Bipyramidal 167

8.3.3 (4+2)-Octahedral <---> Square-Planar 171

8.3.4 Square-Pyramidal <---> Square-Planar 177

8.3.5 Square-Pyramidal <---> Triangular-Bipyramidal 178

8.3.6 Triangular-Bipyramidal <---> Square-Pyramidal 178

8.4 Discussion 183

9. MIXED-LIGAND $Cu^{2+}\Phi_6$ OCTAHEDRA IN MINERALS 188

9.1 Mixed-Ligand $Cu^{2+}\Phi_6$ Octahedra 188

9.2 Rietveld Refinement of the Crystal Structure of Tolbachite, $CuCl_2$ 189

9.2.1 Experimental 189

9.2.2 Structure Refinement 190

9.2.3 Structure Description 191

9.2.4 Synthetic Compounds Containing $Cu^{2+}Cl_6$ Octahedra . . 191

9.3 Mixed-Ligand $Cu^{2+}\Phi_6$ Octahedra in Minerals 196

9.3.1 $Cu^{2+}\Phi_6$ With $\Phi = 4(O^{2-}, OH^-, H_2O)$ and 2Cl 198

9.3.2 $Cu^{2+}\Phi_6$ With $\Phi = 5(O^{2-}, OH^-, H_2O)$ and 1Cl 198

9.3.3 $Cu^{2+}\Phi_6$ With $\Phi = 2(O^{2-}, OH^-, H_2O)$ and 4Cl 201

9.4 Discussion 201

10. *AB INITIO* MOLECULAR-ORBITAL STUDIES OF $Cu^{2+}\phi_6$ MIXED-LIGAND OCTAHEDRA 206

10.1 Introduction 206

10.2 Molecular-Orbital Studies of Mixed-Ligand $Cu^{2+}\Phi_6$ Octahedra 207

10.2.1 Molecular-Orbital Calculations for $Cu^{2+}\phi_6$ Mixed-Ligand Octahedra with $\Phi = 4(O^{2-}, OH^-, H_2O) + 2(Cl)$ 208

10.2.2 Molecular-Orbital Calculations for $Cu^{2+}\phi_6$ Mixed-Ligand Octahedra with $\Phi = 5(O^{2-}, OH^-, H_2O) + 1(Cl)$ 217

10.3 Discussion 222

11. SOLID-SOLUTION IN Cu^{2+} OXYSALT MINERALS 223

11.1 Introduction 223

11.2 The Substitution $M^{2+} \leftrightarrow Cu^{2+}$ in Cu^{2+} Oxysalt Minerals 225

11.2.1 $M^{2+} = Zn$ 225

11.2.2 $M^{2+} = Fe^{2+}$, Ni and Mg 228

11.3 Synthetic Cu^{2+}-Bearing Solid Solutions 228

12. JAHN-TELLER DRIVEN PHASE TRANSITIONS: THE MF_2 RUTILE-TYPE STRUCTURE 231

12.1 Introduction and Previous Work 231

12.2 Synthesis of $(Mg_{1-x}Cu_x^{2+})F_2$, $(Zn_{1-x}Cu_x^{2+})F_2$ and $(Ni_{1-x}Cu_x^{2+})F_2$ . . . 233

12.3 X-Ray Characterization of $(Mg_{1-x}Cu_x^{2+})F_2$, $(Zn_{1-x}Cu_x^{2+})F_2$ and $(Ni_{1-x}Cu_x^{2+})F_2$ 234

12.4 Phase Transitions in $(Mg_{1-x}Cu_x^{2+})F_2$, $(Zn_{1-x}Cu_x^{2+})F_2$ and $(Ni_{1-x}Cu_x^{2+})F_2$ 235

12.5 Rietveld Structure Refinements for $(Mg_{1-x}Cu_x^{2+})F_2$ and $(Zn_{1-x}Cu_x^{2+})F_2$ 246

12.5.1 Rietveld Refinements of MgF_2, ZnF_2 and NiF_2 246

12.5.2 Standard Deviations and Rietveld Structure Refinements 248

12.5.3 CuF_2 258

12.5.4 The $(Zn_{1-x}Cu_x^{2+})F_2$ Series 261

12.5.5 The $(Mg_{1-x}Cu_x^{2+})F_2$ Series 263

12.6 Mechanisms of the Phase Transition in the $(M_{1-x}Cu_x^{2+})F_2$ Series 268

13. JAHN-TELLER DRIVEN PHASE TRANSITIONS: THE KMF_3 PEROVSKITE-TYPE STRUCTURE 277

13.1 Introduction and Previous Work 277

13.2 Synthesis of $K(Zn_{1-x}Cu_x^{2+})F_3$ and $K(Mg_{1-x}Cu_x^{2+})F_3$ 279

13.3 X-Ray Powder-Diffraction Characterization 279

13.4 Rietveld Structure Refinements 285

13.5 The Phase Transition in $K(Zn_{1-x}Cu_x^{2+})F_3$ and $K(Mg_{1-x}Cu_x^{2+})F_3$. 286

14. SUMMARY AND CONCLUSIONS 297

14.1 Purpose of this Research 297

14.2 $Cu^{2+}\phi_6$ Octahedra in Cu^{2+} Oxysalt Minerals 299

14.2.1 Observed $Cu^{2+}\phi_6$ Octahedral Geometries 300

14.2.2 The Dynamic Jahn-Teller Effect in Cu^{2+} Oxysalt Minerals 301

14.2.3 Hartree-Fock Molecular-Orbital Calculations for $Cu^{2+}\phi_6$ Clusters 302

14.2.4 Future Work 303

14.3 Development of a $Cu^{2+}\phi_6$ Anisotropic Potential 304

14.4 Square-Pyramidal and Triangular-Bipyramidal Coordinations 306

14.5 Structural Pathways in Cu^{2+} Oxysalt Minerals 307

14.6 Mixed-Ligand $Cu^{2+}\Phi_6$ Octahedra in Cu^{2+} Oxysalt Minerals . . . 309

14.7 Solid-Solution in Cu^{2+} Oxysalt Minerals 311

14.8 Jahn-Teller Driven Phase Transitions 312

14.8.1 The MF_2 Rutile-Type Structure 312

14.8.2 The KMF_3 Perovskite-Type Structure 313

14.8.3 Jahn-Teller Driven Phase Transitions 314

14.8.4 Future Work 315

14.9 Conclusion 315

REFERENCES 317

APPENDIX A. STEP-SCAN X-RAY POWDER-DIFFRACTION DATA FOR TOLBACHITE 332

APPENDIX B. X-RAY POWDER-DIFFRACTION DATA FOR $(Mg_{1-x}Cu_x^{2+})F_2$ 337

APPENDIX C. X-RAY POWDER-DIFFRACTION DATA FOR $(Zn_{1-x}Cu_x^{2+})F_2$ 349

APPENDIX D. X-RAY POWDER-DIFFRACTION DATA FOR $(Ni_{1-x}Cu_x^{2+})F_2$ 360

APPENDIX E. STEP-SCAN X-RAY POWDER-DIFFRACTION DATA FOR $Cu^{2+}F_2$ 372

APPENDIX F. STEP-SCAN X-RAY POWDER-DIFFRACTION DATA FOR MgF_2 377

APPENDIX G. STEP-SCAN X-RAY POWDER-DIFFRACTION DATA FOR ZnF_2 382

APPENDIX H. STEP-SCAN X-RAY POWDER-DIFFRACTION DATA FOR NiF_2 387

APPENDIX I. STEP-SCAN X-RAY POWDER-DIFFRACTION DATA FOR $(Zn_{1-x}Cu_x^{2+})F_2$ 392

APPENDIX J. STEP-SCAN X-RAY POWDER-DIFFRACTION DATA FOR $(Mg_{1-x}Cu_x^{2+})F_2$ 425

APPENDIX K. X-RAY POWDER-DIFFRACTION DATA FOR $K(Zn_{1-x}Cu_x^{2+})F_2$ 447

APPENDIX L. X-RAY POWDER-DIFFRACTION DATA FOR $K(Mg_{1-x}Cu_x^{2+})F_2$ 454

APPENDIX M. STEP-SCAN X-RAY POWDER-DIFFRACTION DATA FOR $K(Zn_{1-x}Cu_x^{2+})F_3$ 459

APPENDIX N. STEP-SCAN X-RAY POWDER-DIFFRACTION DATA FOR $K(Mg_{1-x}Cu_x^{2+})F_3$ 479

LIST OF FIGURES

FIGURE

1.1. Common Cu^{2+} coordination geometries in Cu^{2+} oxysalt minerals 2

1.2 Polyhedral structure representations of chalcanthite and pentahydrite 5

1.3 Polyhedral structure representations of chalcocyanite and zincosite 6

1.4 The MF_2 rutile-type structures 7

1.5 Comparison of the brucite and spertiniite structures 8

1.6 Examples of Cu^{2+} oxysalt structures with $Cu^{2+}\phi_6$ octahedra . . . 10

1.7 Examples of Cu^{2+} oxysalt structures with $Cu^{2+}\phi_5$ polyhedra . . . 13

1.8 Examples of Cu^{2+} oxysalt structures with $Cu^{2+}\phi_4$ polyhedra . . . 14

2.1 The electron-energy levels for Cu^{2+} in spherical, holosymmetric and distorted octahedral fields 20

2.2 The S_{2a} and S_{2b} displacement coordinates of the E_g mode of octahedral vibration 23

2.3 The Mexican-hat potential 23

2.4 The warped Mexican-hat potential 25

2.5 Circular cross-sections through warped Mexican-hat potentials 27

2.6 Distribution of Cu-ϕ bond-lengths in all symmetrically distinct $Cu^{2+}\phi_6$ octahedra in Cu^{2+} oxysalt minerals 31

2.7 Distribution of <Cu-ϕ_{eq}> distances in all symmetrically distinct $Cu^{2+}\phi_6$ octahedra in Cu^{2+} oxysalt minerals 32

2.8 Distribution of <Cu-ϕ_{ap}> distances in all symmetrically distinct $Cu^{2+}\phi_6$ octahedra in Cu^{2+} oxysalt minerals 33

2.9 Distribution of $\Delta_{ap\text{-}eq}$ in all symmetrically distinct $Cu^{2+}\phi_6$ octahedra observed in Cu^{2+} oxysalt minerals 35

2.10 Distribution of Cu-ϕ bond-lengths in symmetrically distinct (4+2)-distorted $Cu^{2+}\phi_6$ octahedra in Cu^{2+} oxysalt minerals 36

2.11 <Cu-ϕ> bond-length versus Δ for (4+2)-distorted $Cu^{2+}\phi_6$ octahedra in Cu^{2+} oxysalt minerals 38

2.12 The $Cu^{2+}\phi_6$ distorted trigonal-prism in lyonsite 40

2.13 Polyhedral structural representations of demesmaekerite 47

2.14 Polyhedral structural representations of volborthite 49

2.15 Polyhedral structural representations of $KCu_3^{2+}(OH)_2[(AsO_4)H(AsO_4)]$ 52

2.16 Polyhedral structural representations of bayldonite 56

2.17 Bond-length distortion parameters for (4+2)-distorted $Cu^{2+}\phi_6$ octahedra in Cu^{2+} oxysalt minerals 59

2.18 Temperature dependence of the Cu-ϕ bond-lengths in $(NH_4)_2Cu^{2+}(OH_2)_6(SO_4)_2$ 66

2.19 The crystal structure of cyanochroite 73

2.20 Anisotropic-displacement ellipsoids for the $Cu^{2+}\phi_6$ octahedra in $KCu_3^{2+}(OH)_2[(AsO_4)H(AsO_4)]$ 76

2.21 Anisotropic-displacement ellipsoids for the Cu-ϕ bonds in $KCu_3^{2+}(OH)_2[(AsO_4)H(AsO_4)]$ 77

2.22 The local environment of the $Cu^{2+}(1)\phi_6$ octahedron in $KCu_3^{2+}(OH)_2[(AsO_4)H(AsO_4)]$ 78

2.23 Anisotropic-displacement ellipsoids for the AsO_4 tetrahedron in $KCu_3^{2+}(OH)_2[(AsO_4)H(AsO_4)]$ 80

2.24 The anisotropic-displacement ellipsoid for the O(1) position in volborthite 81

2.25 Anisotropic-displacement ellipsoids for $Cu^{2+}\phi_6$ octahedra in bayldonite 83

2.26 Anisotropic-displacement ellipsoids for the AsO_4 tetrahedron in bayldonite 85

2.27 Anisotropic-displacement ellipsoids for the $Cu(1)\phi_6$ octahedron in demesmaekerite 88

4.1 The $[Cu^{2+}(H_2O)_6]^{2+}$ cluster 101

5.1 The potential-energy surface for $[Cu^{2+}(OH)_6]^{4-}$ 115

5.2 Minimum-energy pathway across the $[Cu^{2+}(OH)_6]^{4-}$ potential . . 116

6.1 The crystal structure of tenorite 123

6.2 Polyhedral structure representations of chalcocyanite 127

6.3 Polyhedral structure representations of bonnatite 132

6.4 Polyhedral structure representations of lindgrenite 136

7.1 Five-coordinated copper polyhedra 146

7.2 The $[Cu^{2+}(OH)_5]^{3-}$ clusters 148

8.1 Possible structural pathways in Cu^{2+} oxysalt minerals 153

8.2 The (4+2)-distorted octahedral to square-pyramidal transition . 155

8.3 The (4+2)-distorted octahedral to triangular-bipyramidal transition 158

8.4 The (4+2)-distorted octahedral to square-planar transition 160

8.5 The square-pyramidal to square-planar transition 162

8.6 The square-pyramidal to triangular-bipyramidal transition . . . 164

8.7 The triangular-bipyramidal to square-planar transition 165

8.8 Optimized geometries along the structural pathway from (4+2)-distorted octahedral to square-pyramidal 169

8.9 Cluster energies along the structural pathway from (4+2)-distorted octahedral to square-pyramidal 170

8.10 Optimized geometries along the structural pathway from (4+2)-distorted octahedral to triangular-bipyramidal 173

8.11 Cluster energies along the structural pathway from (4+2)-distorted octahedral to triangular-bipyramidal 174

8.12 Optimized geometries and cluster energies along the structural pathway from (4+2)-distorted octahedral to square-planar 176

8.13 Optimized geometries and cluster energies along the structural pathway from square-pyramidal to square-planar 180

8.14 Cluster energies for the transition from square-pyramidal to triangular-bipyramidal 182

8.15 Optimized geometries and cluster energies along the structural pathway from triangular-bipyramidal to square-planar 185

8.16 Structural pathways between copper polyhedra 186

9.1 Observed and calculated X-ray powder patterns for tolbachite 193

9.2 The tolbachite structure 194

9.3 Average Cu-Cl bond-lengths versus Δ 197

9.4 The $Cu^{2+}\Phi_6$ octahedra in kamchatkite 202

10.1 The $[Cu^{2+}(H_2O)_4Cl_2]$ cluster 209

10.2 The $[Cu^{2+}(H_2O)_4(ClH)_2]^{2+}$ cluster 212

10.3 The potential-energy surface for the $[Cu^{2+}(H_2O)_4(ClH)_2]^{2+}$ cluster 215

10.4 The $[Cu^{2+}(H_2O)_5(ClH)]^{2+}$ cluster 218

10.5 Slices of the potential-energy surface for the $[Cu^{2+}(H_2O)_5(ClH)]^{2+}$ cluster 221

12.1 Octahedral distortion in $M^{2+}F_2$ rutile-type structures 232

12.2 Unit-cell parameters for the $(Mg_{1-x}Cu_x^{2+})F_2$ series 239

12.3 Unit-cell parameters for the $(Zn_{1-x}Cu_x^{2+})F_2$ series 241

12.4 Unit-cell parameters for the $(Ni_{1-x}Cu_x^{2+})F_2$ series 243

12.5 The β unit-cell parameter for the $(Mg_{1-x}Cu_x^{2+})F_2$, $(Zn_{1-x}Cu_x^{2+})F_2$ and $(Ni_{1-x}Cu_x^{2+})F_2$ series 245

12.6 Selected portions of the X-ray powder-diffraction patterns for the $(Zn_{1-x}Cu_x^{2+})F_2$ series 247

12.7 The observed and calculated X-ray powder pattern for MgF_2 . . 252

12.8 The observed and calculated X-ray powder pattern for ZnF_2 . . . 253

12.9 The observed and calculated X-ray powder pattern for NiF_2 . . . 254

12.10 The relationship between E.S.D.s and the Durbin-Watson d-statistic for MgF_2 257

12.11 The observed and calculated X-ray powder pattern for $Cu^{2+}F_2$ 260

12.12 Rietveld unit-cell parameters for the $(Zn_{1-x}Cu_x^{2+})F_2$ series 265

12.13 Octahedral bond-lengths for $(Zn_{1-x}Cu_x^{2+})F_2$ series 267

12.14 Rietveld unit-cell parameters for the $(Mg_{1-x}Cu_x^{2+})F_2$ series 270

12.15 Octahedral bond-lengths for the $(Mg_{1-x}Cu_x^{2+})F_2$ series 273

13.1 The perovskite-type structure 278

13.2 Unit-cell parameters for the $K(Zn_{1-x}Cu_x^{2+})F_3$ series 283

13.3 Unit-cell parameters for the $K(Mg_{1-x}Cu_x^{2+})F_3$ series 284

13.4 Rietveld unit-cell parameters for the $K(Zn_{1-x}Cu_x^{2+})F_3$ series 291

13.5 Bond-lengths for the $K(Zn_{1-x}Cu_x^{2+})F_3$ series 292

13.6 Rietveld unit-cell parameters for the $K(Mg_{1-x}Cu_x^{2+})F_3$ series 293

13.7 Bond-lengths for the $K(Mg_{1-x}Cu^{2+}_x)F_3$ series 294

13.8 The observed and calculated X-ray powder pattern for $KCu^{2+}F_3$ 295

LIST OF TABLES

TABLE

2.1 (2+4)-distorted $Cu^{2+}\phi_6$ geometries in minerals 45

2.2 Unit-cell dimensions and octahedral $Cu^{2+}\phi_6$ bond-lengths in volborthite, bayldonite and $KCu_3^{2+}(OH)_2[(AsO_4)H(AsO_4)]$ 54

2.3 Examples of (2+2+2)-distorted $Cu^{2+}\phi_6$ octahedra in Cu^{2+} oxysalt minerals 61

2.4 Octahedral bond-lengths in $(NH_4)_2Cu^{2+}(OH_2)_6(SO_4)_2$ and $M^+_2Cu^{2+}(OH_2)_6(SO_4)_2$ 65

4.1 Optimized geometries and energies for octahedral clusters 103

4.2 Optimized geometries and energies for the $[Cu^{2+}(OH)_6]^{4-}$ cluster 106

5.1 *Ab initio* octahedral Cu-ϕ potential parameters 119

6.1 Structural parameters for tenorite 124

6.2 Calculated tenorite structures 125

6.3 Structure parameters for chalcocyanite 129

6.4 Calculated chalcocyanite structures 130

6.5 Structure parameters for bonnatite 134

6.6 Selected bond-lengths for minimum-energy bonnatite structures 135

6.7 Structure parameters for lindgrenite 138

6.8 Selected bond-lengths for minimum-energy lindgrenite structures 139

7.1 Cu^{2+} oxysalt minerals with ($Cu^{2+}\phi_5$) polyhedra 144

7.2 Optimized geometries and energies for $Cu^{2+}\phi_5$ clusters 150

8.1 Cu^{2+} oxysalt minerals containing (4+1+1)-distorted $Cu^{2+}\phi_6$ octahedra 156

8.2 Examples of Cu-ϕ coordination geometries intermediate between (4+2)-distorted octahedral and square-planar 161

8.3 Reoptimized $[Cu^{2+}(OH)_6]^{4-}$ cluster geometries along the structural pathway from (4+2)-distorted octahedral to square-pyramidal . 168

8.4 Reoptimized $[Cu^{2+}(OH)_6]^{4-}$ cluster geometries along the structural pathway from (4+2)-distorted octahedral to triangular-bipyramidal 172

8.5 Reoptimized $[Cu^{2+}(OH)_6]^{4-}$ cluster geometries along the structural pathway from (4+2)-distorted octahedral to square-planar 175

8.6 Reoptimized $[Cu^{2+}(OH)_5]^{3-}$ cluster geometries along the structural pathway from square-pyramidal to square-planar 179

8.7 Energies of clusters transitional between triangular-bipyramidal and square-pyramidal 181

8.8 Reoptimized $[Cu^{2+}(OH)_5]^{3-}$ cluster geometries along the structural pathway from triangular-bipyramidal to square-planar 184

9.1 Final structure parameters, R-indices, bond-lengths and bond-angles in tolbachite 192

9.2 $Cu^{2+}Cl_6$ octahedral geometries in inorganic compounds 195

9.3 Mixed-ligand $Cu^{2+}\Phi_6$ octahedra in Cu^{2+} oxysalt minerals with $\Phi = 4(O^{2-}, OH^-, H_2O) + 2Cl$ 199

9.4 Mixed-ligand $Cu^{2+}\Phi_6$ octahedra in Cu^{2+} oxysalt minerals with $\Phi = 5(O^{2-}, OH^-, H_2O) + 1Cl$ 199

9.5 Mixed-ligand $Cu^{2+}\Phi_6$ octahedra in Cu^{2+} oxysalt minerals with $\Phi = 2(O^{2-}, OH^-, H_2O) + 4Cl$ 203

10.1 Optimized geometries for $Cu^{2+}\Phi_6$ mixed-ligand octahedra with $\Phi = 4(O^{2-}, OH^-, H_2O) + 2Cl$ 210

10.2 Optimized geometries for $Cu^{2+}\Phi_6$ mixed-ligand octahedra with $\Phi = 5(O^{2-}, OH^-, H_2O) + 1Cl$ 219

12.1 Unit-cell parameters for the $(Mg_{1-x}Cu_x^{2+})F_2$ series 236

12.2 Unit-cell parameters for the $(Zn_{1-x}Cu_x^{2+})F_2$ series 237

12.3 Unit-cell parameters for the $(Ni_{1-x}Cu_x^{2+})F_2$ series 238

12.4 Refined structure parameters, R-indices and bond-lengths for MgF_2 compared to single-crystal results 249

12.5 Refined structure parameters, R-indices and bond-lengths for NiF_2 compared to single-crystal results 250

12.6 Refined structure parameters, R-indices and bond-lengths for ZnF_2 compared to single-crystal results 251

12.7 Refined structure parameters, R-indices and bond-lengths for CuF_2 259

12.8 Refined structure parameters and R-indices for the $(Zn_{1-x}Cu_x^{2+})F_2$ series 262

12.9 Bond-lengths for the $(Zn_{1-x}Cu_x^{2+})F_2$ series 264

12.10 Refined structure parameters and R-indices for the $(Mg_{1-x}Cu_x^{2+})F_2$ series 269

12.11 Bond-lengths for the $(Mg_{1-x}Cu_x^{2+})F_2$ series 272

13.1 Unit-cell parameters for the $K(Zn_{1-x}Cu_x^{2+})F_3$ series 281

13.2 Unit-cell parameters for the $K(Mg_{1-x}Cu_x^{2+})F_3$ series 282

13.3 Rietveld refined structures and R-indices for the $K(Zn_{1-x}Cu_x^{2+})F_3$ series 287

13.4 Rietveld refined structures and R-indices for the $K(Mg_{1-x}Cu_x^{2+})F_3$ series 288

13.5 Selected bond-lengths for the $K(Zn_{1-x}Cu_x^{2+})F_3$ series 289

13.6 Selected bond-lengths for the $K(Mg_{1-x}Cu_x^{2+})F_3$ series 290

Chapter 1

Introduction

1.1 Cu^{2+} Oxysalt Minerals.

There have been over two hundred and thirty Cu^{2+} oxysalt, oxide and hydroxide minerals (hereafter referred to as Cu^{2+} oxysalt minerals) described to date, and the crystal structure arrangements are known for slightly less than half of these. Cu^{2+} oxysalt minerals show a myriad of structural varieties which are often not isostructural with non-Cu^{2+} oxysalt analogues. The range of structure types in Cu^{2+} oxysalt minerals is largely a result of the diversity of coordination polyhedra associated with the Cu^{2+} ion. Divalent copper is commonly observed in six-coordinated octahedral, five-coordinated square-pyramidal and triangular-bipyramidal, and four-coordinated square-planar geometries (Fig. 1.1). Furthermore, by far the most common coordination geometry is octahedral, which almost invariably involves a very strong distortion away from holosymmetric octahedral symmetry, to the extent that it is often difficult to decide on the most appropriate coordination.

As aptly put by Brown (1992), "It is one of the striking observations of inorganic structural chemistry that most cations do have regular, or near regular coordination spheres and we only find it necessary to explain deviations from this regularity". The highly distorted $Cu^{2+}\phi_6$ ($\phi = O^{2-}$, OH^-, H_2O) octahedra in minerals, organometallic and inorganic compounds are rationalized as being due to the electronic instability of the d^9 configuration of Cu^{2+} in octahedral coordination, as predicted by the Jahn-Teller theorem (Jahn and Teller, 1937). Simply put, Cu^{2+} in a holosymmetric octahedral

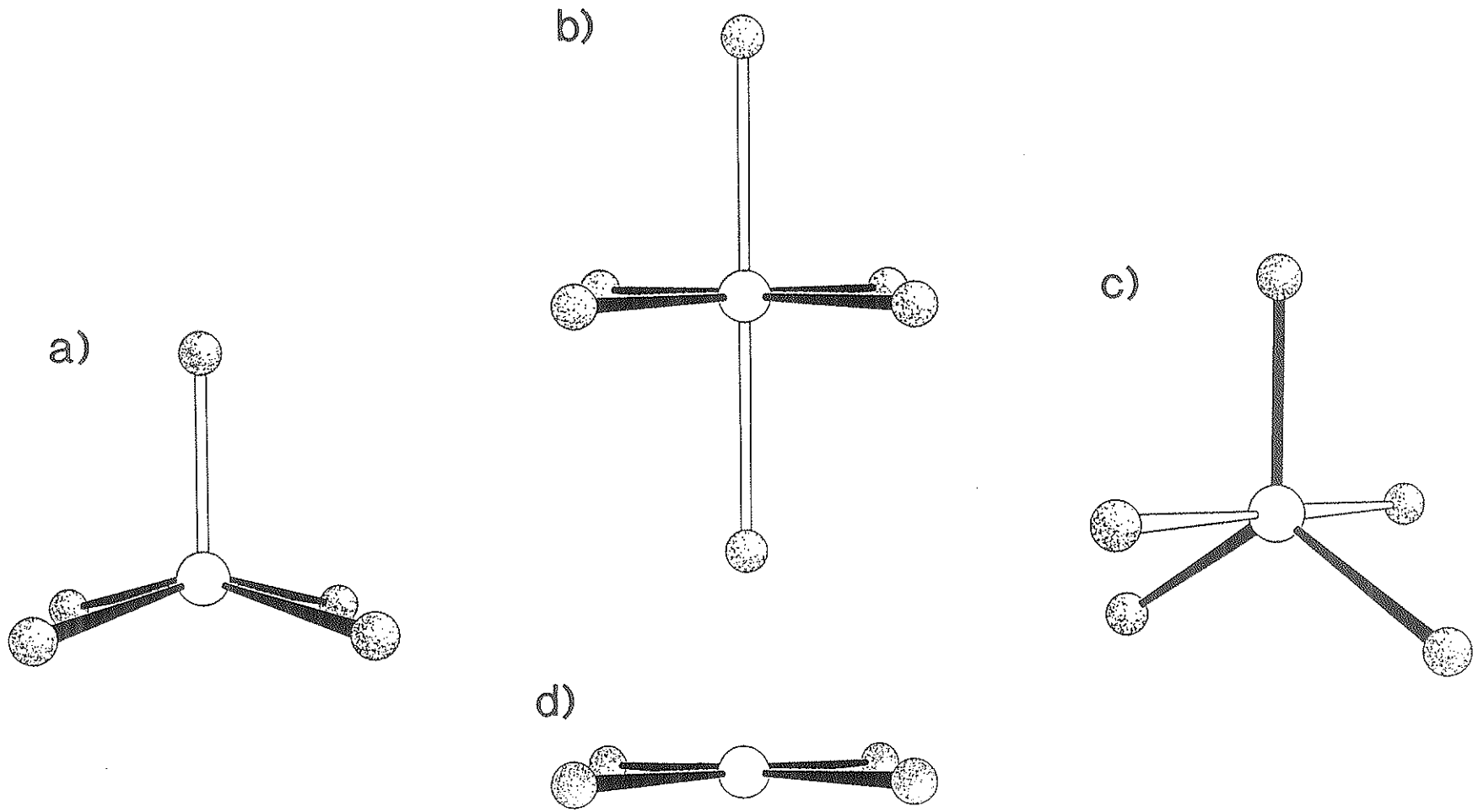

Figure 1.1. Common Cu^{2+} coordination geometries in Cu^{2+} oxysalt minerals. a) square-pyramidal; b) octahedral; c) triangular-bipyramidal; d) square-planar. Cu^{2+} are open circles and the coordinating anions are shaded with a random-dot pattern. Apical bonds are drawn as two parallel lines and equatorial bonds are drawn as heavy lines.

environment has an energetically degenerate state. The Jahn-Teller theorem states that a nonlinear molecule containing a degenerate electronic state is unstable with respect to any distortion that lifts the degeneracy. The $Cu^{2+}\phi_6$ octahedron spontaneously distorts to remove the electronic degeneracy, acquiring additional stabilization energy in the process (see Chapter 2); thus the cation polyhedron is no longer regular.

An oxysalt crystal structure may be envisaged as a three-dimensional array of cation-anion polyhedra that are joined through corner-, edge- or face-sharing, or via hydrogen bonds. If the structure is to be stable, the requirements of cation-anion chemical bonding and the three-dimensional geometrical constraints of the structure must be satisfied. Generally, most mineral structures involve fairly regular polyhedra. In the case of Cu^{2+} oxysalt minerals, the additional constraint that the $Cu^{2+}\phi_6$ octahedron must be distorted is imposed upon the structure. The structure may be able to accommodate the octahedral distortion, thus allowing the Cu^{2+} structure to have the same connectivity as a non-Cu^{2+} analogue. This is most likely in structures that contain a large number of weak bonds, or in structures that contain octahedra that are already distorted due to steric effects. Alternatively, the structure may be significantly destabilized by the octahedral distortion, to the extent that some other structural connectivity will prove to be a more stable alternative. In this case, the Cu^{2+} structure will have a connectivity that differs from that of the non-Cu^{2+} analogue.

Eby (1988) studied various Cu^{2+} oxysalt mineral structures using distance-least-squares (DLS) structural modelling. The DLS procedure determines the structure that best fits operator-controlled bond-length requirements (and includes no consideration of the structure energy). Eby

(1988) found that some Cu^{2+} oxysalt mineral structures could be adjusted to the point where the $Cu^{2+}\phi_6$ octahedra are holosymmetric. Other Cu^{2+} oxysalt minerals have connectivities that *require* a distorted $Cu^{2+}\phi_6$ octahedron. In the latter case, adjustments towards a holosymmetric $Cu^{2+}\phi_6$ octahedron resulted in impossible atomic separations.

Cu^{2+} oxysalt minerals may thus be classified on the basis of their relationships with non-Cu^{2+} oxysalts:

(1) The Cu^{2+} structure is strictly isostructural with the non-Cu^{2+} analogue structure. Examples include chalcanthite [$Cu^{2+}SO_4 \cdot 5H_2O$] and pentahydrite [$MgSO_4 \cdot 5H_2O$], in the space group $P\bar{1}$ (Fig. 1.2), and chalcocyanite [$Cu^{2+}SO_4$] and zincosite [$ZnSO_4$] in the space group Pnma (Fig. 1.3).

(2) The Cu^{2+} structure is a lower-symmetry distortion of the non-Cu^{2+} structure, but the connectivity of the two structures is identical. Examples include the rutile-type structures of $Cu^{2+}F_2$ (space group $P2_1/n$) and MgF_2 (space group $P4_2/mnm$) (Fig. 1.4).

(3) The Cu^{2+} structure shows a different structural connectivity than the non-Cu^{2+} structure. Examples are spertiniite [$Cu^{2+}(OH)_2$] and brucite [$Mg(OH)_2$] (Fig. 1.5).

Eby (1988) and Eby and Hawthorne (1993) developed a structural hierarchy for Cu^{2+} oxysalt minerals that is based upon polyhedral polymerization, and treated 93 Cu^{2+} oxysalt minerals in their classification. The largest group corresponds to those minerals containing Cu^{2+} in octahedral coordination. Within this group, divisions were made on the

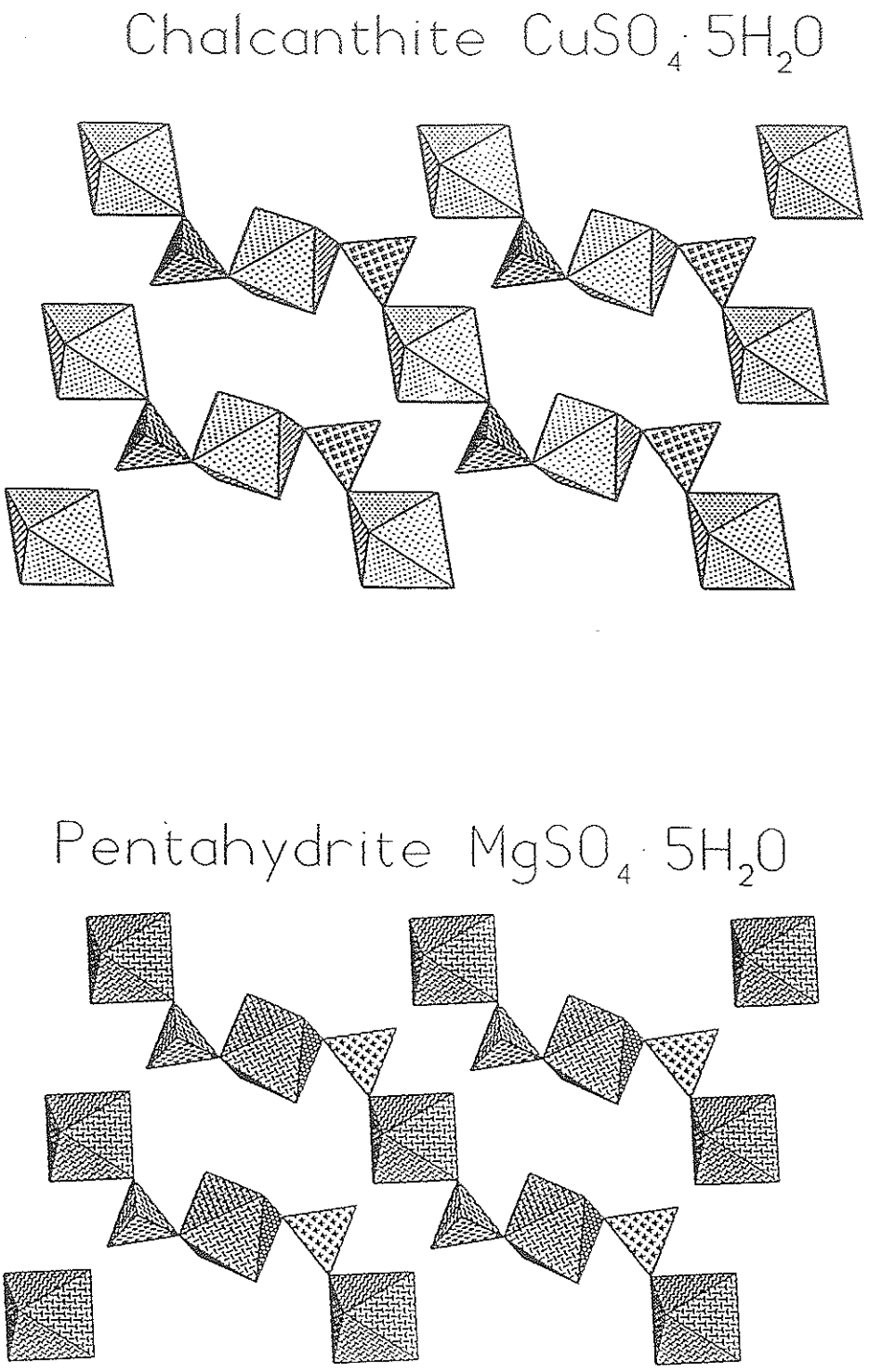

Figure 1.2. Polyhedral structure representations of chalcanthite, $Cu^{2+}SO_4 \cdot 5H_2O$ and pentahydrite, $MgSO_4 \cdot 5H_2O$, which are isostructural in the space group P1. Polyhedral shadings are crosses for sulphur tetrahedra, a regular dot pattern for copper octahedra, and a herring-bone pattern for magnesium octahedra.

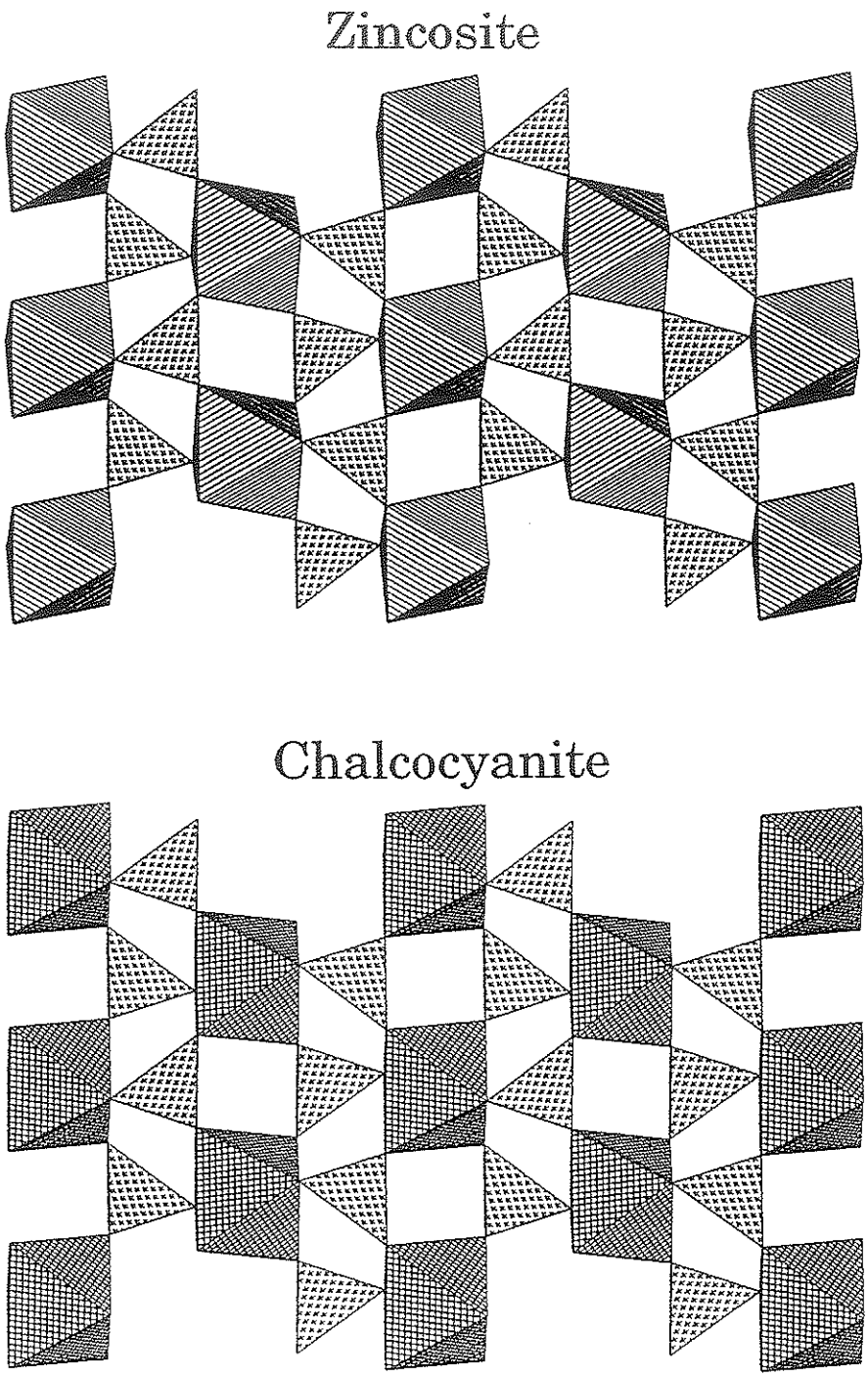

Figure 1.3. Polyhedral structure representations of chalcocyanite, $Cu^{2+}SO_4$, and zincosite, $ZnSO_4$, which are isostructural in the space group Pnma. Polyhedral shadings are crosses for sulphur tetrahedra, parallel lines for zinc octahedra, and cross-hatching for copper octahedra.

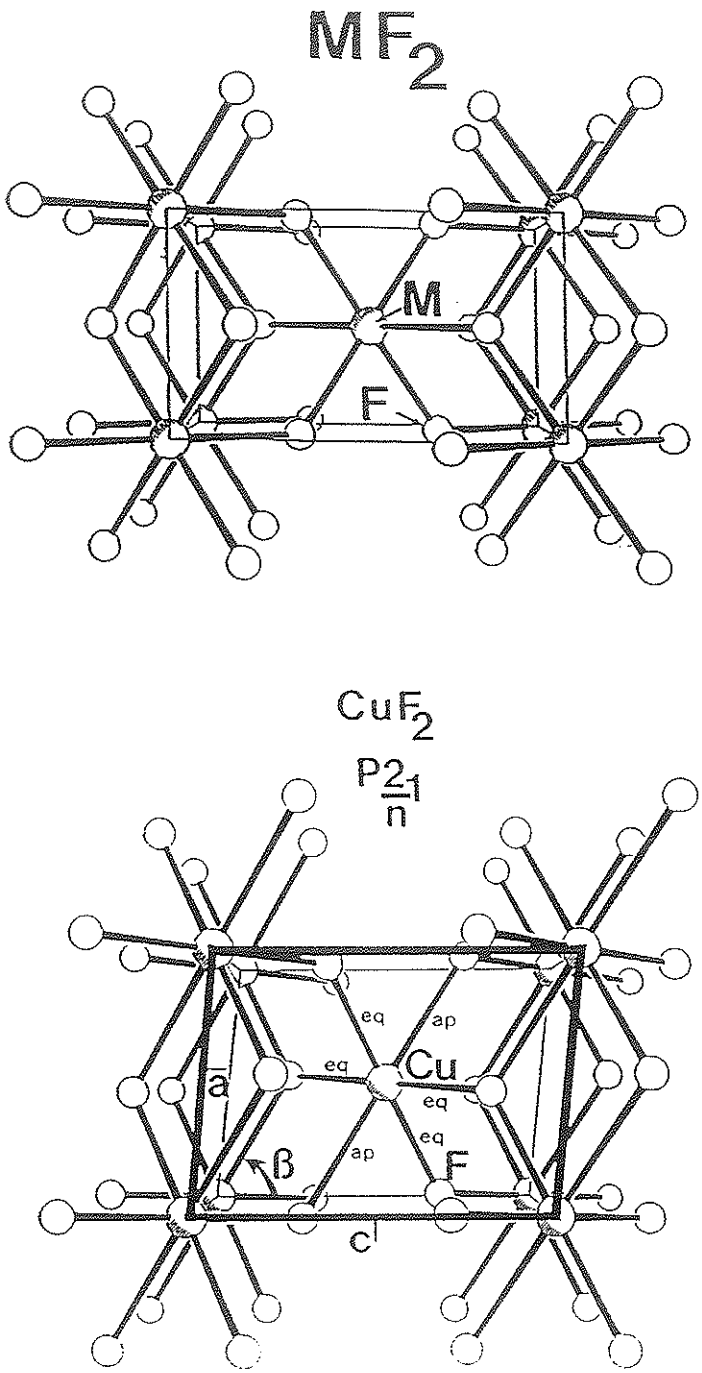

Figure 1.4. The tetragonal rutile-type MF_2 structure compared to the monoclinic $Cu^{2+}F_2$ rutile-derivative structure.

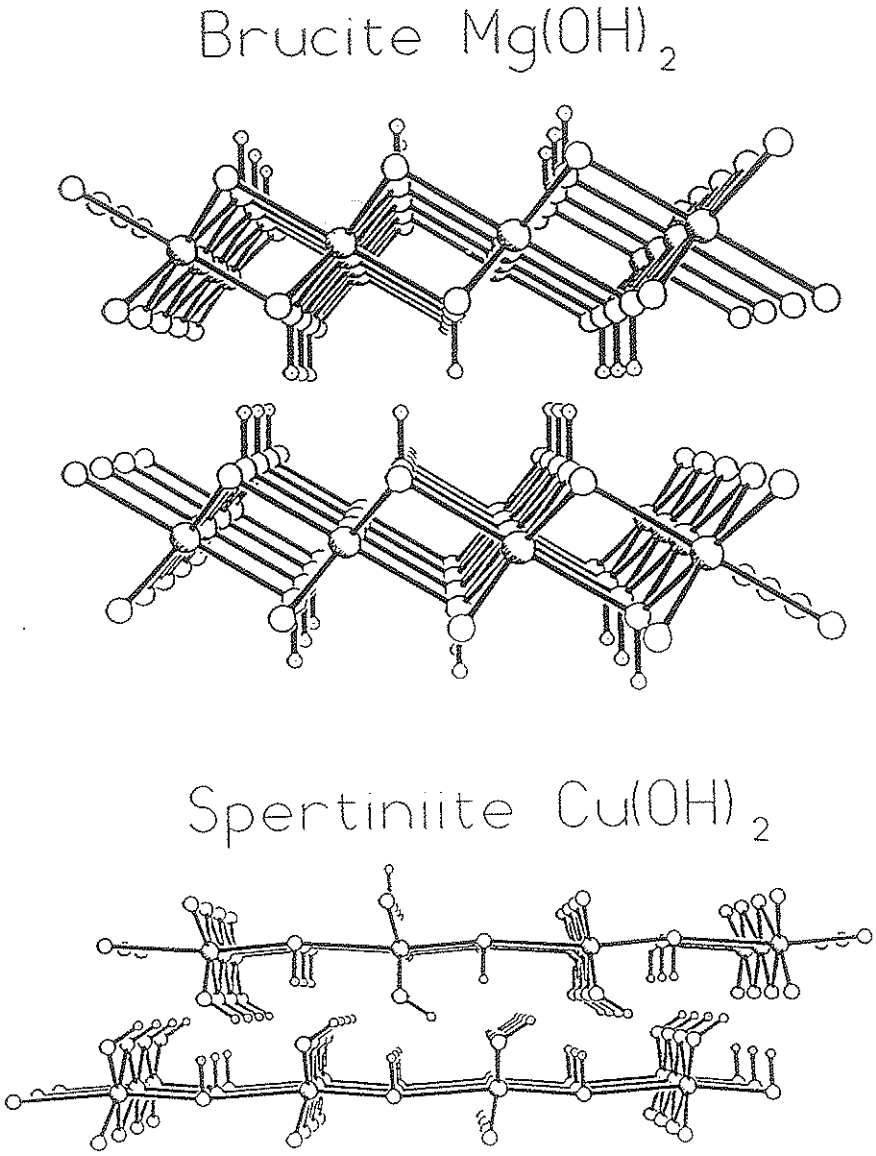

Figure 1.5. The brucite structure compared to the spertiniite structure. Cations are shaded in the lower left corners.

basis of polymerization: structures containing isolated polyhedra, finite polyhedral clusters, infinite one-dimensional polyhedral chains, infinite two-dimensional polyhedral sheets, and infinite three-dimensional polyhedral frameworks. Examples of each of the structural types are given in Figure 1.6. Further subdivisions were made based upon the nature of the polyhedral linkages within the major structural units.

Less-common groups of Cu^{2+} oxysalt minerals are those containing Cu^{2+} in five-coordination (triangular-bipyramidal and square-pyramidal) only (Fig. 1.7), four-coordination (square-planar) only (Fig. 1.8), and combinations of four- and six-coordinate Cu^{2+}, and five- and six-coordinate Cu^{2+}.

The structural hierarchy of Cu^{2+} oxysalt minerals presented by Eby and Hawthorne (1993) illustrates a very important feature of these minerals: There is extreme variety in the Cu^{2+} oxysalt structures, and they are often not related to their non-Cu^{2+} analogues. This diversity may only be rationalized by considering the distortion of $Cu^{2+}\phi_6$ octahedra required by the Jahn-Teller theorem, and the compliable nature of Cu^{2+} coordination polyhedra.

1.2 Outline of the Thesis

This thesis reports a number of theoretical and experimental lines of work on the nature of Cu^{2+} coordination in Cu^{2+} oxysalt minerals. Early parts of the thesis consider the Jahn-Teller effect as it pertains to a d^9 metal in an octahedral ligand-field. Detailed examination of the $Cu^{2+}\phi_6$ octahedral geometries in minerals follows, with a rationalization of the geometries observed, based primarily on consideration of both the static and

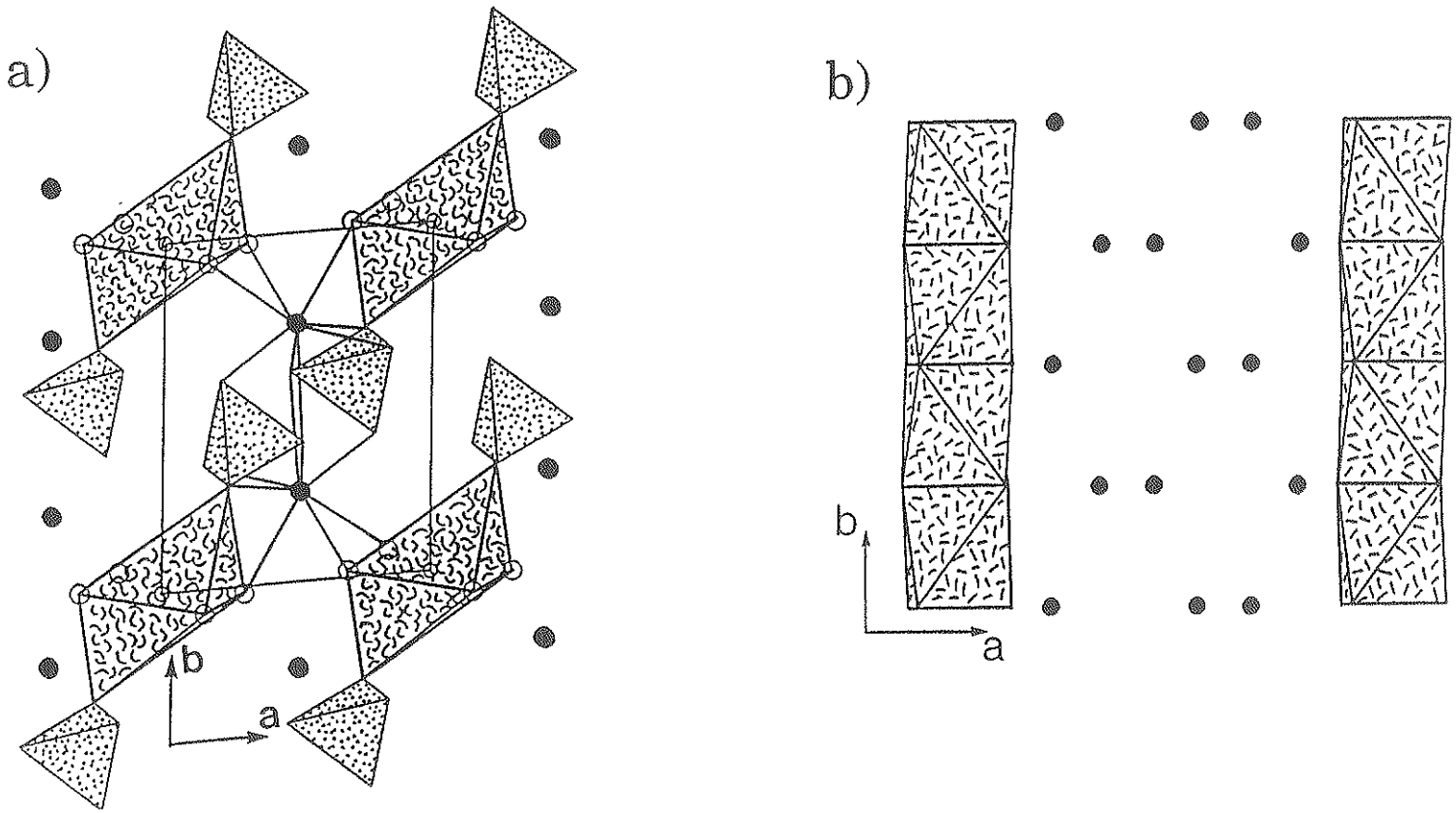

Figure 1.6. a) Henmilite, $Ca_2[Cu^{2+}\{B(OH)_4\}_2(OH)_4]$, a finite-cluster Cu^{2+} oxysalt mineral; $(Cu^{2+}\phi_6)$ octahedra are curl shaded, $(B\phi_4)$ tetrahedra are dot shaded, and most Ca-ϕ bonds are omitted for clarity. b) Chloroxiphite, $Pb_3[Cu^{2+}Cl_2(OH)_2O_2]$, an infinite-chain Cu^{2+} oxysalt mineral; $(Cu^{2+}\phi_6)$ octahedra are dash shaded, long Pb-ϕ bonds are omitted for clarity. Figures from Eby and Hawthorne (1993).

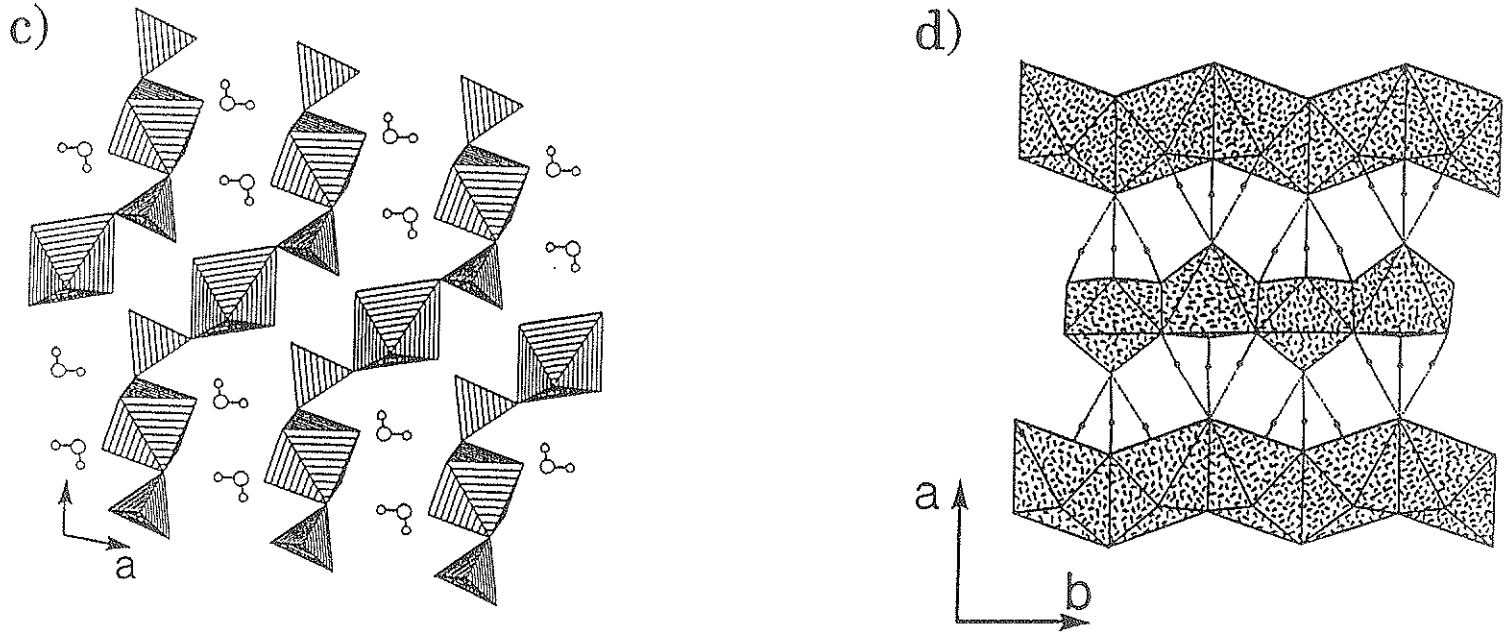

Figure 1.6. c) Chalcanthite, $Cu^{2+}SO_4 \cdot 5H_2O$, an infinite-chain Cu^{2+} oxysalt mineral; $(Cu^{2+}\phi_6)$ octahedra and $(S\phi_4)$ tetrahedra are shaded with parallel lines, hydrogen bonds are omitted for clarity. d) Botallackite, $[Cu_2^{2+}(OH)_3Cl]$, an infinite-sheet Cu^{2+} oxysalt mineral; $(Cu^{2+}\phi_6)$ octahedra are shaded with dashed lines, hydrogen bonds are given as broken lines. Figures from Eby and Hawthorne (1993).

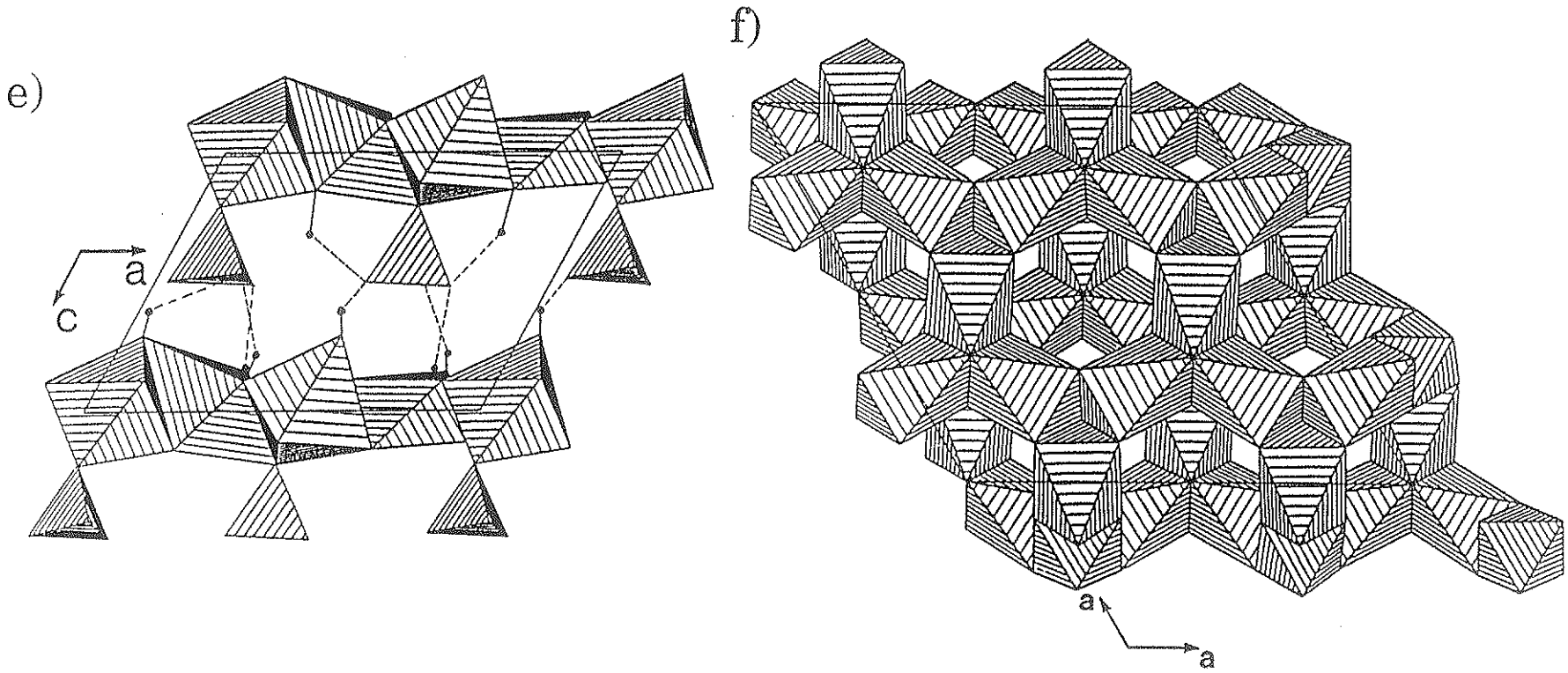

Figure 1.6. e) Posnjakite, $[Cu_4^{2+}(SO_4)(OH)_6(H_2O)]$, an infinite-sheet Cu^{2+} oxysalt mineral; $(Cu^{2+}\phi_6)$ octahedra and $(S\phi_4)$ tetrahedra are shaded with parallel lines, hydrogen bonds are given as broken lines. f) Atacamite, $[Cu_2^{2+}Cl(OH)_3]$, an infinite-framework Cu^{2+} oxysalt mineral; $(Cu^{2+}\phi_6)$ octahedra are shaded with parallel lines. Figures from Eby and Hawthorne (1993).

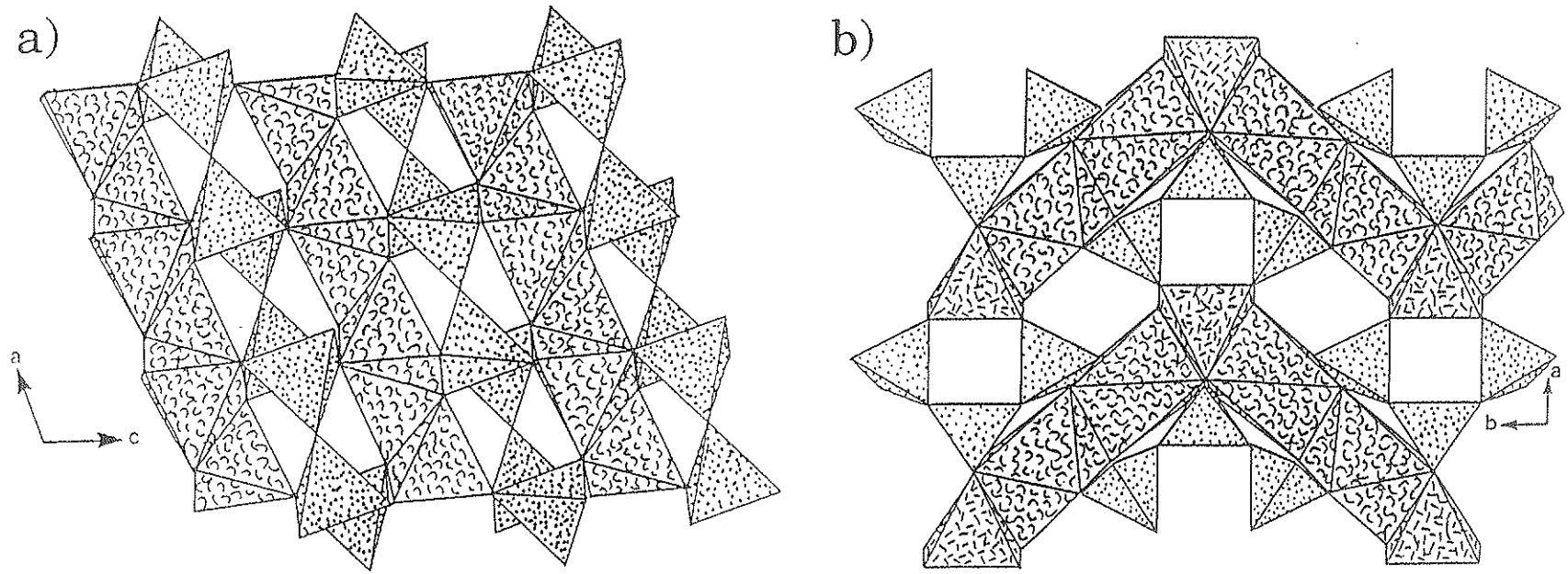

Figure 1.7. Cu^{2+} oxysalt minerals with five-coordinate Cu^{2+} polyhedra. a) Zeisite, $[Cu_2^{2+}(V_2O_7)]$; $(Cu^{2+}\phi_5)$ square-pyramids are curl shaded, $(V\phi_4)$ tetrahedra are dot shaded. b) Kinoite, $Ca_2[Cu_2^{2+}(Si_3O_8)(OH)_4]$; $(Cu^{2+}\phi_5)$ square-pyramids are dash shaded, $(S\phi_4)$ tetrahedra are dot shaded, $(Ca_2\phi_{10})$ dimers are curl shaded. Figures from Eby and Hawthorne (1993).

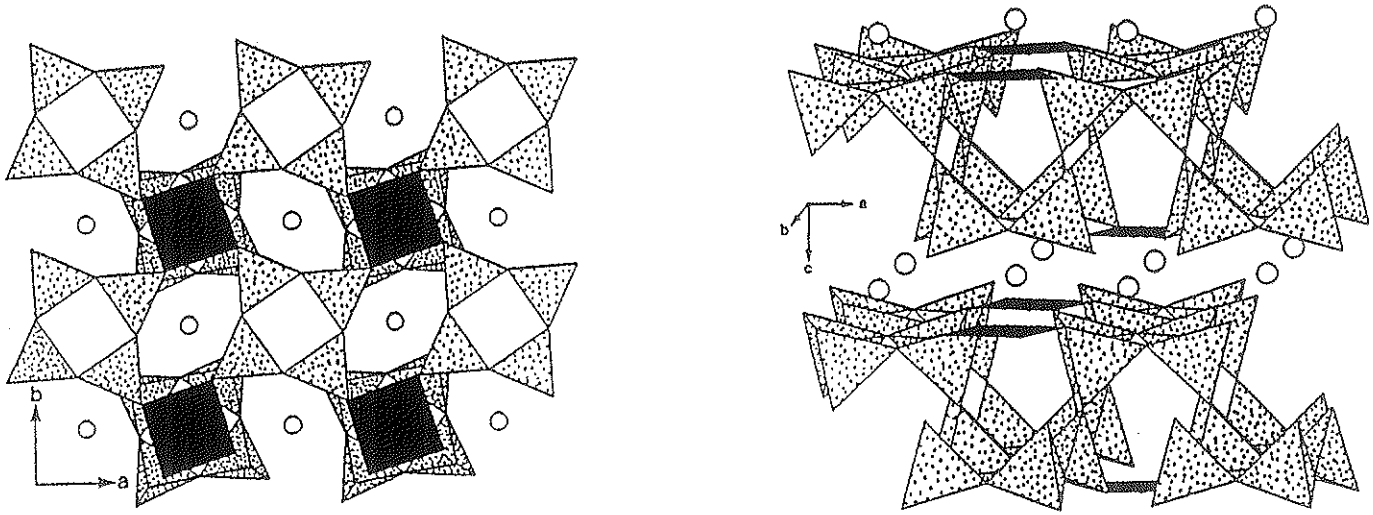

Figure 1.8. Cuprorivaite, $Ca[Cu^{2+}(Si_4O_{10})]$, a Cu^{2+} oxysalt mineral that contains four-coordinated Cu^{2+} polyhedra; $(Cu^{2+}\phi_4)$ squares are shaded black, $(Si\phi_4)$ tetrahedra are dot shaded. Figures from Eby and Hawthorne (1993).

dynamic Jahn-Teller effects. It will become clear that the Jahn-Teller effect exerts a very important influence on the structures of these minerals.

The theoretical work on the Cu^{2+} coordination polyhedra in minerals is based upon *ab initio* molecular-orbital calculations designed to study the common $Cu^{2+}\phi_n$ coordination geometries. The calculations examine the relative energies of the various coordination geometries and give minimum-energy geometries (in the absence of steric effects).

Many calculations involving static-energy minimization of a crystal structure have been done recently, and considerable success has been achieved in predicting structures and physical properties. However, in all such calculations reported to date, the ions involved were spherical and the potentials used were scalar. A potential-energy function for $Cu^{2+}\phi_6$ octahedra that includes the Jahn-Teller effect is developed here using *ab initio* molecular-orbital theory. This represents the first attempt at structural modelling involving ions with non-spherical potentials.

Coordination geometries transitional between the different ideal coordination geometries in Cu^{2+} oxysalt minerals are examined in detail to see if there are continuous "structural pathways" between the ideal geometries. *Ab initio* molecular-orbital calculations are used to examine the energetics and minimum-energy geometries of each of the structural pathways possible in Cu^{2+} oxysalt minerals.

Many Cu^{2+} oxysalt minerals contain mixed-ligand $Cu^{2+}\Phi_6$ octahedra ($\Phi = O^{2-}$, OH^-, H_2O and 1,2 or 4 Cl). The mixed-ligand nature of these octahedra makes identification of the distortion geometry difficult. Based on comparison with non-mixed-ligand octahedra and the $Cu^{2+}Cl_6$ octahedron in tolbachite ($Cu^{2+}Cl_2$), each of these mixed-ligand octahedra are classified

according to their distortion geometry. *Ab initio* molecular-orbital calculations are then used to study the energetics and geometrical relationships.

The interaction of Cu^{2+} ions in crystals is considered in the latter part of the thesis. Solid-solutions with the rutile (MF_2) and perovskite (KMF_3) (M = divalent metal) structures were synthesized, and the resulting materials were characterized by X-ray powder diffraction and Rietveld structure refinement.

1.3 Conventions Used in this Thesis

In $Cu^{2+}\phi_n$ polyhedra, Cu^{2+} is coordinated by *n* ligands with $\phi = O^{2-}$ and/or OH^- and/or H_2O only. If the coordination polyhedron is written as $Cu^{2+}\Phi_n$, the Cu^{2+} ion is coordinated by n ligands, at least one of which is Cl^-, i.e., Φ = Cl and/or O^{2-} and/or OH^- and/or H_2O. The $Cu^{2+}\Phi_n$ polyhedra are termed *mixed-ligand* polyhedra.

Octahedral $Cu^{2+}\phi_6$ geometry is very common in Cu^{2+} oxysalt minerals. However, the octahedron is almost always strongly distorted away from O_h symmetry. Here, octahedral coordination means that Cu^{2+} is coordinated by six ligands in an approximately octahedral arrangement. In the special case where the octahedron has O_h symmetry, the term *holosymmetric* is used. Cu^{2+} octahedra are often elongated such that there are four short equatorial (eq) bonds and two longer apical (ap) bonds. This type of octahedron is referred to as (4+2)-distorted, indicating that there are four short equatorial bonds and two long apical bonds. Likewise, a (2+4)-distorted octahedron has two short apical bonds and four longer equatorial bonds.

Average $Cu^{2+}\phi_n$ polyhedral bond-lengths are denoted by

<Cu-ϕ>. For example, in the case of a (4+2)-distorted $Cu^{2+}\phi_6$ octahedron, <Cu-ϕ> is the average Cu-ligand distance, <Cu-ϕ_{eq}> is the average Cu-equatorial-ligand distance, and <Cu-ϕ_{ap}> is the average Cu^{2+}-apical-ligand distance.

Most quantum chemists report the results of their calculations using *atomic units* (Levine, 1983). The atomic unit of charge is the proton charge (e^{-}), and the unit of energy is the Hartree:

$$1 \text{ Hartree} = e^{-2}/a_o \approx 27.212 \text{ eV} \approx 2625.4997 \text{ kJ/mole}$$

$$a_o = 1 \text{ bohr} \approx 0.52918 \text{ Å}$$

If the results of molecular-orbital calculations are reported in eV or Joules, the values depend on the currently accepted values of the physical constants, whereas reporting results in atomic units avoids this problem (Levine, 1983). Also, the Hartree is a suitable unit for discussion of a molecule's energy. For example, the energy of a H_2O molecule is ≈ 76.0 Hartrees. Using kJ/mole as an energy unit introduces Avogadro's number and gives a more cumbersome value of 199537.9 kJ/mole for the H_2O molecule.

Energies obtained from molecular-orbital calculations are reported here as Hartrees to maintain consistency with the quantum-mechanics literature, and the conversion factor from Hartrees to kJ/mole is given in table and figure captions where Hartrees are used.

Chapter 2

The Jahn-Teller Effect and $Cu^{2+}\phi_6$ ($\phi = O^{2-}$, OH^-, H_2O) Octahedra in Cu^{2+} Oxysalt Minerals

2.1 $Cu^{2+}\phi_6$ Octahedra in Cu^{2+} Oxysalt Minerals.

The $Cu^{2+}\phi_6$ ($\phi = O^{2-}$, OH^-, H_2O) octahedron is the most common Cu^{2+} coordination geometry in Cu^{2+} oxysalt minerals. The octahedral geometry is almost invariably distorted away from the holosymmetric arrangement. In most cases, the distorted octahedron has four short equatorial bonds and two longer apical bonds, a (4+2) distortion.

The prominent distortion of $Cu^{2+}\phi_6$ octahedral geometries is predicted by the Jahn-Teller theorem (Jahn and Teller, 1937) and is a result of the energetically degenerate electronic state of a d^9 ion in a holosymmetric octahedral ligand-field.

2.2 Jahn-Teller Theory

Jahn and Teller (1937) showed that any non-linear molecular system containing an energetically degenerate electronic state will be unstable with respect to some distorted state. A distortion will spontaneously occur, lowering the symmetry of the molecule and splitting the degenerate state.

2.2.1 Screening Arguments

Ligand-field arguments may be used to describe the principal features of metal-ligand bonding when a metal ion is coordinated by six negatively charged ligands in an octahedral arrangement. The metal d_{xy}, d_{yz} and d_{xz} orbitals are equivalent and involve electron density between the axes

containing both the metal ion and the ligands. Both of the d_{z^2} and $d_{x^2-y^2}$ orbitals direct electron density towards the ligands. The octahedral arrangement of ligands around the metal ion splits the five d-orbitals into two sets (Fig. 2.1), one set (t_{2g}) being triply degenerate (corresponding to the copper d_{xy}, d_{yz} and d_{xz} orbitals) and the other (e_g) being doubly degenerate (corresponding to the copper d_{z^2} and $d_{x^2-y^2}$ orbitals). The t_{2g} orbitals are stabilized and the e_g orbitals are destabilized relative to their energies in a spherical field, the energy difference between the t_{2g} and e_g orbitals being designated Δ (Fig. 2.1).

Cu^{2+} has nine d-electrons, giving the electronic configuration $t_{2g}^6 e_g^3$. The Cu^{2+} ion contains a degenerate electronic state (E_g), and according to the Jahn-Teller theorem, distortion of the octahedron will spontaneously occur to remove this degenerate state. There are two possible distortions, depending on whether the lone electron is in the d_{z^2} or $d_{x^2-y^2}$ orbital. If the $d_{x^2-y^2}$ orbital is doubly occupied, the four ligands in the x-y plane will be more screened from the electrostatic attraction of the Cu^{2+} ion than the two ligands on the z-axis. Therefore, the two apical ligands (along the z-axis) would be expected to move closer to the Cu^{2+} ion than the four equatorial ligands (x-y plane), resulting in a compressed octahedron [(2+4) distortion]. If the d_{z^2} orbital is doubly occupied, the four equatorial ligands (x-y plane) will move closer to the Cu^{2+} ion and the two apical ligands (z-axis) will move away, resulting in an elongated octahedron [(4+2) distortion].

As shown in Fig. 2.1, the degenerate e_g orbitals are split due to the distortion, and the doubly occupied orbital drops in energy by the same amount as the singly occupied orbital rises. Therein lies the driving force of the Jahn-Teller distortion of $Cu^{2+}\phi_6$ octahedra: only half the energy gained

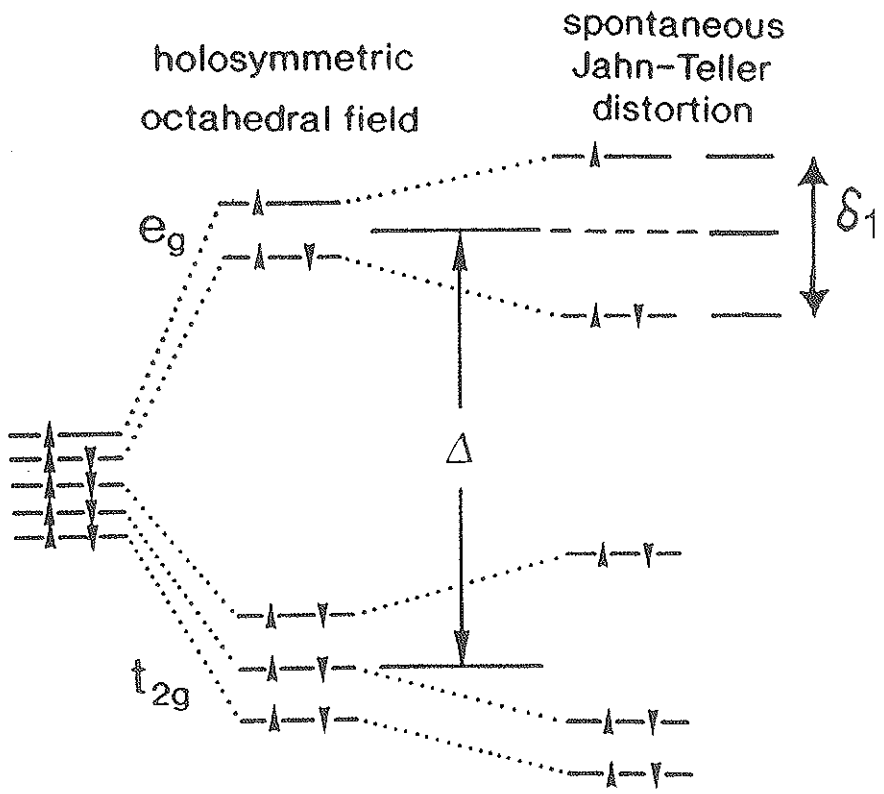

Figure 2.1. The electron-energy levels for Cu^{2+} in a spherical field (left), a holosymmetric octahedral field (middle), and a distorted octahedral field (right).

by reducing the energy of the doubly occupied orbital is cancelled by the increase in energy of the singly occupied orbital. Hence the environment around the Cu^{2+} will spontaneously distort to produce an energy stabilization of $\delta_1/2$ (Fig. 2.1). Note that there is no net energy change in the t_{2g} level of Cu^{2+} due to the distortion.

Ligand-field arguments for a d^9 metal-ion in octahedral coordination indicates that a compressed (2+4) geometry is equally as likely as an elongated (4+2) geometry. However, examination of $^{[6]}$Cu-ϕ bond lengths in Cu^{2+} oxysalt minerals (Fig. 2.7, Section 2.5) indicates that (4+2)-distorted octahedra are very strongly preferred over either the (2+4)-distorted or holosymmetric geometries. The same observation holds true for Cu^{2+} compounds in general (Hathaway, 1984). Contrary to the comments of some previous authors, the details of the Jahn-Teller theory are not readily understood using ligand-field theory. Various authors have considered additional effects in an attempt to remove these discrepancies; these effects are the subject of the next section.

2.3 The Dynamic Jahn-Teller Effect

2.3.1 Variable-Temperature Structure Refinement

Variable-temperature structure refinements have provided considerable insight into the Jahn-Teller effect associated with a d^9 metal in octahedral coordination. For example, holosymmetric octahedral coordination around Cu^{2+} is observed in $K_2Pb[Cu^{2+}(NO_2)_6]$ at room temperature (Sidgwick, 1950; Cullen and Lingafelter, 1971), in apparent violation of the Jahn-Teller theorem. At 195 K, the structure is orthorhombic and the Cu^{2+} octahedron is (2+4)-distorted (Sidgwick, 1950). A

(2+4)-distorted Cu^{2+} octahedron is observed in $Cs_2Pb[Cu^{2+}(NO_2)_6]$ at room temperature (Massey, 1973). The structure becomes cubic by 420 K, with a holosymmetric Cu^{2+} octahedron observed (Mullen et al., 1975). When the structure is cooled to 160 K, it becomes monoclinic with a (4+2)-distorted Cu^{2+} octahedron (Mullen et al., 1975). The temperature-dependent behaviour of the octahedral geometries in these and other Cu^{2+} compounds [see Hathaway (1984) for a review] may not be explained using first-order Jahn-Teller effects alone, and a dynamic Jahn-Teller approach must be used.

2.3.2 Vibronic Coupling and the Jahn-Teller Effect

The energetically degenerate electronic state may couple with the nuclear motion, leading to a dynamic Jahn-Teller effect in which the electronic motion is strongly influenced by the nuclear vibrations that tend to remove the degenerate state. Qualitatively, the electronic properties of the d^9 configuration of the Cu^{2+} ion in an orbitally degenerate ground-state cannot involve separately defined electronic and vibrational energies (i.e., the Born-Oppenheimer approximation is violated).

The even mode of vibration of e_g symmetry is made up of two displacement coordinates, S_{2a}, and S_{2b} (Fig. 2.2), and is the only mode that can couple with the electronically degenerate ground-state in a cubic system (Fig. 2.3) and remove the orbital degeneracy (Hathaway, 1984). Two energy surfaces arise from this coupling (E_- and E_+, Fig. 2.3) and take a form that is known as a Mexican-hat potential (Gazo et al., 1976). The lower-energy surface of the Mexican hat (E_-) has a potential-energy minimum that is stabilized by E_{JT} relative to the energy of the Cu^{2+} octahedron in a

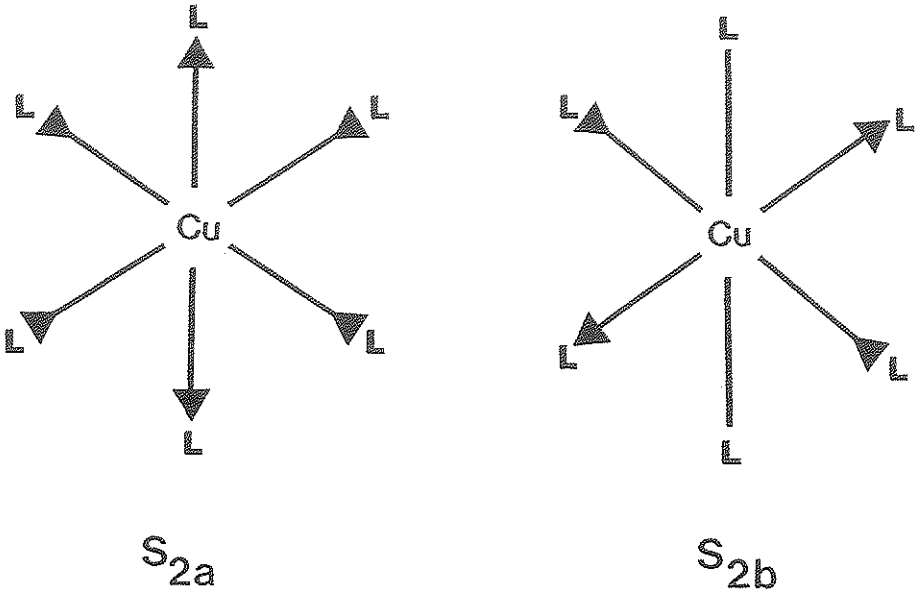

Figure 2.2. The S_{2a} and S_{2b} displacement coordinates of the E_g mode of octahedral vibration. Taken from Hathaway (1984). Arrows indicate the direction of movement away from the holosymmetric geometry, L denotes the ligand.

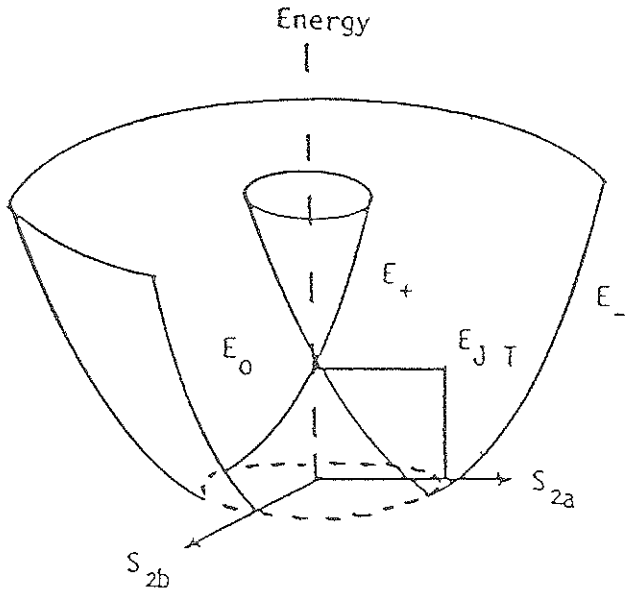

Figure 2.3. The Mexican-hat potential which results from the coupling of the E_g mode of octahedral vibration with the degenerate electronic state. Taken from Gazo et al. (1976). E_o is the energy of a holosymmetric octahedron, E_+ and E- are the energy surfaces produced by the vibronic coupling, E_{JT} is the Jahn-Teller stabilization energy.

holosymmetric configuration (energy E_o). The coupling of the electronic Hamiltonian (for a doubly degenerate state) with the nuclear vibrations gives rise to both linear and non-linear (higher order) terms (Englman, 1972). If only linear coupling terms are important, the Mexican hat has cylindrical symmetry, and the molecule will rotate in the potential-energy minimum (Gazo et al., 1976). However, if there is a strong linear coupling and higher-order coupling terms are important, the Mexican hat will be warped, with three energy-minima and three saddlepoints (Bersuker, 1984) (Fig. 2.4a).

The minima in the warped Mexican-hat potential-energy surface (Fig. 2.4a) may occur at ϕ = 0, 120 and 240° or at ϕ = 60, 180 and 300° (Hathaway, 1984), depending upon the nature of the higher-order coupling terms. In the first case, the energy minima correspond to (4+2)-elongated octahedra, whereas the saddlepoints correspond to (2+4)-compressed octahedra. In the latter case, the energy minima correspond to (2+4)-compressed octahedra. Note that in either case, the molecule rotates through the potential-energy minimum (Fig. 2.4a) and can pass from a (4+2)-elongated octahedron to a (2+4)-compressed octahedron without passing through the energetically unfavourable holosymmetric coordination (Fig. 2.4b).

Consider the case where the energy minima of the warped Mexican-hat potential occur at ϕ = 0, 120 and 240°. The energy minima correspond to (4+2)-elongated octahedra. This is usually the case, as indicated by the dominance of (4+2)-distorted $Cu^{2+}\phi_6$ octahedra in Cu^{2+} oxysalt minerals and Cu^{2+} oxysalt compounds in general. Various authors have proposed factors that are likely to cause the dominance of the (4+2)-distorted arrangement

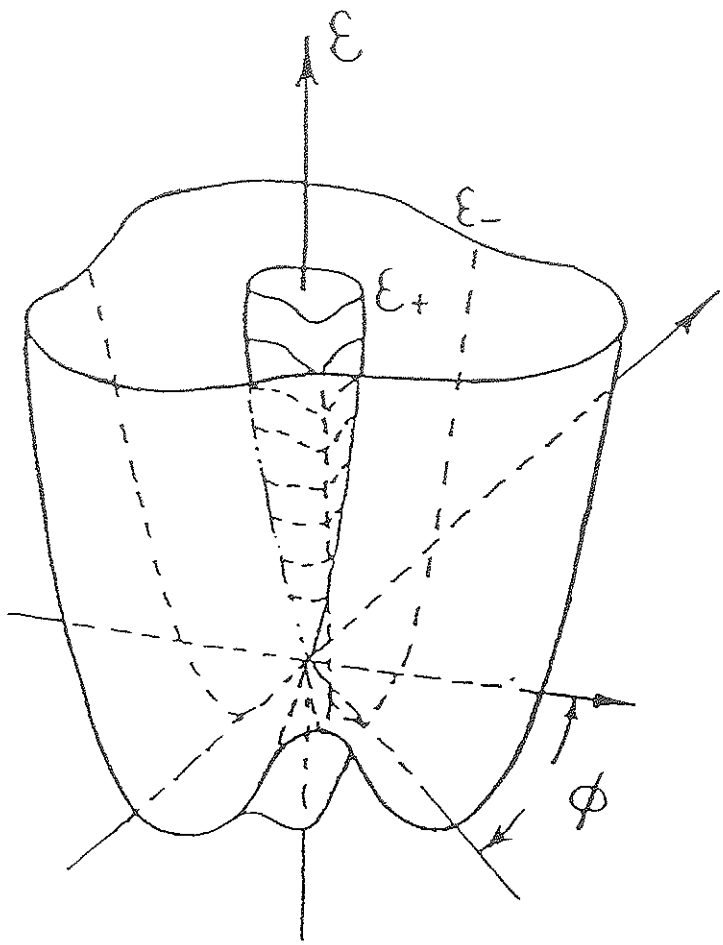

Figure 2.4a. The warped Mexican-hat potential. From Bersuker (1984). E, E- and E+ as in Fig. 2.3.

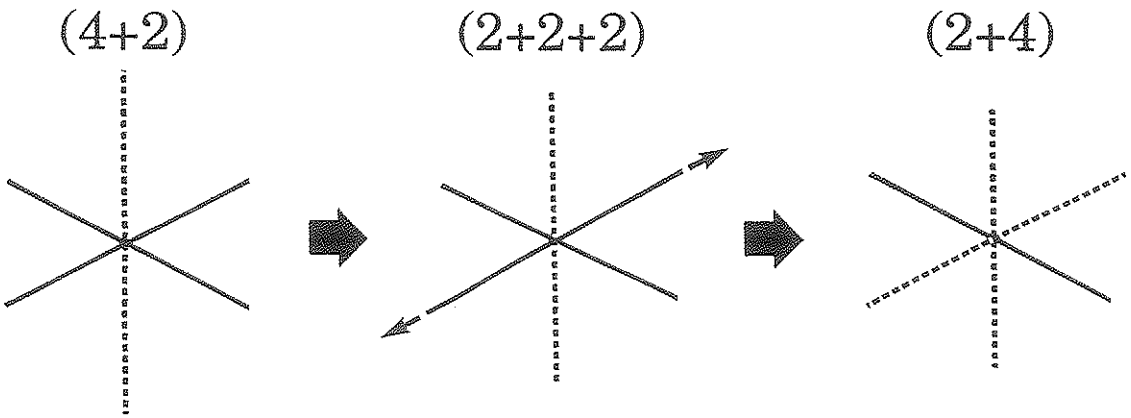

Figure 2.4b. The pathway from a (4+2)-distorted to a (2+4)-distorted octahedron. Long bonds are drawn as broken lines.

(i.e., Öpik and Pryce, 1957; Liehr and Ballhausen, 1958; Lohr and Lipscomb, 1963; Bacci, 1979; Yamatera, 1979; Deeth and Hitchman, 1986):

(1) The addition of an anharmonic term to the vibrational potential;
(2) The extension to second order of the electronic terms in the total potential-energy expression;
(3) The configuration interaction between the 4s and $3dz^2$ metal orbitals.

Deeth and Hitchman (1986) indicate that each of these factors is of similar magnitude, and that (1) and (3) favour a (4+2)-distortion whereas (2) favours a (2+4)-distortion.

The circular cross-section through the minimum of the potential-energy surface for energy minima at $\phi = 0$, 120 and 240° (Fig. 2.4a) is given in Fig. 2.5. In this case, the energy maxima correspond to (2+4)-compressed octahedra; each of the three energy wells (Fig. 2.5a) have the same energy, and the energy barriers between the wells have the value B. If B is less than the thermal energy (ca. 200 cm^{-1}, Hathaway, 1984), there will be equal populations in each of the three wells. The distortion direction of any given octahedron will vary continuously as the energy barrier B is overcome. The result is that a completely symmetric $Cu^{2+}\phi_6$ octahedron will be observed by (time averaging) crystallographic techniques, as is the case in $K_2Pb[Cu^{2+}(NO_2)_6]$ at room temperature (Sidgwick, 1950) and $Cs_2Pb[Cu^{2+}(NO_2)_6]$ at 420 K (Mullen et al., 1975).

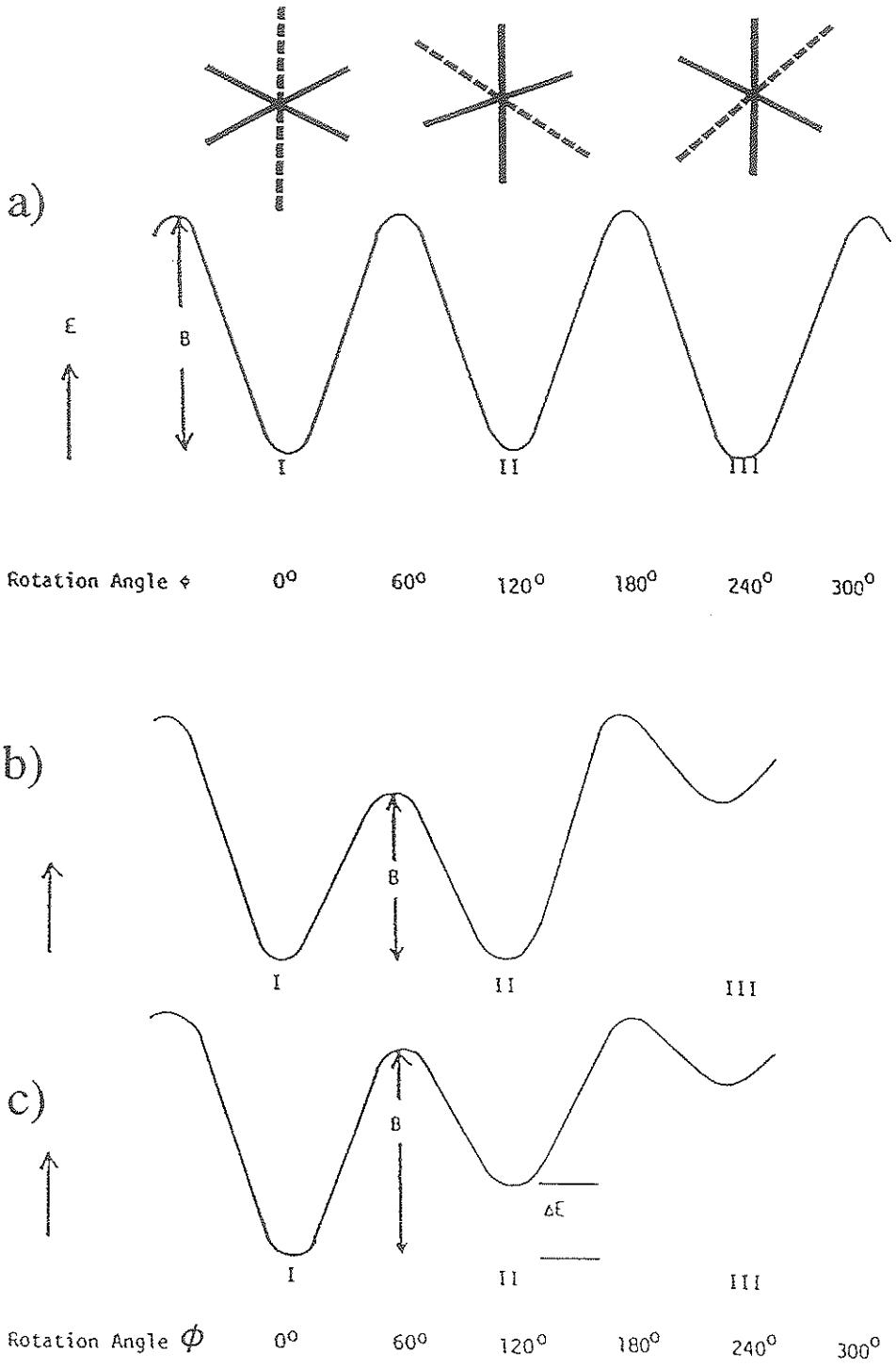

Figure 2.5. Circular cross-sections though warped Mexican-hat potentials. a) Three equal-energy wells, b) two equal-energy wells, c) three unequal-energy wells. ϕ as in Fig. 2.4, the long bonds in the octahedra are dashed.

In crystals, long-range effects are always present and may result in a further warping of the Mexican-hat surface (Bersuker, 1984). Two possibilities then arise: (1) there may be two equivalent wells of lower energy than the third well (Fig. 2.5b); (2) one well may have a lower energy than the other two wells (Fig. 2.5c). In (1), if the energy B is less than the thermal energy, equal populations will occur in the two lower-energy wells. The two wells contain octahedra that are elongated in different directions, with dynamic interchange between the orientations of the elongated axis. The net result will be an apparent (2+4)-compressed octahedron. By the same reasoning, case (2) would result in an apparently elongated rhombic octahedron, with a (2+2+2)-distortion. A (2+2+2) octahedron has two short *trans* Cu-ϕ bonds, two intermediate *trans* Cu-ϕ bonds, and two long *trans* Cu-ϕ bonds.

The above observations suggest that both (2+4)-compressed and holosymmetric $Cu^{2+}\phi_6$ octahedra observed in minerals and other phases may sometimes be a result of the dynamic Jahn-Teller effect. It may also be argued that these octahedra are due to static disorder of the octahedral ligands, but the dynamic Jahn-Teller effect is required to rationalize the temperature dependence of $Cu^{2+}\phi_6$ octahedral coordination geometries in both $K_2Pb[Cu^{2+}(NO_2)_6]$ and $Cs_2Pb[Cu^{2+}(NO_2)_6]$, and in various other Cu^{2+} compounds (Hathaway, 1984). As expected, X-ray data collected for these phases also shows anisotropic-displacement parameters consistent with dynamically distorted copper octahedra. Furthermore, ESR (electron-spin-resonance) spectra for these compounds indicate that (2+4)-distorted and holosymmetric $Cu^{2+}\phi_6$ octahedra are both a result of the dynamic Jahn-Teller effect. According to Hathaway et al. (1981), there are no compounds

that have been conclusively demonstrated to contain **statically** (2+4)-distorted or holosymmetric $Cu^{2+}\phi_6$ octahedra. It has been noted, however, that dilute concentrations of $Cu^{2+}\phi_6$ octahedra in a parent structure *may* be (2+4)-distorted, as indicated by ESR spectroscopy (e.g., Hitchman et al., 1986; Rienen and Krause, 1981).

2.4 Static Jahn-Teller Effects and the Cooperative Jahn-Teller Effect.

2.4.1 Static Jahn-Teller Effects

The dynamic Jahn-Teller effect does not occur in most Cu^{2+} oxysalt minerals, as shown by crystal-structure refinements. In most cases, a static Jahn-Teller effect predominates, with the $Cu^{2+}\phi_6$ octahedron trapped in one of the energy wells. However, if two or three of the wells are of about the same energy, directional disorder of the distortion could occur, such that long-range averaging (as occurs in diffraction experiments) will show symmetrical octahedra (three equal wells) or (2+4)-compressed octahedra (two equal wells).

2.4.2 Cooperative Jahn-Teller Effect

Cu^{2+} oxysalt minerals usually have (4+2)-elongated octahedra, indicating that one energy well is of a lower energy that the other two wells. The elongation directions of the octahedra are ordered, and this ordering is referred to as the cooperative Jahn-Teller effect (Bersuker, 1984). Ordering of the distortion centres is due to strong electron-phonon coupling that links the effects of adjacent distortion centres.

2.5 $Cu^{2+}\phi_6$ Geometries in Cu^{2+} Oxysalt Minerals

Tabulation and comparison of $Cu^{2+}\phi_6$ geometries in Cu^{2+} oxysalt minerals has been done by Eby (1988). However, over the past few years, high-quality structural data for Cu^{2+} oxysalt minerals has continued to accumulate at the rate of several structures per year. Today, the structures of 91 $^{[6]}Cu^{2+}$ oxysalt minerals are known, and 166 symmetrically distinct $Cu^{2+}\phi_6$ octahedra occur in these minerals. The following sections consider the stereochemical characteristics of these octahedra. Mixed-ligand $Cu^{2+}\Phi_6$ octahedra ($\Phi = O^{2-}$, OH^-, H_2O and at least one Cl) will be considered in Chapter 9.

2.5.1 General Features of $Cu^{2+}\phi_6$ Octahedral Geometries

The Cu-ϕ bond-length distribution for all symmetrically distinct $Cu^{2+}\phi_6$ octahedra contained in Cu^{2+} oxysalt minerals is shown in Figure 2.6. There is a bimodal distribution, with maxima at ~ 1.95 Å and ~ 2.40 Å, reflecting the dominance of (4+2)-distorted octahedra. The <Cu-ϕ_{eq}> distance is 1.983 Å and the <Cu-ϕ_{ap}> distance is 2.484 Å. The population at ~ 1.98 Å is quite narrow (σ = 0.07 Å), demonstrating the relatively limited range of Cu-ϕ_{eq} distances in (4+2)-distorted $Cu^{2+}\phi_6$ octahedra. In contrast, the population at ~ 2.48 Å is much broader (σ = 0.22 Å), reflecting the larger range shown by Cu-ϕ_{ap} bond-lengths in (4+2)-distorted octahedra. The population at ~ 1.98 Å is approximately twice as large as that at ~ 2.48 Å, reflecting the (4+2) nature of the distorted octahedral geometries.

Equatorial and apical <Cu-ϕ> bond-length distributions are illustrated separately in Figures 2.7 and 2.8, respectively. Most <Cu-ϕ_{eq}> distances fall in the range 1.925-2.025 Å (Fig. 2.7). However, several <Cu-

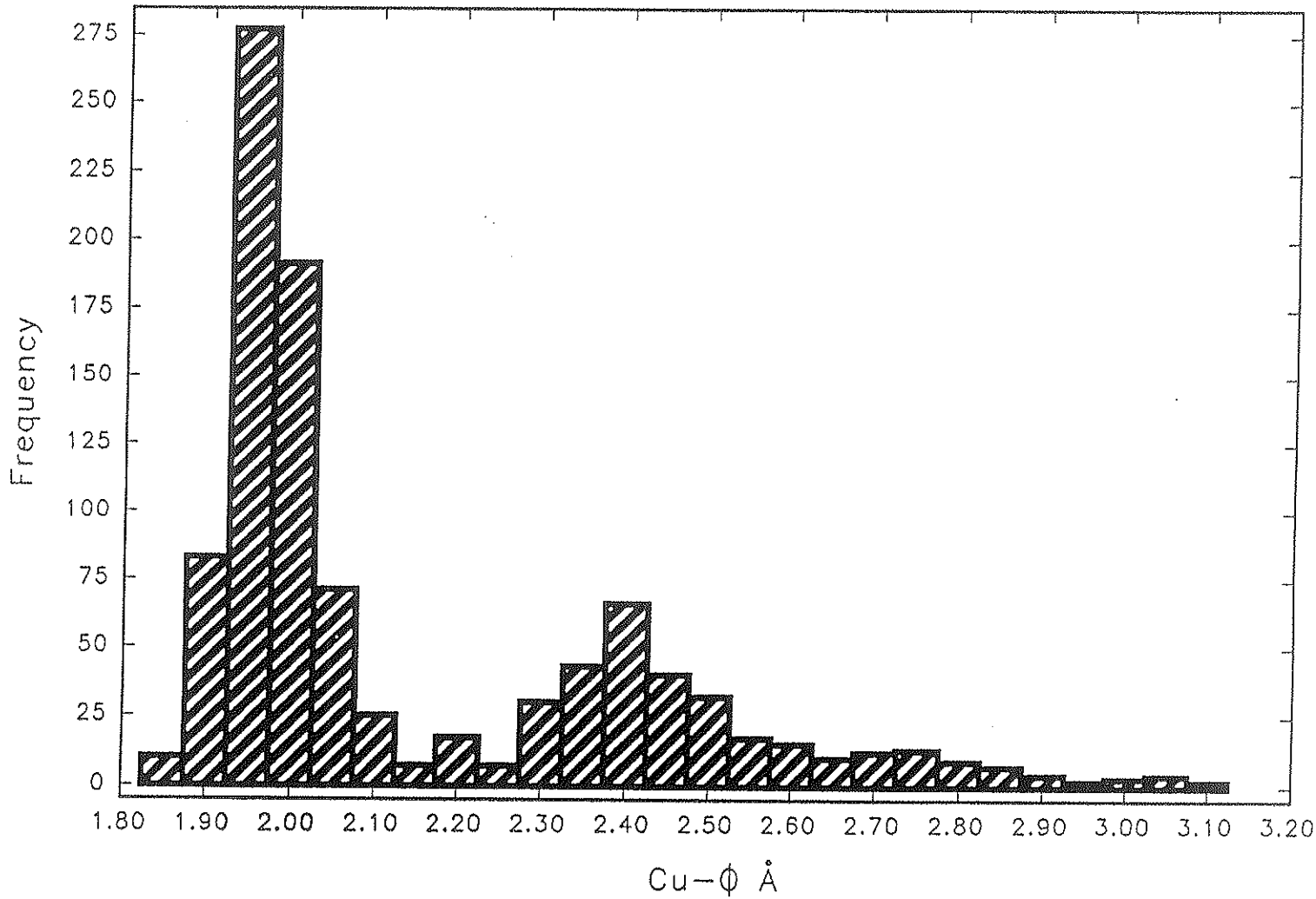

Figure 2.6. The distribution of Cu-ϕ bond-lengths in all symmetrically distinct $Cu^{2+}\phi_6$ octahedra in Cu^{2+} oxysalt minerals.

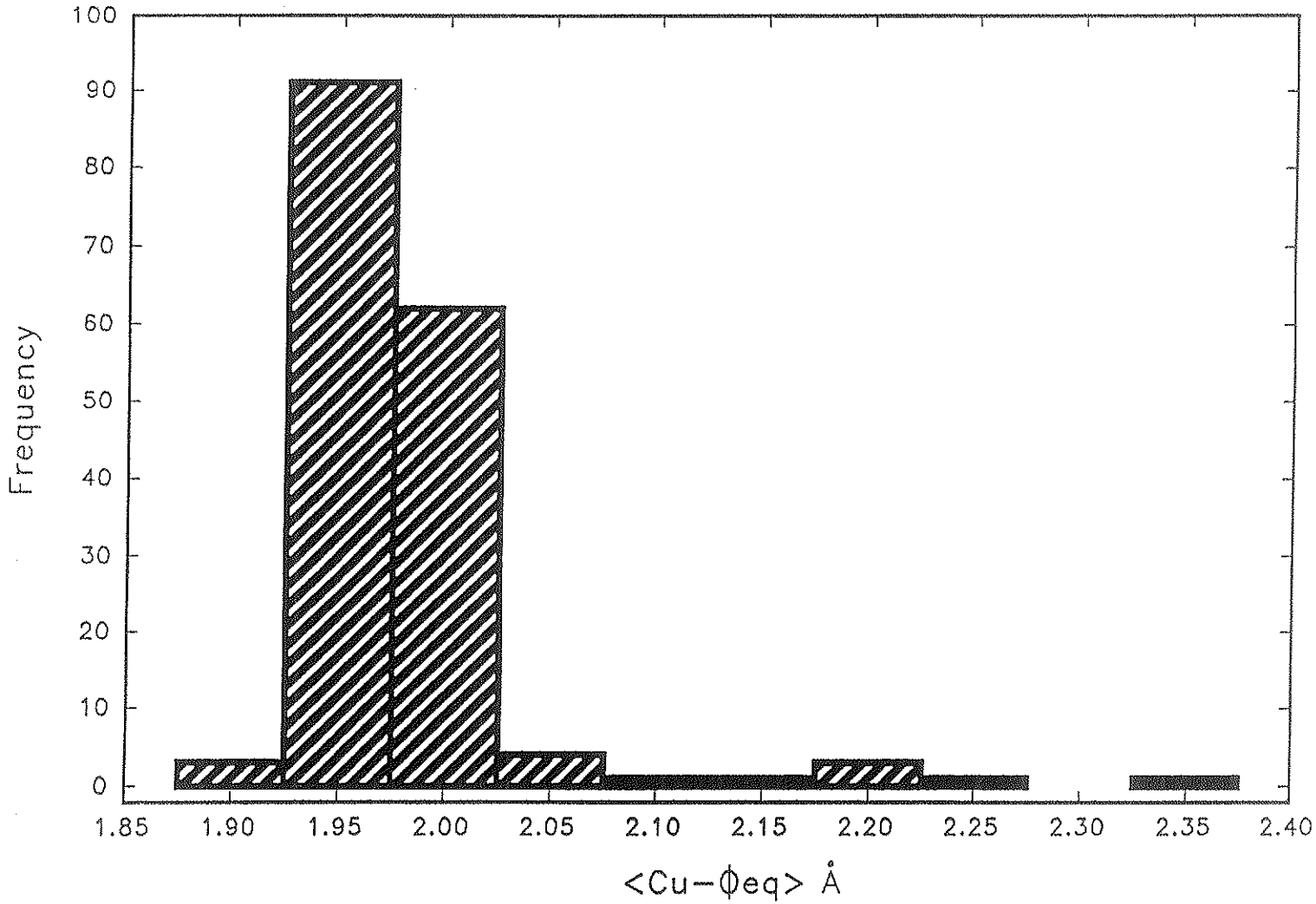

Figure 2.7. The distribution of <Cu-ϕ_{eq}> distances in all symmetrically distinct $Cu^{2+}\phi_6$ octahedra in Cu^{2+} oxysalt minerals.

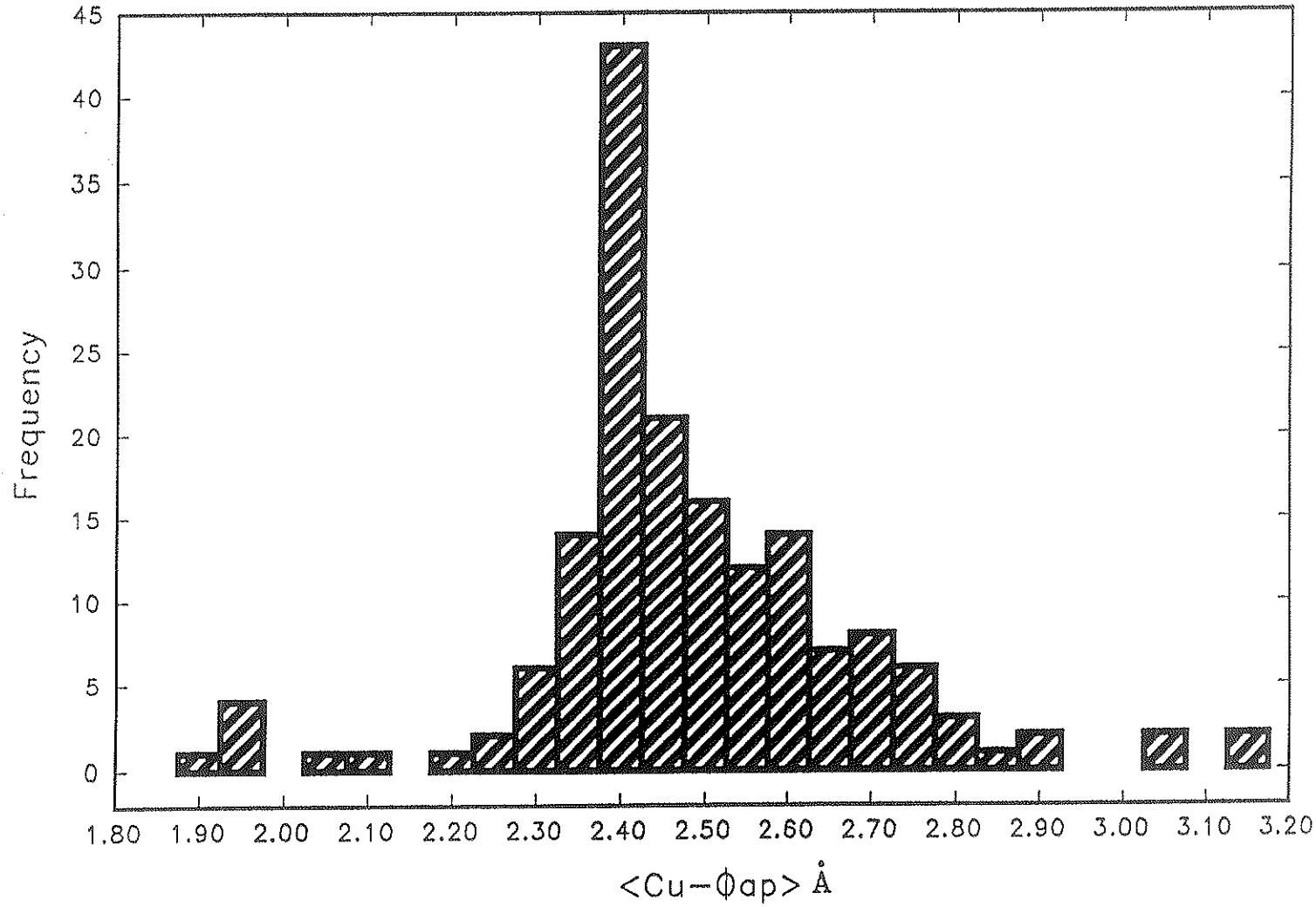

Figure 2.8. The distribution of <Cu-ϕ_{ap}> distances in all symmetrically distinct $Cu^{2+}\phi_6$ octahedra in Cu^{2+} oxysalt minerals.

ϕ_{eq}> distances are above the average, within the range 2.075 to 2.375 Å (Fig. 2.7); these values are not representative of (4+2)-distorted $Cu^{2+}\phi_6$ octahedra. Likewise, several <Cu-ϕ_{ap}> bond-lengths fall well below the typical range of 2.275 to 2.925 Å (Fig. 2.8). These short <Cu-ϕ_{ap}> distances, as well as the long <Cu-ϕ_{eq}> distances, are a result of the presence of (2+4)-distorted and holosymmetric $Cu^{2+}\phi_6$ octahedra in Cu^{2+} oxysalt minerals.

A measure of the Jahn-Teller distortion of $Cu^{2+}\phi_6$ octahedra is obtained by plotting the frequency of $\Delta_{ap\text{-}eq}$ = [<Cu-ϕ_{ap}> - <Cu-ϕ_{eq}>] (Figure 2.9). The maximum of the $\Delta_{ap\text{-}eq}$ distribution is in the range 0.30 Å to 0.70 Å, with the majority of $\Delta_{ap\text{-}eq}$ values falling between 0.40 and 0.50 Å. The $\Delta_{ap\text{-}eq}$ distribution is skewed towards lower values of $\Delta_{ap\text{-}eq}$, and an abrupt lower limit of $\Delta_{ap\text{-}eq}$ = 0.30 Å is observed (Fig. 2.9). However, a few $Cu^{2+}\phi_6$ octahedra show values of $\Delta_{ap\text{-}eq}$ < 0.30 Å; $\Delta_{ap\text{-}eq}$ = 0 corresponds to holosymmetric octahedra, and $\Delta_{ap\text{-}eq}$ < 0 denotes (2+4)-distorted octahedra.

Each subclass of $Cu^{2+}\phi_6$ geometries, i.e., (4+2)-distorted, (2+4)-distorted and holosymmetric, is dealt with separately in the following sections.

2.5.2 Examination of (4+2)-Distorted $Cu^{2+}\phi_6$ Octahedral Geometries

By far the most common subclass of $Cu^{2+}\phi_6$ octahedral geometries observed in minerals is the (4+2)-distorted octahedron. There are 159 symmetrically unique (4+2)-distorted octahedra in 90 different Cu^{2+} oxysalt minerals.

The Cu-ϕ bond-length distribution for (4+2)-distorted $Cu^{2+}\phi_6$ octahedra (Fig. 2.10) is strongly bimodal, with essentially all of the Cu-ϕ_{eq} distances in the range 1.875 to 2.125 Å and the Cu-ϕ_{ap} distances in the range 2.225 to

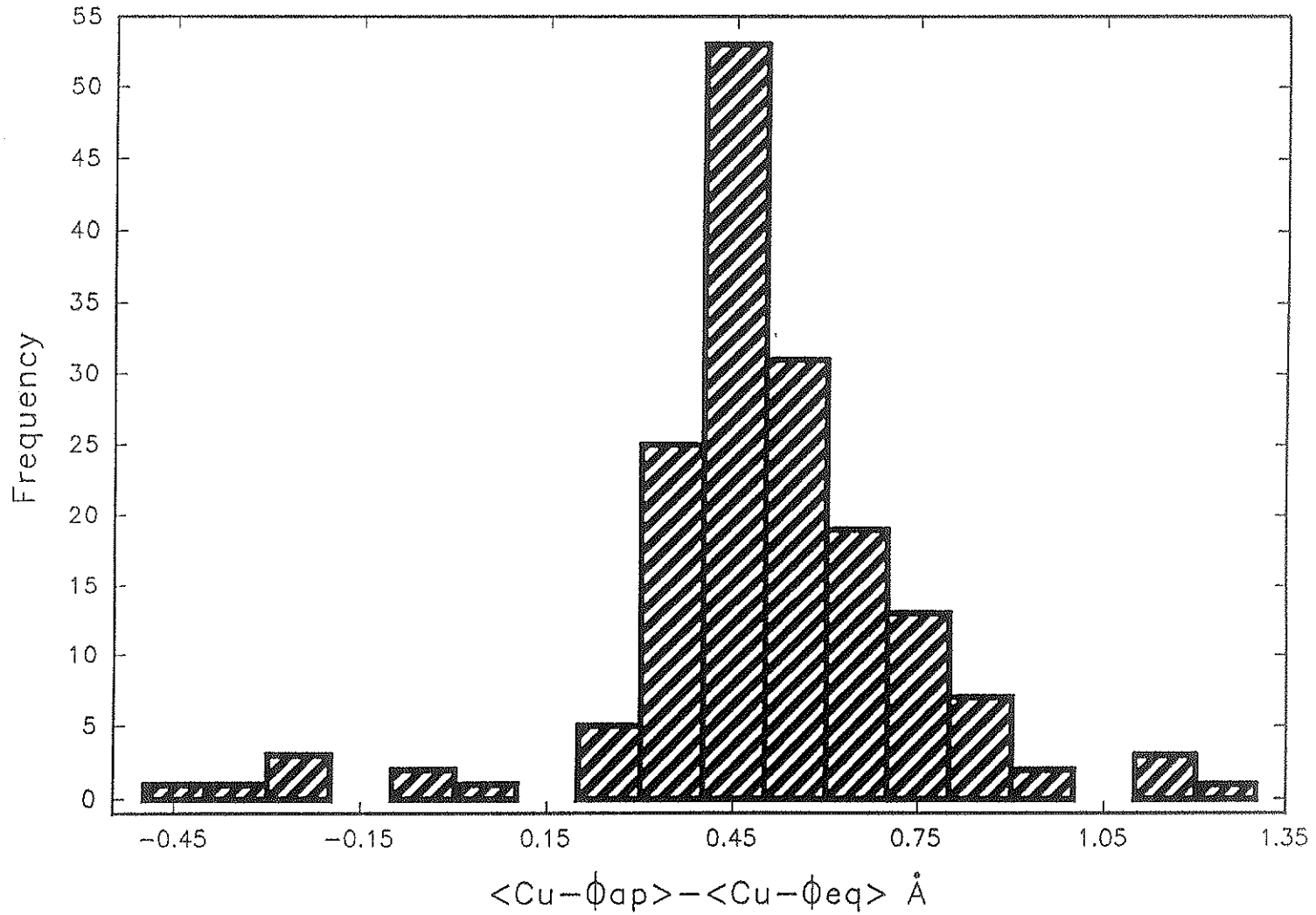

Figure 2.9. The distribution of $\Delta_{ap\text{-}eq}$ in all symmetrically distinct $Cu^{2+}\phi_6$ octahedra observed in Cu^{2+} oxysalt minerals.

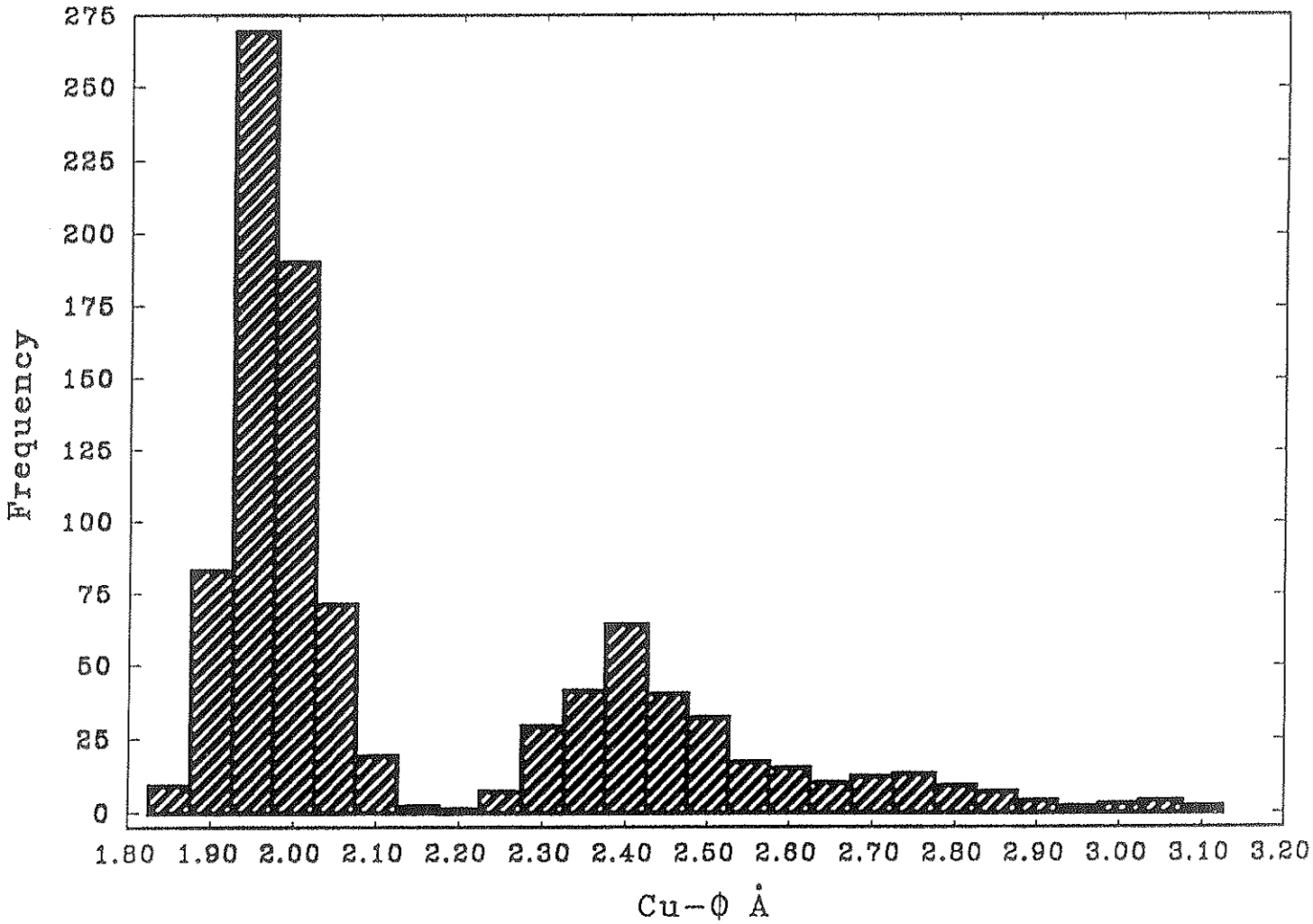

Figure 2.10. The distribution of Cu-ϕ bond-lengths in symmetrically distinct (4+2)-distorted $Cu^{2+}\phi_6$ octahedra in Cu^{2+} oxysalt minerals (i.e., holosymmetric and (2+4)-distorted octahedra are not represented here).

3.125 Å. The <Cu-ϕ> distance is 2.150 Å, with a standard deviation of 0.28 Å. The <Cu-ϕ_{eq}> distance is 1.973 Å and the <Cu-ϕ_{ap}> distance is 2.505 Å. The equatorial bond-lengths span a much smaller range than the apical bond-lengths, with a standard deviation of 0.048 Å compared to 0.205 Å for the apical bond-lengths.

Bond-valence theory (Brown, 1981) predicts that distorted coordination polyhedra will show longer mean bond-lengths than corresponding regular coordination polyhedra because of the exponential form of the bond-valence interaction. This was shown to be the case for $Cu^{2+}\phi_6$ octahedra by Eby (1988) who described polyhedral distortion using the parameter Δ:

$$\Delta = 1/6\Sigma[(l_i-l_o)/l_o]^2 \qquad (2.1)$$

where l_i is a Cu-ϕ distance and l_o is the <Cu-ϕ> distance. The value of Δ for each (4+2)-distorted $Cu^{2+}\phi_6$ octahedron is plotted versus <Cu-ϕ> in Figure 2.11. Extrapolation to $\Delta = 0$ gives the expected <Cu-ϕ> distance of 2.083 Å for an undistorted $Cu^{2+}\phi_6$ octahedron, in agreement with the value of 2.084 Å reported by Eby (1988).

2.5.3 Holosymmetric $Cu^{2+}\phi_6$ Octahedra in Cu^{2+} Oxysalt Minerals

The occurrence of holosymmetric $Cu^{2+}\phi_6$ octahedra in Cu^{2+} oxysalt minerals is unexpected as it violates the Jahn-Teller theorem. However, examination of Figure 2.9 shows $Cu^{2+}\phi_6$ octahedra with little or no distortion. These octahedra occur in lyonsite, buttgenbachite and paratacamite.

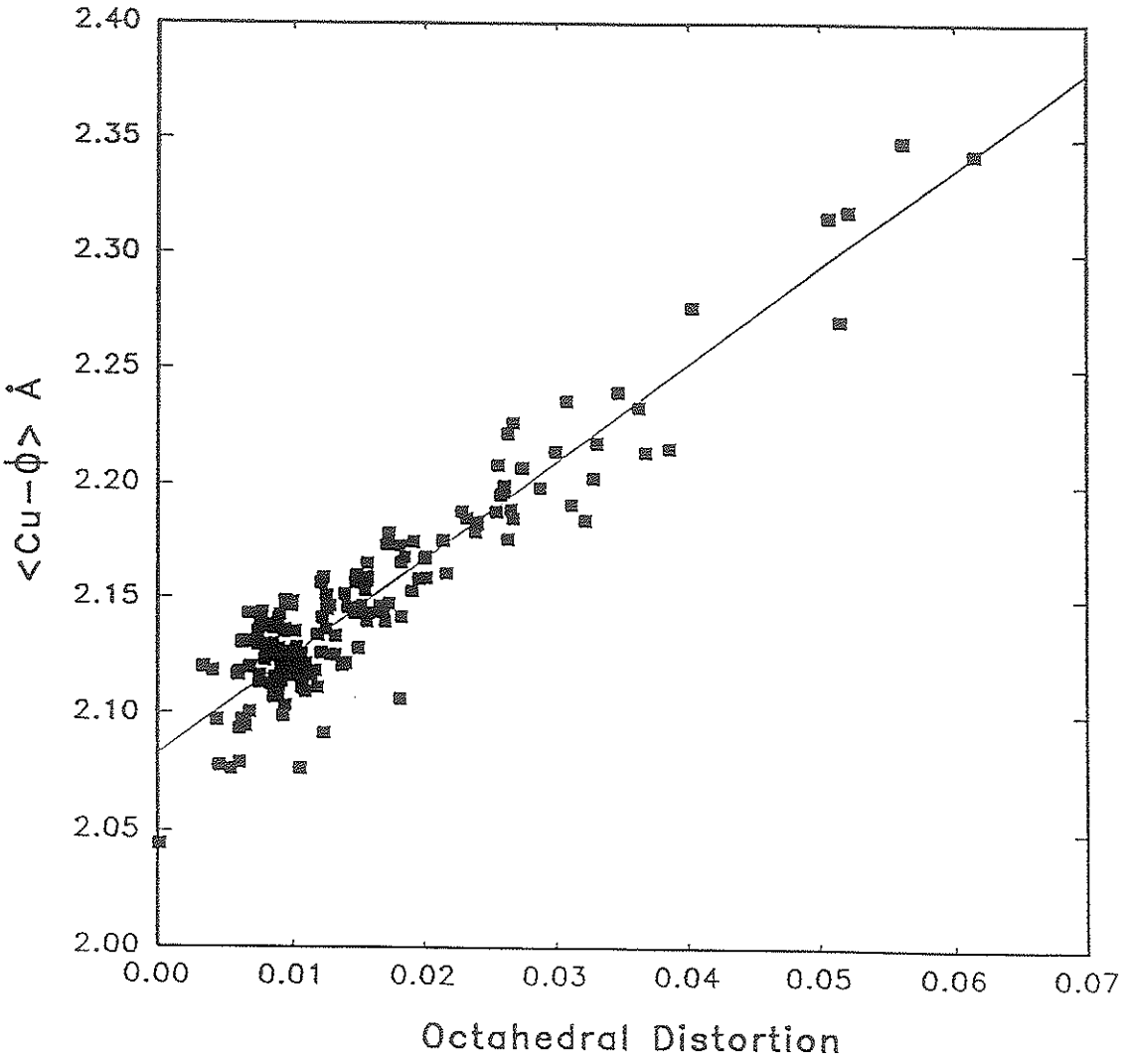

Figure 2.11. The <Cu-ϕ> bond-length versus octahedral distortion (Δ) for (4+2)-distorted $Cu^{2+}\phi_6$ octahedra in Cu^{2+} oxysalt minerals. The least-squares line intercept is at <Cu-ϕ> = 2.083 Å for Δ = 0.0.

Lyonsite

Lyonsite, $Cu_3^{2+}Fe_4^{3+}(VO_4)_6$, is a rare high-temperature fumarolic sublimate described by Hughes et al. (1987). The lyonsite structure is based on a pseudohexagonal close-packed oxygen array, and contains two symmetrically distinct Cu^{2+} polyhedra, one of which [Cu(2)] shows a very unusual $Cu^{2+}\phi_6$ coordination: a distorted trigonal-prism (Fig. 2.12). The Cu(1) site involves a $Cu^{2+}\phi_6$ octahedron that is only very weakly distorted [Cu(1)-O(1) x2 = 2.031(5), Cu(1)-O(1) x2 = 2.030(5), Cu(1)-O(6) x2 = 2.070(7) Å]. Further examination of the lyonsite structure shows that adjacent $Cu^{2+}(1)\phi_6$ octahedra share faces, with adjacent Cu(1) positions only 2.455 Å apart. Such a configuration suggests that adjacent Cu(1) sites are probably not both occupied; site-scattering refinement shows the Cu(1) site to be half-occupied, consistent with this situation.

When a site is partly occupied, as is the case for the Cu(1) site here, the local atomic configurations are expected to be very different when the site is occupied or vacant. The long-range average measured by X-ray diffraction consists of the sum of these two configurations, and may not resemble either of the local configurations very closely. The fact that regular $Cu^{2+}\phi_6$ configurations are not found (when the site is completely filled by Cu^{2+}) suggests that the long-range average observed in lyonsite (and buttgenbachite) consists of distorted $Cu^{2+}\phi_6$ and distorted $\square\phi_6$ configurations that *average out* to regular octahedral geometry. Adding to the uncertainty as to the precise nature of the Cu(1) site is the approximately 50% vacancy and the marked anisotropy of the electron density at the Cu(1) site. The electron-density anisotropy suggests that the room-temperature structure may represent a space average of disordered

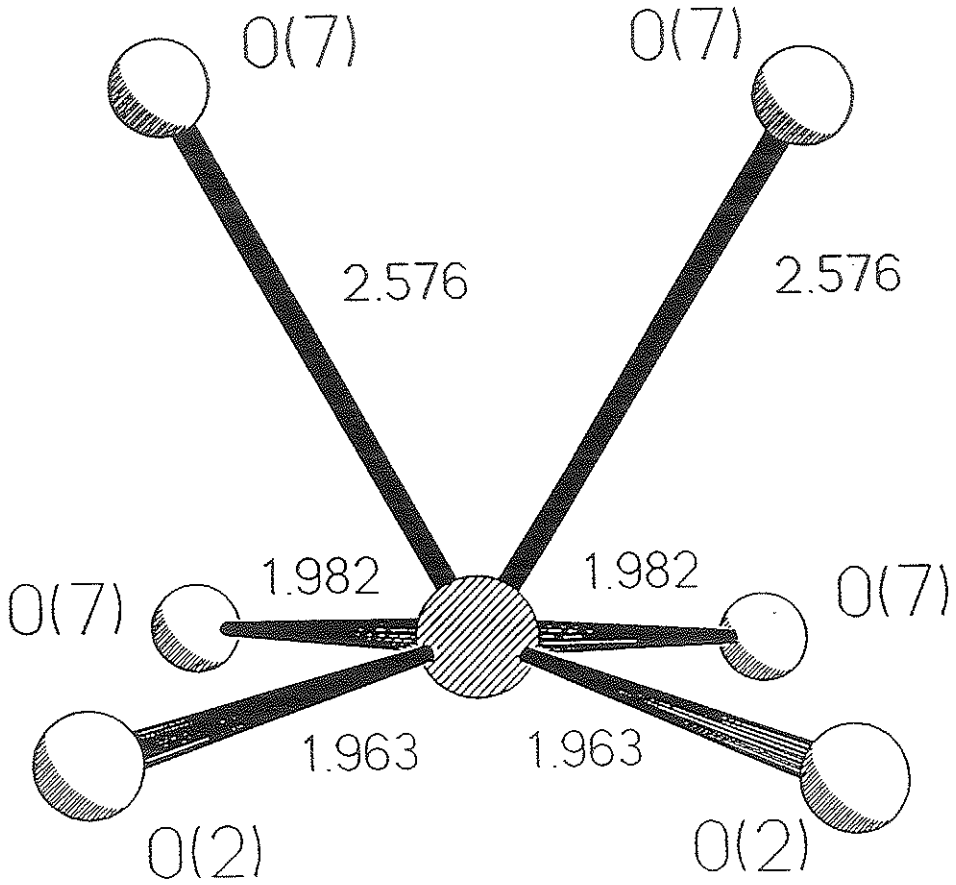

Figure 2.12. The $Cu(2)^{2+}\phi_6$ distorted trigonal-prism observed in lyonsite. Bond-lengths are in Å.

Cu(1) positions within the octahedron (Hughes et al., 1987). Although it is not possible to directly prove this model, the preponderance of partly-filled sites in holosymmetric $Cu^{2+}\phi_6$ configurations suggests that this is the case.

Buttgenbachite

The structure of buttgenbachite, $Cu^{2+}_{36.6}Cl_{6.7}(NO_3)_{2.6}(OH)_{63.2}\cdot 2.1H_2O$ (Fanfani et al., 1973), contains an infinite three-dimensional framework of Cu^{2+} polyhedra with large channels containing (NO_3) and Cl. There are five symmetrically distinct Cu^{2+} sites. Three of these sites are octahedrally coordinated and show typical (4+2)-distortions (although two contain mixed ligands, see Chapter 9), whereas the fourth Cu^{2+} is in square-planar coordination. The fifth Cu^{2+} site is in holosymmetric octahedral coordination, with Cu(5)-OH(2) x6 = 2.210(7) Å. According to site-scattering information, this site is only 1/3 occupied. The argument given for lyonsite also applies to buttgenbachite: the regular arrangement observed around the Cu(5) site is probably a superposition of two distorted $Cu^{2+}\phi_6$ and $\square\phi_6$ configurations.

Paratacamite

Paratacamite is one of the polymorphic forms of $Cu_2^{2+}(OH)_3Cl$. The structure is rhombohedral, with a distinct substructure (Fleet, 1975). The structure contains four symmetrically distinct Cu^{2+} positions. Two of these positions are in (4+2)-distorted mixed-ligand octahedral coordination, and the third Cu^{2+} site has (2+4)-distorted octahedral coordination. The Cu(1) site contains 1/16 of the copper in the paratacamite structure, and occurs on a $\bar{3}$ axis; the octahedron is holosymmetric with Cu(1)-O x6 = 2.12 Å. This

site is 100% occupied, unlike the holosymmetric octahedron in buttgenbachite or the near-holosymmetric octahedron in lyonsite.

The <Cu-ϕ> value of 2.12 Å is somewhat longer than the expected <Cu-ϕ> distance of 2.083 Å for an undistorted $Cu^{2+}\phi_6$ octahedron. There are two possibilities here: (1) Fleet (1975) reported the structure of a natural paratacamite specimen, but did not report a chemical analysis. If the octahedral site was occupied by Zn^{2+}, the average octahedral distance expected would be 2.10 Å (i.e., 1.36 Å + 0.74 Å, Shannon, 1976). In light of the reported occurrence of zinc-rich paratacamite (Kracher and Pertlik, 1983), it is possible that the holosymmetric octahedron in paratacamite contains Zn^{2+} rather than Cu^{2+}. (2) Positional disorder of the central Cu^{2+} atom would result in *locally* distorted environments *and* an observed <Cu-ϕ> distance longer than the ideal distance for a holosymmetric $Cu^{2+}\phi_6$ octahedron. Which of these two possibilities is the case is, as yet, unresolved.

Synthetic compounds

There are no well-documented examples of holosymmetric octahedra filled with Cu^{2+} in minerals, as predicted by the Jahn-Teller theorem. Holosymmetric $Cu^{2+}\phi_6$ octahedra have been observed in certain synthetic structures by crystallographic techniques. One such example occurs in $[Cu^{2+}(H_2O)_6](BrO_3)_2$, where the <Cu-$\phi$> distance is 2.079 Å (Blackburn et al., 1991), a value in good agreement with the predicted <Cu-ϕ> distance of 2.083 Å for an undistorted $Cu^{2+}\phi_6$ octahedron (Section 2.5.2). However, the holosymmetric octahedron observed in $[Cu^{2+}(H_2O)_6](BrO_3)_2$, as well as all other holosymmetric Cu^{2+} octahedra (there are 6 known), is attributed to a

dynamic Jahn-Teller effect that persists at room temperature (Blackburn et al., 1991; Hathaway, 1984). Supporting evidence comes from anisotropic-displacement parameters, variable-temperature structure refinements, and ESR spectroscopy measurements (Blackburn et al., 1991; Hathaway, 1984).

2.5.4 Occurrences of (2+4)-Distorted $Cu^{2+}\phi_6$ Octahedra in Cu^{2+} Oxysalt Minerals

Ligand-field theory indicates that either a (4+2)- or (2+4)-distortion will relieve the energetically degenerate electronic state associated with Cu^{2+} in a holosymmetric octahedral ligand-field. To first-order, either distortion is equally likely (i.e., each octahedral configuration is energetically equivalent). However, as noted in previous sections, examination of $Cu^{2+}\phi_6$ geometries in Cu^{2+} oxysalt minerals (Figs. 2.6, 2.7, 2.8), and Cu^{2+} compounds in general, shows that this is not the case; the great majority of $Cu^{2+}\phi_6$ octahedra show strong (4+2)-distortion. The clear preference for (4+2)-distorted geometries must be attributed to higher-order Jahn-Teller effects (see Section 2.3).

Examination of $\Delta_{ap\text{-}eq}$ values (Fig. 2.9) shows that five $Cu^{2+}\phi_6$ octahedra in Cu^{2+} oxysalt minerals have a $<Cu\text{-}\phi_{eq}>$ distance that is longer than the $<Cu\text{-}\phi_{ap}>$ distance. These five (2+4)-distorted $Cu^{2+}\phi_6$ octahedra occur in campigliaite, paratacamite, demesmaekerite and volborthite.

Hathaway et al. (1981) suggested that genuine (2+4)-distorted $Cu^{2+}\phi_6$ octahedra do not occur in Cu^{2+} compounds. Most (or all) examples of (2+4)-distorted $Cu^{2+}\phi_6$ octahedra have been shown to be time-averaged results of the dynamic Jahn-Teller effect (Section 2.3.2). These apparent (2+4)-distorted $Cu^{2+}\phi_6$ octahedra result from the time averaging of (4+2)-distorted

octahedra aligned in two directions. However, some spectroscopists have postulated statically (2+4)-distorted $Cu^{2+}\phi_6$ octahedra in some Cu^{2+}-doped systems (Hitchman et al., 1986; Reinen and Krause, 1981) from ESR measurements. As (2+4)-distorted $Cu^{2+}\phi_6$ octahedra are rare (or non-existent) in concentrated Cu^{2+} compounds, it is appropriate to consider each of the mineral examples in some detail.

Campigliaite

Campigliaite, $Cu_4^{2+}Mn^{2+}(SO_4)(OH)_6{\cdot}4H_2O$, contains sheets of $Cu^{2+}\phi_6$ octahedra interconnected through SO_4 tetrahedra and hydrogen bonding. The crystal structure (Sabelli, 1982) is of low precision due to poor crystal quality and the presence of polysynthetic twinning. Both the Cu(1) and Cu(3) sites seem to be in (2+4)-distorted octahedral coordination (Table 2.1). However, it is likely that the observed octahedra are twin-averaged, rather than real (2+4)-distorted octahedra.

Paratacamite

The paratacamite structure (Fleet, 1975) was discussed in the previous section with reference to the Cu(1) site which is in a holosymmetric octahedral environment. It was pointed out that paratacamite may contain considerable amounts of Zn, and that the holosymmetric octahedron in paratacamite may contain Zn rather than Cu^{2+}. Paratacamite also contains one (2+4)-distorted $Cu^{2+}\phi_6$ octahedron (Cu(2), Table 2.1). As this (2+4)-distorted octahedral geometry is very similar to those observed in volborthite and demesmaekerite (Table 2.1), it seems likely that the Cu(2) site does contain Cu^{2+} (rather than Zn^{2+}, as argued for the Cu(1) site).

Table 2.1: (2+4)-distorted $Cu^{2+}\phi_6$ bond-lengths (Å) in minerals

Mineral		Bonds		Reference
Volborthite	Cu(1)	O(2): 2.172(4) x4	O(4): 1.945(4) x2	1
Demesmaekerite	Cu(1)	O(8): 2.21(2) x2 O(9): 2.21(1) x2	OH(1): 1.93(2) x2	2
Paratacamite*	Cu(2)	O(2): 2.19 x2 O(3): 2.20 x2	O(1): 1.93 x2	3
Campigliaite	Cu(1)	O(1): 2.22(5) O(4): 2.34(5) O(3): 2.37(5) O(3): 2.42(5)	O(4): 1.94(5) O(2): 1.93(5)	4
	Cu(3)	O(2): 2.17(5) O(8): 2.21(5) O(5): 2.29(5) O(3): 2.41(5)	O(7): 1.84(5) O(1): 1.99(5)	
$KCu_3^{2+}(OH)_2[(AsO_4)H(AsO_4)]$**	Cu(1)	O(3): 2.186(1) x4	OH: 1.899(2) x2	5

* Standard deviations were not given by the original author.
** Not a mineral
References: 1: Basso et al. (1988); 2: Ginderow and Cesbron (1983); 3: Fleet (1975); 4: Sabelli (1982); 5: Effenberger (1989).

Demesmaekerite

The structure of demesmaekerite, $Pb_2Cu_5^{2+}(SeO_3)_6(UO_2)_2(OH)_6{\cdot}2H_2O$ (Ginderow and Cesbron, 1983), consists of layers of $[Cu^{2+}(O,OH,H_2O)_6]$ octahedra parallel to (010), cross-linked by oblique chains of corner-sharing ($U\phi_7$) and (SeO_3) polyhedra (Fig. 2.13). The structure contains three symmetrically distinct Cu^{2+} sites, two of which are in octahedral coordination with (4+2)-distorted geometries. The Cu(1) site lies on a centre of symmetry, and shows a (2+4)-distorted $Cu^{2+}\phi_6$ octahedral geometry (Table 2.1). Note that this configuration is not a requirement of the site symmetry.

Volborthite

Volborthite, $Cu_3^{2+}(OH)_2V_2O_7{\cdot}2H_2O$ (Basso et al., 1988) contains sheets of edge-sharing $Cu^{2+}\phi_6$ octahedra. These octahedral sheets may be derived from a $Mg(OH)_2$ (brucite) layer in which 25% of the octahedral positions are vacant (Fig. 2.14). VO_4 tetrahedra link to each side of the sheet (Fig. 2.14), and bonding between adjacent sheets is through the apical oxygens of opposing VO_4 tetrahedra and through hydrogen bonding associated with the interstitial H_2O groups (Fig. 2.14).

The volborthite structure contains two symmetrically distinct Cu^{2+} positions. The Cu(2) position occurs at a centre of symmetry, and is surrounded by a (4+2)-distorted octahedron. The Cu(1) position has point symmetry 2/m and the Cu(1) octahedron is (2+4)-distorted (Table 2.1). The chemical composition of the material used for the structure study (Basso et al., 1988) rules out substitution of another cation at the Cu(1) site. Note that the (2+4)-distorted geometries in volborthite, paratacamite and demesmaekerite (Table 2.1) are very similar.

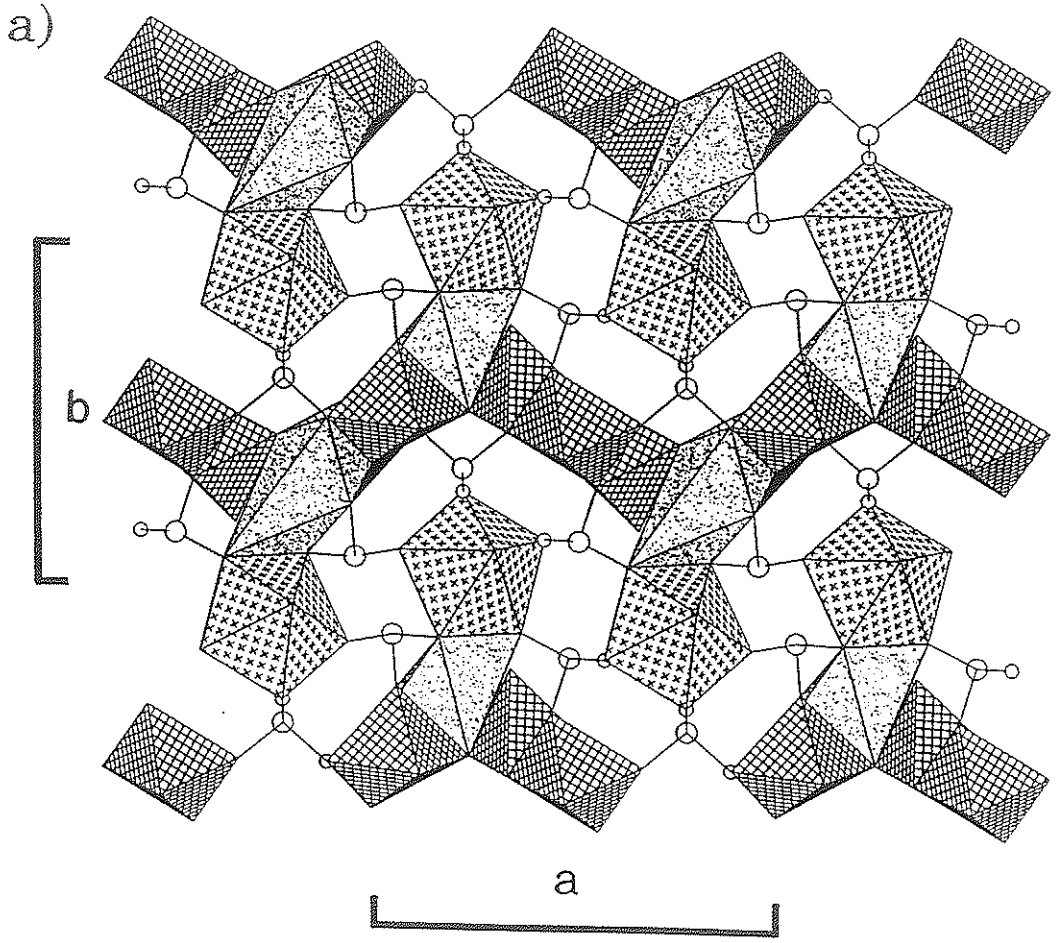

Figure 2.13. Polyhedral structure representations of demesmaekerite. Copper octahedra are cross-hatched, lead polyhedra are shaded with a random dot pattern, uranium pentagonal-bipyramids are shaded with crosses, selenium atoms are large open circles, and oxygen atoms are small open circles: a) the structure projected onto (001); b) the copper octahedral sheet projected onto (010).

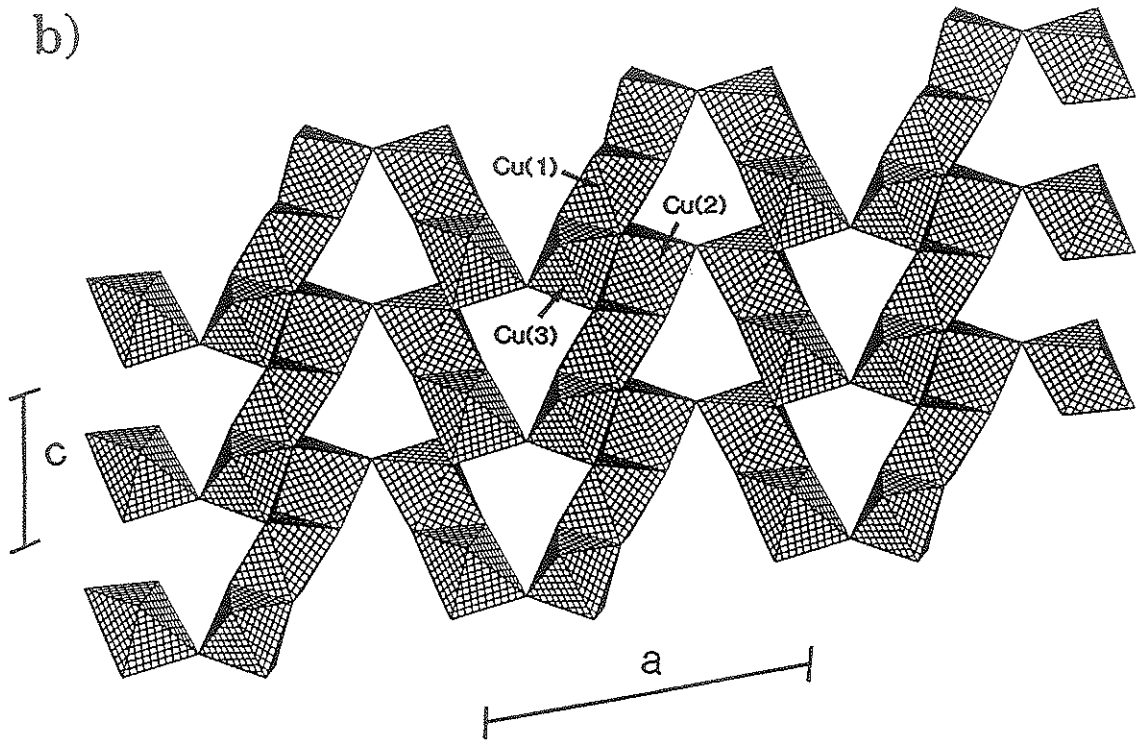

Figure 2.13. Continued

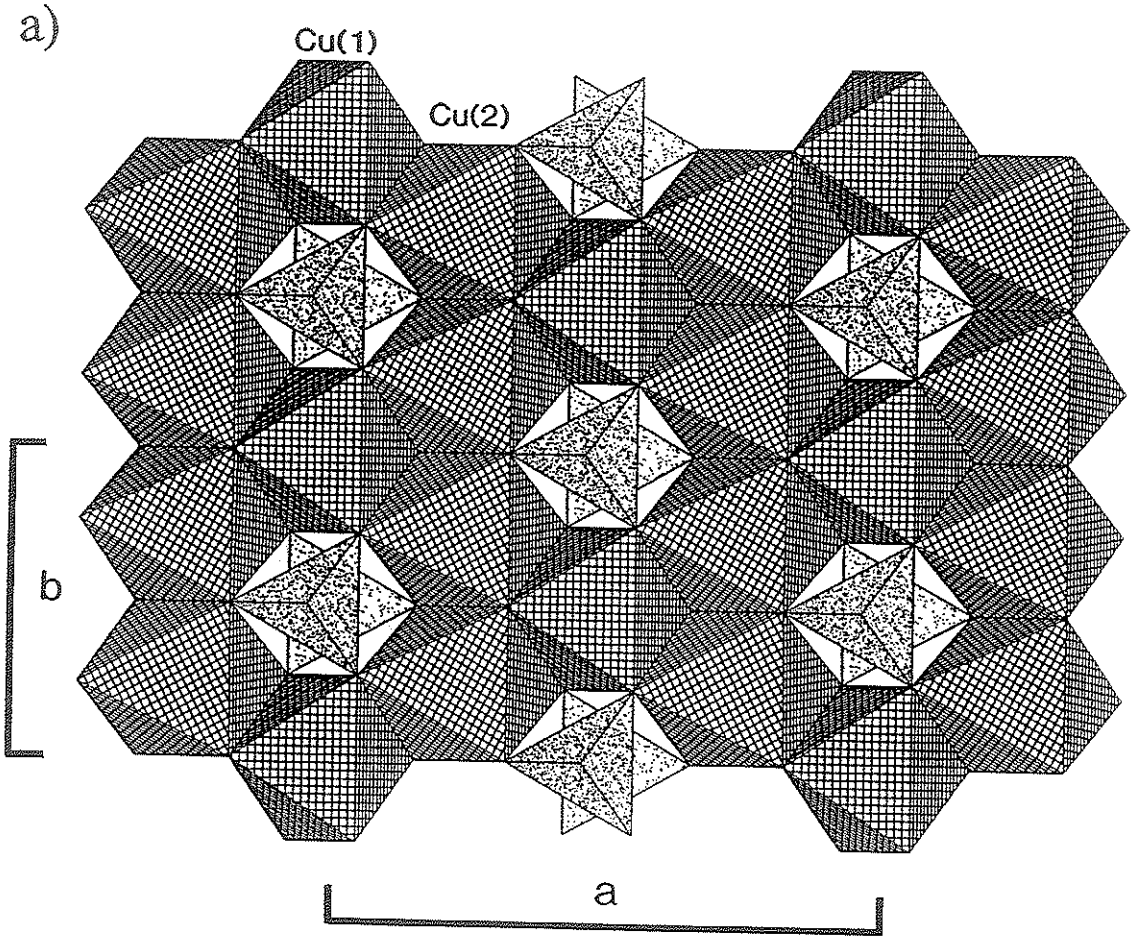

Figure 2.14. Polyhedral representations of the crystal structure of volborthite, $Cu_3^{2+}(OH)_2V_2O_7 \cdot 2H_2O$. The copper octahedra are cross hatched, vanadium tetrahedra are shaded with a random dot pattern, the oxygen atoms of the H_2O groups are shaded with a herring-bone pattern and the hydrogen positions are given as open circles. a) The octahedral-tetrahedral sheet projected onto (001), b) the structure projected onto (010), c) the structure projected onto (100).

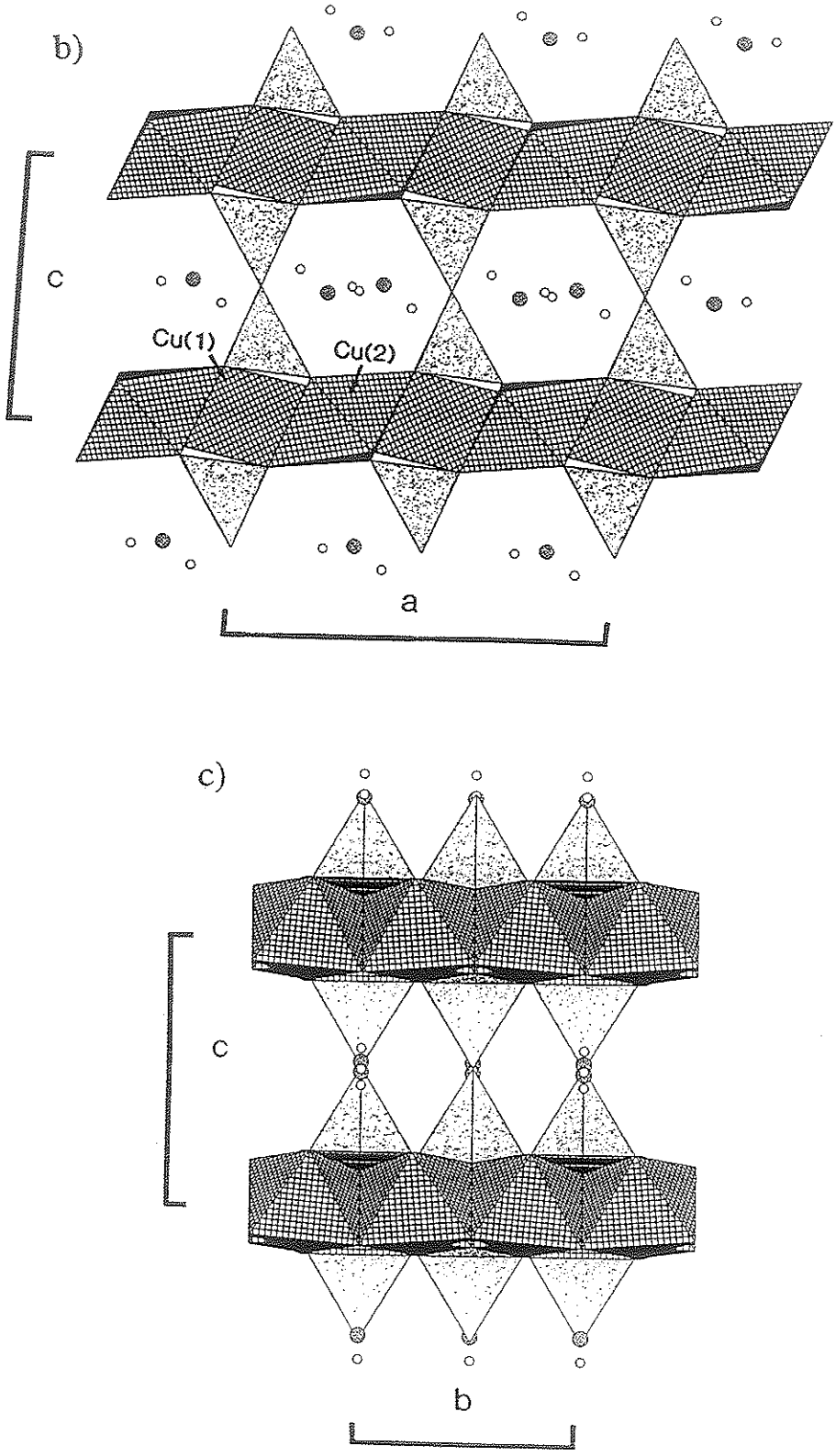

Figure 2.14. Continued

$KCu_3^{2+}(OH)_2[(AsO_4)H(AsO_4)]$

Recently, Effenberger (1989) reported a (2+4)-distorted $Cu^{2+}\phi_6$ octahedron in the structure of $KCu_3^{2+}(OH)_2[(AsO_4)H(AsO_4)]$, which has not yet been described as a mineral. This material crystallizes in the space group C2/m and its structure is closely related to volborthite. The structure contains the same octahedral-tetrahedral sheets as volborthite, with AsO_4 tetrahedra replacing the VO_4 tetrahedra (Fig. 2.15). However, unlike volborthite, adjacent octahedral-tetrahedral sheets are offset, with intersheet bonding provided by 10-coordinated K and hydrogen bonds (Fig. 2.15). The Cu(1) position, which has 2/m symmetry, is at the centre of a (2+4)-distorted octahedron (Table 2.2). The Cu(1)-ϕ bond-lengths are similar to those in volborthite, but the $<Cu\text{-}\phi_{eq}>$ distance is slightly longer and the $<Cu\text{-}\phi_{ap}>$ distance is significantly shorter (Table 2.1). The Cu(2) site is in (4+2)-distorted octahedral coordination, similar to that observed in volborthite.

The occurrence of a (2+4)-distorted $Cu^{2+}\phi_6$ octahedral geometry in both volborthite and $KCu_3^{2+}(OH)_2[(AsO_4)H(AsO_4)]$ suggests that the octahedral geometry results from connectivity constraints associated with the particular octahedral-tetrahedral sheets that occur in both structures. Possibly a (2+4)-distorted octahedron is energetically preferred over a (4+2)-distorted octahedron at the Cu(1) site, with this very unusual situation somehow tied to the connectivity requirements of the sheets. However, the existence of the mineral bayldonite indicates otherwise.

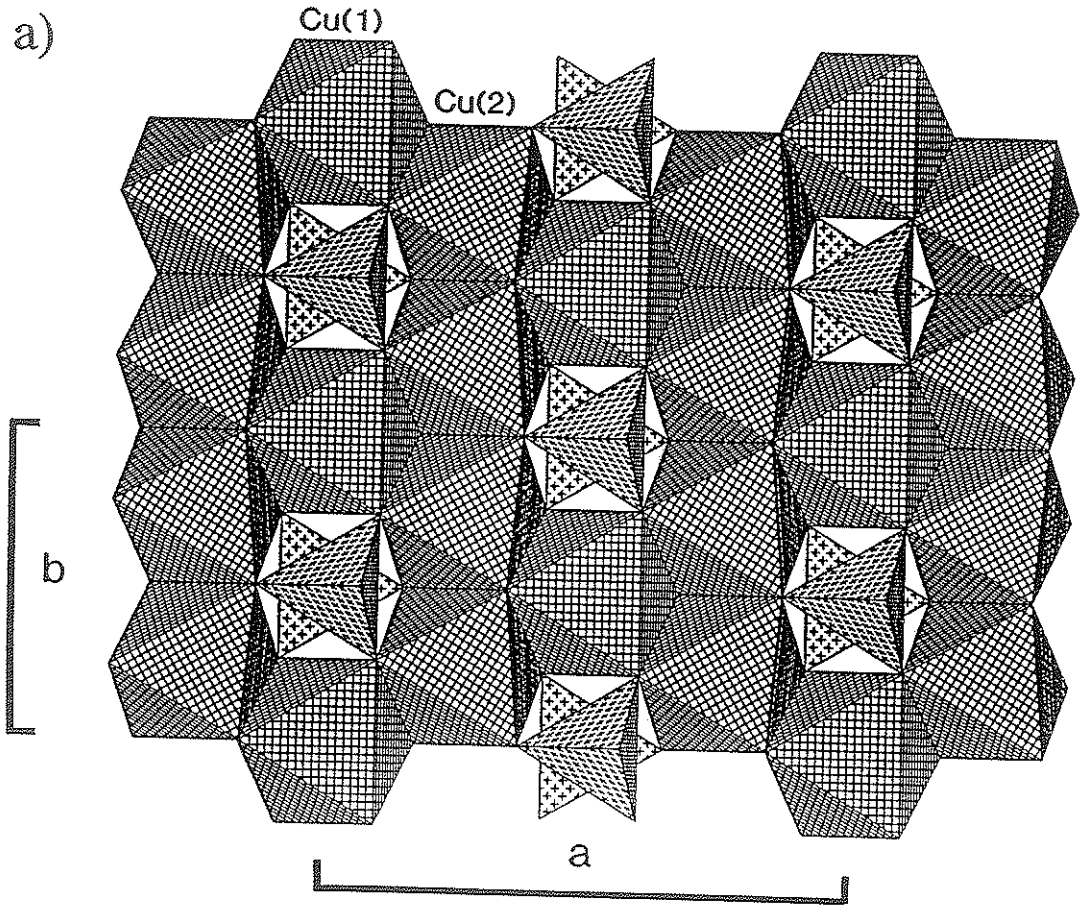

Figure 2.15. Polyhedral representations of the crystal structure of $KCu_3^{2+}(OH)_2[(AsO_4)H(AsO_4)]$. The copper octahedra are cross-hatched, arsenic tetrahedra are shaded with crosses and the potassium atoms are shaded with a regular dot pattern. a) The octahedral-tetrahedral sheet projected onto (001), b) the structure projected onto (010), c) the structure projected onto (100).

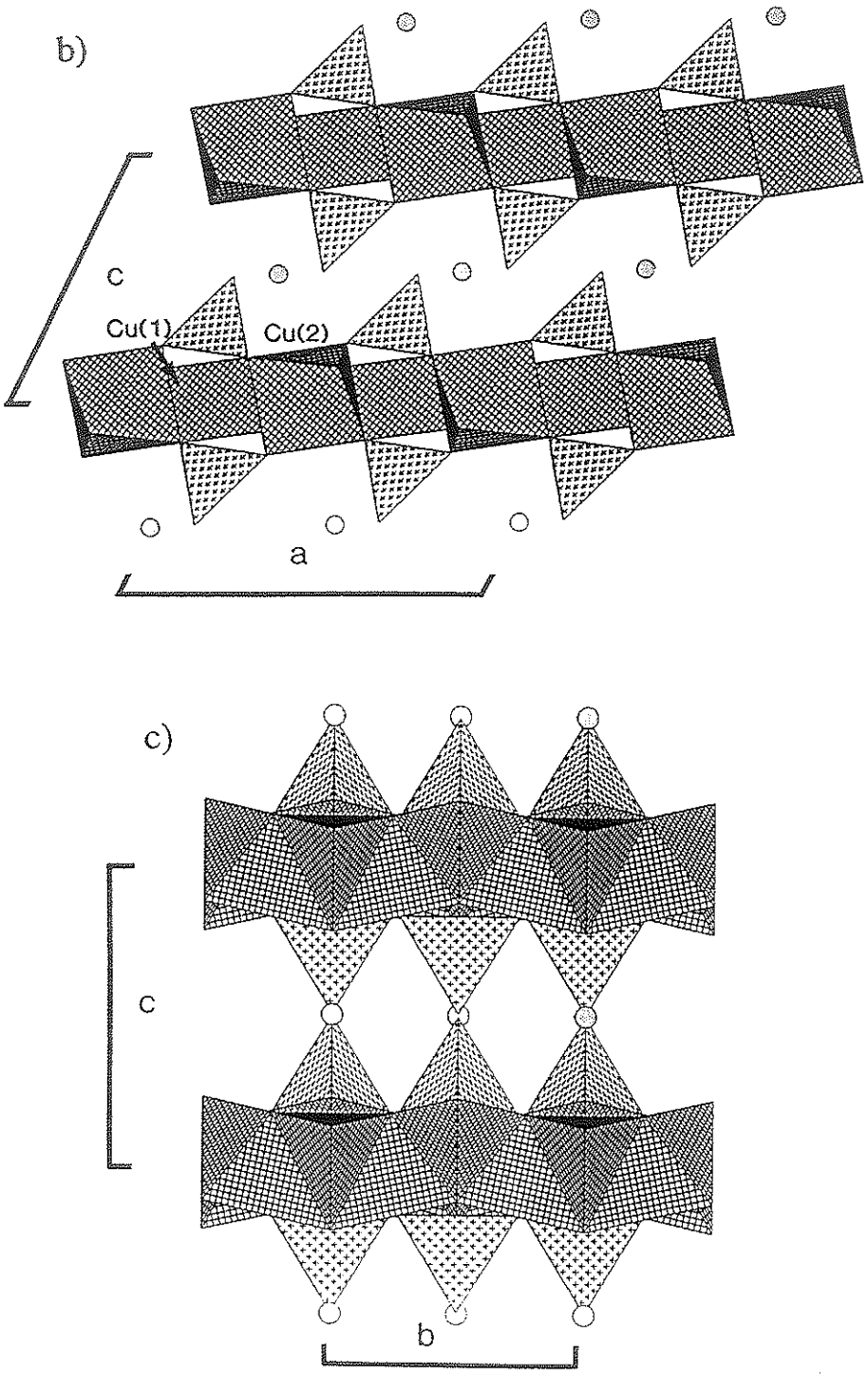

Figure 2.15. Continued

Table 2.2 Comparison of unit-cell parameters (Å) and octahedral $Cu^{2+}\phi_6$ bond-lengths (Å) for volborthite, bayldonite and $KCu_3^{2+}(OH)_2[(AsO_4)H(AsO_4)]$.

	a	b	c	β	Space Group	Ref.
Volborthite $Cu_3^{2+}(OH)_2V_2O_7\cdot 2H_2O$	10.610(2)	5.866(1)	7.208(1)	95.04(2)	C2/m	1
Bayldonite $Cu_3^{2+}Pb(AsO_4)_2(OH)_2$	10.147(2)	5.892(1)	14.081(2)	106.05(1)	C2/c	2
$KCu_3^{2+}(OH)_2[(AsO_4)H(AsO_4)]$	10.292(5)	5.983(3)	7.877(4)	117.86(2)	C2/m	3

Octahedral bond distances

Volborthite	Cu(1)	1.945(4) x2 2.172(4) x4	Cu(2)	1.922(3) x2 2.031(3) x2 2.414(3) x2		
Bayldonite	Cu(2)	1.878(7) x2 2.087(10) x2 2.272(9) x2	Cu(3)	1.924(9) x2 2.000(8) x2 2.454(8) x2	Cu(1)	1.891(7) x2 2.039(8) x2 2.423(10) x2
$KCu_3^{2+}(OH)_2[(AsO_4)H(AsO_4)]$	Cu(1)	1.899(2) x2 2.186(1) x4	Cu(2)	1.934(1) x2 2.000(1) x2 2.428(1) x2		

References: 1: Basso et al. (1988); 2: Ghose and Wan (1979); 3: Effenberger (1989).

Bayldonite

Bayldonite, $Cu_3^{2+}Pb(AsO_4)_2(OH)_2$ (Ghose and Wan, 1979), space group C2/c, has a unit cell that is very similar to those of volborthite and $KCu_3^{2+}(OH)_2[(AsO_4)H(AsO_4)]$ (Table 2.2). Bayldonite contains $Cu^{2+}\phi_6$ octahedral-tetrahedral sheets that are graphically identical to the octahedral-tetrahedral sheets in volborthite and $KCu_3^{2+}(OH)_2[(AsO_4)H(AsO_4)]$ (Fig. 2.16). Adjacent octahedral-tetrahedral sheets in bayldonite are connected through irregular $Pb^{2+}\phi_8$ polyhedra and hydrogen bonding (Fig 2.16). The c dimension of bayldonite is double that of volborthite and $KCu_3^{2+}(OH)_2[(AsO_4)H(AsO_4)]$, and there are three distinct Cu^{2+} positions, each of which is located at a centre of symmetry. The $Cu^{2+}\phi_6$ bond-lengths in bayldonite are compared to those in volborthite and $KCu_3^{2+}(OH)_2[(AsO_4)H(AsO_4)]$ in Table 2.2. Note that the Cu(2) site in bayldonite is related to the Cu(1) sites in volborthite and $KCu_3^{2+}(OH)_2[(AsO_4)H(AsO_4)]$, but the ligand arrangement is not (2+4)-distorted. Instead, the Cu(2) octahedron in bayldonite shows an elongated-rhombic distortion, best referred to as a (2+2+2)-distorted octahedron.

The (2+4)-distorted $Cu^{2+}\phi_6$ octahedra observed in Cu^{2+} oxysalt minerals are derived from X-ray diffraction data, and as such may be the result of:

(i) The presence of a statically (2+4)-distorted octahedron;

(ii) The dynamic time averaging of two non-aligned (4+2)-distorted octahedra;

(iii) The static disorder of (4+2)-distorted octahedra.

I propose that the (2+4)-distorted $Cu^{2+}\phi_6$ octahedra in volborthite and $KCu_3^{2+}(OH)_2[(AsO_4)H(AsO_4)]$, and the (2+2+2)-distorted octahedron in

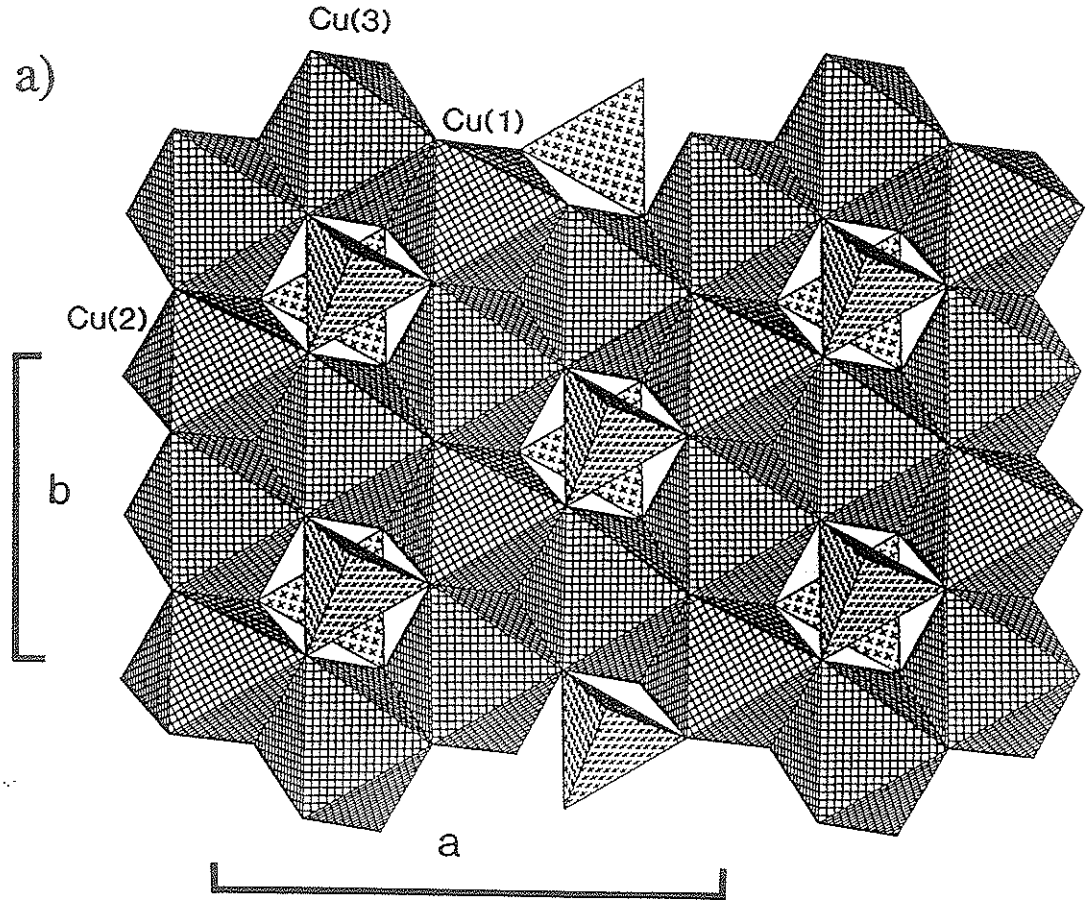

Figure 2.16. Polyhedral representations of the crystal structure of bayldonite, $Cu_3^{2+}Pb(AsO_4)_2(OH)_2$. The copper octahedra are cross-hatched, arsenic tetrahedra are shaded with crosses and the lead atoms are cross-hatched circles. a) The octahedral-tetrahedral sheet projected onto (001), b) the structure projected onto (010), c) the structure projected onto (100).

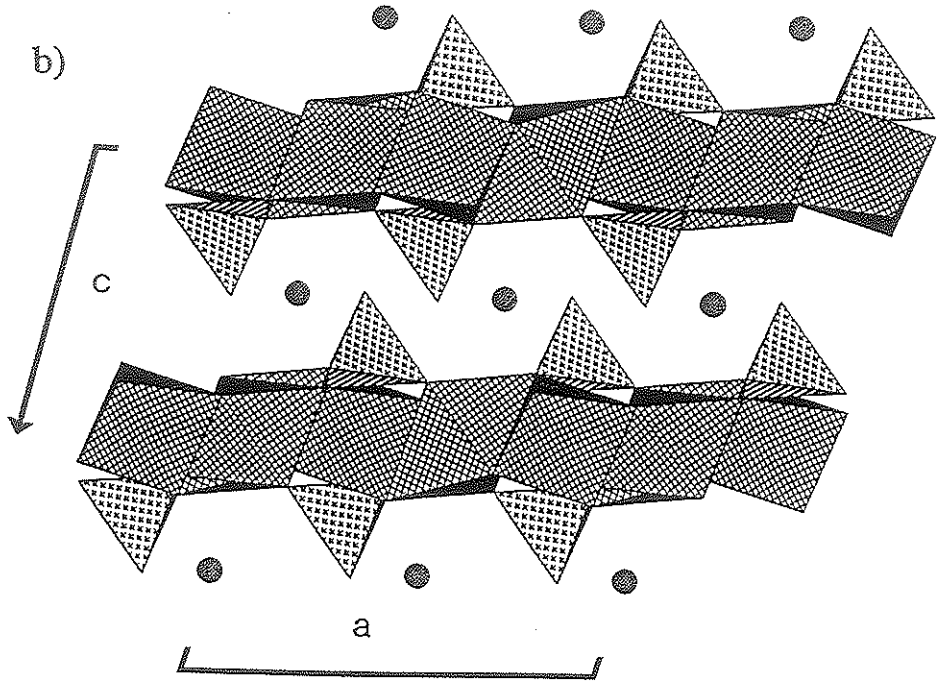

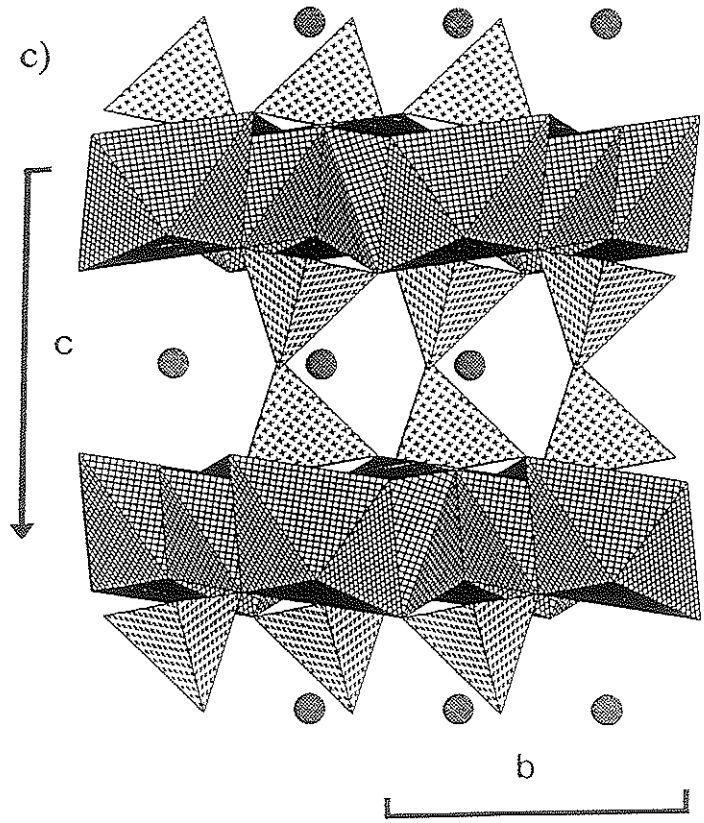

Figure 2.16. Continued

bayldonite, are the result of a dynamic Jahn-Teller effect. Supporting arguments are given in section 2.9, but first it is necessary to consider (2+2+2)-distorted $Cu^{2+}\phi_6$ geometries, and the dynamic Jahn-Teller effect, in more detail.

2.5.5 Occurrences of (2+2+2)-Distorted $Cu^{2+}\phi_6$ Octahedra in Cu^{2+} Oxysalt Minerals

The ligand-field arguments presented in section 2.2.1 indicate that either a (4+2) or (2+4) tetragonal distortion of the $Cu^{2+}\phi_6$ octahedral environment will remove the energetically degenerate electronic state and stabilize the octahedron. However, examination of $Cu^{2+}\phi_6$ octahedra in Cu^{2+} oxysalt minerals shows that tetragonally distorted octahedra are rare: to date, only five such $Cu^{2+}\phi_6$ octahedra occur in minerals.

Apical and equatorial Cu-ϕ distortion parameters may be defined individually as:

$$\Delta_{ap} = 1/2\Sigma[(l_{ap,i}-l_{ap,o})/l_{ap,o}]^2 \qquad (2.2)$$

$$\Delta_{eq} = 1/4\Sigma[(l_{eq,i}-l_{eq,o})/l_{eq,o}]^2 \qquad (2.3)$$

where l_o is the average bond-length. The values of Δ_{ap} and Δ_{eq} for all (4+2)-distorted $Cu^{2+}\phi_6$ octahedra in minerals are shown in Figure 2.17. For ranges of Δ_{eq} from 0.0 to 0.00075, there is a considerable range of Δ_{ap} observed, i.e., from 0.0 to 0.023. However, for values of Δ_{eq} ranging from 0.00075 to 0.003, there is generally a very narrow range of Δ_{ap}.

Of the 159 (4+2)-distorted $Cu^{2+}\phi_6$ octahedra in Cu^{2+} oxysalt minerals, 42 occur on a centre of symmetry. Each of these octahedra must have Δ_{ap} =

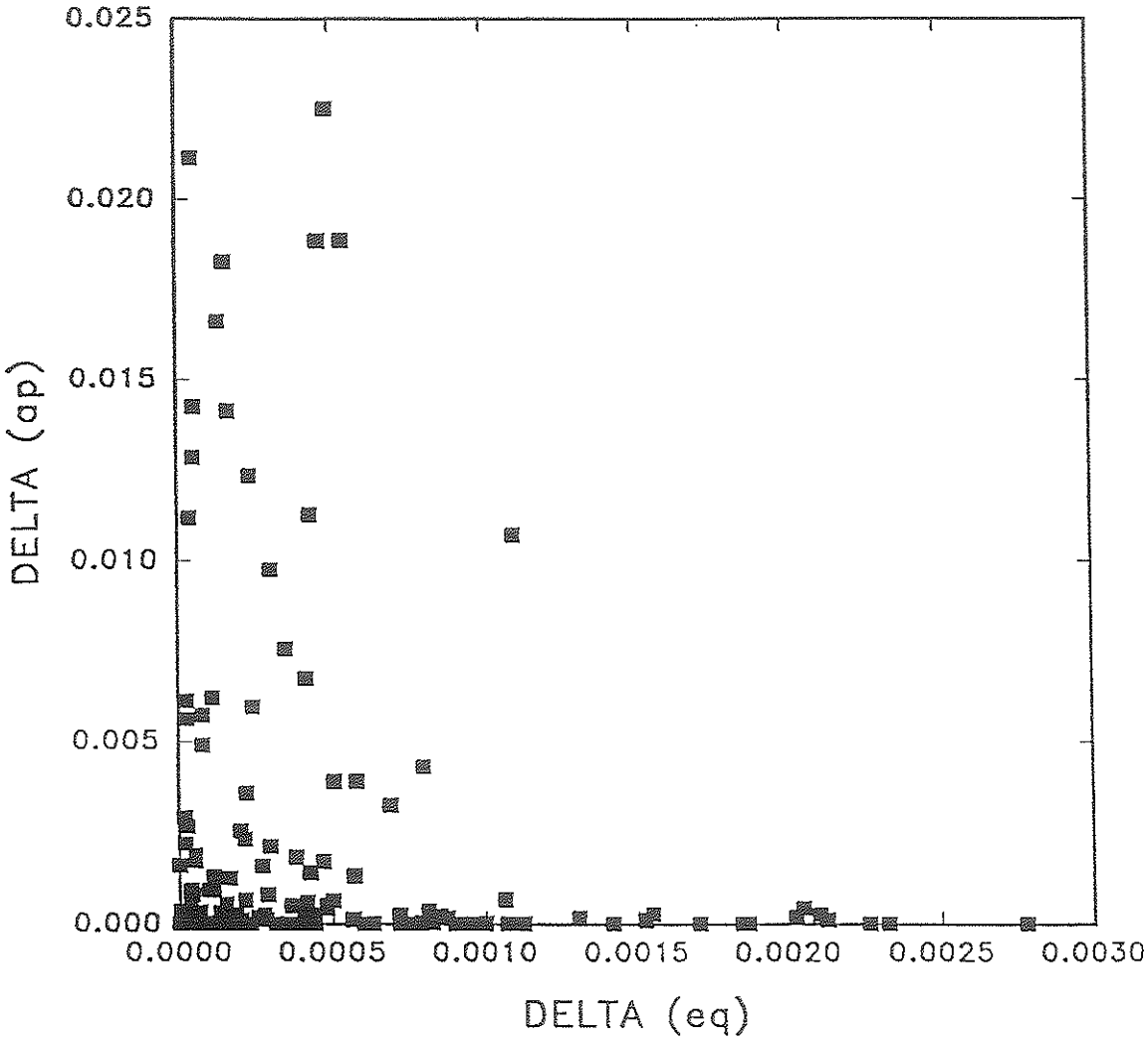

Figure 2.17. Apical and equatorial bond-length distortion parameters for (4+2)-distorted $Cu^{2+}\phi_6$ octahedra in Cu^{2+} oxysalt minerals; note the different scales on each axis.

0.0, and plot along the horizontal axis in Figure 2.17. Many of these centrosymmetric $Cu^{2+}\phi_6$ octahedra show very large Δ_{eq} values. Note also that there are several occurrences of $Cu^{2+}\phi_6$ octahedra that have large Δ_{eq} values but low Δ_{ap} values which are not on centres of symmetry (i.e., $\Delta_{ap} \neq 0.0$).

The $Cu^{2+}\phi_6$ octahedra with high values of Δ_{eq} and low values of Δ_{ap} are rhombically elongated octahedra, and typically have two short *trans* Cu-ϕ_{eq} distances, two long *trans* Cu-ϕ_{ap} distances and two intermediate *trans* Cu-ϕ_{eq} distances. Such a distortion is best referred to as a (2+2+2) distortion and can be considered as a subclass of the (4+2)-distorted $Cu^{2+}\phi_6$ octahedra, as the two intermediate Cu-ϕ_{eq} distances are invariably closer to the short Cu-ϕ_{eq} distances than to the long Cu-ϕ_{ap} distances. Examples of (2+2+2)-distorted $Cu^{2+}\phi_6$ octahedra in minerals are given in Table 2.3, which contains only (2+2+2)-distorted octahedra in which the average intermediate Cu-ϕ_{eq} distance is greater than 0.10 Å longer than the average short Cu-ϕ_{eq} distance.

For centrosymmetric (2+2+2)-distorted $Cu^{2+}\phi_6$ octahedra, the degree to which a (2+2+2) distortion is present is conveniently given by the parameter Δ_T where:

$$\Delta_T = [(Cu\text{-}\phi_{eq,short}) + (Cu\text{-}\phi_{eq,intermed.})] / [(Cu\text{-}\phi_{eq,intermed.}) + (Cu\text{-}\phi_{ap})] \qquad 2.4$$

Values of Δ_T (Table 2.3) range from 0.857 in lubjibaite to a maximum of 0.923 in cyanochroite; note that cyanochroite and bayldonite are the only Cu^{2+} oxysalt minerals which contain (2+2+2)-distorted $Cu^{2+}\phi_6$ octahedra with $\Delta_T > 0.90$.

Table 2.3 Examples of (2+2+2)-distorted $Cu^{2+}\phi_6$ octahedra observed in Cu^{2+} oxysalt minerals; bond-lengths in Å.

	Octahedra on a centre of symmetry			Ref.	Δ_T
Bayldonite	1.878 x2	2.087 x2	2.272 x2	1	0.910
	1.891 x2	2.039 x2	2.423 x2		0.881
Cyanochroite	1.944 x2	2.069 x2	2.279 x2	2	0.923
Turquois	1.915 x2	2.109 x2	2.422 x2	3	0.888
Chalcosiderite	1.914 x2	2.079 x2	2.484 x2	4	0.875
Dolerophanite	1.992 x2	2.070 x2	2.526 x2	5	0.884
Volborthite	1.922 x2	2.031 x2	2.414 x2	6	0.889
Ludjibaite	1.918 x2	2.04 x2	2.578 x2	7	0.857
Vauquelinite	1.94 x2	2.06 x2	2.44 x2	8	0.889
Chalcocyanite	1.916 x2	2.049 x2	2.373 x2	9	0.897
Cornubite	1.911 x2	2.031 x2	2.467 x2	10	0.876

	Octahedra not on a centre of symmetry						Ref.
Campigliaite	1.86	2.00	2.08	2.09	2.39	2.47	11
Kamchatkite	1.86	1.98	2.03	2.04	2.37	2.47	12
Conichalcite	1.95	1.95	2.04	2.09	2.38	2.38	13
Calciovolborthite	1.906	1.909	2.056	2.071	2.337	2.415	14
Duftite	1.91	1.94	2.10	2.11	2.29	2.35	15
Malachite	1.918	1.915	2.049	2.115	2.372	2.369	16
	1.898	1.911	1.996	2.055	2.509	2.642	
Pseudomalachite	1.884	1.884	1.974	1.985	2.395	2.755	17
Antlerite	1.906	1.923	2.024	2.033	2.344	2.414	18
Demesmaekerite	1.95	1.95	2.04	2.07	2.38	2.39	19
Fornacite	1.84	1.95	2.02	2.08	2.36	2.46	20
Devillite	1.90	2.00	2.10	2.12	2.37	2.37	21
	1.89	1.93	2.07	2.11	2.38	2.43	
	1.85	1.91	1.99	2.05	2.44	2.49	

References: 1: Ghose and Wan (1979); 2: Robinson and Kennard (1972); 3: Cid-Dresdner (1965); 4: Giuseppetti et al. (1989); 5: Effenberger (1985); 6: Basso et al. (1988); 7: Shoemaker et al. (1981); 8: Fanfani and Zanazzi (1968); 9: Wildner and Giester (1988); 10: Sieber et al. (1984); 11: Sabelli (1982); 12: Varaksina et al. (1990); 13: Qurashi and Barnes (1963); 14: Basso et al. (1989); 15: Effenberger and Pertlik (1988); 16: Figan et al. (1977); 17: Shoemaker et al. (1977); 18: Hawthorne et al. (1989); 19: Ginderow and Cesbron (1983); 20: Cocco et al. (1966); 21: Sabelli and Zanazzi (1972).

2.6 The Dynamic Jahn-Teller Effect Revisited

In the case of a dynamic Jahn-Teller effect, the energetically degenerate electronic state associated with a d^9 metal in an octahedral coordination is removed by vibrational distortion of the octahedral cluster. In this case, the distortions are not static and there is a continuous interchange of distortion direction. The dynamic Jahn-Teller effect was introduced in Section 2.3.2.

The Mexican-hat potential for the coupling of the E_g vibrational modes with the electronic state of $Cu^{2+}\phi_6$ is given in Figure 2.4. The three possible types of circular cross-sections through the minimum of the potential-energy surface of Figure 2.4 are given in Figure 2.5. The energy minima occur at ϕ = 0, 120 and 240°, and positions I, II and III correspond to a (4+2)-distorted $Cu^{2+}\phi_6$ octahedron elongated in each of the three possible axial directions.

As noted earlier (Section 2.3.2), if the energy barrier B is less than the thermal energy, a dynamic interchange of elongation directions of the (4+2)-distorted octahedron will continually occur as the energy barrier is overcome. The $Cu^{2+}\phi_6$ geometry observed by crystallographic techniques will be a time-averaged geometry. Depending on the relative energies of the wells, either a holosymmetric, (2+4)-distorted or a rhombically elongated octahedron [(2+2+2)-distorted] will be observed (see Section 2.3.2, Fig. 2.5).

The energies of the wells will depend on the linear coupling and higher-order terms that result in warping of the lower surface of the Mexican-hat potential (Hathaway, 1984). Long-range effects in a crystal will tend to stabilize one or two of the energy wells with respect to the others (Bersuker, 1984).

Also of considerable importance when considering dynamic Jahn-Teller effects is the height of the energy barriers between the wells involved. The energy barriers between the I, II and III (4+2)-distorted octahedra in Figure 2.5 correspond to (2+4)-distorted octahedra compressed down each of the three axial directions. If the energy barrier is about the same or less than the thermal energy of the system, continuous interchange between the (4+2)-distorted octahedra will occur.

The complete range of dynamic Jahn-Teller behaviour is shown by the $Cu^{2+}(NO_2)_6$ octahedron in $Cs_2PbCu^{2+}[NO_2]_6$. The structure is cubic at 420 K, with a holosymmetric $Cu^{2+}(NO_2)_6$ octahedron [Cu-N x6 = 2.17 Å] (Mullen et al., 1975); at room temperature, it is orthorhombic with a (2+4)-distorted $Cu^{2+}(NO_2)_6$ octahedron [Cu-N x4 = 2.227, Cu-N x2 = 2.070 Å] (Massey, 1973); at 160 K, it is monoclinic with a rhombically elongated octahedron [(2+2+2)-distorted] [Cu-N x2 = 2.073, Cu-N x2 = 2.115, Cu-N x2 = 2.300 Å] (Mullen et al., 1975).

The $Cs_2PbCu^{2+}[NO_2]_6$ structure shows the entire range of possible dynamic Jahn-Teller effects, from a holosymmetric octahedron associated with three equal energy wells, through a (2+4)-distorted octahedron associated with two energy wells of equal energy and one of considerably higher energy, to a (2+2+2)-distorted octahedron associated with two energy wells of similar but unequal energy and a third well of considerably higher energy. Few materials show the whole range of dynamic Jahn-Teller effects, due at least in part to thermal instability.

A structure that contains a statically (4+2)-distorted $Cu^{2+}\phi_6$ octahedron does not include any dynamic Jahn-Teller effects. As the structure is heated, an apparent (2+2+2)-distorted octahedron may ensue as

a dynamic interchange between the two lowest-energy wells develops. The distribution between the two wells will be controlled by the Boltzman distribution law. As the temperature is increased, the thermal population of the two lower-energy wells will become more similar, and the time-averaged effect will be an apparent (2+2+2)-distorted $Cu^{2+}\phi_6$ octahedron that becomes increasingly (2+4) in character as the intermediate and long Cu-ϕ bond-lengths become similar. A phase change to a higher symmetry is likely to ensue, such that the new symmetry will reflect the time-averaged presence of the (2+4)-distorted $Cu^{2+}\phi_6$ octahedron. The same sort of process occurs again as the system goes from a (2+4)-distorted to a holosymmetric $Cu^{2+}\phi_6$ octahedron with increasing temperature.

Copper Tutton's salts show dynamic Jahn-Teller effects. Considerable variable-temperature structural work has been done for $(NH_4)_2Cu^{2+}(H_2O)_6(SO_4)_2$, with the structure studied at 295 K (Webb et al., 1965; Montgomery and Lingafelter, 1966; Brown and Chibambaram, 1969), 203 and 123 K (Alcock et al., 1984). The room-temperature structure contains a $Cu^{2+}\phi_6$ octahedron of rhombically elongated octahedral geometry [a (2+2+2) distortion] (Table 2.4, Fig. 2.18). This strong (2+2+2) distortion suggests that the octahedron may be a result of the dynamic Jahn-Teller effect involving two energy wells of similar but unequal energies and a third well of considerably higher energy. The octahedron is elongated in the Cu-O(7) direction most of the time, but the nearby energy well corresponding to elongation in the Cu-O(8) direction is also significantly occupied, and a dynamic interchange between these two distortion directs occurs.

The temperature-dependent nature of the Cu-ϕ bond-lengths in the $(NH_4)_2Cu^{2+}(H_2O)_6(SO_4)_2$ structure (Table 2.4, Fig. 2.18) indicates that a

Table 2.4 Octahedral bond-lengths (Å) in $(NH_4)_2Cu^{2+}(H_2O)_6(SO_4)_2$ and $(M^+)_2Cu^{2+}(H_2O)_6(SO_4)_2$, M^+ = K, Rb, Cs, Tl.

	$(NH_4)_2Cu^{2+}(H_2O)_6(SO_4)_2$		
	295 K	203 K	123 K
Cu-O(7)	2.219(5)	2.250(2)	2.278(2)
Cu-O(8)	2.095(5)	2.041(2)	2.012(1)
Cu-O(9)	1.961(5)	1.967(2)	1.970(1)
Ref.	1	2	2

	$(M^+)_2Cu^{2+}(H_2O)_6(SO_4)_2$				
	K	Rb	Rb(77 K)	Cs	Tl
Cu-O(8)	2.278(2)	2.307(3)	2.317(5)	2.315(5)	2.317(5)
Cu-O(7)	2.069(3)	2.031(3)	2.000(5)	2.004(4)	2.017(4)
Cu-O(9)	1.943(3)	1.957(3)	1.978(5)	1.966(5)	1.957(5)
Ref.	3	4	5	6	7

References: 1: Montgomery and Lingafelter (1966); 2: Alcock et al. (1984); 3: Robinson and Kennard (1972); 4: Van der Zee et al. (1972); 5: Smith et al. (1975); 6: Shields and Kennard (1972); 7: Shields et al. (1972).

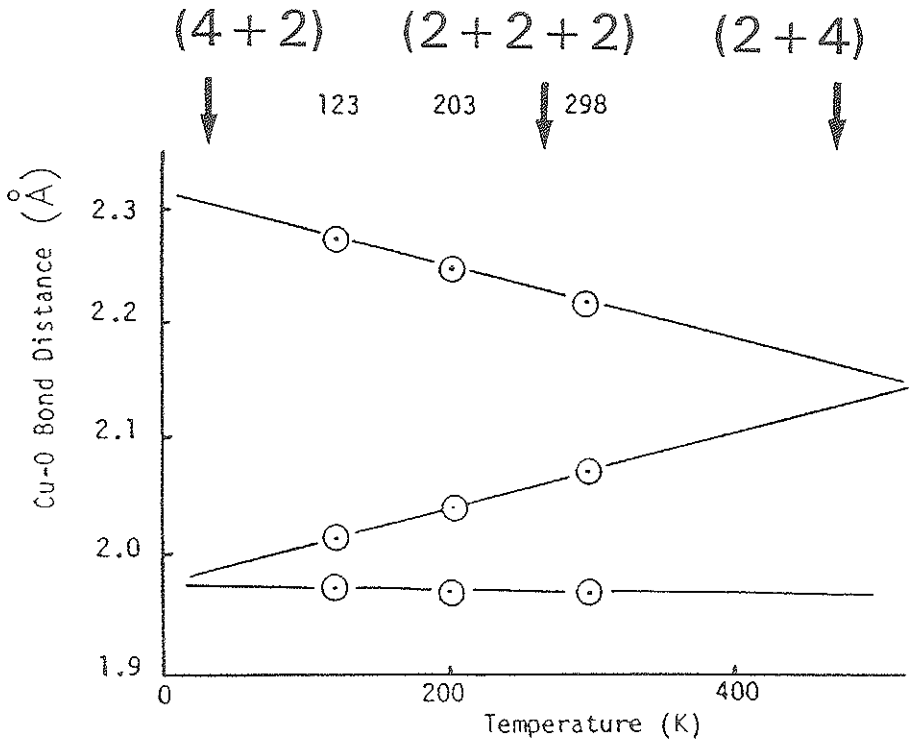

Figure 2.18. The temperature dependence of Cu-ϕ bond-lengths in $(NH_4)_2Cu^{2+}(H_2O)_6(SO_4)_2$. From Hathaway (1984).

dynamic Jahn-Teller effect does occur in this structure (Alcock et al., 1984). Continued cooling results in a steady increase of the Cu-O(7) distance, a steady decrease in the Cu-O(8) distance, and no significant change in the Cu-O(9) distance (Table 2.4).

The structures of some other copper Tutton's salts have also been reported. These include $K_2Cu^{2+}(H_2O)_6(SO_4)_2$ (Robinson and Kennard, 1972), $Rb_2Cu^{2+}(H_2O)_6(SO_4)_2$ (Van der Zee et al., 1972; Smith et al., 1975), $Cs_2Cu^{2+}(H_2O)_6(SO_4)_2$ (Shields and Kennard, 1972) and $Tl_2Cu^{2+}(H_2O)_6(SO_4)_2$ (Shields et al., 1972); of these, $K_2Cu^{2+}(H_2O)_6(SO_4)_2$ is the mineral cyanochroite. The bond-lengths for the $Cu^{2+}\phi_6$ octahedron in each of these structures are included in Table 2.4. Note that the long Cu-O bond is to O(8) in each case rather than to O(7) as in $(NH_4)_2Cu^{2+}(H_2O)_6(SO_4)_2$.

Each of the $(M^+)_2Cu^{2+}(H_2O)_6(SO_4)_2$ structures contain a rhombically elongated $Cu^{2+}\phi_6$ octahedron, i.e., a (2+2+2)-distorted octahedron. Alcock et al. (1984) suggest that the Cs salt probably contains a static (2+2+2)-distorted $Cu^{2+}\phi_6$ octahedron with only the lowest-energy well of the potential occupied. They indicate that the $Cu^{2+}\phi_6$ octahedron in the Rb salt has a small but significant dynamic component, as apparently verified by the low-temperature structure determination. Alcock et al. (1984) suggest that the K salt (cyanochroite) has a considerable dynamic component, with significant thermal population of the two lower-energy wells. Variable-temperature data for the K salt is not yet available, but comparison of the $Cu^{2+}\phi_6$ geometries in $(NH_4)_2Cu^{2+}(H_2O)_6(SO_4)_2$ and $(M^+)_2Cu^{2+}(H_2O)_6(SO_4)_2$ does suggest a significant dynamic component in $K_2Cu^{2+}(H_2O)_6(SO_4)_2$.

2.7 Possible Dynamic Jahn-Teller Effects in Minerals

Most Cu^{2+} oxysalt minerals and Cu^{2+} compounds contain (4+2)-distorted $Cu^{2+}\phi_6$ octahedra that show little or no evidence of a dynamic Jahn-Teller component. As minerals are typically very stable compounds, it has generally been assumed that dynamic Jahn-Teller effects will not occur in their structures. However, the arguments developed here suggest otherwise. The presence of (2+4)-distorted and (2+2+2)-distorted $Cu^{2+}\phi_6$ octahedra in minerals suggests that some of them may show dynamic Jahn-Teller effects. As a dynamic Jahn-Teller effect may lead to observation of each of these coordination geometries, care must be taken to determine whether a static or dynamic effect is observed.

2.8 Recognition of Dynamic Jahn-Teller $Cu^{2+}\phi_6$ Octahedra in Minerals

Cu^{2+} oxysalt minerals containing (2+4)- or (4+2)-distorted $Cu^{2+}\phi_6$ octahedra should be investigated further to determine if the configuration is static, dynamic or a result of static disorder. There are three possible means of obtaining this information: (i) variable-temperature crystallographic studies; (ii) crystal-structure refinement followed by the study of anisotropic-displacement parameters; (iii) electron-spin-resonance (ESR) spectroscopy.

2.8.1 Variable-Temperature Crystallography

The dynamic Jahn-Teller effect is temperature dependent. The effect is due to a dynamic interchange of elongation directions of the (4+2)-distorted $Cu^{2+}\phi_6$ octahedron, and the relative energies of the three distortion

directions are represented by energy wells (Fig. 2.4, Section 2.6). The interchange of elongation direction is a function of the relative energies of the wells, and of the energy barrier between the wells. If the total energy of the system is sufficient to overcome the energy barrier between the wells, the population of the wells will be a Boltzman distribution. Variation of the temperature of the system will alter the populations of the energy wells, thus changing the apparent Cu-ϕ bond-lengths. Marked sensitivity of Cu-ϕ bond-lengths to temperature, such as is observed in the structure of $(NH_4)_2Cu^{2+}(H_2O)_6(SO_4)_2$ (Section 2.6), indicates that the $Cu^{2+}\phi_6$ octahedron is dynamic.

2.8.2 Anisotropic-Displacement Parameters

Dynamic Jahn-Teller distortion of a $Cu^{2+}\phi_6$ octahedron should be accompanied by marked anisotropic motion of the octahedral ligands involved. Non-dynamic $M\phi_6$ octahedra are expected to have maximum anion anisotropic-displacement parameters sub-perpendicular to the M-ϕ bond axis (provided there is no static disorder), reflecting the relative ease of bond bending compared to bond stretching. However, in the case of a dynamic Jahn-Teller configuration, the opposite applies, such that the maximum anisotropic displacement of the anions is more-or-less parallel to the Cu-ϕ bond axis. The best way to identify dynamic Jahn-Teller $Cu^{2+}\phi_6$ octahedra using anisotropic-displacement parameters is to compare the root-mean-square displacements of the ligands in the $Cu^{2+}\phi_6$ octahedron with those observed for non-Jahn-Teller distorted $M^{2+}\phi_6$ octahedra in isostructural compounds (Hathaway et al., 1981).

Application of this approach to the identification of dynamically distorted $Cu^{2+}\phi_6$ octahedra in minerals is hindered by the lack of non-Cu^{2+} analogues of most Cu^{2+} oxysalt structures. Also, many Cu^{2+} oxysalt mineral structure refinements in the literature are of low precision because of poor crystal quality, and the anisotropic-displacement parameters (if given) may be seriously in error on this account.

The anisotropic-displacement parameters for a dynamic Jahn-Teller $Cu^{2+}\phi_6$ octahedron give specific information on the nature of the distortion:

(i) An apparent holosymmetric $Cu^{2+}\phi_6$ octahedron results when there is a dynamic interchange between all three of the possible elongation directions. In this case, each octahedral ligand should show maximum anisotropic displacement along each Cu-ϕ bond.

(ii) An apparent (2+4)-distorted octahedron results from the dynamic interchange of two elongation directions. In this case, only four of the six octahedral ligands should show maximum anisotropic displacements parallel to the Cu-ϕ bonds.

(iii) The effect will not be as strong in partially dynamic systems that result in (2+2+2)-distorted $Cu^{2+}\phi_6$ octahedra. In these cases, the dynamic Jahn-Teller effect will be more difficult to recognize on the basis of anisotropic-displacement parameters alone.

2.8.3 Electron-Spin-Resonance Spectroscopy

Electron-spin-resonance spectroscopy has been used in the study of dynamic Jahn-Teller $Cu^{2+}\phi_6$ octahedra (Hathaway, 1984). The method is usually able to distinguish between static Jahn-Teller distorted $Cu^{2+}\phi_6$ octahedra and apparent holosymmetric octahedra that are a result of the

dynamic Jahn-Teller effect. However, the ESR spectrum of an *apparently* (2+4)-distorted octahedron (that arises due to the dynamic interchange between two distortion directions) is very similar to that of a static octahedron (Hathaway, 1984). Also, ESR spectra for dilute Cu^{2+} compounds are more informative than for non-dilute Cu^{2+} compounds, as spectra of the latter are complicated by exchange coupling (Hathaway, 1984). However, the temperature dependence of the ESR spectra of some Cu^{2+} compounds has been used to suggest a dynamic Jahn-Teller effect (i.e., Rubins and Drumheller, 1987; Rubins et al., 1984).

2.9 Possible Dynamic $Cu^{2+}\phi_6$ Octahedra in Minerals

Various minerals contain $Cu^{2+}\phi_6$ octahedra that may be dynamically distorted. Several examples are considered in the following sections, and although a strong case may be made for the presence of dynamic $Cu^{2+}\phi_6$ octahedra, further verification by variable-temperature structure refinements is desirable.

2.9.1 A Dynamic (2+2+2)-Distorted $Cu^{2+}\phi_6$ Octahedron in Cyanochroite

Cyanochroite, $K_2Cu^{2+}(H_2O)_6(SO_4)_2$, has been described from Mount Vesuvius, Italy, where it occurs as a volcanic exhalative. It is a Tutton's salt, all of which have the general formula $M^{+}M^{2+}(H_2O)_6(X^{6+}O_4)_2$. Cyanochroite is a member of the picromerite group, which includes picromerite, $K_2Mg(H_2O)_6(SO_4)_2$, möhrite, $(NH_4)_2Fe(H_2O)_6(SO_4)_2$, boussingaultite, $(NH_4)_2Mg(H_2O)_6(SO_4)_2$ and nickel-boussingaultite, $(NH_4)_2(Ni,Mg)(H_2O)_6(SO_4)_2$. The structure of cyanochroite (Robinson and

Kennard, 1972) (Fig. 2.19) contains isolated $Cu^{2+}(H_2O)_6$ octahedra that are weakly bonded to the remainder of the structure by K-O bonds and a network of hydrogen bonds. The Tutton's-salt structure allows considerable flexibility of the $M^{2+}(OH_2)_6$ octahedral geometry (Eby and Hawthorne, 1993), allowing the structure to accommodate a Jahn-Teller distortion of the octahedral environment; thus Cu^{2+} Tutton's salts are strictly isostructural with non-Cu^{2+} Tutton's salts.

Given the structural compliance of the octahedron in the Tutton's-salt structure, it is surprising that the $Cu^{2+}\phi_6$ octahedron in cyanochroite shows the strongest rhombic elongation [(2+2+2)-distortion] of any mineral, as indicated by the Δ_T parameter (Table 2.3). If such a compliant arrangement were to accommodate a statically distorted $Cu^{2+}\phi_6$ octahedron, it should show an essentially tetragonal (4+2)-distortion geometry. The observed (2+2+2)-distorted $Cu^{2+}\phi_6$ geometry in cyanochroite is only consistent with a dynamically distorted octahedron, as predicted by Alcock et al. (1984) and as reviewed in Section 2.6.

2.9.2 Dynamic $Cu^{2+}\phi_6$ Octahedra in the Structures of Bayldonite, Volborthite and $KCu_3^{2+}(OH)_2[(AsO_4)H(AsO_4)]$

Only two minerals contain (2+2+2)-distorted $Cu^{2+}\phi_6$ octahedra with $\Delta_T > 0.90$ (Table 2.3). One of these minerals is cyanochroite, in which I have proposed a dynamic Jahn-Teller effect. The other is the $Cu^{2+}(2)\phi_6$ octahedron in bayldonite. The Cu-ϕ bond-length distributions in the two minerals with $\Delta_T > 0.90$ are quite similar (Table 2.3), raising the possibility that the $Cu^{2+}(2)\phi_6$ octahedron in bayldonite is also dynamic.

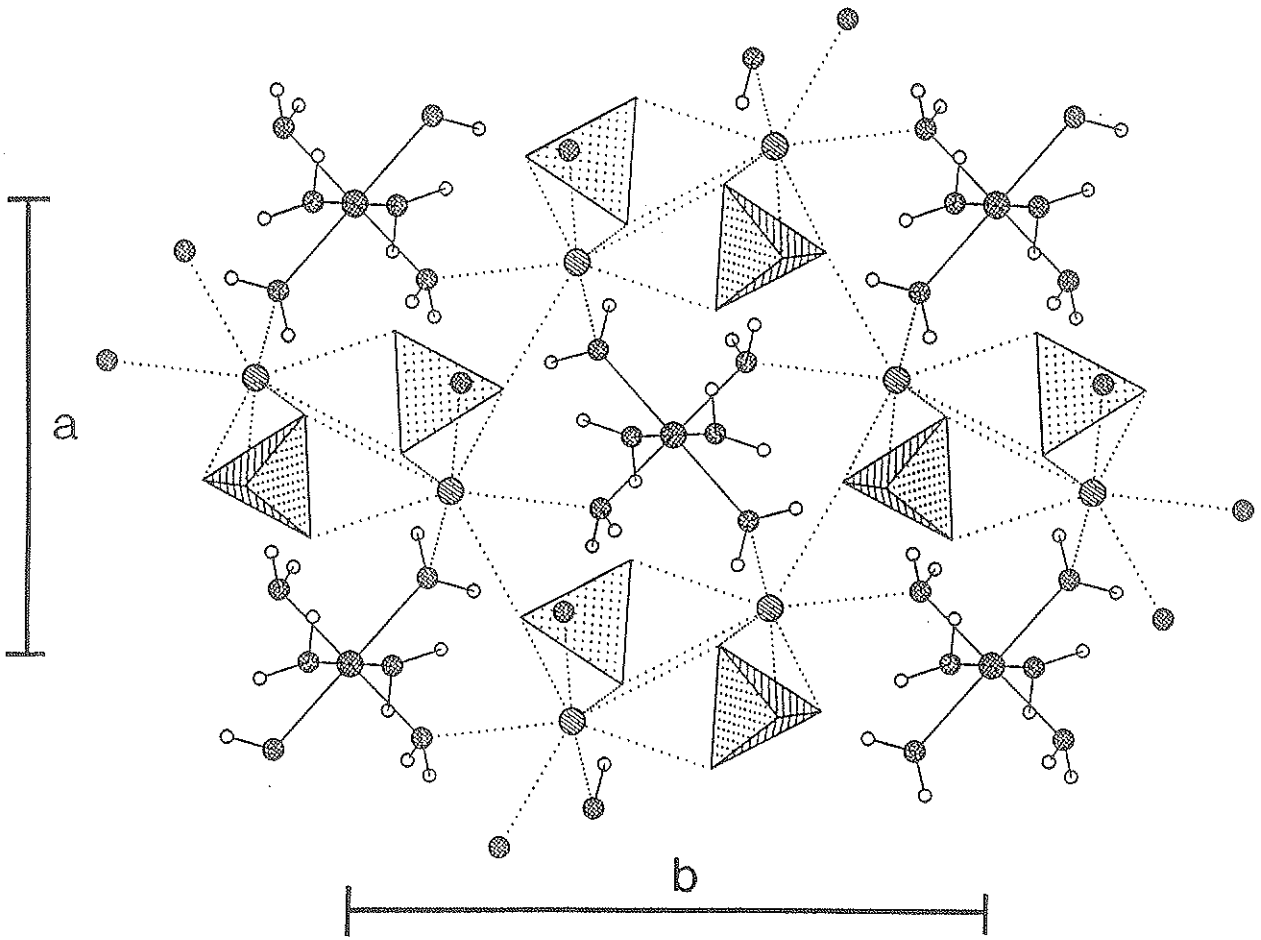

Figure 2.19. The crystal structure of cyanochroite projected onto (001). Copper atoms are cross-hatched circles, potassium atoms are circles shaded with parallel lines, sulphur tetrahedra are shaded with a regular dot pattern, oxygen atoms are open circles shaded with a cross-hatch pattern, and hydrogen atoms are small open circles. K-O bonds are drawn as dotted lines, Cu-O and O-H bonds are drawn as solid lines.

As noted in section 2.5.4, bayldonite, volborthite and $KCu_3^{2+}(OH)_2[(AsO_4)H(AsO_4)]$ all contain graphically identical octahedral-tetrahedral sheets (Figs. 2.14, 2.15, 2.16). The (2+2+2)-distorted $Cu^{2+}(2)\phi_6$ octahedron in the lower-symmetry sheets in bayldonite is graphically equivalent to the (2+4)-distorted $Cu^{2+}(1)\phi_6$ octahedra in volborthite and $KCu_3^{2+}(OH)_2[(AsO_4)H(AsO_4)]$. I propose that all three of these octahedra are the result of a dynamic Jahn-Teller effect.

Evidence supporting a dynamic Jahn-Teller $Cu^{2+}\phi_6$ octahedron in bayldonite, volborthite and $KCu_3^{2+}(OH)_2[(AsO_4)H(AsO_4)]$ should be obtainable from the anisotropic-displacement parameters for the octahedral ligands. However, anisotropic-displacement parameters were only reported for two of the oxygen atoms in volborthite. The structure refinement reported for $KCu_3^{2+}(OH)_2[(AsO_4)H(AsO_4)]$ (Effenberger, 1989) is of good quality, and anisotropic-displacement parameters are available. Therefore, the discussion of the anisotropic-displacement parameters that follows is largely in reference to that structure.

$KCu_3^{2+}(OH)_2[(AsO_4)H(AsO_4)]$

The structure of $KCu_3^{2+}(OH)_2[(AsO_4)H(AsO_4)]$ contains two symmetrically distinct $Cu^{2+}\phi_6$ octahedra; one shows a (2+4)-distortion [Cu(1)] and the other shows a (4+2)-distortion [Cu(2)]. The Cu(1) site has 2/m point symmetry such that the four equatorial Cu-O(3) bonds are equivalent, as are the two apical Cu-OH bonds (Table 2.2). The Cu(2) site has $\bar{1}$ symmetry, and the octahedron is somewhat (2+2+2)-distorted (Table 2.2).

Anisotropic-displacement parameters for the $Cu^{2+}(1)\phi_6$ and $Cu^{2+}(2)\phi_6$ octahedra in $KCu_3^{2+}(OH)_2[(AsO_4)H(AsO_4)]$ are shown in Figure 2.20. The

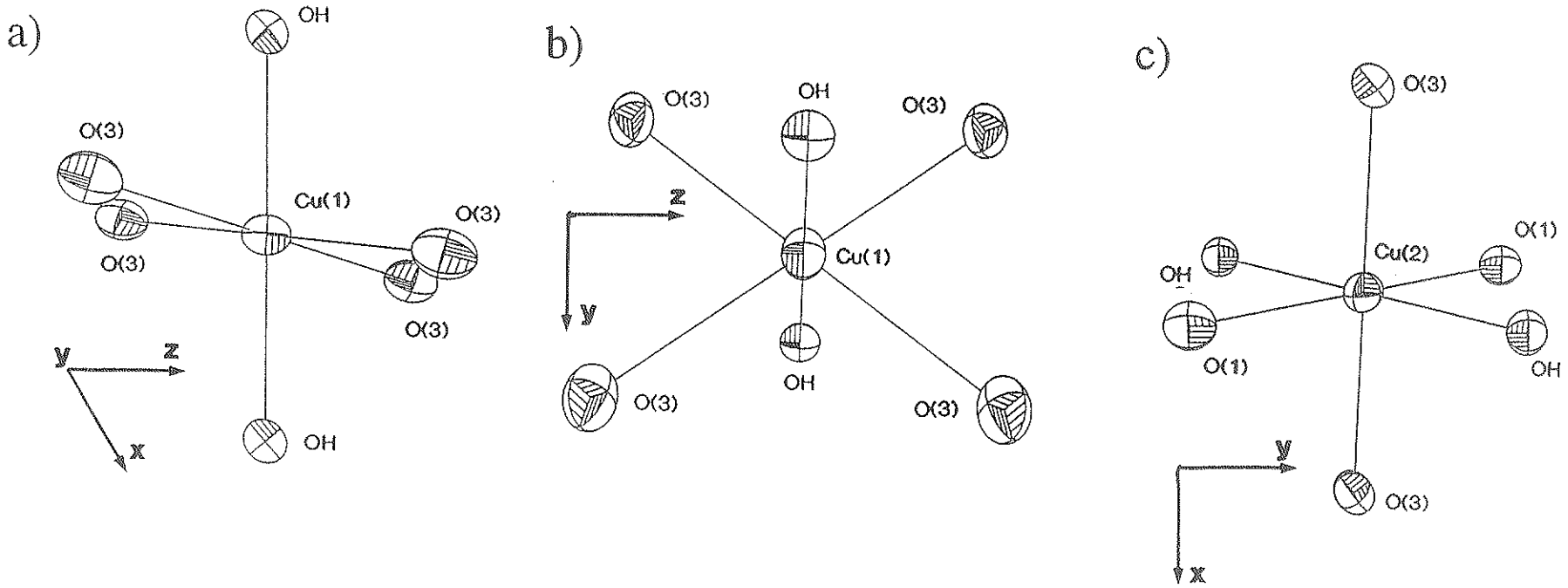

Figure 2.20. Anisotropic-displacement ellipsoids for the $Cu^{2+}\phi_6$ octahedra in $KCu_3^{2+}(OH)_2[(AsO_4)H(AsO_4)]$: a) $Cu^{2+}(1)\phi_6$, b) $Cu^{2+}(1)\phi_6$, c) $Cu^{2+}(2)\phi_6$.

parameters for the anions of the $Cu^{2+}(1)\phi_6$ octahedron are consistent with the $Cu^{2+}(1)\phi_6$ octahedron being dynamically distorted. The maximum principal axis of the O(3) displacement ellipsoid is sub-parallel to the Cu(1)-O(3) direction as shown in Figure 2.21. The OH anisotropic-displacement ellipsoid is nearly spherical (Figs. 2.20, 2.21), as is normal for a static M-ϕ bond.

The $Cu^{2+}(2)\phi_6$ octahedron shows anion anisotropic-displacement parameters consistent with static Jahn-Teller distortion (Figs. 2.20, 2.21). In this case, the maximum principal axes of the anion anisotropic-displacement ellipsoids are not parallel to the Cu-ϕ bond directions.

The dynamic $Cu^{2+}(1)\phi_6$ octahedron must be accommodated by the rest of the structure of $KCu_3^{2+}(OH)_2[(AsO_4)H(AsO_4)]$. Unlike most compounds that show dynamic Jahn-Teller $Cu^{2+}\phi_6$ octahedra, the $Cu^{2+}(1)\phi_6$ octahedron has strong bonds between the octahedral ligands and other cations in the structure (i.e., Cu^{2+} and As^{6+}). The environment of the dynamic $Cu^{2+}(1)\phi_6$ octahedron is shown in Figure 2.22. The Cu(1)-O(3) bond is dynamic, whereas the Cu(1)-OH bond is static. Each O(3) ligand is also bonded to Cu(2) and As. The dynamic movement of the O(3) ligand on the $Cu^{2+}(1)\phi_6$ octahedron must result in a distortion of the $Cu^{2+}(2)\phi_6$ octahedron and a tilting of the AsO_4 tetrahedron. The As position is bonded to two O(3) atoms, an O(1) atom and an O(2) atom (Fig. 2.22). The O(1) position is a static ligand shared by two Cu(2) atoms and acts as an anchor for the AsO_4 tetrahedron. The O(2) atom is located at the (AsO_4) apex, and is only very weakly bonded by two long bonds to K (3.24 Å, Effenberger, 1989) and by two hydrogen bonds. Tilting of the AsO_4 tetrahedron can easily occur due to the weak bonding to O(2), and may happen in two ways. The coupled

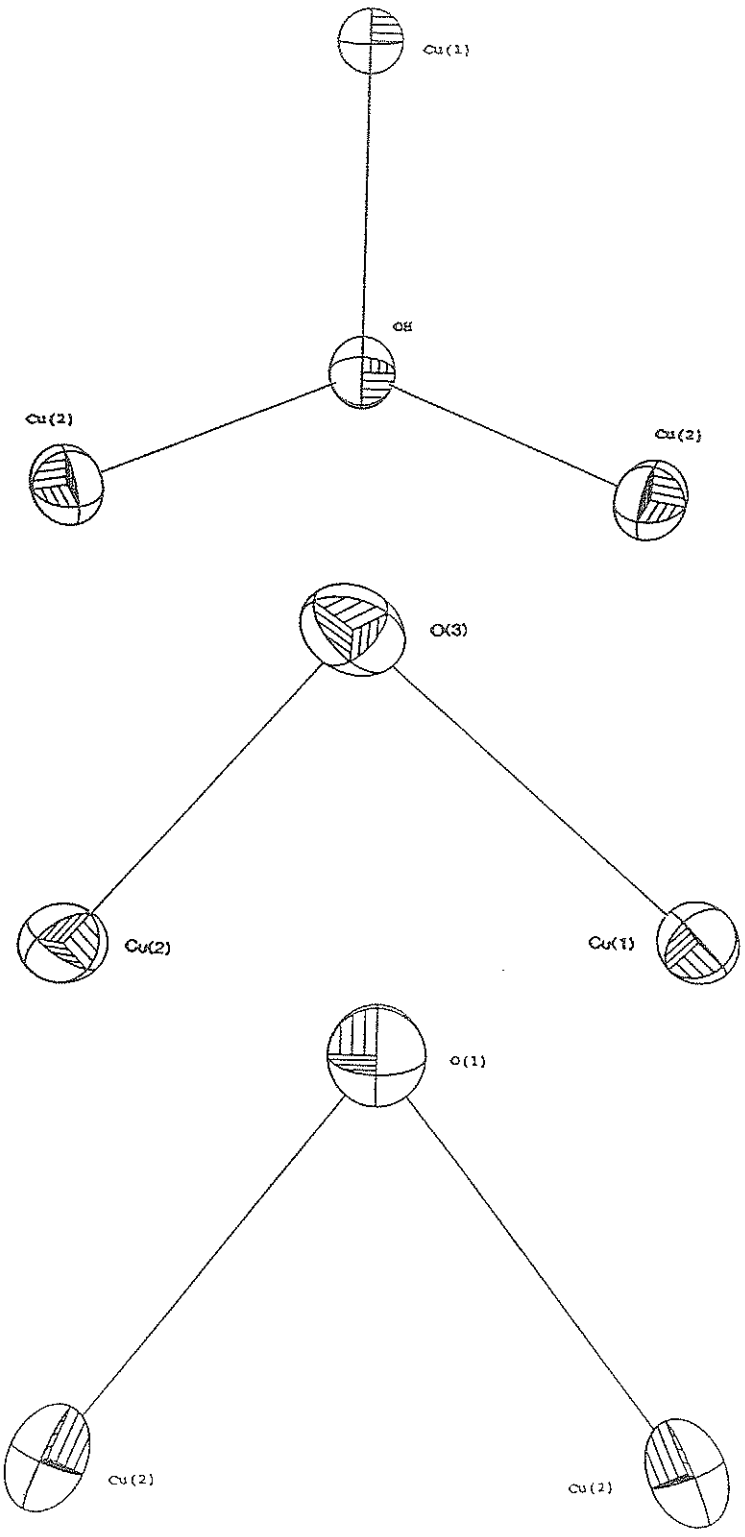

Figure 2.21. Anisotropic-displacement ellipsoids for Cu-ϕ bonds in $KCu_3^{2+}(OH)_2[(AsO_4)H(AsO_4)]$.

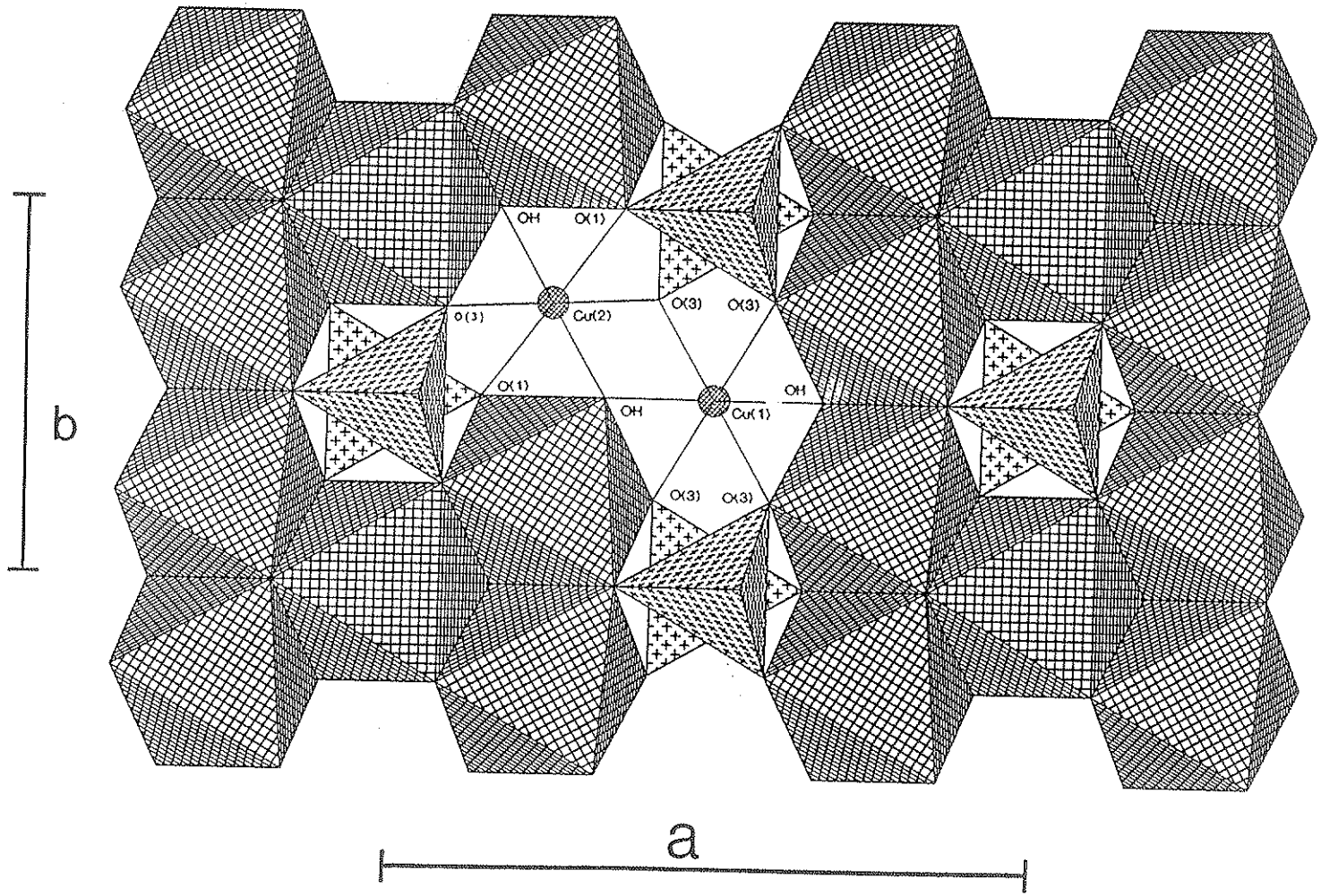

Figure 2.22. The detailed environments of the $Cu^{2+}(1)\phi_6$ and $Cu^{2+}(2)\phi_6$ octahedra in $KCu_3^{2+}(OH)_2[(AsO_4)H(AsO_4)]$. Copper octahedra are cross-hatched, arsenic tetrahedra are shaded with parallel lines.

motion of both O(3) atoms in the same direction will move the O(3)-O(3) edge of the tetrahedron up and down, such that the O(2) apical oxygen will move back and forth along the [100] direction. It is also possible that the two O(3) atoms will move out of phase, such that one moves up while the other moves down. In this case, the AsO_4 tetrahedron would rotate about the As-O(1) bond and the O(2) oxygen atom would move back-and-forth in the [010] direction. Examination of the anisotropic-displacement parameters for the O(2) position (Fig. 2.23) clearly shows significant anisotropic displacement in the [010] direction, indicating that the motion of the two O(3) ligands belonging to one AsO_4 tetrahedron are out-of-phase.

Volborthite

The volborthite structure (Basso et al., 1988) contains a $Cu^{2+}(1)\phi_6$ octahedron analogous to the $Cu^{2+}(1)\phi_6$ octahedron in $KCu_3^{2+}(OH)_2[(AsO_4)H(AsO_4)]$. However, Basso et al. (1988) only give anisotropic-displacement parameters for two of the oxygen atoms, both of which show anomalously high values. One of these oxygens belongs to the interlayer H_2O group, and the other [O(1)] is the apical (non-sheet) oxygen of the VO_4 tetrahedron. In volborthite, this oxygen is shared between two VO_4 tetrahedra that link adjacent sheets, and the V-O-V bond is linear by symmetry constraints. However, Basso et al. (1988) argue that the large displacement parameters associated with the O(1) position indicate positional disorder and a non-linear V-O-V bond. The local environment around the VO_4 tetrahedron is shown in Figure 2.24. Note that the Cu(1)-O(2) bonds are predicted to be dynamic in this case, as O(2) in volborthite is graphically equivalent to O(3) in $KCu_3^{2+}(OH)_2[(AsO_4)H(AsO_4)]$. The O(1)

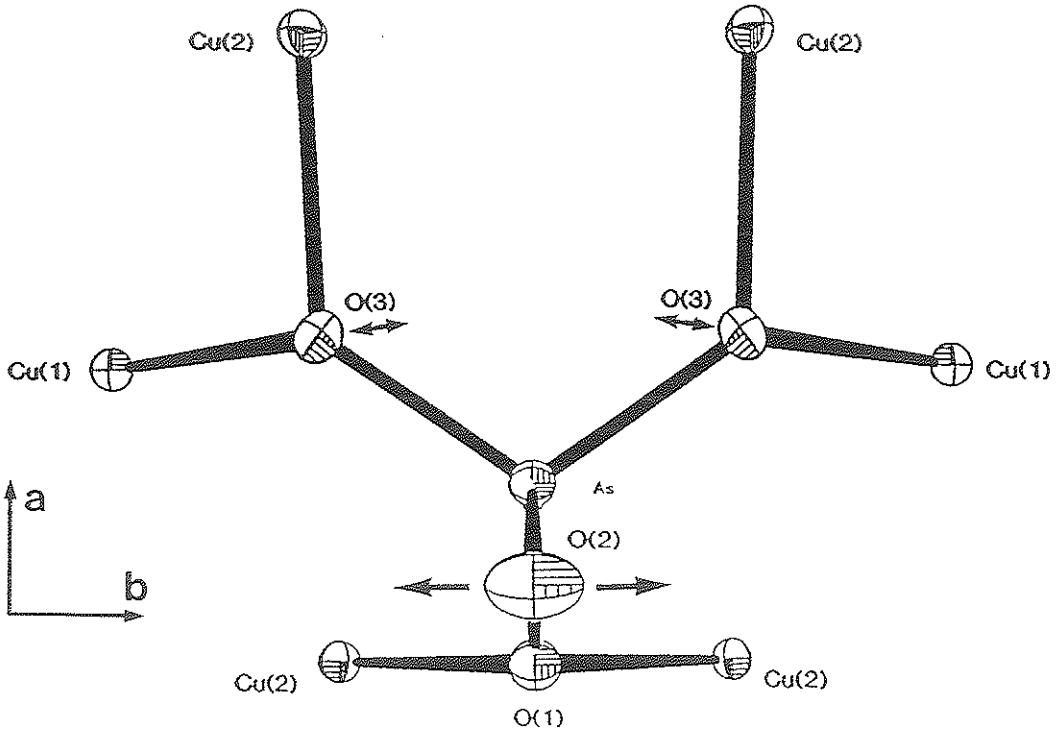

Figure 2.23. Anisotropic-displacement ellipsoids for the AsO_4 tetrahedron in $KCu_3^{2+}(OH)_2[(AsO_4)H(AsO_4)]$.

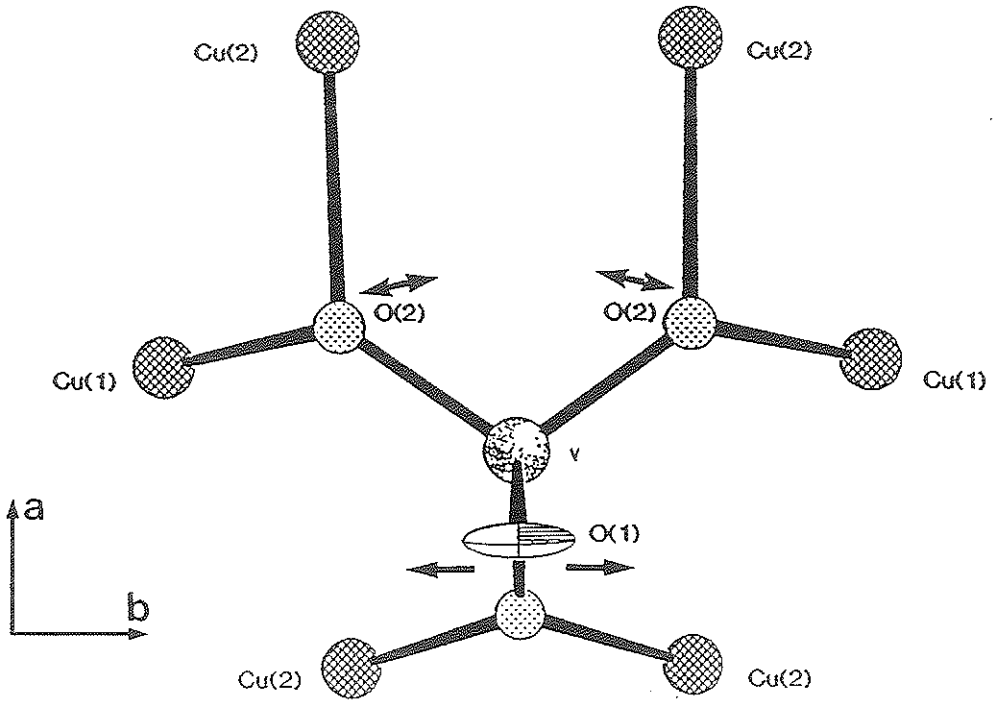

Figure 2.24. Anisotropic-displacement ellipsoid for the O(1) position in volborthite.

anisotropic-displacement ellipsoid in volborthite is elongated in the same way as the O(2) displacement ellipsoid in $KCu_3^{2+}(OH)_2[(AsO_4)H(AsO_4)]$ (Fig. 2.24), consistent with a dynamic $Cu^{2+}(1)\phi_6$ octahedron, as well as a non-linear V-O-V bond.

Bayldonite

Arguments based upon the structural relationships between bayldonite, volborthite and $KCu_3^{2+}(OH)_2[(AsO_4)H(AsO_4)]$ (see above) lead to the prediction that the (2+2+2)-distorted $Cu^{2+}(2)\phi_6$ octahedron in bayldonite is dynamically distorted, whereas the $Cu^{2+}(1)\phi_6$ and $Cu^{2+}(3)\phi_6$ octahedra are statically distorted. The dynamically (2+2+2)-distorted $Cu^{2+}(2)\phi_6$ octahedron is elongated in the Cu(2)-O(3) direction ⅔ of the time and the Cu(2)-O(2) direction ⅓ of the time. The predicted dynamic interchange of the distortion directions should lead to markedly anisotropic anion displacement ellipsoids with their maximum principal axes parallel to the Cu-ϕ bonds. The anisotropic-displacement ellipsoids for each $Cu^{2+}\phi_6$ octahedron in bayldonite (Ghose and Wan, 1979) are shown in Figure 2.25. The anisotropic-displacement parameters are of low precision, owing to the high X-ray absorption (μ = 372 cm^{-1}) and poor crystal quality, and some of the ellipsoids apparently show anomalous shapes (i.e., OH in Fig. 2.25). However, the anisotropic-displacement parameters are generally consistent with the proposed dynamic $Cu^{2+}\phi_6$ octahedron in bayldonite, and so they are included here. The anisotropic-displacement ellipsoids for the $Cu^{2+}(2)\phi_6$ octahedron (Fig. 2.25) show that the maximum principal axis of the O(3) displacement ellipsoid is parallel to the Cu(2)-O(3) bond. However, the O(2) displacement ellipsoid is elongated essentially perpendicular to the Cu(2)-O(2) bond. The

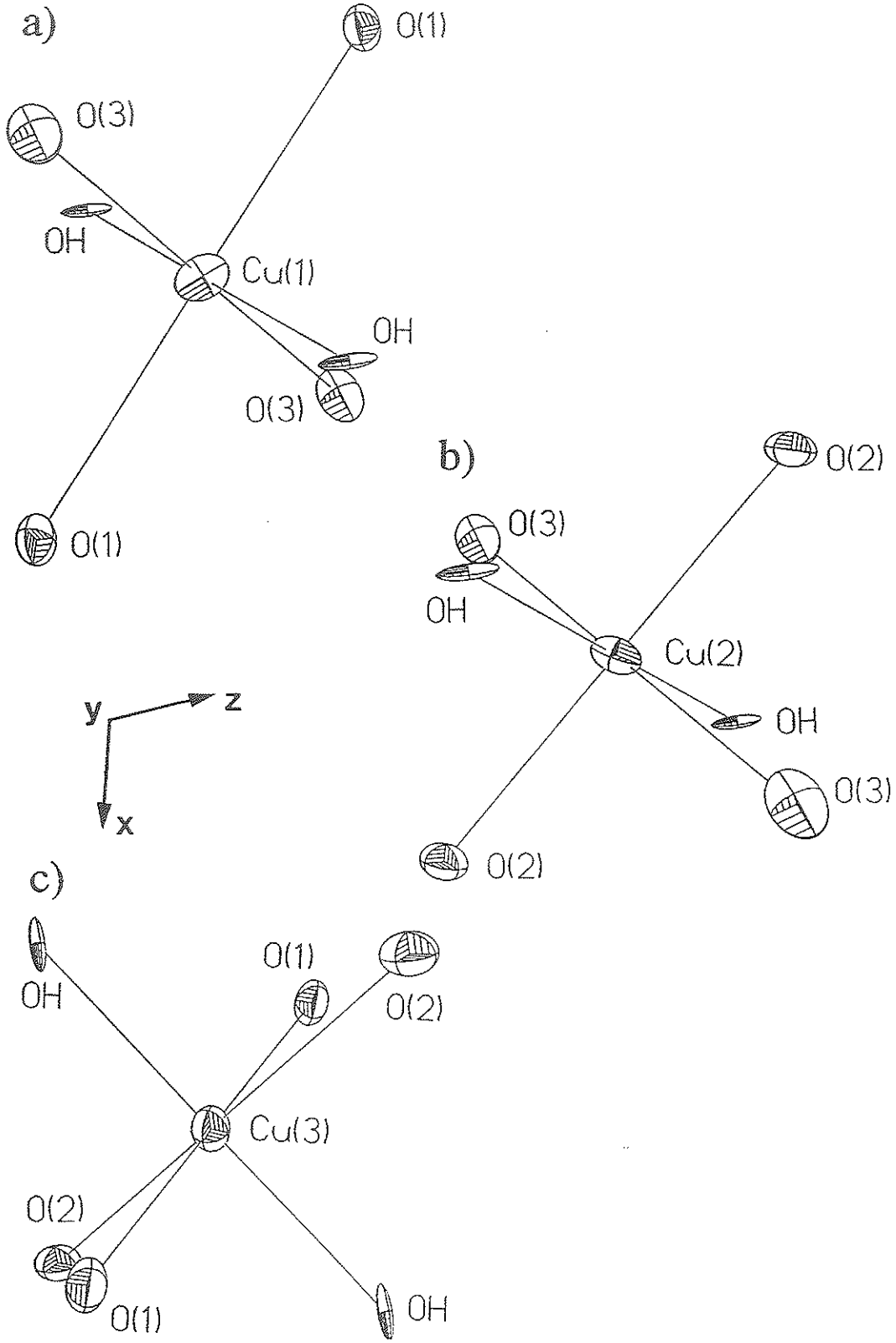

Figure 2.25. Anisotropic-displacement ellipsoids for $Cu^{2+}\phi_6$ octahedra in bayldonite: a) $Cu(1)\phi_6$, b) $Cu(2)\phi_6$, c) $Cu(3)\phi_6$.

displacement ellipsoids for the Cu(1) and Cu(3) octahedra (Fig. 2.25) are consistent with the octahedra being statically distorted.

The dynamic distortion of the $Cu^{2+}(1)\phi_6$ octahedra in volborthite and $KCu_3^{2+}(OH)_2[(AsO_4)H(AsO_4)]$ is accommodated by a tilting of the tetrahedral group, as shown in Figures 2.23 and 2.24. Note that in both cases, the tetrahedral cation is located on a mirror plane. The coupled movement of the ligands on either side of the mirror plane causes the apical tetrahedral ligand to sweep out a path perpendicular to the mirror plane, as shown by the anisotropic-displacement ellipsoids (Figs. 2.23, 2.24).

The situation is somewhat more complicated in bayldonite. The local environment of the AsO_4 tetrahedron is shown in Figure 2.26. The As is located on a general position in the space group C2/c, and each of the four tetrahedral ligands are symmetrically distinct. Also, the tetrahedron shares its ligands with two pairs of three symmetrically distinct Cu^{2+} ions. Of these, only the $Cu^{2+}(2)\phi_6$ octahedron is dynamically distorted. The effect of the dynamic ligands on the tetrahedron is somewhat different from that observed in volborthite and $KCu_3^{2+}(OH)_2[(AsO_4)H(AsO_4)]$. In this case, the Cu(2)-O(3) and Cu(2)-O(2) bonds are dynamic, as indicated by arrows in Figure 2.26. Also, the Cu(2)-O(3) bond is elongated ⅔ of the time whereas the Cu(2)-O(2) bond is only elongated ⅓ of the time. For a given AsO_4 tetrahedron, the Cu(2)-O(3) bond is elongated while the Cu(2)-O(2) bond is shortened, and the Cu(2)-O(3) bond is shortened while the Cu(2)-O(2) bond is elongated. This coupled dynamic movement rotates the tetrahedron such that the apical O(4) position rocks back-and-forth, as clearly shown by the O(4) displacement ellipsoid in Figure 2.26.

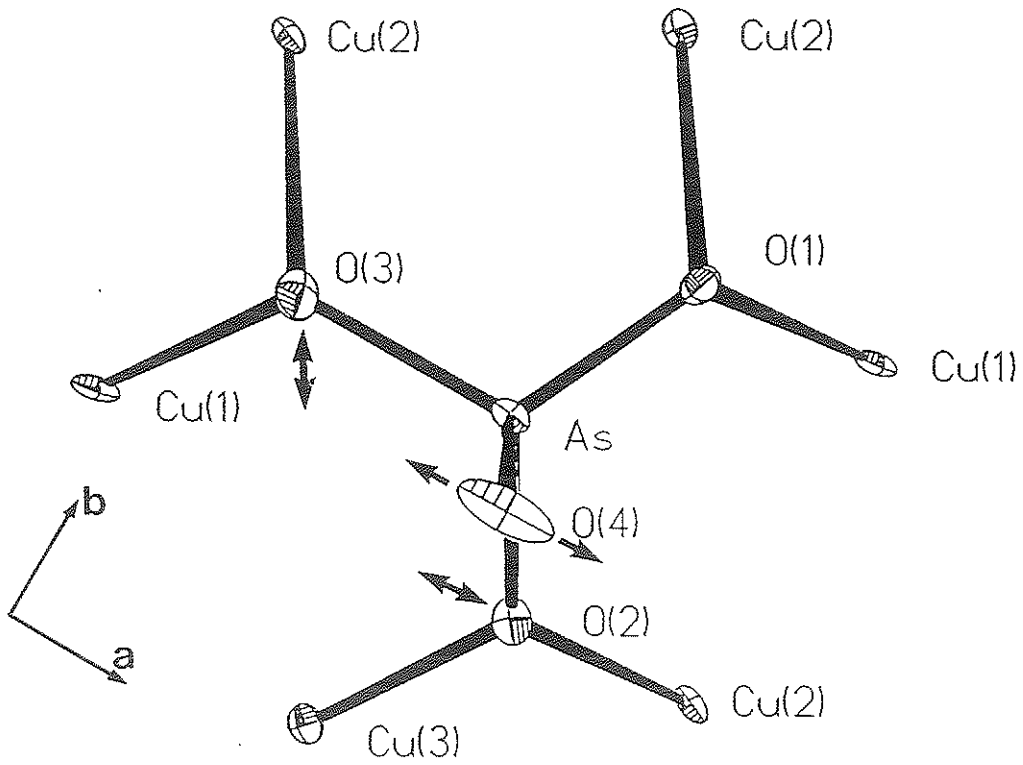

Figure 2.26. Anisotropic-displacement ellipsoids for the AsO_4 tetrahedron in bayldonite.

In summary, the available structural data indicates that the (2+4)-distorted $Cu^{2+}\phi_6$ octahedra in volborthite and $KCu_3^{2+}(OH)_2[(AsO_4)H(AsO_4)]$, and the (2+2+2)-distorted $Cu^{2+}\phi_6$ octahedron in bayldonite, are a direct result of the dynamic Jahn-Teller effect. It is my intention to pursue the details of these structures at a later date using variable-temperature crystal-structure refinement.

2.10 Discussion

It is only after careful examination of all $Cu^{2+}\phi_6$ octahedral geometries in Cu^{2+} oxysalt minerals that the true importance of the Jahn-Teller effect is apparent. It has been shown in the previous sections that probably every $Cu^{2+}\phi_6$ octahedron observed in Cu^{2+} oxysalt minerals is distorted due to the Jahn-Teller effect: *there is no conclusive example of a holosymmetric $Cu^{2+}\phi_6$ octahedron in these minerals.*

The (4+2)-distorted $Cu^{2+}\phi_6$ octahedral geometry is by far the most common in Cu^{2+} oxysalt minerals, as is the case for Cu^{2+} compounds in general. However, a considerable range of Cu-ϕ bond-lengths are observed in these octahedra, with the apical bond-lengths showing the most dispersion. The (4+2)-distorted $Cu^{2+}\phi_6$ octahedron is flexible and responds to steric effects of the crystal structure.

It remains unclear as to whether or not any (2+4)-distorted $Cu^{2+}\phi_6$ octahedra occur in minerals. Possible examples are in campigliaite, paratacamite, volborthite and demesmaekerite. Of these, those observed in campigliaite are from such an imprecise structure refinement that the bond-lengths cannot be considered reliable. Volborthite contains a (2+4)-distorted $Cu^{2+}\phi_6$ octahedron, but strong arguments have been advanced here that the

octahedron is a dynamically distorted, a time average of two unaligned (4+2)-distorted octahedra. The paratacamite structure reportedly contains a (2+4)-distorted octahedron (Fleet, 1975), but the refinement involved a complex superstructure, and as a consequence, anisotropic-displacement parameters were not refined for the octahedral ligands. This octahedron may also be dynamically distorted, or it may possibly be occupied by Zn rather than Cu^{2+}. Finally, there is a single (2+4)-distorted $Cu^{2+}\phi_6$ octahedron in demesmaekerite. This octahedron is the most persuasive example of a true (2+4)-distorted $Cu^{2+}\phi_6$ octahedron as the anisotropic-displacement ellipsoids reported by Ginderow and Cesbron (1983) (Fig. 2.27) do not conclusively indicate that the octahedron is dynamically distorted.

Mineralogists have always assumed that dynamically distorted $Cu^{2+}\phi_6$ octahedra do not occur in minerals. However, it seems probable that dynamically distorted $Cu^{2+}\phi_6$ octahedra do occur in cyanochroite, volborthite and bayldonite; two of these structures have (2+2+2)-distorted octahedra. Furthermore, a number of other Cu^{2+} oxysalt minerals also show (2+2+2)-distorted octahedra (Table 2.3), and it is possible that some of these may also be dynamically distorted.

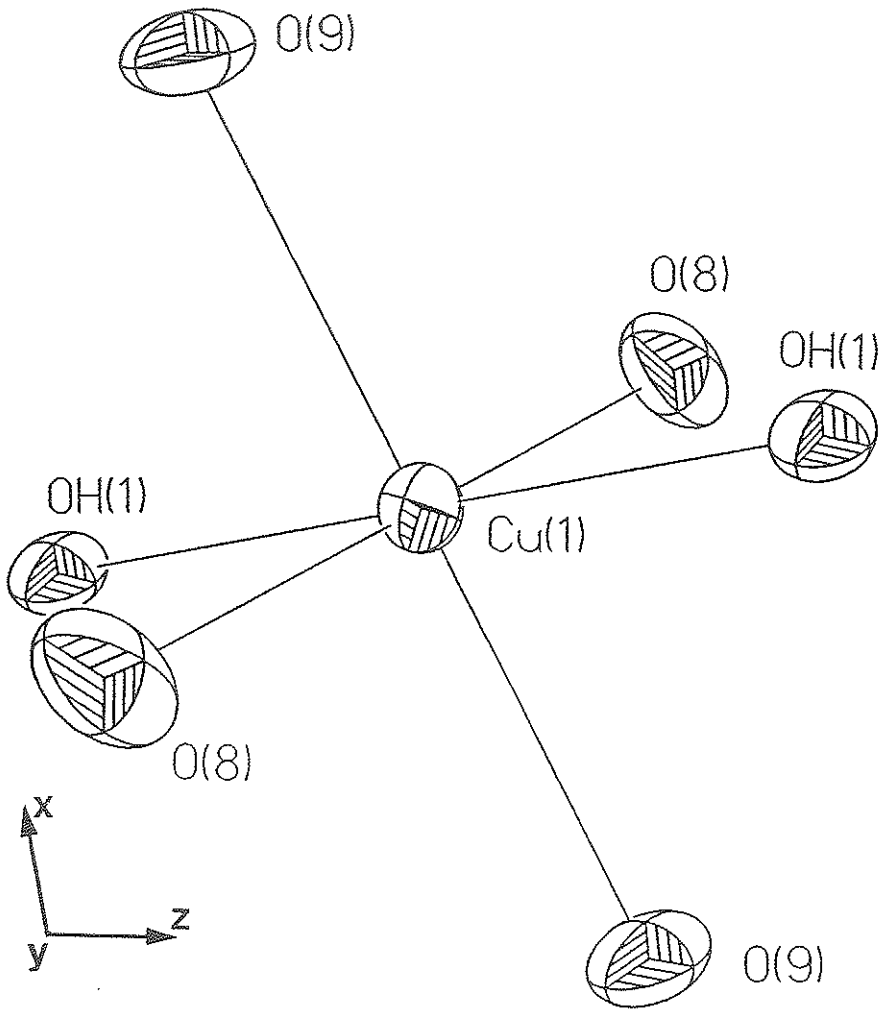

Figure 2.27. Anisotropic-displacement ellipsoids for the Cu(1)ϕ_6 octahedron in demesmaekerite.

Chapter 3

Molecular-Orbital Methods

Molecular-orbital (MO) methods have been used by theoretical chemists for at least twenty years, primarily to predict geometries, energetics and stabilities of molecules. Molecular-orbital methods are based upon quantum mechanics, and range from empirical methods, which include an experimentally determined component, to *ab initio* methods, which include no experimentally determined parameters (apart from "universal" constants).

MO methods have been applied to relatively small molecules with considerable success, but it has only been quite recently that computational sophistication and power have reached levels which allow application of these methods to minerals.

3.1 The Molecular-Orbital Method Applied to Minerals.

At the present time, MO methods are being applied extensively to the study of properties of a range of minerals with closed-shell molecular wavefunctions. Large-scale *ab initio* MO calculations that include entire crystal structures (with appropriate boundary conditions) are presently restricted to a small number of "simple" minerals. However, crystal MO methods have been quite successful in predicting the properties of such minerals as quartz (Nada et al., 1990) and spinel (D'Arco et al., 1991).

As crystal MO calculations can only be done for a few minerals at today's level of computational power, there have been a considerable number of calculations done for molecular clusters of varying size as an

approximation of local conditions in a crystal structure (i.e., McCammon et al., 1991; Lasaga and Gibbs, 1990, 1988, 1987; Gibbs, 1982; Newton and Gibbs, 1980). These cluster calculations are, at best, only an approximation of the local environment in a structure; there are many long-range effects in an extended periodic structure that are ignored by such calculations. Nevertheless, this type of calculation has proven to be of considerable value in the interpretation of some structural variations in minerals.

3.2 Molecular-Orbital Models.

The *ab initio* MO method is an approximate method of describing electron distribution and motion. The method assigns individual electrons to one-electron functions referred to as *spin orbitals*. These orbitals are made up of a product of spatial functions known as *molecular orbitals*, $\psi_1(x,y,z,)$, $\psi_2(x,y,z)$, $\psi_3(x,y,z)$..... and either α or β *spin-components*. These orbitals are used to form the *many-electron wavefunction*, a MO approximation of the solution to the Schrödinger equation.

Due to computational difficulties, the molecular orbitals are often constructed as linear combinations of N (known) *one-electron functions* Φ_i:

$$\psi_i = \Sigma c_{ui} \Phi_u \qquad (3.1)$$

The functions Φ_i are known as *basis functions*, the collection of which constitutes the *basis-set*. Often, basis functions are *atomic orbitals* for the atoms constituting the molecule; this is referred to as the *Linear Combination of Atomic Orbitals* (LCAO) approximation.

3.3 The Born-Oppenheimer Approximation.

The *Born-Oppenheimer* approximation assumes that the electronic terms of the molecular Hamiltonian[1] are separable from the nuclear terms when the nuclear positions are held fixed. This is normally done by doing calculations for a series of nuclear-nuclear separations. The Schrödinger time-independent non-relativistic equation is solved for all electrons in the system:

$$\hat{H}\psi^{elec} = E\psi^{elec} \tag{3.2}$$

where $\hat{H}$ is the electronic Hamiltonian, and ψ^{elec} is the electronic wave-function. The solutions of equation 3.2 are known as *eigenvalues*, E; they give the electronic energy of the system and are a function of the nuclear-nuclear separations.

3.4 The Hartree-Fock Method.

The principal problem to be addressed is finding a suitable function for ψ^{elec}. In the *Hartree-Fock approximation*, the electronic wavefunction ψ^{elec} is an antisymmetrized[2] product of one-electron functions ψ_i. These molecular orbitals (ψ_i) are linear combinations of atomic orbitals Φ_u:

$$\psi_i = \Sigma c_{ui}\Phi_u \tag{3.3}$$

---

[1]The Hamiltonian ($\hat{H}$) is a differential operator that represents the total (kinetic and potential) energy of the system.

[2]The *Pauli principle* (or the *exclusion principle*) is a postulate of quantum mechanics which states that the wavefunction of a system of electrons must be antisymmetric with respect to interchange of any two electrons (i.e., the sign of the wavefunction must change).

where c_{ui} are known as the *molecular-orbital expansion coefficients*, and are to be determined in the calculation.

The Hartree-Fock wavefunction is a determinantal wavefunction that is constructed from molecular orbitals, which in turn may be expanded as a set of basis functions (Φ_u). In Hartree-Fock theory, the optimal values of the expansion coefficients c_{ui} are determined using the variational method (which may be applied to determine the optimum orbitals of a single determinant wavefunction, Hehre et al., 1986). The variational theorem indicates that for any antisymmetric normalized wavefunction Φ, the expectation energy (E′) may be obtained from the integral:

$$E' = \int \Phi^* \hat{H} \Phi d\tau \qquad (3.4)$$

The variational theorem indicates that if Φ is the exact wavefunction, it will satisfy the Schrödinger equation and the expectation energy (E′) will be the correct energy of the system within the limits of quantum-mechanics theory. Otherwise, the expectation energy (E′) provides an upper bound to the correct energy (E) of the system. The molecular-orbital expansion coefficients c_{ui} are adjusted for a given basis-set by minimizing the expectation energy (E′) of the system:

$$\frac{\partial E'}{\partial c_{ui}} = 0 \text{ (all u,i)} \qquad (3.5)$$

How close the Hartree-Fock energy is to the correct energy depends on the single-determinant wavefunction and the basis-set used.

The variation condition (equation 3.5) gives rise to a series of algebraic equations for c_{ui} which are collectively referred to as the Roothaan-Hall equations. These equations are not linear, thus their solution involves an iterative process known as self-consistent-field (SCF) theory.

Hartree-Fock calculations have been widely used in the study of ground states of molecules, for which the theory is generally adequate (Hehre et al., 1986). However, the Hartree-Fock method is based upon a single-determinant wavefunction, and it is not possible to express an exact wavefunction as a single determinant. As a result, the Hartree-Fock approach provides an inadequate description of the *correlation* between the motions of electrons. Hartree-Fock wavefunctions do not account for correlation of the motions of electrons of different spin, and correlation between the motion of electrons of the same spin is only partly accounted for. The correlation of the motion of electrons which are unaccounted for in Hartree-Fock theory lead to calculated energies that are higher than the correct values:

$$E(\text{correct}) = E(\text{Hartree-Fock}) + E(\text{correlation})$$

Bond-breaking processes are not well described by Hartree-Fock calculations. It has been shown (Hehre et al., 1986) that *closed-shell* Restricted Hartree-Fock (RHF) wavefunctions do not dissociate correctly when the corresponding nuclei are moved to infinite separation; *open-shell* Unrestricted Hartree-Fock (UHF) calculations do better in these circumstances. Bond-dissociation energies may be seriously underestimated

if electron correlation between the bonding pair of electrons is not properly taken into account.

3.5 Basis-Set Selection.

Basis-set selection is the most important decision made when doing Hartree-Fock calculations, and the choice is complicated by the large number of basis-sets available in the literature. When selecting basis-sets for MO calculations, desired accuracy is balanced against the cost of the calculations, as the computational expense of a Hartree-Fock MO calculation is proportional to the fourth power of the number of basis functions (Hehre et al., 1986). Optimally, the smallest basis-set that gives the required level of accuracy for the problem at hand should be chosen. It must also be kept in mind that comparison of results obtained with a given basis-set is less prone to error (due to the limited size of the basis-set) than are the absolute properties of the system.

The simplest basis-set used in *ab initio* theory is the minimal basis-set which comprises exactly the number of functions required to accommodate all of the electrons of the atom, while maintaining overall spherical symmetry (Hehre et al., 1986). The STO-3G* minimal basis-set (Hehre et al., 1969; Collins et al., 1976) is perhaps the most widely used basis-set. In the STO-3G* basis-set, each Slater-type[3] atomic orbital is

---

[3]Slater-Type Orbitals (STO) have an exponential radial part and provide a reasonable representation of atomic orbitals, but they are not well-suited to computational work. Gaussian-type orbitals are powers of x, y, z multiplied by $\exp(-\alpha r^2)$ where α is a constant giving the size of the function. Gaussian-type orbitals are theoretically less satisfactory than Slater-type orbitals as they do not have a cusp at the origin. However, Gaussian-type orbitals are well-suited to computational work, and they have been used in many MO studies.

approximated by a linear combination of three Gaussian-type (3G) functions. The STO-3G* basis-set for first-row transition metals has been widely used for the calculation of molecular properties. Although there are shortcomings in the minimal STO-3G* basis-set, some aspects of bonding, particularly in organometallic complexes, are well described (Dobbs and Hehre, 1987). For example, Gibbs (1982) described the use of the STO-3G* basis-set for geometry optimization of 18 hydroxyacid molecules with [3]-, [4]- and [6]-coordinate first- and second-row ions. The calculated bond-lengths differed on average by less than 0.04 Å from the mean observed bond-lengths. Pople (1976) reported that the mean absolute deviation from experiment for SCF STO-3G bond-lengths in several dozen molecules containing H, C, N, O and F is 0.030 Å. More recently, McCammon et al. (1991) and Lasaga and Gibbs (1988) have used the STO-3G minimal basis-set to calculate physical properties of minerals. The main attraction of the STO-3G* basis-set (other than the relatively low cost of the calculations) is its effectiveness in predicting geometries, due at least in part to the fortuitous cancellation of defects in the calculations (Davidson and Feller, 1986).

The 3-21G* split-valence basis-set (Dobbs and Hehre, 1987; Binkley et al., 1980; Gordon et al., 1982; Pietro et al., 1982) is also commonly used for many-electron systems. Each of the core-electron orbitals is represented by three Gaussian-type functions. The valence orbitals are also represented by three Gaussian-type functions, two of the functions being contracted and the third being a diffuse function.

Other basis-sets used in this study include the STD-SET(1) and DZC-SET(1) sets which have been reported for transition metals (Tatewaki and

Huzinaga, 1979). The basis-sets are minimal basis-sets, but they result in Hartree-Fock energies considerably lower than other transition-metal basis-sets; in some cases, the energies are as low as those determined using the double-zeta (DZ) basis-set, which is formed by the doubling of all functions of the minimal representation. However, these basis-sets have not been extensively tested, and it is not known how well they reproduce experimental geometries.

Recently, new basis-sets including effective core potentials for chemically-inert core electrons have been reported for atoms from Na to Bi (Hay and Wadt, 1985a, 1985b; Wadt and Hay, 1985). These basis-sets, referred to as the Los Alamos National Laboratory effective core potential sets, contain valence-electron descriptions that are either minimal (LANL1MB) or double zeta (LANL1DZ). A double-zeta basis-set has two contracted functions per atomic orbital. The representation of the chemically-inert inner-core electrons using effective core potentials has increased the scope of quantum chemistry by greatly decreasing the cost of heavy-atom calculations.

3.6 Post-Hartree-Fock Methods

Various post-Hartree-Fock MO methods have been designed to overcome the weaknesses associated with the Hartree-Fock method. Post-Hartree-Fock methods start where the Hartree-Fock calculation terminates. The procedures begin with a single-determinant Hartree-Fock wavefunction, and attempt to correct for electron correlation. Hehre et al. (1986) have listed four features that are desirable in any post-Hartree-Fock method (or any MO method):

(1) The method should be well defined, and applicable in a continuous manner to any arrangement of nuclei and any number of electrons.

(2) The method must not lead to such a rapid increase in required computation with molecular size as to preclude its use in systems of chemical (and mineralogical) interest.

(3) The model must be size consistent; any method must give additive results when applied to an assembly of isolated molecules.

(4) The calculated electronic energy should be variational; it should correspond to an upper bound of the energy from exact solution of the Schrödinger equation.

Hartree-Fock methods meet each of the above requirements, but practical post-Hartree-Fock models typically do not. Possible post-Hartree-Fock methods include full configuration interaction, limited configuration interaction, and Møller-Plesset perturbation theory to 2^{nd}, 3^{rd} and 4^{th} order. Each of these methods are based upon quantum mechanics, but are too involved for review here. The interested reader is referred to Hehre et al. (1986) who give details of these methods.

Full configuration-interaction (CI) calculations are the most rigorous electron-correlation description available within the limits imposed by the basis-set. The method depends upon the use of large numbers of substitutional determinants to construct the wavefunctions, and is not practical except for very small systems. The commonly chosen way around this problem is to limit the number of substitutional determinants to double

substitutions only (CID). These calculations satisfy only three of the above four requirements; they fail to satisfy the size-consistency requirement. Møller-Plesset perturbation theory of 2nd, 3rd and 4th order (MP2, MP3 and MP4, respectively) is an alternate approach to dealing with the electron-correlation problem. Møller-Plesset perturbation theory also only satisfies three of the above four requirements, with the theory failing to provide a variational energy that is guaranteed to be an upper bound to the true energy of the system.

The various methods that may be used to account for the electron-correlation energy ignored by the Hartree-Fock treatment result in huge computational expense. Typically, calculations including post-Hartree-Fock treatment of electron correlation take an order of magnitude more time than corresponding Hartree-Fock calculations. Routine calculations should be done to the Hartree-Fock level, with electron-correlation treatment introduced only in those cases where it is expected to contribute significantly to the conclusions that are based upon the calculations. This may be the case, for example, where the calculations involve bond breaking.

Chapter 4

Ab Initio Molecular-Orbital Calculations for $Cu^{2+}\phi_6$ Octahedra

4.1 Introduction

Jahn-Teller distortion of $Cu^{2+}\phi_6$ octahedra has a strong influence on the structural connectivity of Cu^{2+} oxysalt minerals. As holosymmetric and (2+4)-distorted octahedra are not observed, the energetic preference for a (4+2)-distortion presumably dominates over steric effects. The exact nature of the Jahn-Teller distortion must therefore be understood in order to gain a full appreciation of the underlying energetics of Cu^{2+} oxysalt structures.

Ab initio MO calculations are a direct means by which to investigate stereochemical and energetic features at the atomic scale. Molecular-orbital calculations are based on quantum mechanics (chapter 3), and will automatically include a static Jahn-Teller effect if one is present in the system. They are not applicable to the study of a *dynamic* Jahn-Teller system, as the strong coupling between nuclear and electron motion associated with this effect is a direct violation of the Born-Oppenheimer approximation, which assumes electron motion to be independent of nuclear motion. Fortunately, Jahn-Teller distortions of $Cu^{2+}\phi_6$ octahedra in Cu^{2+} oxysalt minerals are usually static effects.

Molecular-orbital calculations at the Hartree-Fock level were done for $Cu^{2+}\phi_6$ octahedral clusters designed to model the local environment in Cu^{2+} oxysalt minerals. The calculations reported in this chapter were done using Gaussian 86 (Frisch et al., 1984) and Gaussian 92 (Frisch et al., 1992).

4.2 Previous Work

Beagley et al. (1989) did Hartree-Fock MO calculations for the $[Cu^{2+}(H_2O)_6]^{2+}$ cluster using effective core potentials (ECP) for the inner-shell electrons [Cu(1s,2s,2p), O(1s)] and a large basis-set for copper; the latter was made up of the basis-set suggested by Roos et al. (1971), as well as two additional diffuse *p* functions and an additional diffuse *d* function. The basis-set for oxygen was based on the triple-zeta type (Huzinaga, 1965) which also contained an additional diffuse *p* function. The hydrogen basis-set was the Huzinaga 4*s* basis (Huzinaga, 1965) contracted to 2*s* with the exponents scaled by a factor of 1.25.

Beagley et al. (1989) optimized the geometry of the cluster for the holosymmetric, (4+2)-distorted and (2+4)-distorted octahedra. The holosymmetric structure optimized to a Cu-O bond-length of 2.115 Å, the (4+2)-distorted octahedron to Cu-ϕ_{ap} = 2.250 Å, Cu-ϕ_{eq} = 2.057 Å, and the (2+4)-distorted octahedron to Cu-ϕ_{ap} = 2.024 Å, Cu-ϕ_{eq} = 2.172 Å. The (4+2)-distorted octahedron had the lowest energy, with a Jahn-Teller stabilization energy (E_{JT}, the difference between the energy of the holosymmetric and distorted octahedra) of 0.0030 Hartrees, less than half the value expected from experimental studies (Beagley et al., 1989).

4.3 Molecular-Orbital Calculations: $Cu^{2+}\phi_6$ Geometries.

Optimization of the holosymmetric, (4+2)- and (2+4)-distorted octahedral geometries was done for both the $[Cu^{2+}(OH)_6]^{4-}$ and $[Cu^{2+}(H_2O)_6]^{2+}$ clusters (Fig. 4.1). The calculations are UHF (spin unrestricted) calculations with no spin contamination observed in the final wavefunctions. Calculations using the STO-3G* basis-set were done for each cluster, and

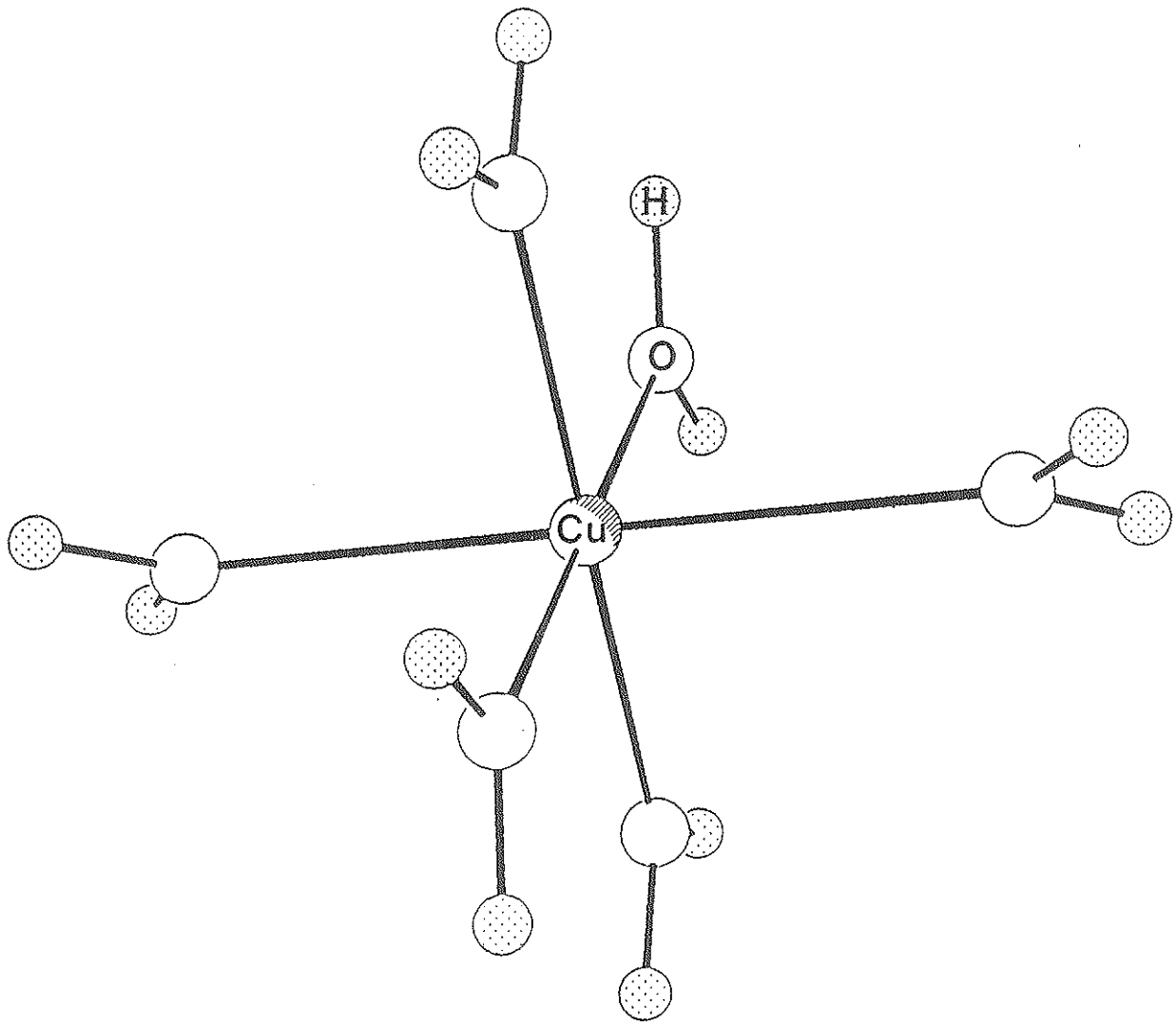

Figure 4.1. The $[Cu^{2+}(H_2O)_6]^{2+}$ cluster.

calculations using the 3-21G* basis-set were done for the $[Cu^{2+}(H_2O)_6]^{2+}$ cluster. Spin contamination was encountered using the 3-21G* basis-set to calculate wavefunctions for the $[Cu^{2+}(OH)_6]^{4-}$ clusters; these calculations were not completed.

The Cu-O-H bond-angle was fixed at 110° and the O-H bond-length was fixed at 0.98 Å for the $[Cu^{2+}(OH)_6]^{4-}$ cluster (c.f., Lasaga and Gibbs, 1988); the H-O-H bond-angle was fixed at 104.5° and the H-O bond-length was fixed at 0.957 Å for the $[Cu^{2+}(H_2O)_6]^{2+}$ cluster (c.f. Beagley et al., 1989). In each case, geometries were optimized until the maximum forces on any atom did not exceed 0.00045 Hartrees/Bohr and the maximum displacement of any atom in the previous cycle did not exceed 0.0009 Å. All six copper-oxygen bond-lengths were constrained to be equivalent during the optimization of the holosymmetric octahedron. In the case of the distorted octahedra, the four Cu-ϕ_{eq} bond-lengths were constrained to be equivalent, as were the two Cu-ϕ_{ap} bond-lengths. The optimized geometries, cluster energies and Jahn-Teller stabilization energies are listed in Table 4.1.

4.4 Discussion of Results

All calculations indicate that both the (4+2)- and (2+4)-distorted octahedra are more energetically favourable that the holosymmetric octahedron, as predicted by the Jahn-Teller theorem. Qualitatively, *Hartree-Fock MO theory predicts the distortion of Cuϕ_6 octahedra observed in minerals.*

The optimized geometries of the copper-oxygen octahedra are clearly basis-set and cluster-charge dependent (Table 4.1). However, the cluster charge must be either -4 or +2, as using different ligand combinations to

Table 4.1: Optimized geometries*, cluster energies and Jahn-Teller stabilization energies for octahedral clusters.

	$[Cu^{2+}(H_2O)_6]^{2+}$	
Basis Set:	STO-3G*	3-21G*
Holosymmetric Cu-ϕ	2.148	2.113
E(SCF, Hartrees**)	-2071.2700	-2084.1968
(4+2) Cu-ϕ_{ap}	2.074	2.161
Cu-ϕ_{eq}	1.988	2.049
E(SCF, Hartrees)	-2071.6249	-2084.2150
(2+4) Cu-ϕ_{ap}	2.013	1.992
Cu-ϕ_{eq}	2.051	2.134
E(SCF, Hartrees)	-2071.5842	-2084.2190
EJT [Hartrees, (4+2)]	-0.3629	-0.0182
EJT [Hartrees, (2+4)]	-0.3143	-0.0222
<Cu-ϕ> (4+2)	2.017	2.087
<Cu-ϕ> (2+4)	2.038	2.086

	$[Cu^{2+}(OH)_6]^{4-}$
Basis set:	STO-3G*
Holosymmetric <Cu-ϕ>	2.178
E(SCF, Hartrees)	-2066.5677
(4+2) <Cu-ϕ_{ap}>	2.427
<Cu-ϕ_{eq}>	2.081
E(SCF, Hartrees)	-2066.5749
(2+4) <Cu-ϕ_{ap}>	2.061
<Cu-ϕ_{eq}>	2.240
E(SCF, Hartrees)	-2066.5729
EJT [Hartrees (4+2)]	-0.0072
EJT [Hartrees (2+4)]	-0.0052
<Cu-ϕ> (4+2)	2.180
<Cu-ϕ> (2+4)	2.196

* Bond-lengths are in Å. ** 1 Hartree = 2625.4997 kJ/mole

neutralize the cluster charge (e.g. $Cu^{2+}[(OH)_2(H_2O)_4]^0$) will introduce an intrinsic distortion into the octahedron. As the main purpose of this work is to calculate the tendency for Cu^{+2} octahedral arrangements to distort due to the Jahn-Teller effect, care must be taken to ensure that the calculations are not biased by cluster symmetry.

The Jahn-Teller stabilization energy predicted for the $[Cu^{2+}(H_2O)_6]^{2+}$ cluster using the STO-3G* basis-set is greatly overestimated (in comparison to values given by Beagley et al., 1989), and the energy obtained using the 3-21G* basis-set is about two and a half times the value expected from experimental studies. The bond-lengths obtained using the 3-21G* basis-set are fairly similar to those obtained by Beagley et al. (1989). The Cu-O bond-length predicted for an undistorted $Cu^{2+}\phi_6$ octahedron in a Cu^{2+} oxysalt mineral (2.083 Å, Chapter 2) is in good agreement with the average Cu-ϕ bond-lengths obtained using the 3-21G* basis-set. None of the calculations for the $[Cu^{2+}(H_2O)_6]^{2+}$ clusters predict copper-oxygen bond-lengths similar to the averages observed in Cu^{2+} oxysalt minerals ($<Cu\text{-}\phi_{eq}>$ = 1.973 Å, $<Cu\text{-}\phi_{ap}>$ = 2.505 Å). However, the calculations for the $[Cu^{2+}(OH)_6]^{4-}$ clusters using the STO-3G* basis-set do agree fairly well (Cu-ϕ_{eq} = 2.081 Å, Cu-ϕ_{ap} = 2.427 Å) with the observed averages in Cu^{2+} oxysalt minerals (Fig. 2.10). The predicted Jahn-Teller stabilization energy for the $[Cu^{2+}(OH)_6]^{4-}$ cluster, determined using the STO-3G* basis-set, is in good agreement with the value indicated by experiment. Both calculations using the STO-3G* basis-set indicate that the (4+2)-distortion is favoured over the (2+4)-distortion. However, the opposite is predicted by the calculations for the $[Cu^{2+}(H_2O)_6]^{2+}$ cluster using the 3-21G* basis-set.

This work was done in order to find the basis-set and molecular-cluster combination that gives optimized geometries in best agreement with Cu-ϕ octahedral bond-lengths in Cu^{2+} oxysalt minerals. The calculations of Beagley et al. (1989) were redone and their results (given above) were reproduced; these calculations were very expensive and yet did not give optimized geometries comparable to those observed in Cu^{2+} oxysalt minerals. Instead, due at least in part to the fortuitous cancellation of errors (Davidson and Feller, 1986), *the STO-3G* minimal basis-set gave optimized geometries that best agree with those observed in Cu^{2+} oxysalt minerals.*

4.5 Post-Hartree-Fock Calculations for $[Cu^{2+}(OH)_6]^{4-}$ Clusters

Post-Hartree-Fock calculations were done for the $[Cu^{2+}(OH)_6]^{4-}$ cluster using the STO-3G* minimal basis-set to determine the effects of electron correlation on cluster geometry and energy. The geometry of the cluster was reoptimized based on energy derivatives from configuration interaction, including double-substitutions (CID) with the same geometrical constraints as the previous calculations (Section 4.3). The resulting geometries and CID, MP2 and MP3 energies for the holosymmetric, (2+4)-distorted and (4+2)-distorted octahedra are given in Table 4.2.

The optimized geometries obtained using the energy derivatives of the CID calculations (Table 4.2) are somewhat different from those of the UHF Hartree-Fock calculations (Table 4.1). For the (4+2)-distorted octahedron, the Cu-ϕ_{eq} distances shorten [UHF = 2.081 Å, CID = 2.069 Å] and the Cu-ϕ_{ap} distances lengthen [UHF = 2.427 Å, CID = 2.475 Å] when electron correlation is taken into account. These bond-length changes are toward the average Cu-ϕ bond-lengths for (4+2)-distorted octahedra in minerals

Table 4.2. Optimized geometries* (Å), cluster energies** (Hartrees) and Jahn-Teller stabilization energies for the $[Cu^{2+}(OH)_6]^{4-}$ cluster.

Optimized Geometry

	$Cu\text{-}\phi_{ap}$	$Cu\text{-}\phi_{eq}$	$\langle Cu\text{-}\phi \rangle$
Holosymmetric	2.180	2.180	2.180
(4+2)	2.475	2.069	2.204
(2+4)	2.056	2.244	2.181

Cluster Energy

	Holosymmetric	(4+2)	(2+4)	$E_{JT}(4+2)$	$E_{JT}(2+4)$
UHF	-2066.5677	-2066.5749	-2066.5729	0.0072	0.0052
CID	-2066.8922	-2066.9012	-2066.8984	0.0090	0.0062
MP2***	-2066.8913	-2066.9027	-2066.8983	0.0114	0.0070
MP3	-2066.9194	-2066.9282	-2066.9256	0.0088	0.0062

* Optimized geometries are for the CID calculation.
** 1 Hartree = 2625.4997 kJ/mole
*** MP = Møllet-Plessert

[<Cu-ϕ_{eq}> = 1.973 Å, <Cu-ϕ_{ap}> = 2.505 Å, Chapter 2]. Thus, accounting for electron correlation results in a larger Jahn-Teller distortion and a better reproduction of experimental Cu-ϕ bond-lengths in this cluster.

The CID, MP2 and MP3 calculations give lower cluster energies than the Hartree-Fock UHF calculations (Table 4.2). The CID calculations result in a correlation energy of about 0.32 Hartrees. Each calculation indicates that the (4+2)-distorted octahedron is more stable than the (2+4)-distorted octahedron. These results are in line with those obtained using Hartree-Fock theory, and with the observed Cu-ϕ octahedral bond-length distribution in minerals.

When accounting for electron correlation, the calculations favour the (4+2)-distorted octahedron over the (2+4)-distorted octahedron. The CID and MP3 calculations indicate that the (4+2)-distorted octahedron is 0.26 to 0.28 Hartrees more favourable than the (2+4)-distorted octahedron, whereas the UHF calculations give a value of 0.20 Hartrees. Also, the predicted Jahn-Teller stabilization energy for either distortion is increased when electron correlation is included in the calculations.

4.6 Summary

From these calculations, the following conclusions may be made:

(1) These MO calculations indicate that the (2+4)- and (4+2)-distorted $Cu^{2+}\phi_6$ octahedra are more stable than the holosymmetric configuration, in line with the Jahn-Teller theorem.

(2) Calculations done for the $[Cu^{2+}(OH)_6]^{4-}$ cluster using the STO-3G* basis-set:

(i) give Cu^{2+}-ϕ bond-lengths that are in the best agreement with the averages in minerals

(ii) indicate that the (4+2)-distorted $Cu^{2+}\phi_6$ octahedron is favoured over the (2+4)-distorted $Cu^{2+}\phi_6$ octahedron

(iii) give Jahn-Teller stabilization energies in good agreement with experimental values.

(3) Treatment of the electron correlation in the $[Cu^{2+}(OH)_6]^{4-}$ cluster:

(i) results in a larger predicted distortion away from the holosymmetric configuration

(ii) gives lower cluster energies

(iii) further stabilizes the (4+2)-distorted $Cu^{2+}\phi_6$ octahedron relative to the (2+4)-distorted $Cu^{2+}\phi_6$ octahedron.

Chapter 5

An *Ab Initio* Potential-Energy Function for $Cu^{2+}\phi_6$ Octahedra

5.1 Introduction.

Over the past decade, there has been considerable effort spent on the simulation/calculation of crystal structures and mineral properties based on various forms of interatomic potential-energy functions (e.g., Abbott, 1991; Lasaga and Gibbs, 1991; Lam et al., 1990; Purton and Catlow, 1990; Burnham, 1990). This approach allows the calculation of physical properties (e.g., vibrational spectra, elastic properties, thermal expansion, etc.), and generally leads to a more sophisticated understanding of crystal structures. This is of particular importance to Earth Sciences as knowledge of mineral properties (e.g., thermal conductivity, elastic properties, etc.) is of great importance in studies of the mantle and core of the Earth (and planets), as the conditions of the systems are beyond our current experimental capabilities.

The interatomic potentials used in these calculations have generally been semi-empirical, with parameters derived from observed structures and physical or spectroscopic measurements; these have been very successful in calculating mineral structures and their properties. More recently, such potentials have been derived by *ab initio* MO methods (Kramer et al., 1991; Lasaga and Gibbs, 1987, 1988, 1991). With regards to such potentials, work has focused on atoms with spherically symmetrical electron distributions and no degenerate electron states. However, this is not an intrinsic restriction of the technique. Such features as the spontaneous distortion of

a $Cu^{2+}\phi_6$ octahedron can be included in such a potential-energy function as long as there is allowance for directional anisotropy.

The development of a potential-energy function that will account for the energetics of the $Cu^{2+}\phi_6$ octahedron is of central importance in the understanding of Cu^{2+} oxysalt structures. Such a potential would allow calculation of the crystal structures of Cu^{2+} oxysalt minerals, thus bridging the gap between the localized cluster calculations reported in the previous chapter and actual mineral structures. Deriving the potential-energy function using Hartree-Fock methods will ensure that the spontaneous distortion of the octahedron to lift the electronic degeneracy will be expressed in the potential.

5.2 Computational Methods of Structure-Energy Minimization.

Crystal-structure energy-minimization calculations normally begin with (approximate) atomic positions and unit-cell dimensions of the known structure. The atomic positions are adjusted such that the energy of the structure is minimized, giving a static structure which is, strictly speaking, appropriate for T=0 K and P=0 (Burnham, 1990). The program WMIN (Busing, 1981) allows the crystal-structure energy to be minimized in an automated fashion, and has been used in this study.

A complete expression for the structure energy must include terms that encompass both bonding and non-bonding effects. Bonding descriptions include terms for bond stretching and bond bending, and are needed to describe the interaction of any bonded pair if their relative positions are to be adjusted. Non-bonded interactions include Coulomb energy, van der Waals attraction, and short-range (Born) repulsion.

5.2.1 Non-Bonded Energy

The non-bonded energy in many crystal structures may be adequately described by a Coulombic-type expression (Post and Burnham, 1987; Burnham, 1990):

$$U_c = q_i q_j r_{ij}^{-1} \quad (5.1)$$

where q is the formal charge of the ions i and j, and r_{ij} is the interatomic distance. The program WMIN uses the Ewald (1921) and Bertaut (1952) methods for summing the Coulombic part of the structure energy.

5.2.2 Potential Forms for Bonding Interactions.

Structure calculations have been done with a variety of interatomic potential-energy functions to describe bonding interactions. The rigid-ion two-body model is perhaps the most simple, and has been used extensively in mineral calculations (e.g., Lam et al., 1990; Purton and Catlow, 1990). This model incorporates a short-range repulsive interaction that counterbalances the electrostatic forces given as Coulomb (U_C) energy (Equation 5.1). The short-range repulsive energy (U_R) may be given as a Buckingham potential, where

$$U_R = A_{ij}\exp(-r_{ij}/\rho_{ij}) - C_{ij}r^{-6} \quad (5.2)$$

The variables required (A_{ij}, ρ_{ij} and C_{ij}) for the Buckingham potential are obtained either by fitting to observed crystal structures (i.e., Miyamoto and Takeda, 1984; Price and Parker, 1984; Busing and Parker, 1984) or from theoretical (either empirical or *ab initio*) techniques. For example, Post and Burnham (1987) derived parameters for use in feldspar structure-energy

calculations using electron gas (EG) and modified electron gas (MEG) methods.

More complex interatomic potentials have been used for some mineral calculations (e.g., Sanders et al., 1984; Purton and Catlow, 1990). These potentials are designed to overcome inadequacies of the two-body approach (i.e., deviations from the Cauchy relationship). Extensions of the two-body potential often also include three-body terms for bond bending.

Lasaga and Gibbs (1987, 1988, 1991) have taken a somewhat different approach to obtaining the necessary potential parameters for Si-O bonds. They began by deriving the short-range repulsion parameters (A_{ij} and ρ_{ij}) from *ab initio* MO calculations for the H_4SiO_4 tetrahedral cluster using Hartree-Fock techniques and the STO-3G basis-set. The full electron *ab initio* description given by Hartree-Fock theory was used to derive the parameters for a potential which did not include bond-bending terms. The potential was then used, in combination with Mg-O and Al-O potentials derived from MEG theory, to calculate the structures of forsterite and pyrope. The resulting structures were in fair agreement with the structures obtained by X-ray diffraction techniques. The same Si-O potential also was used to calculate the structures of quartz and cristobalite, again in fair agreement with the experimental structures. These latter calculations represent the first such calculations done using interatomic potentials derived strictly from *ab initio* methods. Lasaga and Gibbs (1987) noted, however, that large errors in Si-O-Si bond-angles resulted when using this potential-energy function.

A more detailed description of the Si-O bonds in the SiO_4 tetrahedra was derived by Lasaga and Gibbs (1987). To overcome the inadequacies

associated with the previous model, they used a potential derived for the $H_6Si_2O_7$ cluster using MO calculations at the Hartree-Fock level with the STO-3G basis-set. This new potential explicitly included Si-O-Si bond-bending terms, and thus had a directional component built in:

$$V=1/2\ \Sigma\ K_{SiO}(r-r^\circ_{SiO})^2 + 1/2\ \Sigma\ K_{OSiO}(\theta-\theta^\circ_{OSiO})^2 \qquad (5.3)$$
$$+1/2\ \Sigma\ K_{SiOSi}(\theta-\theta^\circ_{SiOSi})^2 + 1/2\ \Sigma\ K_{r\theta}(r-r^\circ_{SiO})(\theta-\theta^\circ_{SiOSi})$$

The constants in this new potential were derived by least-squares fitting to potential-energy surfaces obtained by *ab initio* MO techniques. Such an Si-O potential-energy function is markedly different from the two-body Si-O potential, mainly because the potential function is designed specifically to model SiO_4 tetrahedra and Si-O-Si inter-tetrahedral bond-angles rather than just individual Si-O bonds. This potential improved the results obtained for the quartz structure.

5.2.3 Methods of Energy Minimization.

The program WMIN (Busing, 1981) allows considerable operator flexibility during structure-energy minimization. The initial stages of minimization usually rely on modified Rosenbrock search methods (Rosenbrock, 1960) to minimize the structure energy by varying structure parameters. This approach calculates the total crystal energy for various trial values of the structure parameters and selects the best (i.e., lowest energy) values (i.e., the Simplex method). Also included in WMIN is the method of steepest descents. This method minimizes the structure energy using a gradient vector in parameter space that is defined by the first

derivative of the energy with respect to the structure parameters. For models close to the energy minimum, Newton's method may be used, minimizing the energy using the structure parameters as variables and the energy derivatives with respect to these parameters as observations.

5.3 Calculation of a Potential-Energy Surface for $[Cu^{2+}(OH)_6]^{4-}$.

A potential-energy surface was calculated for the $[Cu^{2+}(OH)_6]^{4-}$ octahedron using Hartree-Fock MO methods and the STO-3G* basis-set. The calculations were done using the methods described in Chapter 4. The $[Cu^{2+}(OH)_6]^{4-}$ cluster and STO-3G* basis-set were used because this combination gives calculated $Cu^{2+}\phi_6$ geometries in best agreement with the geometries observed in minerals.

The Hartree-Fock UHF SCF energy was calculated for an apical-equatorial Cu-ϕ bond-length grid by fixing each Cu-ϕ_{eq} bond-length and iterating through a range of Cu-ϕ_{ap} distances. This approach gives a two-dimensional (equatorial-apical) potential-energy surface for the octahedron that includes holosymmetric as well as (2+4)- and (4+2)-distorted octahedral geometries (Fig. 5.1). Due to the computational expense, grid points for any cluster with less than D_{4h} symmetry were not included. Therefore, the potential-energy surface calculated does not allow for bond-bending effects.

The potential-energy surface calculated for the $[Cu^{2+}(OH)_6]^{4-}$ cluster using the STO-3G* basis-set shows two energy minima, corresponding to the (4+2)- and (2+4)-distorted octahedra, respectively. The energy minima are separated by a saddle point (Fig. 5.2) corresponding to the energetically unfavourable holosymmetric octahedron. The shape of the (4+2)-distorted octahedron energy-minimum is in good qualitative agreement with bond-

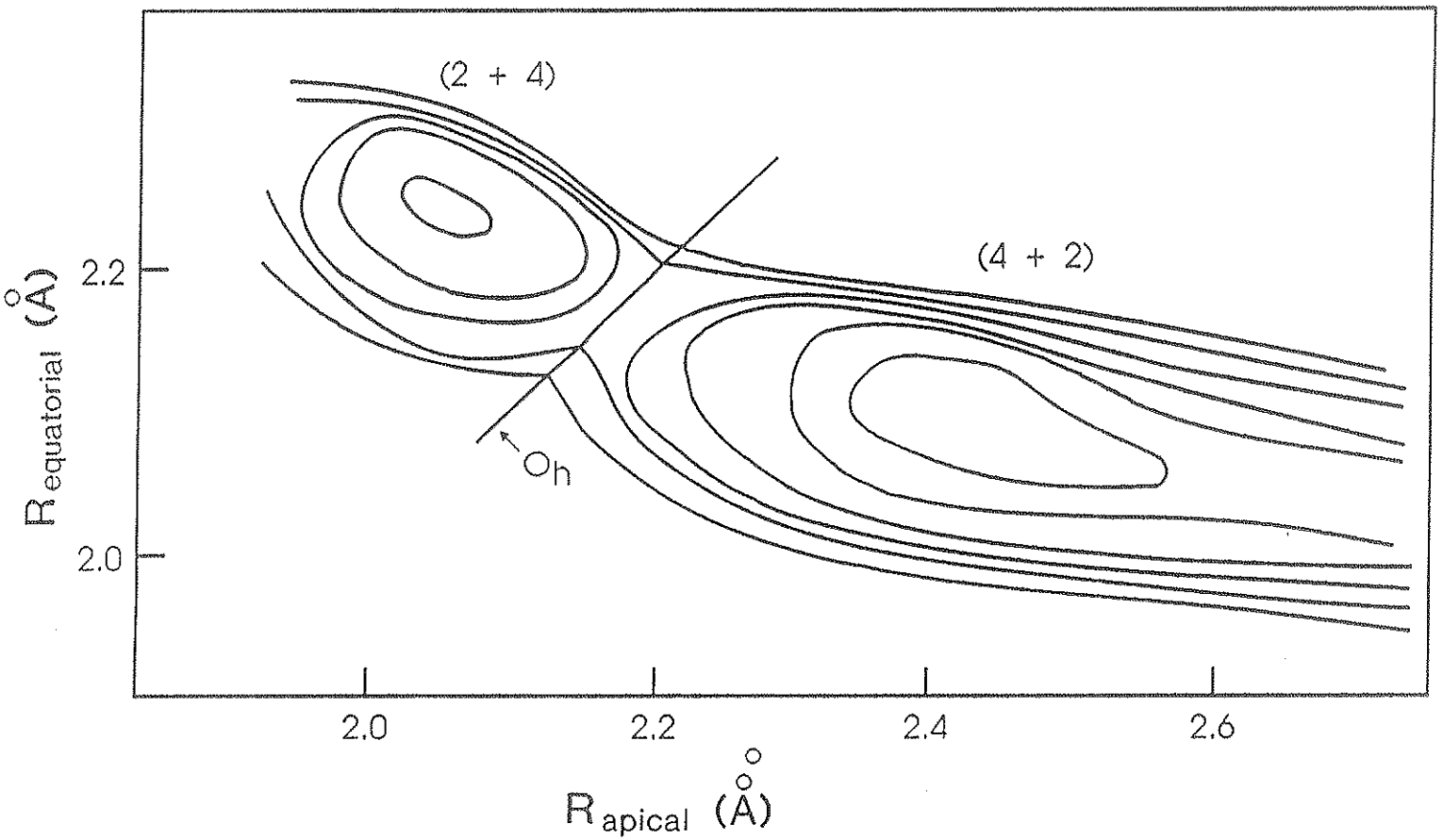

Figure 5.1. The potential-energy surface calculated for the $[Cu^{2+}(OH)_6]^{4-}$ cluster using Hartree-Fock theory and the STO-3G* basis-set. The surface is contoured with a 0.008 Hartree interval. 1 Hartree = 2625.4997 KJ/mole.

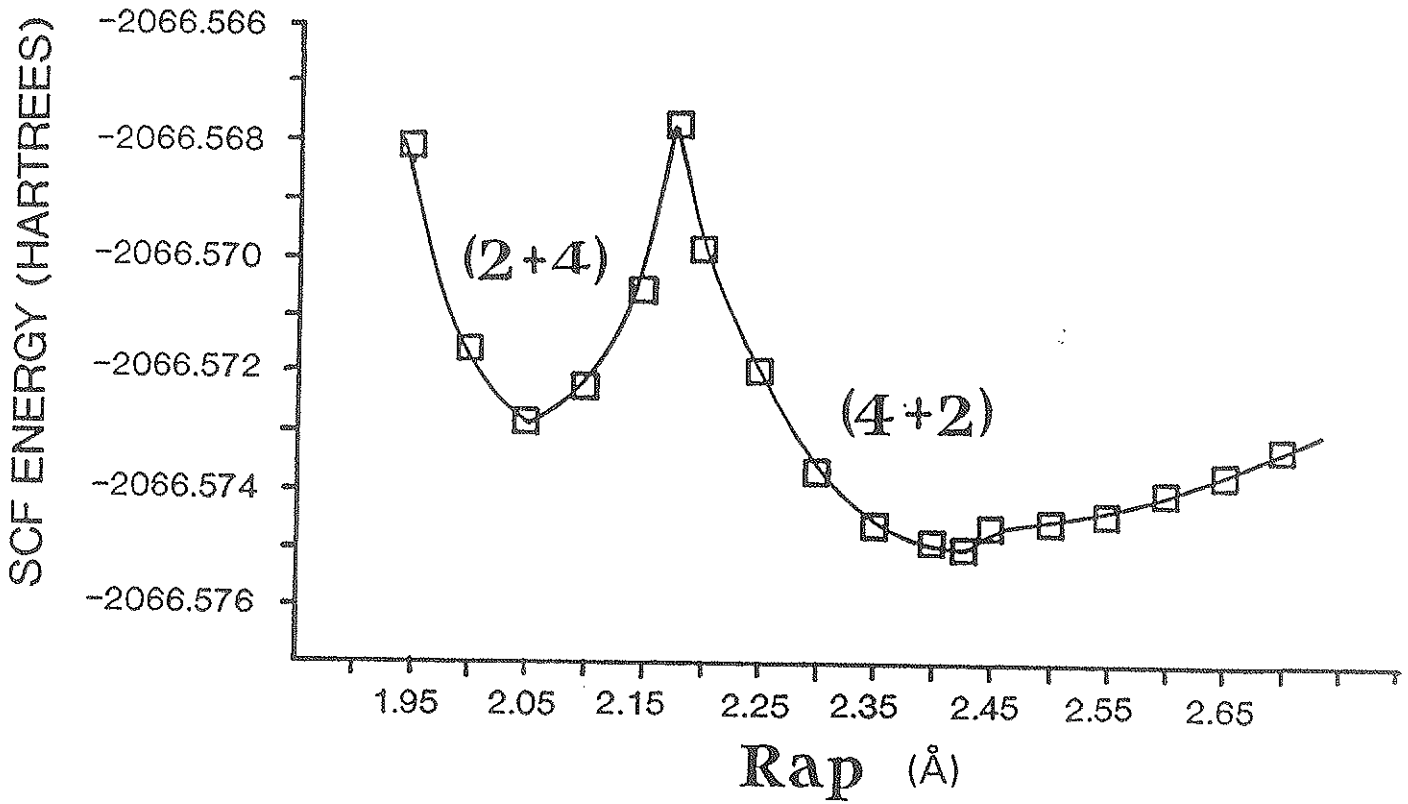

Figure 5.2. The minimum-energy pathway across the $[Cu^{2+}(OH)_6]^{4-}$ potential surface given in Figure 5.1. 1 Hartree = 2625.4997 KJ/mole.

length distribution in Cu^{2+} oxysalt minerals (Fig. 2.10) as indicated by the following points:

(1) The potential surface falls away quite slowly from the saddle axis, ensuring that there will be a strong bimodal distribution of $^{[6]}Cu\text{-}\phi$ bond-lengths.

(2) The potential surface has a much stronger curvature parallel to the equatorial bond-length axis than parallel to the apical bond-length axis; this is in line with the much lower dispersion shown by the equatorial bond-length population relative to the apical bond-length population.

(3) The potential surface has a much stronger curvature at short apical bond-lengths than at long apical bond-lengths. This 'softness' in the potential at longer distances is compatible with the skewed distribution of apical bond-lengths in Cu^{2+} oxysalt minerals.

5.4 Fitting a Potential-Energy Function to the *Ab Initio* Potential-Energy Surface.

The *ab initio* potential-energy surface for $[Cu^{2+}(OH)_6]^{4-}$ (Fig. 5.1) gives the energy of the $[Cu^{2+}(OH)_6]^{4-}$ cluster for various $Cu\text{-}\phi_{eq}$ - $Cu\text{-}\phi_{ap}$ bond-lengths within the overall constraint of D_{4h} symmetry. The energy information may then be used to describe the octahedral distortion geometries of (4+2)-distorted $Cu^{2+}\phi_6$ octahedra in Cu^{2+} oxysalt minerals during structure-energy minimization. In order that the potential-energy of the $Cu^{2+}\phi_6$ octahedron may be computer coded, a potential-energy function

must be derived by fitting some analytical function to the (4+2)-distorted *ab initio* potential-energy surface.

Various forms of potential-energy functions may be used to model the potential-energy surface. However, the surface shape for (4+2)-distorted octahedra (Fig. 5.1) depends on both the Cu-ϕ_{ap} and Cu-ϕ_{eq} bond-lengths, and is distinctly asymmetric. I found that the following function best describes the potential-energy surface:

$$V = K_1(r_{ap}-r^{\circ}_{ap}) + K_2(r_{ap}-r^{\circ}_{ap})^2 + K_3(r_{ap}-r^{\circ}_{ap})^3 + K_4(r_{eq}-r^{\circ}_{eq}) + K_5(r_{eq}-r^{\circ}_{eq})^2 + K_6(r_{eq}-r^{\circ}_{eq})^3 + K_7(r_{eq}-r^{\circ}_{eq})(r_{ap}-r^{\circ}_{ap}) + K_8 \quad (5.4)$$

In this function, K_1-K_8 are constants, and r°_{ap} and r°_{eq} are the equilibrium Cu-ϕ_{ap} and Cu-ϕ_{eq} bond-lengths, respectively (Table 4.1). The function gives V (the total energy of the octahedron) for a combination of Cu-ϕ_{ap} and Cu-ϕ_{eq} bond-lengths.

The function (Equation 5.4) was fitted to the *ab initio* potential-energy surface for (4+2)-distorted Cu-O octahedral geometries using least-squares analysis as outlined by Orvis (1990). The constants (K_i) thus obtained are given in Table 5.1.

Table 5.1 *Ab Initio* Octahedral Cu-ϕ Potential Parameters

	Value (Hartrees)		Value (Hartrees)
K_1	-0.0121	K_5	0.8395
K_2	0.1288	K_6	-1.1191
K_3	-0.1033	K_7	0.3647
K_4	0.0218		

Chapter 6

Calculation of Cu^{2+} Oxysalt Mineral Structures Using the *Ab Initio* $^{[6]}$Cu-ϕ Potential Function.

6.1 Implementation of the Potential.

The potential-energy function for $Cu^{2+}\phi_6$ octahedra derived in Chapter 5 using *ab initio* MO calculations will, in principle, allow calculation of the energy of a $Cu^{2+}\phi_6$ octahedron embedded in a crystal structure. Towards this goal, the potential-energy function may be computer coded and included in WMIN calculations of the structure energy of Cu^{2+} oxysalt minerals as an expression of the bonding interaction in the $Cu^{2+}\phi_6$ octahedron. In combination with other cation-anion and anion-anion potentials, the Cu-ϕ potential will allow calculation of Cu^{2+} oxysalt structures.

The applicability of this potential to structure calculations is limited by the techniques used in its derivation. The *ab initio* calculations were done for clusters that were restricted to D_{4h} symmetry in order to reduce computational expense. This limitation is reflected in the potential function, as it suggests that the cluster has four equivalent equatorial and two equivalent apical Cu-ϕ bond-lengths. The symmetry restrictions included in the *ab initio* calculations also dictate that the resultant Cu-ϕ potential does not include any terms for bond bending.

These limitations have been somewhat offset by the way that the Cu-ϕ potential has been coded. Each Cu-ϕ bond has been included in the code as a separate entity, rather than using average values of Cu-ϕ bond-lengths. For example, the term $K_1(r_{ap}-r^{\circ}_{ap})$ (Equation 5.4) has been coded as $K_1/2(r_{ap,1}-r^{\circ}_{ap}) + K_1/2(r_{ap,2}-r^{\circ}_{ap})$. The lack of Cu-$\phi$ bond-bending terms in the Cu-ϕ

potential-energy function has been partly accounted for by including O-O repulsion terms for oxygen pairs in the same octahedron.

6.2 Determination of Optimal Potential-Energy Parameters.

The potential for $Cu^{2+}\phi_6$ octahedra was obtained by fitting Equation 5.4 to the *ab initio* potential-surface calculated for the $[Cu^{2+}(OH)_6]^{4-}$ cluster. This cluster has an excess charge of -4 which is expected to destabilize the complex, thus lengthening the Cu-OH bond-lengths and resulting in a potential-energy surface with slopes that are too shallow in the area of the minimum. To offset these effects, the location of the minimum in the (4+2)-distorted octahedron energy surface may be varied by changing the values of r°_{ap} and r°_{eq} used in the function. Slopes of the surface in the area of the energy minimum may be varied by scaling the entire potential, such that $K_i = CK_i$, where C is a scaling constant.

As with other bonding potential-energy functions, it is desirable to select values of r°_{ap}, r°_{eq} and C that will result in the maximum transferability of the potential between various Cu^{2+} structures. The purpose of this section is to derive the most appropriate values for these constants from structure-energy minimizations of a selection of Cu^{2+} minerals.

Minimization for each of the Cu^{2+} oxysalt mineral structures was done with the Cu-ϕ bonding interaction described by the *ab initio* Cu-ϕ potential function. Non-bonding interactions were assumed to be Coulombic for Cu^{2+}, S^{6+}, Mo^{6+}, O^{2-} and H^+ and also included additional short-range O-O repulsion terms of the Born-type with parameters derived by Post and Burnham (1987) from MEG theory. The O-H interactions were modelled

using Coulombic attraction balanced by short-range O-H repulsion terms of the Born-type derived for amphiboles by Abbott (1991) using hydrogen positions and the principal OH-stretching frequencies. The SO_4 tetrahedra in chalcocyanite and bonnatite, and the MO_4 tetrahedron in lindgrenite, were constrained to be rigid bodies with full translational and rotational movement allowed during energy minimization. Structure-energy minimizations were done using the Rosenbrock search method followed by Newton's method.

6.2.1 Tenorite ($Cu^{2+}O$): Structure-Energy Minimization.

The simplest Cu^{2+}-oxide mineral, from the point of view of structure-energy minimization, is tenorite ($Cu^{2+}O$), as the only bonded interactions in this mineral are Cu-O interactions. The crystal structure of tenorite was refined by Åsbrink and Norrby (1970). Tenorite is monoclinic, space group C2/c. The copper and oxygen atoms are both on special positions, such that only the y coordinate of the oxygen position is not fixed by symmetry constraints. Tenorite contains Cu-O octahedra distorted such that there are four short (equatorial) distances and two long (apical) distances, a (4+2)-distortion. The tenorite structure is an infinite three-dimensional linkage of these octahedra, as shown in Figure 6.1; the structure parameters are given in Table 6.1.

Structure-energy minimizations were done for the tenorite structure using 150 different combinations of the *ab initio* Cu-ϕ potential function constants r°_{ap}, r°_{eq} and C, with ranges r°_{ap} = 2.20-2.50 Å, r°_{eq} = 1.90-2.00 Å, C = 6-24. In total, only 15 of the structure-energy minimizations resulted in convergence to structures in agreement with the X-ray structure (Table 6.2).

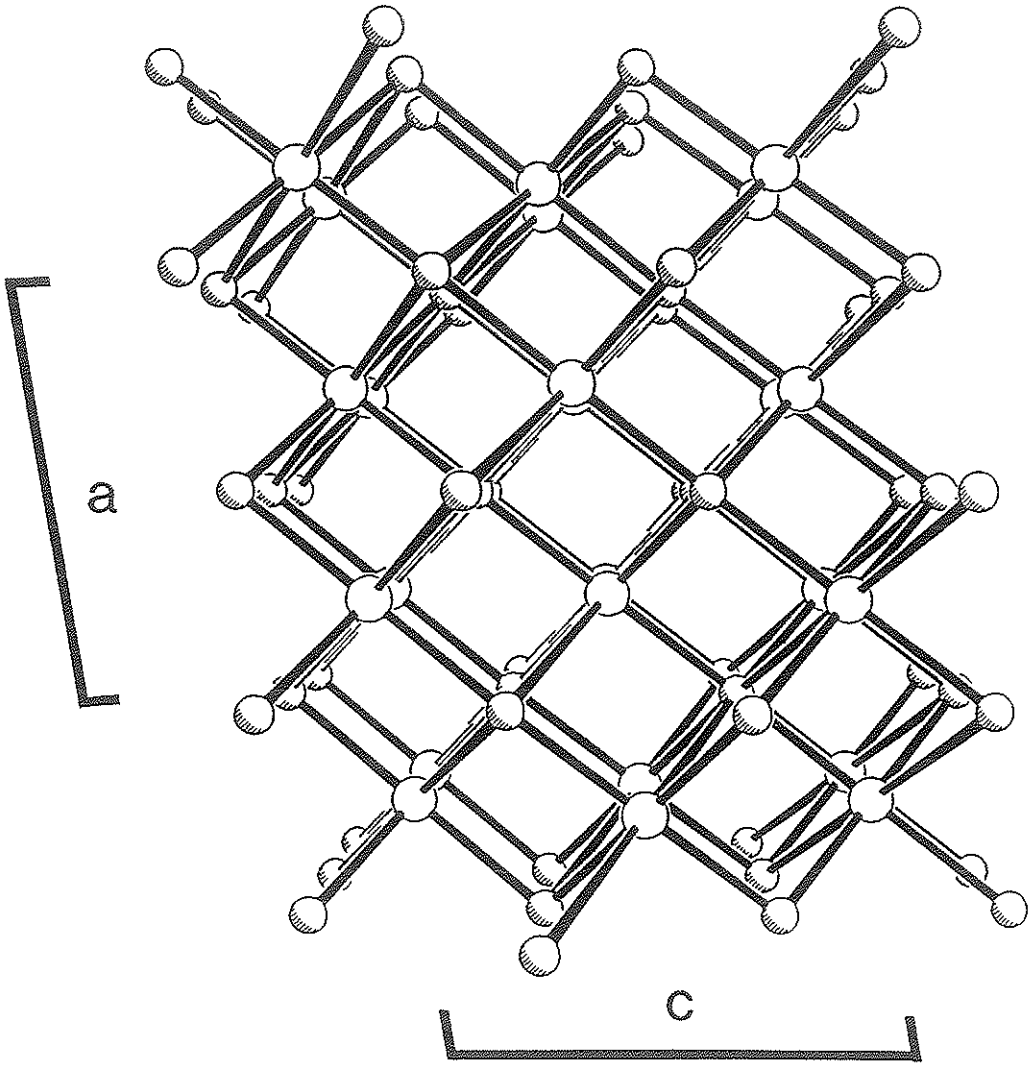

Figure 6.1. The crystal structure of tenorite projected onto (010). Copper atoms are large open circles and oxygen atoms are smaller circles with shading in the lower left corners.

Table 6.1 Structure parameters for tenorite* (CuO)

Space Group	C2/c
a = 4.6837(5) Å	β = 99.54(1)°
b = 3.4226(5)	V = 81.08(2) Å^3
c = 5.1288(6)	Z = 4

4 Cu at 4(*c*): (1/4,1/4,0; 3/4,3/4,0; 1/4,3/4,1/2; 3/4,1/4,1/2)

4 O at 4(*e*): (0,y,1/4; 1/2,1/2+y,1/4; 0,ȳ,3/4; 1/2,1/2-y,3/4)

Cu-O	x2	1.961(1) Å
Cu-O(iii)	x2	1.951(3)
Cu-O(i)	x2	2.784(4)

* From Åsbrink and Norrby (1970)

Table 6.2 Structural parameters for tenorite calculated using various $r°_{ap}$ (Å), $r°_{eq}$ (Å) and C values.

		$r°_{ap},r°_{eq},C$		
	Observed	2.30,1.90 16	2.30,1.925 19	2.30,1.95 22
O(y)	0.4184(13)	0.4183	0.4184	0.4185
Cu-O x2	1.9608(13)	1.9608	1.9610	1.9611
Cu-O(iii) x2	1.9509(26)	1.9512	1.9508	1.9507
Cu-O(i) x2	2.7840(37)	2.7839	2.7845	2.7846
		$r°_{ap},r°_{eq},C$		
	2.30,1.975 24	2.30,2.00 27	2.40,1.90 10	2.40,1.925 12
O(y)	0.4186	0.4180	0.4192	0.4180
Cu-O x2	1.9612	1.9606	1.9617	1.9606
Cu-O(iii) x2	1.9505	1.9516	1.9492	1.9517
Cu-O(i) x2	2.7849	2.7833	2.7864	2.7832
		$r°_{ap},r°_{eq},C$		
	2.40,1.95 13	2.40,1.975 14	2.40,2.00 14	2.50,1.90 10
O(y)	0.4182	0.4181	0.4182	0.4180
Cu-O x2	1.9608	1.9606	1.9608	1.9607
Cu-O(iii) x2	1.9512	1.9516	1.9512	1.9517
Cu-O(i) x2	2.7838	2.7834	2.7839	2.7834
		$r°_{ap},r°_{eq},C$		
	2.50,1.925 11	2.50,1.95 12	2.50,1.975 13	2.50,2.00 13
O(y)	0.4183	0.4183	0.4180	0.4182
Cu-O x2	1.9609	1.9609	1.9606	1.9608
Cu-O(iii) x2	1.9510	1.9510	1.9517	1.9513
Cu-O(i) x2	2.7841	2.7841	2.7833	2.7837

Values of r°_{ap}, r°_{eq} and C outside of the above ranges did not lead to convergence. Thus, there are 15 equally good choices for these three potential-energy function parameters when only tenorite is considered.

6.2.2 Chalcocyanite ($Cu^{2+}SO_4$): Structure-Energy Minimization.

Chalcocyanite is a rare mineral that occurs as a volcanic exhalation. The crystal structure of chalcocyanite was reported by Kokkoros and Rentzeperis (1958) and subsequently refined by Rao (1961), Almodovar et al. (1965) and Wildner and Giester (1988). Chalcocyanite is orthorhombic, space group Pnma, and Cu^{2+} is in (4+2)-distorted octahedral coordination. The octahedra share edges to form chains parallel to [010]; these chains are linked by SO_4 tetrahedra to form the framework of the structure (Fig. 6.2). The structure parameters are given in Table 6.3.

Minimizations were attempted for the 15 combinations of r°_{ap}, r°_{eq} and C that gave satisfactory results for the tenorite structure (Table 6.2). Of the attempted minimizations, only four combinations of r°_{ap}, r°_{eq} and C led to a reasonable structure. Of these combinations, all had r°_{ap} = 2.30 Å and C > 16 (Table 6.4). In each of these cases, the apical Cu-O bond-lengths are somewhat long. However, the potential does an excellent job of predicting the distorted nature of the Cu^{2+} environment.

6.2.3 Bonnatite ($Cu^{2+}SO_4 \cdot 3H_2O$): Structure-Energy Minimization.

The crystal structure of bonnatite ($Cu^{2+}SO_4 \cdot 3H_2O$) was determined by Zahrobsky and Baur (1968). Bonnatite is monoclinic, space group Cc. The Cu^{2+} cation is in (4+2)-distorted octahedral coordination, and copper polyhedra do not share any anions with other copper polyhedra. Both apical

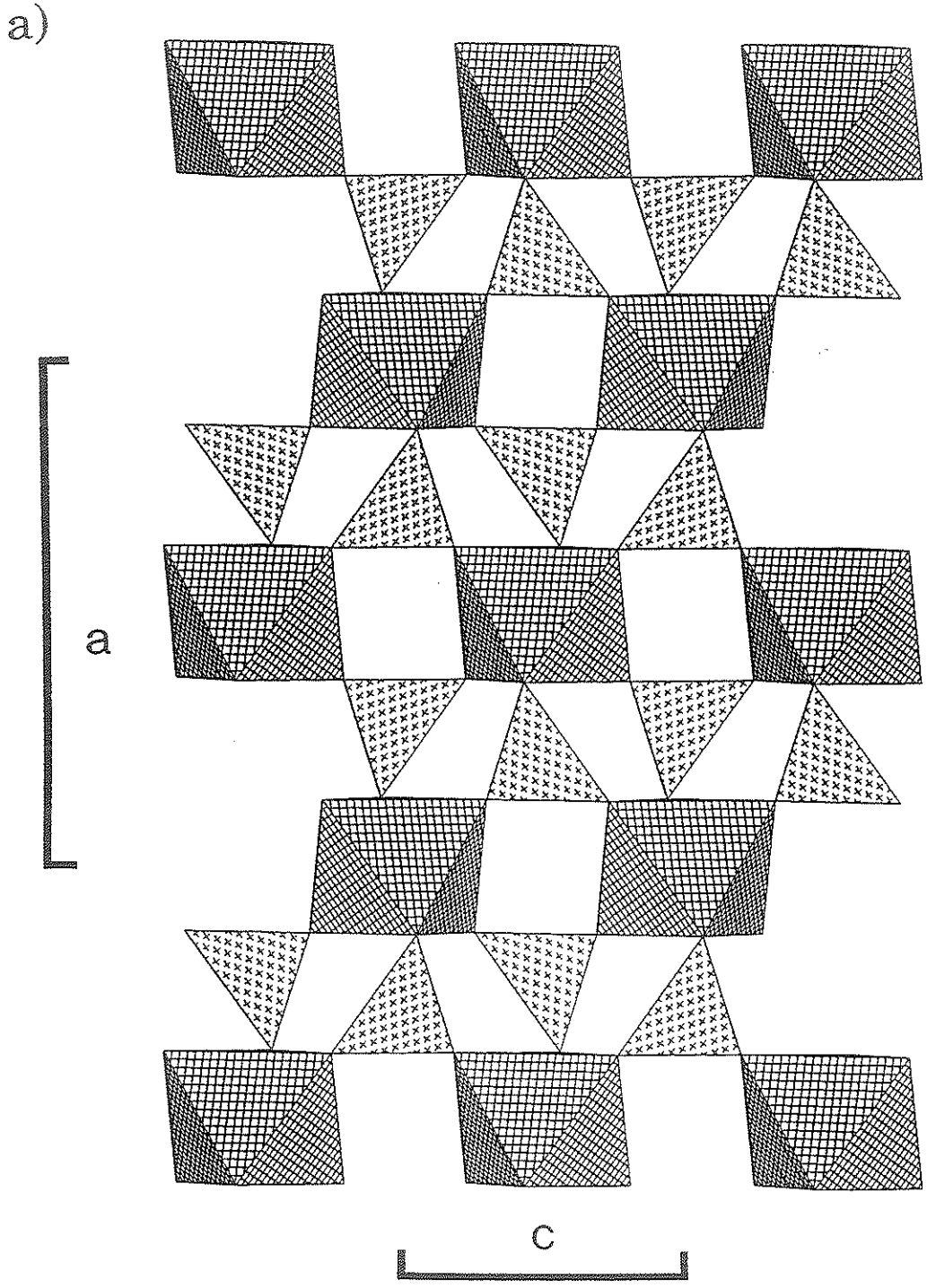

Figure 6.2. Polyhedral structure representations of chalcocyanite. Copper octahedra are cross-hatched and sulphur tetrahedra are shaded with crosses. a) structure projected onto (010), b) structure projected onto (001).

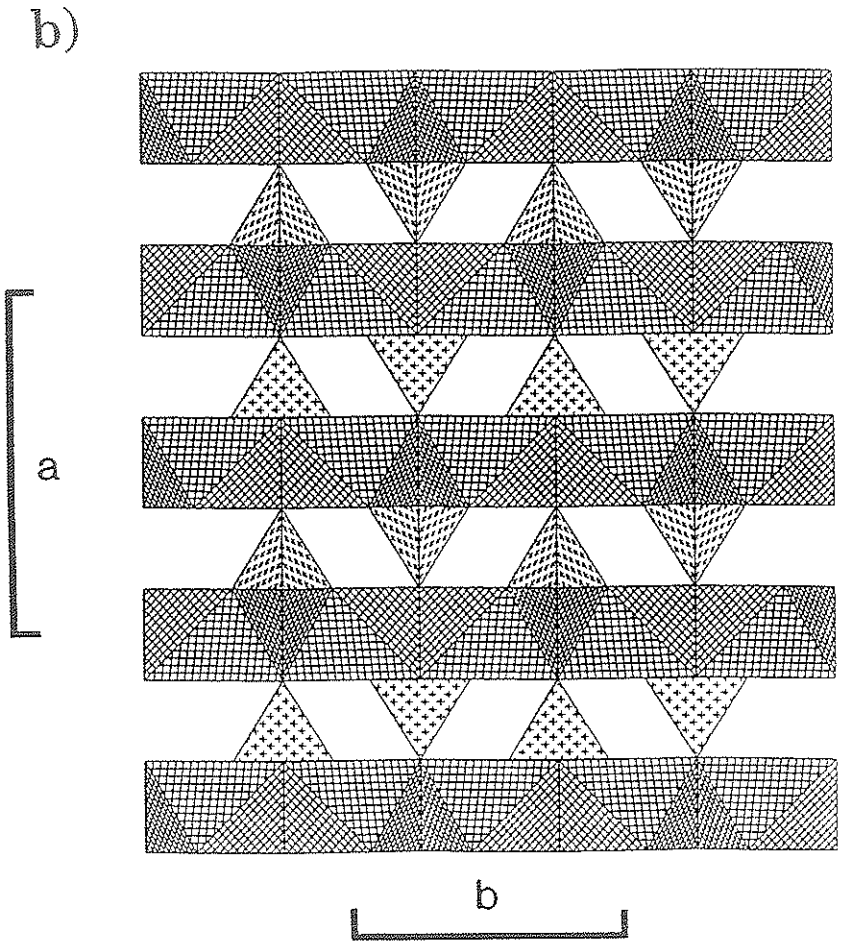

Figure 6.2. Continued.

Table 6.3 Structure parameters* for chalcocyanite ($Cu^{2+}SO_4$).

Space Group	Pnma		
a = 8.409(1) Å	V = 272.65 Å^3		
b = 6.709(1)	Z = 4		
c = 4.833(1)			
	x	y	z
Cu	0	0	0
S	0.18363(10)	1/4	0.44979(16)
O(1)	0.1293(3)	1/4	0.7353(5)
O(2)	0.3646(3)	1/4	0.4385(6)
O(3)	0.1328(2)	0.0674(3)	0.3083(4)
Cu-O(1) x2	2.373(1) Å	S-O(1)	1.453(2) Å
Cu-O(2) x2	2.049(1)	S-O(2)	1.523(2)
Cu-O(3) x2	1.916(1)	S-O(3) x2	1.467(1)

* From Wildner and Giester (1988).

Table 6.4. Structures of chalcocyanite calculated using various r°_{ap}, r°_{eq} and C values.

r°_{ap}	1.90	1.925	1.95	1.975	
r°_{eq}	2.30	2.30	2.30	2.30	
C	16	19	22	24	
					Observed*
S (x)	0.1951	0.1966	0.1966	0.1952	0.1836(1)
S (z)	0.4318	0.4335	0.4389	0.4475	0.4498(2)
O(1) (x)	0.1366	0.1384	0.1414	0.1456	0.1293(3)
O(1) (z)	0.7148	0.7167	0.7239	0.7357	0.7353(5)
O(2) (x)	0.3762	0.3777	0.3776	0.3759	0.3646(3)
O(2) (z)	0.4287	0.4297	0.4294	0.4271	0.4385(6)
O(3) (x)	0.1464	0.1477	0.1462	0.1420	0.1328(2)
O(3) (z)	0.2881	0.2899	0.2969	0.3087	0.3083(4)
Cu-O(1) x2+	2.456	2.458	2.451	2.438	2.373(1)
Cu-O(2) x2	2.004	1.997	1.997	2.007	2.049(1)
Cu-O(3) x2	1.913	1.926	1.943	1.964	1.916(1)
Ave $\|\Delta\|$**	0.044	0.049	0.052	0.052	

* Wildner and Giester (1988)
\+ Bond distances are in Å
** Δ = calculated - observed bond-length

ligands of the (4+2)-distorted copper octahedron are oxygen atoms shared with adjacent SO_4 tetrahedra. One equatorial ligand is shared with an adjacent SO_4 tetrahedron, and the other three are H_2O groups. The copper octahedra are linked via SO_4 tetrahedra and hydrogen bonding to form a framework structure (Fig. 6.3). The structure parameters are listed in Table 6.5.

Structure-energy minimizations were done using values of r°_{ap}, r°_{eq} and C that gave good results for both tenorite and chalcocyanite (Table 6.4). Convergence was obtained for three of these combinations. The calculated Cu-O bond-lengths and hydrogen bonding for each minimum-energy structure are given in Table 6.6.

6.2.4 Lindgrenite $[Cu_3^{2+}(MoO_4)_2(OH)_2]$: Structure-Energy Minimization.

Lindgrenite, $Cu_3^{2+}(MoO_4)_2(OH)_2$, occurs in massive quartz veins as the result of oxidation of primary molybdenite. The structure was reported by Calvert and Barnes (1957) and refined by Hawthorne and Eby (1985). Lindgrenite is monoclinic, space group $P2_1/n$, with two distinct copper octahedra, both of which show (4+2)-distorted geometry. The octahedra share edges to form strips which are cross-linked by MoO_4 tetrahedra (Fig. 6.4). The structure parameters are given in Table 6.7.

Structure-energy minimizations were done using the three combinations of r°_{ap}, r°_{eq} and C that resulted in the best structure-energy minimizations for tenorite, chalcocyanite and bonnatite. The resulting Cu-O and hydrogen bonds are given in Table 6.8.

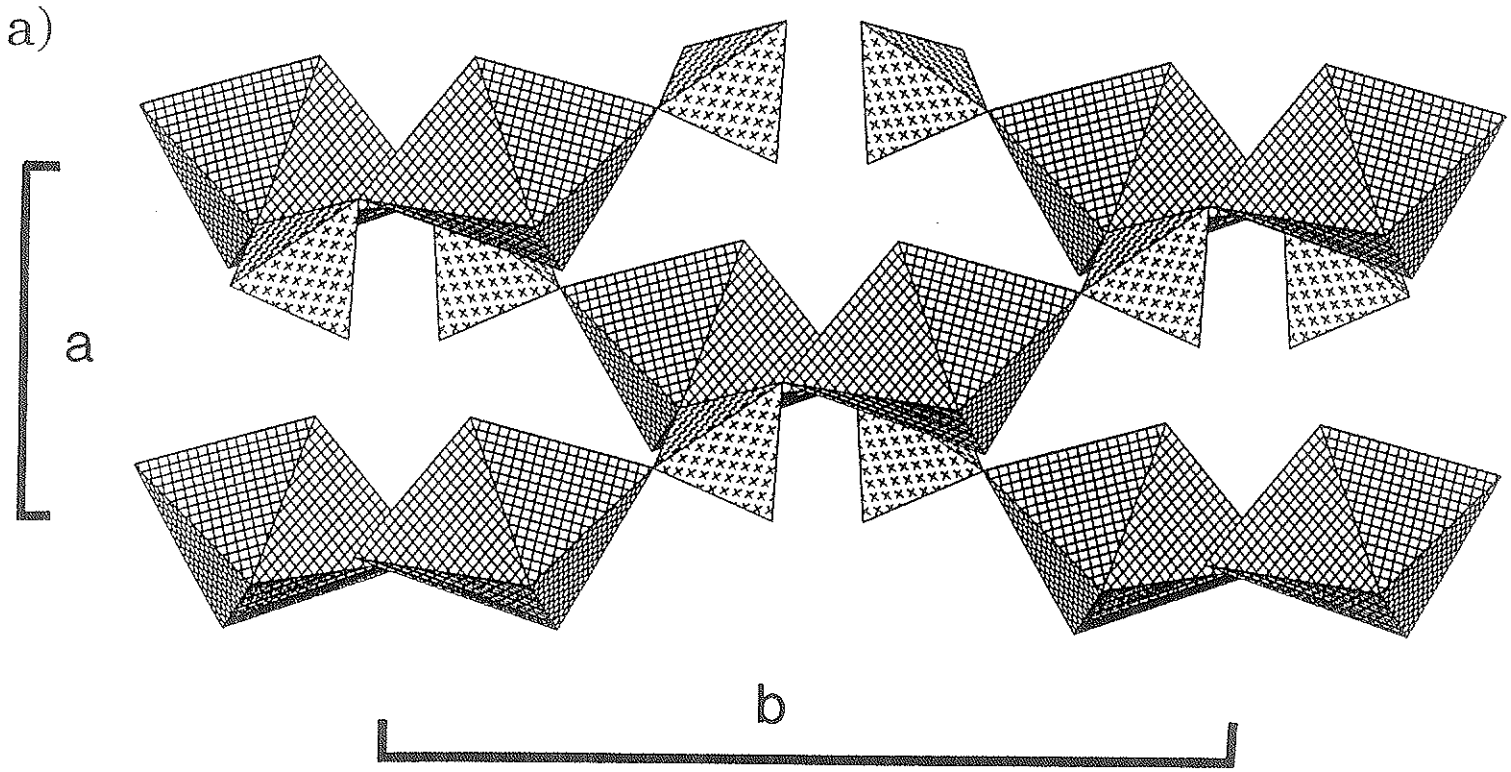

Figure 6.3. Polyhedral structure representations of bonnatite. Copper octahedra are cross-hatched and sulphate tetrahedra are shaded with crosses. a) structure projected onto (001), b) structure projected onto (100).

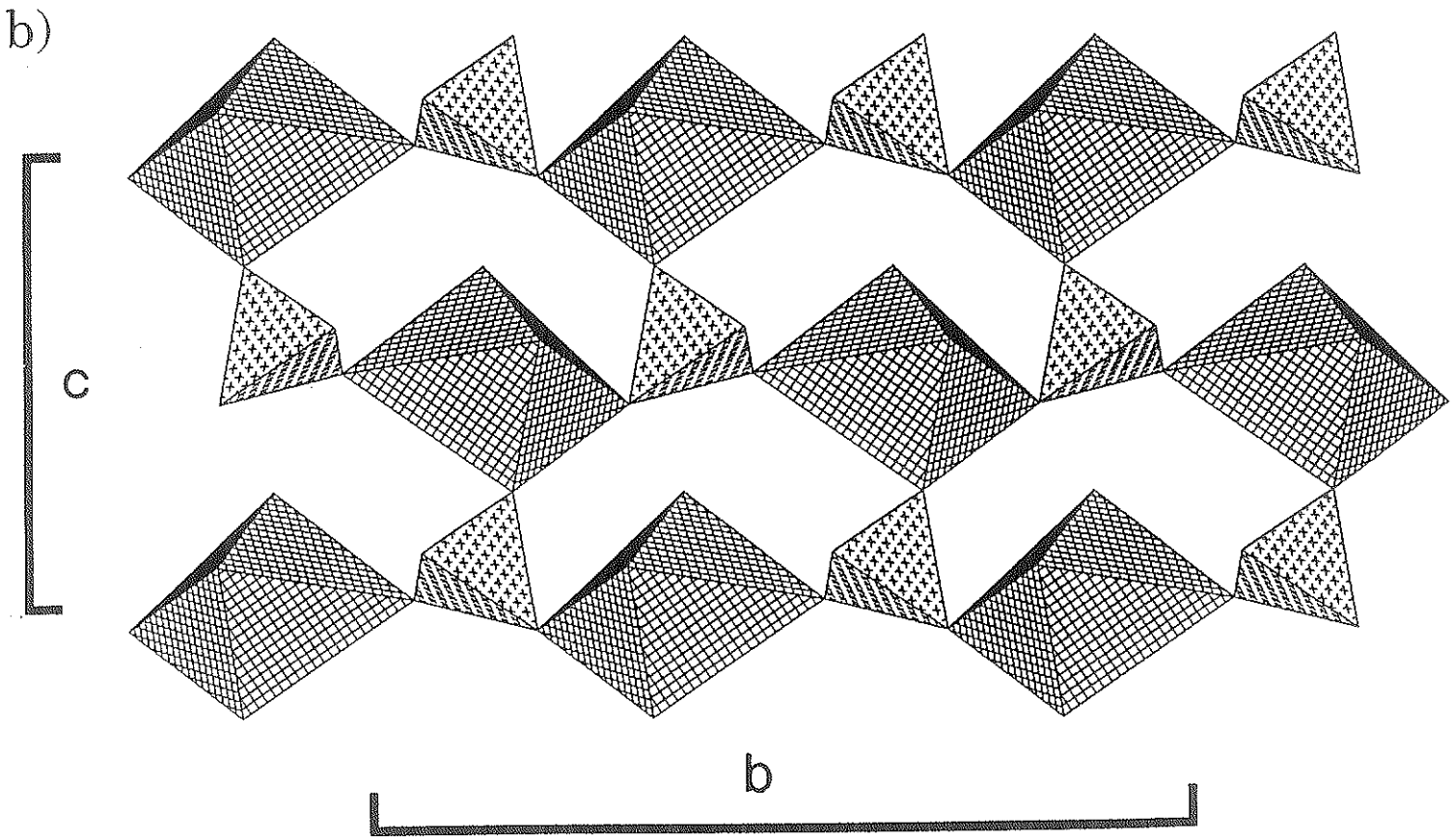

Figure 6.3. Continued.

Table 6.5 Structure parameters* for bonnatite ($Cu^{2+}SO_4 \cdot 3H_2O$)

Space Group		Cc	
a = 5.592(5) Å		β = 97.05(11)°	
b = 13.029(10)		V = 531(1) Å^3	
c = 7.341(6)		Z = 4	
	x	y	z
Cu	1/2	0.3640(1)	1/2
S	0.2643(2)	0.1115(1)	0.4168(2)
O(1)	0.1618(10)	0.1639(5)	0.2446(7)
O(2)	0.8319(9)	0.3057(5)	0.0505(6)
O(3)	0.4788(9)	0.0536(5)	0.3805(8)
O(4)	0.0866(8)	0.9562(5)	0.9825(7)
OW(1)	0.3360(9)	0.3725(4)	0.2462(8)
OW(2)	0.6940(8)	0.0911(4)	0.0809(7)
OW(3)	0.7840(7)	0.3041(5)	0.4103(6)
H(1)	0.428	0.397	0.151
H(2)	0.174	0.355	0.192
H(3)	0.635	0.093	0.200
H(4)	0.604	0.040	0.003
H(5)	0.930	0.276	0.476
H(6)	0.795	0.304	0.280
Cu-O(1)	1.943(5) Å	S-O(1)	1.488(5) Å
Cu-O(2)	2.448(6)	S-O(2)	1.476(5)
Cu-O(4)	2.399(6)	S-O(3)	1.469(5)
Cu-OW(1)	1.976(7)	S-O(4)	1.455(5)
Cu-OW(2)	1.968(5)		
Cu-OW(3)	1.955(5)		

* From Zahrobsky and Baur (1968).

Table 6.6. Selected bond-lengths (Å) for minimum-energy structures of bonnatite.

		r°_{ap}, r°_{eq}, C		
	Observed+	2.30, 1.90, 16	2.30, 1.925, 19	2.30, 1.95, 22
Cu-O(1)	1.943(5)	1.932	1.943	1.957
Cu-O(2)	2.448(6)	2.451	2.450	2.450
Cu-O(4)	2.399(6)	2.438	2.439	2.439
Cu-OW(1)	1.976(7)	1.925	1.939	1.953
Cu-OW(2)	1.968(5)	1.927	1.939	1.954
Cu-OW(3)	1.955(5)	1.925	1.938	1.953
Ave $\|\Delta\|$*		0.029	0.021	0.016
H(1)-OW(1)		1.119	1.114	1.123
H(1)-O(4)		1.645	1.629	1.644
H(2)-OW(1)		1.113	1.119	1.115
H(2)-O(1)		1.872	1.880	1.891
H(3)-OW(2)		1.090	1.090	1.084
H(3)-O(3)		1.789	1.784	1.740
H(4)-OW(2)		1.188	1.189	1.197
H(4)-O(3)		1.510	1.506	1.519
H(5)-OW(3)		1.104	1.118	1.080
H(5)-OW(2)		1.731	1.744	1.837
H(6)-OW(3)		1.142	1.136	1.145
H(1)-H(2)		1.960	1.959	1.962
H(3)-H(4)		1.992	1.992	2.018
H(5)-H(6)		1.960	1.959	1.954

+ Bond-lengths are from Zahrobsky and Baur (1968).
* Δ = calculated - observed bond-length

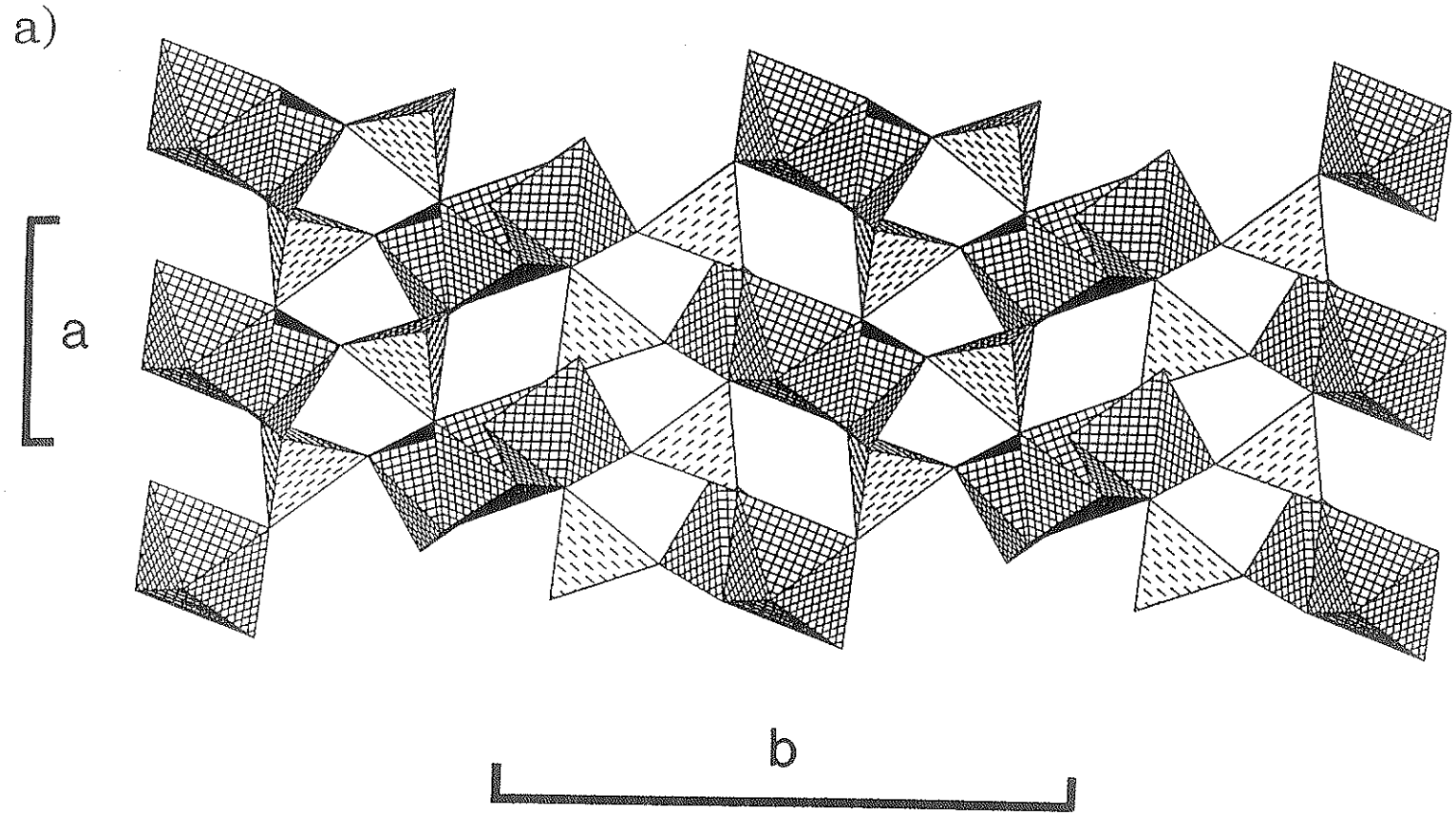

Figure 6.4. Polyhedral structure representations of lindgrenite. Copper octahedra are cross-hatched and molybdenum tetrahedra are shaded with dashed lines.

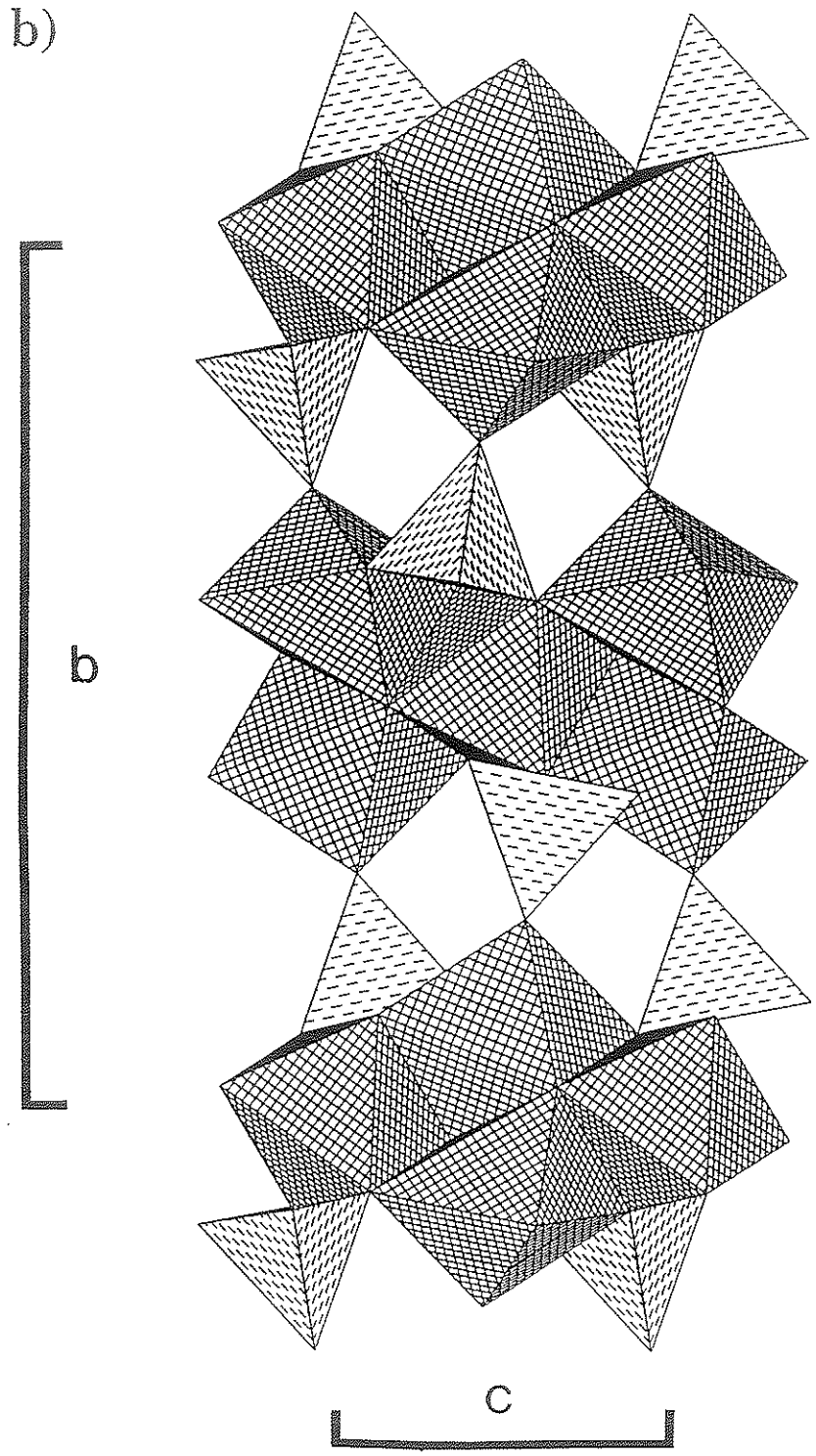

Figure 6.4. Continued.

Table 6.7. Structure parameters* for lindgrenite $[Cu_3^{2+}(MoO_4)_2(OH)_2]$.

Space Group		$P2_1/n$	
a = 5.394(1) Å		β = 98.50(1)°	
b = 14.023(3)		V = 419.5(1) Å^3	
c = 5.608(1)		Z = 2	
	x	y	z
Cu(1)	0	0	0
Cu(2)	0.8638(1)	0.09393(4)	0.4870(1)
Mo	0.45592(7)	0.15456(3)	0.87716(7)
O(1)	0.9801(7)	0.2234(2)	0.4358(7)
O(2)	0.6505(7)	0.0918(3)	0.1009(7)
O(3)	0.5532(6)	0.1299(3)	0.5938(6)
O(4)	0.1448(6)	0.1130(3)	0.8730(6)
O(5)	0.1312(6)	0.0306(2)	0.3405(6)
H(5)	0.27(1)	0.048(4)	0.35(1)

Cu(1)-O(2) x2	2.418(4) Å	Cu(2)-O(1)	1.956(4) Å
Cu(1)-O(4) x2	1.947(4)	Cu(2)-O(2)	2.298(4)
Cu(1)-O(5) x2	1.984(3)	Cu(2)-O(3)	1.928(4)
		Cu(2)-O(4)	2.466(3)
Mo-O(1)	1.743(3)	Cu(2)-O(5)	1.978(3)
Mo-O(2)	1.749(4)	Cu(2)-O(5)	1.995(3)
Mo-O(3)	1.779(4)		
Mo-O(4)	1.774(3)		

* From Hawthorne and Eby (1985).

Table 6.8 Selected bond-lengths (Å) for lindgrenite minimum-energy structures.

		r°_{ap}, r°_{eq}, C		
	Observed+	2.30,1.90 16	2.30,1.925 19	2.30,1.95 22
Cu(1)-O(2)x2	2.418(4)	2.512	2.482	2.480
Cu(1)-O(4)x2	1.947(4)	1.901	1.921	1.941
Cu(1)-O(5)x2	1.948(3)	1.912	1.929	1.947
Cu(2)-O(1)	1.956(4)	2.047	2.031	2.027
Cu(2)-O(2)	2.298(4)	2.390	2.393	2.400
Cu(2)-O(3)	1.928(4)	2.051	2.038	2.035
Cu(2)-O(4)	2.466(3)	2.390	2.397	2.405
Cu(2)-O(5)	1.978(3)	2.022	2.013	2.014
Cu(2)-O(5)	1.995(3)	2.028	2.019	2.019
Ave $\|\Delta\|$*		0.073	0.058	0.051
H(1)-O(5)	0.79(6)	1.115	1.109	1.109
H(1)-O(3)		1.721	1.719	1.692

+ From Hawthorne and Eby (1985).
* Δ = calculated - observed bond-length

6.2.5 Optimal r°_{ap}, r°_{eq} and C Parameters for Maximum Transferability of the $Cu^{2+}\phi_6$ Potential.

There are three combinations of r°_{ap}, r°_{eq} and C (2.30, 1.90, 16; 2.30, 1.925, 19; 2.30, 1.95, 22) that result in reasonable calculated structures for tenorite, chalcocyanite, bonnatite and lindgrenite. The combination that gives the best results for each mineral may be selected on the basis of the mean absolute difference between the calculated and observed bond-lengths ($|\Delta|$, Tables 6.4, 6.6 and 6.8). Each of the three combinations give equivalent results for tenorite; r°_{ap} = 2.30 Å, r°_{eq} = 1.90 Å, C = 16 gives the best results for chalcocyanite ($|\Delta|$ = 0.044 < 0.049 < 0.052) and r°_{ap} = 2.30 Å, r°_{eq} = 1.95 Å, C = 22 gives the best results for both bonnatite ($|\Delta|$ = 0.016 < 0.021 < 0.029) and lindgrenite ($|\Delta|$ = 0.051 < 0.058 < 0.073). Therefore, the constant values are fixed at r°_{ap} = 2.30 Å, r°_{eq} = 1.95 Å, C = 22 to obtain maximum transferability of the $Cu^{2+}\phi_6$ potential between various Cu^{2+} oxysalt structures.

6.3 Discussion.

The structure-energy minimizations reported in the previous sections indicate that the *ab initio* Cu-ϕ potential function for $Cu^{2+}\phi_6$ octahedra, as derived directly from Hartree-Fock calculations for the $[Cu^{2+}(OH)_6]^{4-}$ cluster (Chapter 5), is not effective in modelling $Cu^{2+}\phi_6$ octahedra in Cu^{2+} oxysalt minerals. However, when the location of the minimum is moved to r_{ap} = 2.30, r_{eq} = 1.95 Å and the function is scaled by a factor of 22, the potential function adequately describes $Cu^{2+}\phi_6$ octahedra occurring in minerals, and is reasonably transferable from one structure to another.

The values of r°_{ap} = 2.30, r°_{eq} = 1.95 Å and C = 22 do not agree with the values obtained through *ab initio* molecular-orbital cluster geometry optimizations for $[Cu^{2+}(OH)_6]^{-4}$ (Table 4.1, r°_{ap} = 2.427 Å, r°_{eq} = 2.081 Å and C = 1). This is not exactly unexpected as the net charge of -4 on the $[Cu^{2+}(OH)_6]^{4-}$ cluster will have a destabilizing effect in comparison to a $Cu^{2+}\phi_6$ octahedron embedded in a crystal structure. This destabilization should be reflected by (1) lengthened Cu-ϕ bond-lengths, and (2) a shallower energy minimum in the potential-energy surface. Also, the inclusion of O-O repulsions for $Cu^{2+}\phi_6$ octahedra during the minimization results in some of the repulsion energy being counted twice, as the all-electron Hartree-Fock calculations used to derive the potential function already included some of these effects. Thus, the value of C=22 has no physical meaning. *The need to adjust r°_{ap}, r°_{eq} and C in order to obtain a good description of Cu-ϕ octahedral bonding in crystals does not detract from the fact that a transferable $Cu^{2+}\phi_6$ octahedral potential function has been obtained.* However, the potential should no longer be referred to as an *ab initio* potential, but rather as an empirical *ab initio* potential function.

The $Cu^{2+}\phi_6$ octahedral potential function reported here is the first reported bonding-interaction function that incorporates a Jahn-Teller distortion. The required directional anisotropy makes the potential function capable of describing the Jahn-Teller distortion of $Cu^{2+}\phi_6$ octahedra. This places somewhat of a restriction on the use of the potential function, as the user must define the direction of octahedral elongation before attempting an energy minimization. However, there are only three possible orientations, and calculations may be done for all three possibilities.

The structure-energy minimizations for tenorite, chalcocyanite, bonnatite and lindgrenite indicate that this $Cu^{2+}\phi_6$ potential results in (4+2)-distorted octahedra in the calculated structures. The magnitude of the octahedral distortion is also quite well predicted (Tables 6.2, 6.4, 6.6, 6.8). Individual Cu-O bond-lengths calculated using the $Cu^{2+}\phi_6$ potential show only fair agreement with the observed bond-lengths for the respective structures, with the average absolute difference between calculated and X-ray bond-lengths generally falling in the range 0.0-0.05 Å, with a maximum average error of 1.8 - 2.6 %.

Improvements to the $Cu^{2+}\phi_6$ octahedral potential-energy function will result if *ab initio* calculations for lower-symmetry clusters are incorporated. Lower symmetry coordinations such as (4+1+1)-distorted octahedra [i.e., as observed in agardite (Aragu and Nakai, 1985) and spertiniite (Oswald et al., 1990)] may be better represented by such a potential. Inclusion of Cu-ϕ bond-bending terms, also by considering lower-symmetry clusters, should also improve the overall description of the copper environment. These lower-symmetry calculations require huge amounts of computer CPU time, and are currently impractical.

Chapter 7

Ab Initio Molecular-Orbital Investigations of Five-Coordinated Cu^{2+} Clusters

7.1 $Cu^{2+}\phi_5$ Geometries in Cu^{2+} Oxysalt Minerals.

Sixteen Cu^{2+} oxysalt minerals contain Cu^{2+} in five coordination (Table 7.1). There are two five-coordinate geometries shown: elongated square-pyramidal and compressed triangular-bipyramidal (Fig. 7.1). As shown by Eby and Hawthorne (1990), the angular characteristics of these two geometries are quite distinct, and in Cu^{2+} oxysalt minerals, there seem to be no transitional intermediates between the two coordination geometries. Eby and Hawthorne (1990) suggested this apparent lack of transitional geometries as possibly being due to (1) an energy barrier between the two geometries; or (2) lack of sufficient samples.

A number of inorganic compounds (in addition to minerals) contain Cu^{2+} in both square-pyramidal and triangular-bipyramidal coordination geometries (Hathaway, 1984). Effenberger (1988a) considered a number of inorganic compounds (including some minerals) containing five-coordinate Cu^{2+}, and showed that there is a continuous transition between the two ideal coordination polyhedra. Hathaway (1984) states that the cation distortion isomers of $[Cu^{2+}(bipy)_2Cl]x, nH_2O$ and $[Cu^{2+}(dien)(bipyam)]X_2$ series represent individual structures along the structural pathway of the regular triangular-bipyramidal to square-pyramidal stereochemistries. Thus, in light of these studies, it is not clear as to why minerals containing five-coordinate $Cu^{2+}\phi_5$ polyhedra do not also show the complete range of transitional geometries between square-pyramidal and triangular-

Table 7.1 Cu^{2+} oxysalt minerals with ($Cu^{2+}\phi_5$) polyhedra.

		Square-Pyramidal			
		Cu-ϕ_{eq}	Cu-ϕ_{eq}	Cu-ϕ_{ap}	Ref.
Clinoclase	Cu(2)	1.905 Å 1.907	1.956 Å 2.016	2.519 Å	1
	Cu(3)	1.916 1.976	2.000 2.033	2.275	
Litidionite	Cu	1.931 1.948	1.944 1.953	2.265	2
Callaghanite	Cu	1.926 1.934	1.959 1.957	2.483	3
Kinoite	Cu(1)	1.942 1.942	1.944 1.944	2.453	4
	Cu(2)	1.959 1.959	1.968 1.968	2.240	
Teinite	Cu	1.926 1.953	1.961 1.967	2.347	5
Ziesite	Cu	1.931 1.948	1.953 1.950	2.265	6
Blossite	Cu	1.880 1.943	1.955 1.972	2.542	7
Balyakinite	Cu	1.94 1.97	1.97 1.98	2.38	8
Chalcomenite	Cu	1.934 1.955	1.965 1.986	2.333	9
Fedotovite	Cu(1)	1.918 1.963	1.973 2.026	2.198	10
	Cu(2)	1.912 1.928	1.978 2.036	2.333	

Table 7.1 Continued.

		Triangular-Bipyramidal			
		Cu-ϕ_{ap}	Cu-ϕ_{eq}	Cu-ϕ_{eq}	Ref.
Stoiberite	Cu(3)	1.932 1.924	1.969 2.034	2.287	11
	Cu(5)	1.890 1.930	1.964 2.034	2.230	
Dolerophanite	Cu(2)	1.906 1.907	2.155 2.000	2.155	12
Fingerite	Cu(6)	1.929 1.907	1.971 2.147	2.102	13
Olivenite	Cu(1)	1.92 1.98	1.99 2.16	2.05	14
Libethenite	Cu(2)	1.927 1.939	2.041 2.053	2.053	15
Mcbirneyite	Cu(2)	1.914 1.923	2.014 2.124	2.097	16

References 1: Eby and Hawthorne (1990); 2: Pozas et al. (1975); 3: Brunton (1973); 4:Laughon (1971); 5: Effenberger (1977); 6: Hughes and Brown (1989); 7: Calvo and Faggiani (1975); 8: Lindquist (1972); 9: Pasero and Perchiazzi (1989); 10: Starova et al. (1991).11: Shannon and Calvo (1973); 12: Effenberger (1985); 13: Hughes and Hadidiacos (1985); 14: Toman (1977); 15: Cordsen (1978); 16: Shannon and Calvo (1972).

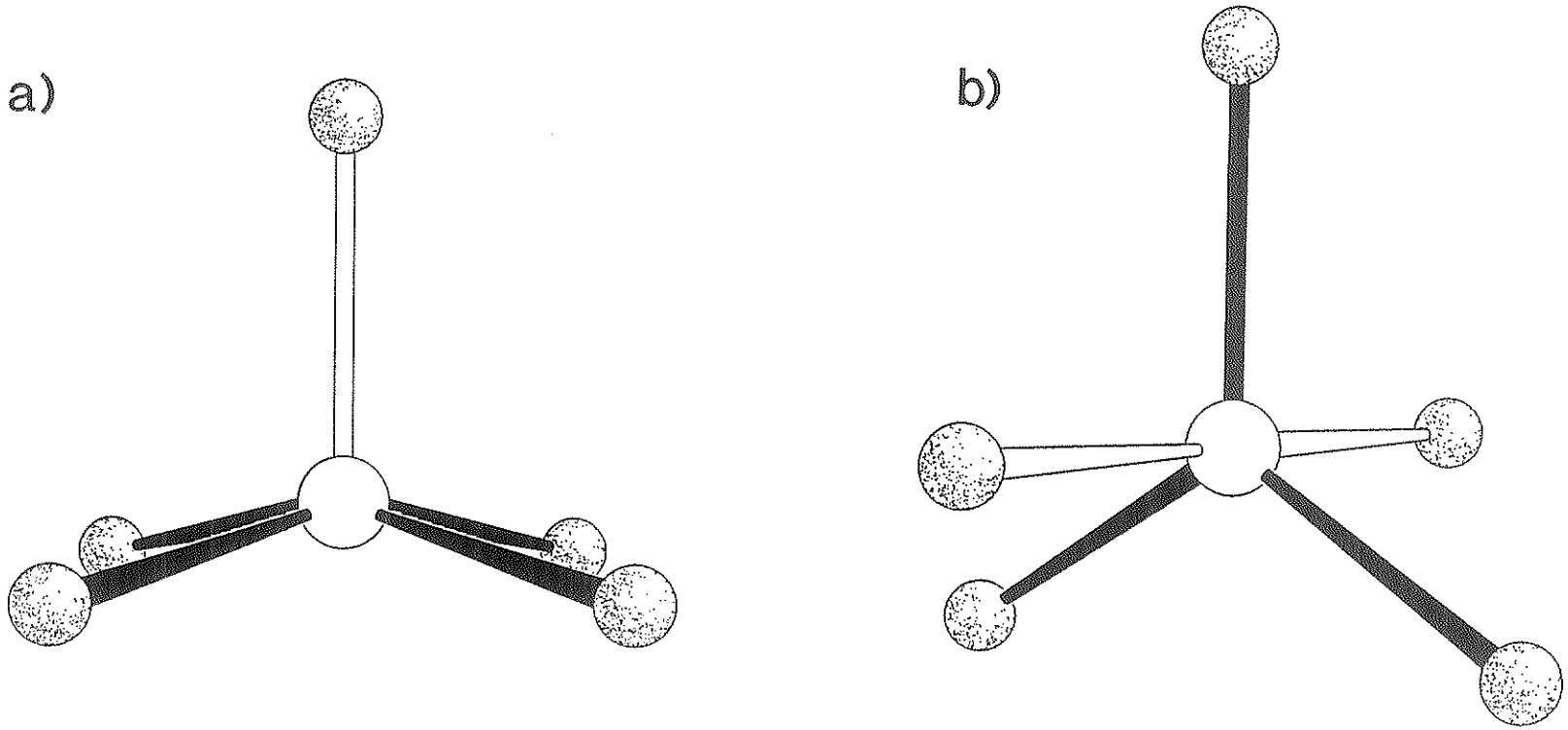

Figure 7.1. Five-coordinated copper polyhedra: a) square-pyramidal; b) triangular-bipyramidal. Apical bonds are drawn as two parallel lines and equatorial bonds are drawn as heavy lines.

bipyramidal. This apparent lack of transitional geometries in Cu^{2+} oxysalt minerals may only be a reflection of the small sample size. However, the $Cu^{2+}\phi_5$ square-pyramid coordination is favoured over the triangular-bipyramid coordination in minerals, suggesting that square-pyramidal geometry is more energetically favourable than triangular-bipyramidal geometry. *Ab initio* MO calculations should give an indication of the relative energies of the two coordination geometries.

7.2 Molecular-Orbital Calculations for $Cu^{2+}\phi_5$ Polyhedra.

Ab initio Hartree-Fock calculations were done for the $[Cu^{2+}(OH)_5]^{3-}$ and $[Cu^{2+}(H_2O)_5]^{2+}$ clusters (Fig. 7.2) using Gaussian 86 (Frisch et al., 1984). The calculations are UHF (spin unrestricted) calculations with no spin contamination observed in the final wavefuntions. Calculations using STO-3G* and 3-21G* basis-sets (described in Chapter 3) were done on the $[Cu^{2+}(H_2O)_5]^{2+}$ cluster in both square-pyramidal and triangular-bipyramidal geometries. However, convergence problems arose in the 3-21G* calculations for the triangular-bipyramidal geometry, and those results are not reported. Calculations using the STO-3G* basis-set were done for the $[Cu^{2+}(OH)_5]^{3-}$ cluster in both triangular-bipyramidal and square-pyramidal geometries.

During geometry optimization of the square-pyramid, each of the Cu-ϕ_{eq} bond-lengths were constrained to be equivalent, as were the four ϕ_{ap}-Cu-ϕ_{eq} bond-angles. Triangular-bipyramidal geometries were constrained such that the Cu-ϕ_{eq} bond-lengths were equivalent; the same constraint was placed on the Cu-ϕ_{ap} bond-lengths, and the ϕ-Cu-ϕ bond-angles were held fixed at 90° and 120°, respectively (Figure 7.1). The Cu-O-H bond-angle

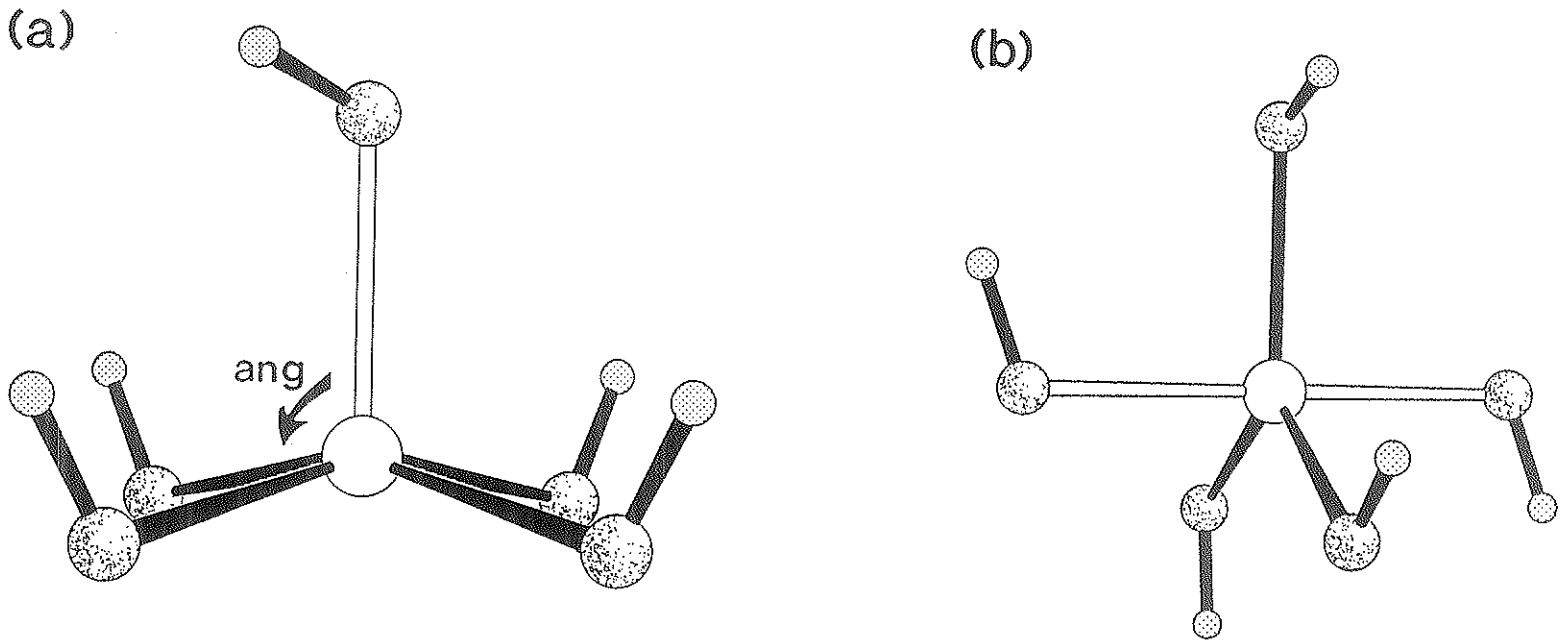

Figure 7.2. The $[Cu^{2+}(OH)_5]^{3-}$ clusters used to model the (a) square-pyramidal and (b) triangular-bipyramidal $Cu^{2+}\phi_5$ geometries. Apical bonds are drawn as two parallel lines and equatorial bonds are drawn as heavy lines.

was fixed at 110° and the O-H distances at 0.98 Å for the $[Cu^{2+}(OH)_5]^{3-}$ cluster; the H-O-H bond-angle was fixed at 104.5° and the H-O bond-length at 0.957 Å for the $[Cu^{2+}(H_2O)_5]^{2+}$ cluster. In each case, geometries were optimized until the maximum forces on any atom did not exceed 0.00045 Hartrees/Bohr and the maximum displacement of any atom in the previous cycle did not exceed 0.0009 Å. The optimized geometries and cluster energies are given in Table 7.2.

The optimized geometries obtained for each $Cu^{2+}\phi_5$ cluster (Table 7.2) are in reasonable agreement with typical $Cu^{2+}\phi_5$ geometries in Cu^{2+} oxysalt minerals (Table 7.1). All optimized triangular-bipyramidal clusters indicate that a triangular-bipyramid compressed down the unique axis is preferred. All calculations also indicate that the triangular-bipyramidal $Cu^{2+}\phi_5$ coordination is energetically favourable over square-pyramidal geometry. These results contrast with the observation that square-pyramids are the more common five-coordinate Cu^{2+} geometries in Cu^{2+} oxysalt minerals (Table 7.1). As a further check of these results, the calculations were repeated for the $[Cu^{2+}(H_2O)_5]^{2+}$ clusters in both the square-pyramidal and triangular-bipyramidal geometries using the more robust double-zeta basis-set given by Gianolio et al. (1978); these calculations (Table 7.2) verified the previous results.

7.3 Possible Explanations of Why Square-Pyramids Seem to be Favoured Over Triangular-Bipyramids.

Kepert (1982) reports that electron-pair repulsion calculations show that the most energetically favourable five-coordinate geometry is an elongated triangular-bipyramid, which is slightly preferred to a compressed

Table 7.2 Optimized geometries* and Hartree-Fock energies for ($Cu^{2+}\phi_5$) clusters.

Square-pyramidal $[Cu^{2+}(H_2O)_5]^{2+}$			
Basis Set	STO-3G*	3-21G*	Double-Zeta
R_{ap}	1.987	2.064	2.099
R_{eq}	1.995	2.066	2.091
ang	101.23°	101.47°	98.91°
E(SCF, Hartrees)	-1996.9358	-2008.5622	-2012.3087

Triangular-Bipyramidal $[Cu^{2+}(H_2O)_5]^{2+}$			
Basis Set	STO-3G*	3-21G*	Double-Zeta
R_{ap}	1.931		2.009
R_{eq}	1.976		2.100
E(SCF, Hartrees)	-1996.9358		-2012.3319

$[Cu^{2+}(OH)_5]^{3-}$		
	Square-Pyramidal	Triangular-Bipyramidal
Basis Set	STO-3G*	STO-3G*
R_{ap}	2.112	2.017
R_{eq}	2.040	2.079
ang	101.14°	
E(SCF Hartrees)	-1992.9160	-1992.9203

* Bond-lengths are in Å. ** 1 Hartree = 2625.4997 kJ/mole

square-pyramid. However, Cu^{2+} oxysalt minerals contain either compressed triangular-bipyramids or, more commonly, elongated square-pyramids (Table 5.1). The Hartree-Fock calculations for $Cu^{2+}\phi_5$ clusters reported in the previous section indicate that the compressed triangular-bipyramid is energetically favourable over the elongated triangular-bipyramid, as is the elongated square-pyramid over the compressed square-pyramid. The Hartree-Fock calculations also indicated that the compressed triangular-bipyramid is more energetically favourable than the elongated square-pyramid.

The ground states of Cu^{2+} in triangular-bipyramidal and square-pyramidal coordinations do not contain energetically degenerate electronic states, and there is no Jahn-Teller effect. However, Reimin and Atansov (1989) argue that the vibronic interaction between the A_1' ground state and the excited E' state leads to a stabilization of the elongated square-pyramid, as the excited state is Jahn-Teller active. Therefore, a quasi-Jahn-Teller effect in Cu^{2+} square-pyramids may lead to a net stabilization of elongated square-pyramidal geometries. The Hartree-Fock calculations reported in the previous section were specifically for the ground states of $Cu^{2+}\phi_5$ geometries, and this effect was not included in the calculations.

Chapter 8

Coordination Geometry Structural Pathways in Cu^{2+} Oxysalt Minerals

8.1 Introduction

The $Cu^{2+}\phi_n$ (n = 4, 5 or 6) coordination geometries observed in a number of Cu^{2+} oxysalt minerals are significantly distorted from the principal ideal types (i.e. (4+2)-distorted octahedral, square-pyramidal, triangular-bipyramidal and square-planar). These intermediate geometries may be considered as intermediates between the different regular coordination geometries and may define structural pathways between the different (ideal) coordination arrangements. The concept of structural pathways in Cu^{2+}-bearing inorganic compounds has been discussed previously (Hathaway, 1984), but has not been applied specifically to minerals.

8.2 Structural Pathways in Cu^{2+} Oxysalt Minerals

Structural data for about 100 refined Cu^{2+} oxysalt minerals have been examined to determine which specific structural pathways are represented. The relative energetics and minimum-energy geometries of the possible structural pathways were examined using MO calculations for $Cu^{2+}\phi_n$ cluster geometries designed to model these pathways. The different possible pathways are shown in Figure 8.1

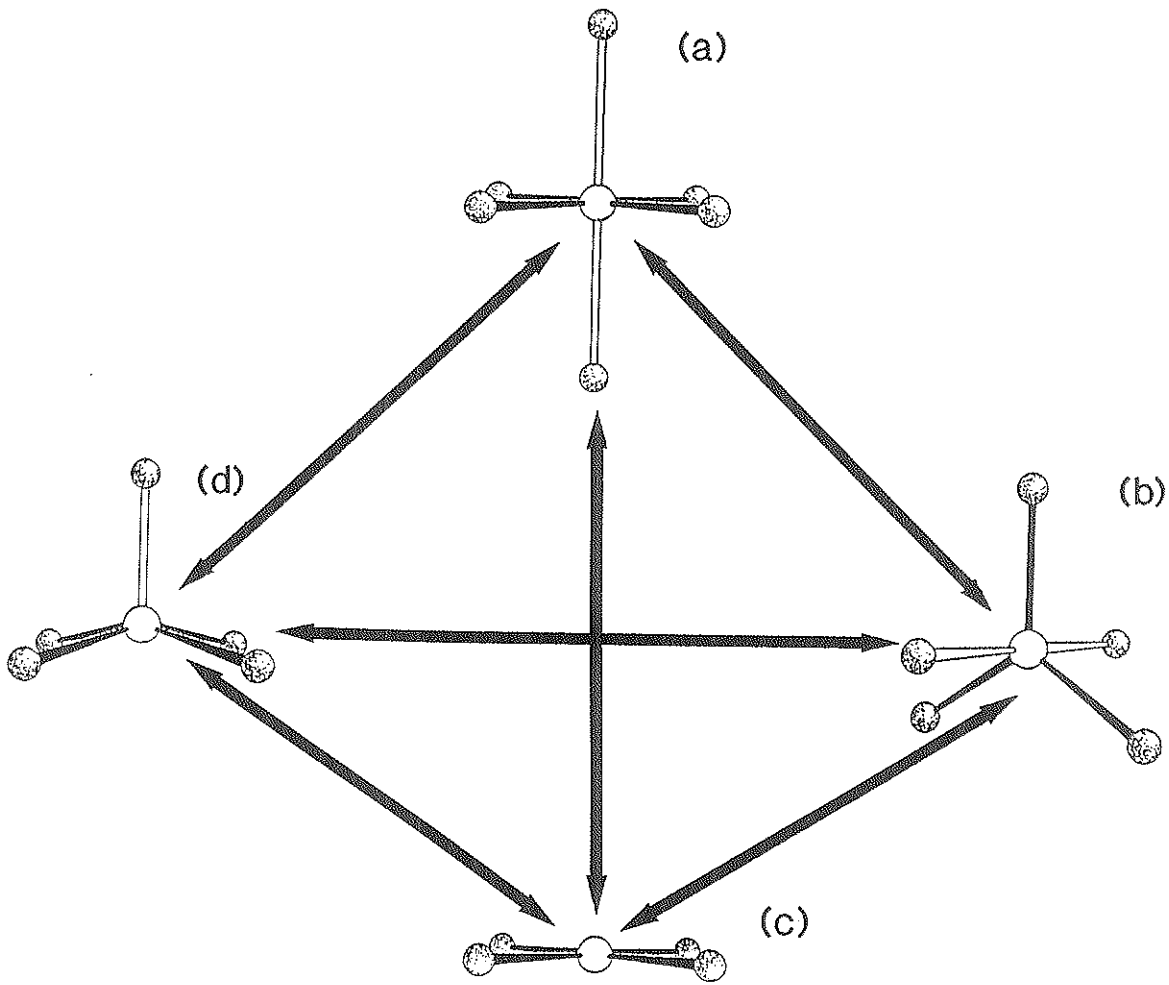

Figure 8.1. Possible structural pathways in Cu^{2+} oxysalt minerals. (a) (4+2)-distorted octahedral, (b) triangular-bipyramidal, (c) square-planar, (d) square-pyramidal.

8.2.1 (4+2)-Octahedral <---> Square-Pyramidal

The most common Cu^{2+} coordination geometry observed is (4+2)-distorted octahedral (Chapter 2). Square-pyramidal geometry may be derived from the (4+2)-distorted octahedral geometry by removing one of the apical ligands and moving the Cu^{2+} cation to above the equatorial plane in the direction of the remaining apical ligand (Fig. 8.2). This pathway intrinsically contains (4+1+1)-distorted octahedral geometries, such that there are four short Cu-ϕ_{eq} bonds, one long Cu-ϕ_{ap} bond and one very long Cu-ϕ apical bond (Fig. 8.2).

The division between (4+2)-distorted and (4+1+1)-distorted octahedral geometries is taken as the (arbitrary but reasonable) point at which one Cu-ϕ_{ap} bond is 12.5% longer than the other. With this criterion, there are a number of (4+1+1)-distorted octahedra in Cu^{2+} oxysalt minerals (Table 8.1). *There is a continuous series of $Cu^{2+}\phi_6$ geometries between (4+2)-octahedral and square-pyramidal*, and the (4+2)-octahedral to square-pyramidal structural pathway is well represented in Cu^{2+} oxysalt minerals.

8.2.2 (4+2)-Octahedral <---> Triangular-Bipyramidal

Ideally, the $Cu^{2+}\phi_5$ triangular-bipyramid may be derived from a (4+2)-distorted $Cu^{2+}\phi_6$ octahedron by removing one equatorial ligand and allowing the three remaining ligands to move to the corners of an equilateral triangle centered on the Cu^{2+} ion (Fig. 8.3). This is a potential structural pathway which includes (3+1+2)-distorted, (3+3)-distorted and (3+2+1)-distorted octahedral geometries. There are no examples of these geometries in Cu^{2+} oxysalt minerals, and this structural pathway is not represented. The equatorial ligands are more tightly bonded to the Cu^{2+} ion than the apical

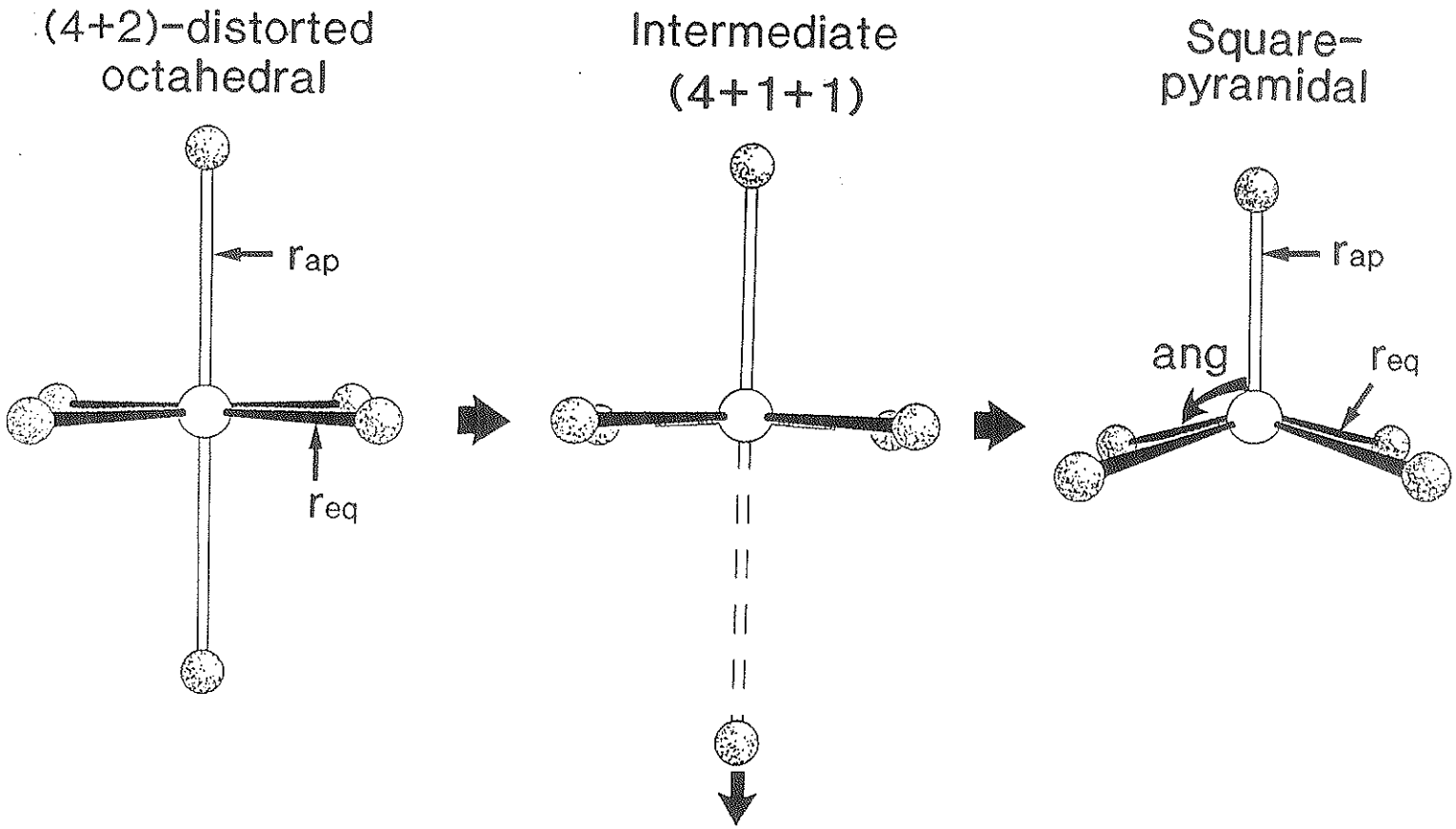

Figure 8.2. The (4+2)-distorted octahedral to square-pyramidal transition. The copper atoms are open circles and the oxygen atoms are shaded with a random-dot pattern.

Table 8.1 Cu-ϕ bond-lengths (Å) in Cu^{2+} oxysalt minerals containing (4+1+1)-distorted $Cu^{2+}\phi_6$ octahedra.

		$Cu\text{-}O_{eq}$		$Cu^{2+}\text{-}O_{ap}$		Ref.
Lammerite	Cu(2)	1.941 (Å)	1.947	2.282	2.782	1
		1.972	2.028			
Euchroite	Cu(2)	1.922	1.956	2.394	2.794	2
		1.983	2.004			
Cornetite	Cu(1)	1.923	1.940	2.470	3.087	3
		1.984	1.996			
	Cu(3)	1.925	1.930	2.280	2.821	
		1.988	2.023			
Plancheite	Cu(2)	1.934	1.975	2.310	2.617	4
		2.017	2.054			
Likasite	Cu(2)	1.96	1.96	2.42	2.83	5
		1.98	1.98			
Agardite	Cu	1.908	1.924	2.321	3.14	6
		1.991	2.011			
Kipushite	Cu(1)	1.97	1.97	2.24	2.94	7
		1.98	2.03			
	Cu(2)	1.99	1.99	2.15	2.73	
		2.03	2.05			
Clinoclase	Cu(1)	1.895	1.938	2.332	2.871	8
		1.992	2.074			
	Cu(2)	1.905	1.907	2.519	3.321	
		1.956	2.016			
	Cu(3)	1.916	1.976	2.272	2.995	
		2.000	2.033			
Wroewolfeite	Cu(3)	1.92	1.92	2.31	2.72	9
		1.98	2.01			
Posnjakite	Cu(2)	1.95	1.97	2.28	2.95	10
		1.99	2.01			
	Cu(4)	1.91	1.96	2.31	2.75	
		1.97	2.01			
Pseudo-malachite	Cu(2)	1.939	1.958	2.395	2.755	11
		1.974	1.985			

Table 8.1 Continued

Spertiniite	Cu	1.948 1.972	1.948 1.972	2.356	2.915	12
Azurite	Cu(2)	1.938 1.965	1.943 1.990	2.358	2.761	13
Papagoite	Cu	1.936 1.964	1.936 1.964	2.402	3.016	14

References 1: Hawthorne (1986); 2: Eby and Hawthorne (1989a); 3: Eby and Hawthorne (1989b); 4: Evans and Mrose (1977); 5: Effenberger (1986); 6: Aruga and Nakai (1985); 7: Piret et al. (1985); 8: Eby and Hawthorne (1990); 9: Hawthorne and Groat (1985); 10: Mellini and Merlino (1979); 11: Shoemaker et al. (1977); 12: Oswald et al. (1990); 13: Figan and Schuster (1972); 14: Groat and Hawthorne (1987)

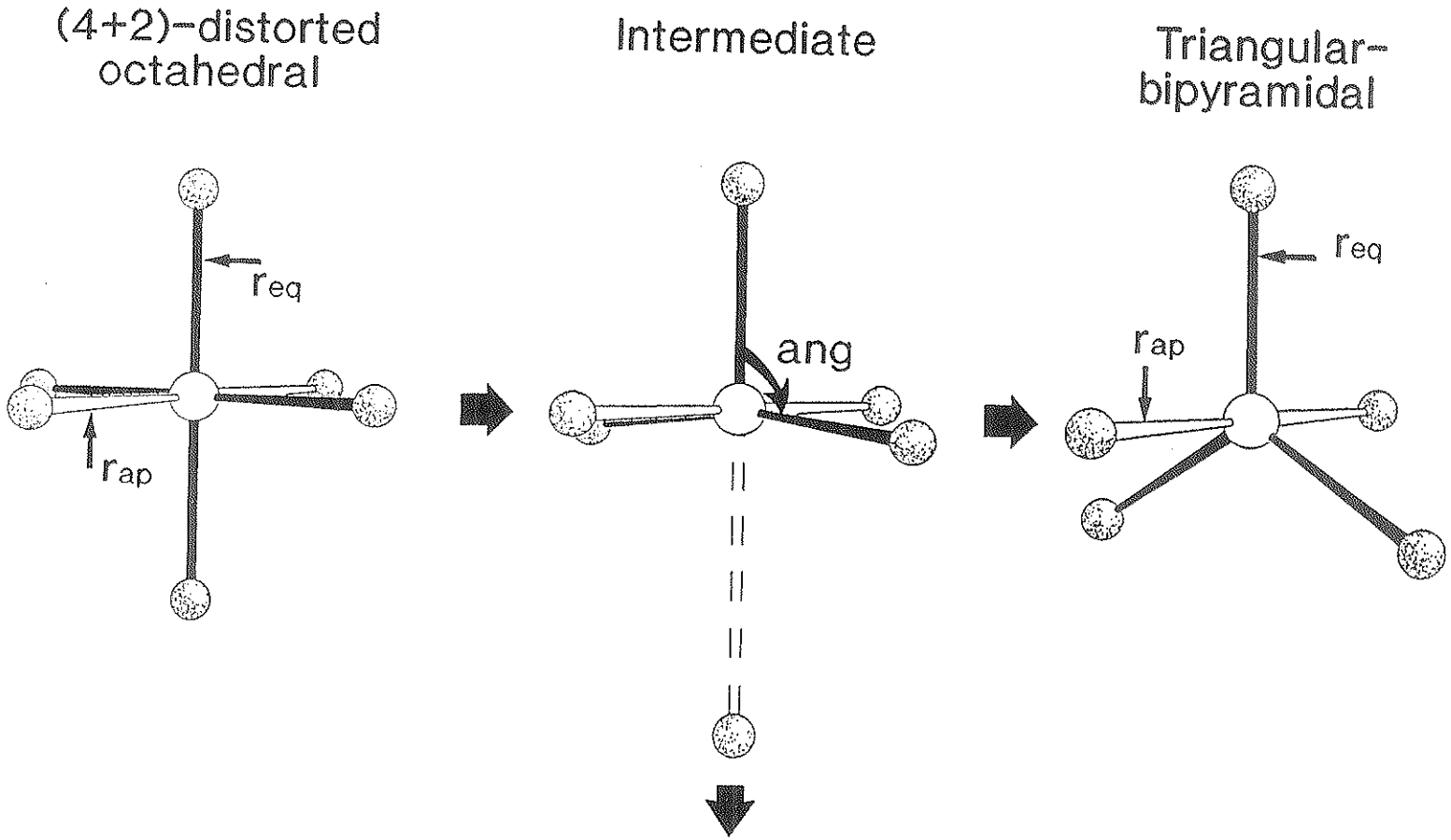

Figure 8.3. The (4+2)-distorted octahedral to triangular-bipyramidal transition. The copper atoms are open circles and the oxygen atoms are shaded with a random-dot pattern.

ligands, and the removal of an equatorial ligand may be energetically unfavourable.

8.2.3 (4+2)-Octahedral <---> Square-Planar

Square-planar geometry is relatively rare in Cu^{2+} oxysalt minerals, but there are a few examples (Eby and Hawthorne, 1993). Square-planar geometry may be derived from (4+2)-distorted octahedral geometry by removing both of the apical ligands (Fig. 8.4). The structural pathway between (4+2)-distorted octahedral and square-planar geometries includes (4+2)-distorted octahedral geometries with two Cu-ϕ_{ap} bonds that are longer than the normal Cu-ϕ_{ap} bond-length observed in (4+2)-distorted octahedra. A number of Cu^{2+} oxysalt minerals contain such octahedra, and *are members of a structural pathway between (4+2)-distorted octahedral and square-planar geometries.* Examples with Cu-ϕ_{ap} > 2.70 Å are given in Table 8.2.

8.2.4 Square-Pyramidal <---> Square-Planar

Removal of the apical ligand from the elongated square-pyramid allows the remaining atoms to rearrange into a square-planar geometry (Fig. 8.5). Both of these geometries are unusual in Cu^{2+} oxysalt minerals. However, $Cu^{2+}\phi_5$ square-pyramids show a considerable range of Cu-ϕ_{ap} bond-length (Chapter 7, 2.24 to 2.52 Å) (all of which are longer than the geometries predicted by the Hartree-Fock calculations of Chapter 7), indicating that *the structural pathway from square-pyramidal to square-planar is represented in Cu^{2+} oxysalt minerals.*

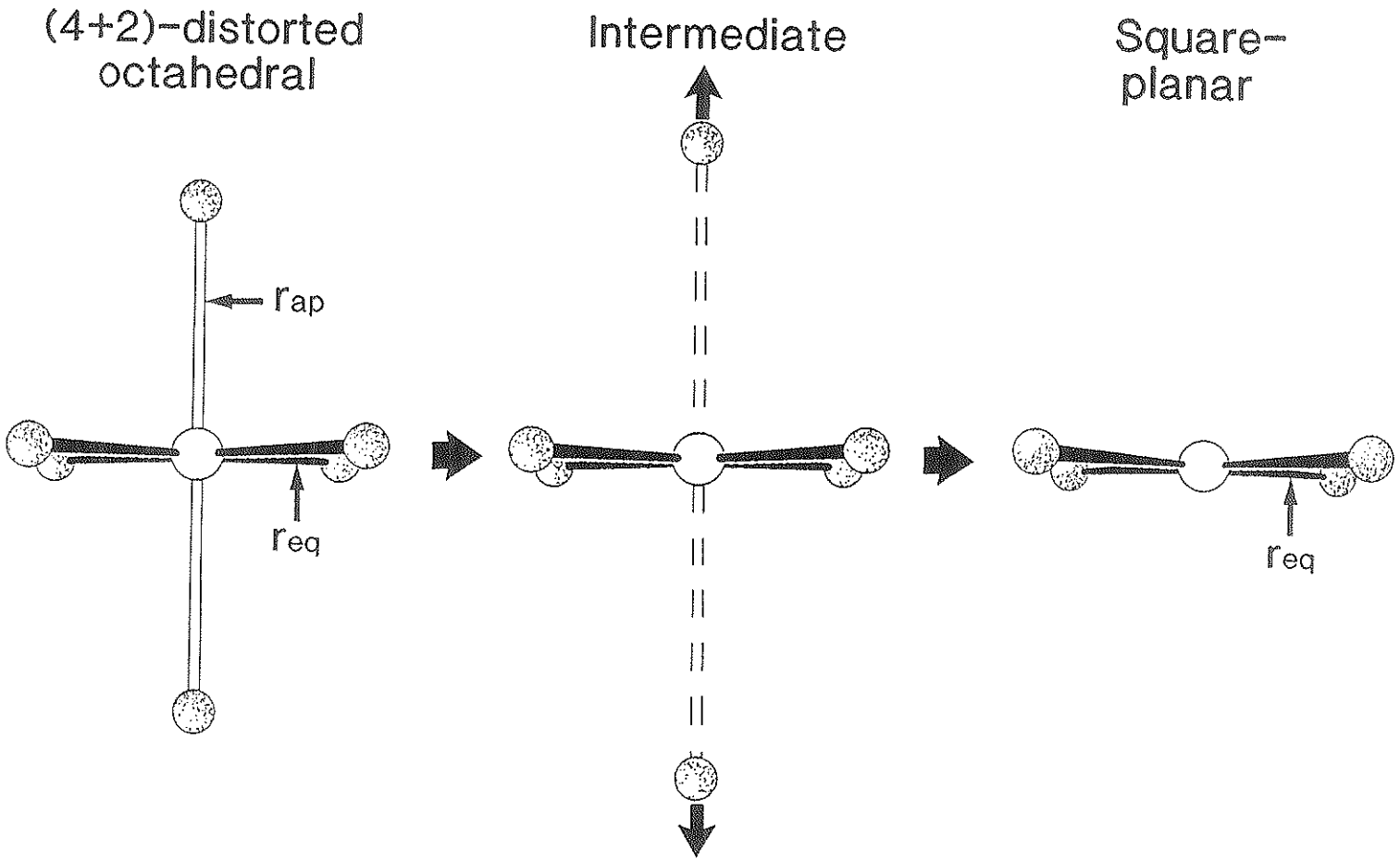

Figure 8.4. The (4+2)-distorted octahedral to square-planar transition. The copper atoms are open circles and the oxygen atoms are shaded with a random-dot pattern.

Table 8.2 Cu-ϕ bond-lengths (Å) in examples of Cu-ϕ coordination geometries intermediate between (4+2)-distorted octahedral and square-planar.

		r_{eq}		r_{ap}	Ref.
Lammerite	Cu(1)	1.933	1.933	2.923	1
		1.974	1.974	2.923	
Likasite	Cu(3)	1.96	1.96	2.83	2
		1.93	1.93	2.83	
Stringhamite	Cu(1)	1.918	1.972	3.383	3
		1.918	1.972	3.385	
	Cu(2)	1.934	1.934	3.053	
		1.960	1.960	3.053	
Azurite	Cu(1)	1.930	1.930	2.983	4
		1.946	1.946	3.323	
Henmilite	Cu	1.939	1.939	3.067	5
		1.949	1.949	3.067	
Buttenbachite	Cu(1)	1.967	1.967	2.732	6
		1.967	1.967	2.732	
Stranskiite	Cu	1.907	1.907	3.134	7
		2.005	2.005	3.134	

References 1: Hawthorne (1986); 2: Effenberger (1986); 3: Hawthorne (1985b); 4: Figan and Schuster (1972); 5: Nakai et al. (1986); 6: Fafani et al. (1973); 7: Keller et al. (1979).

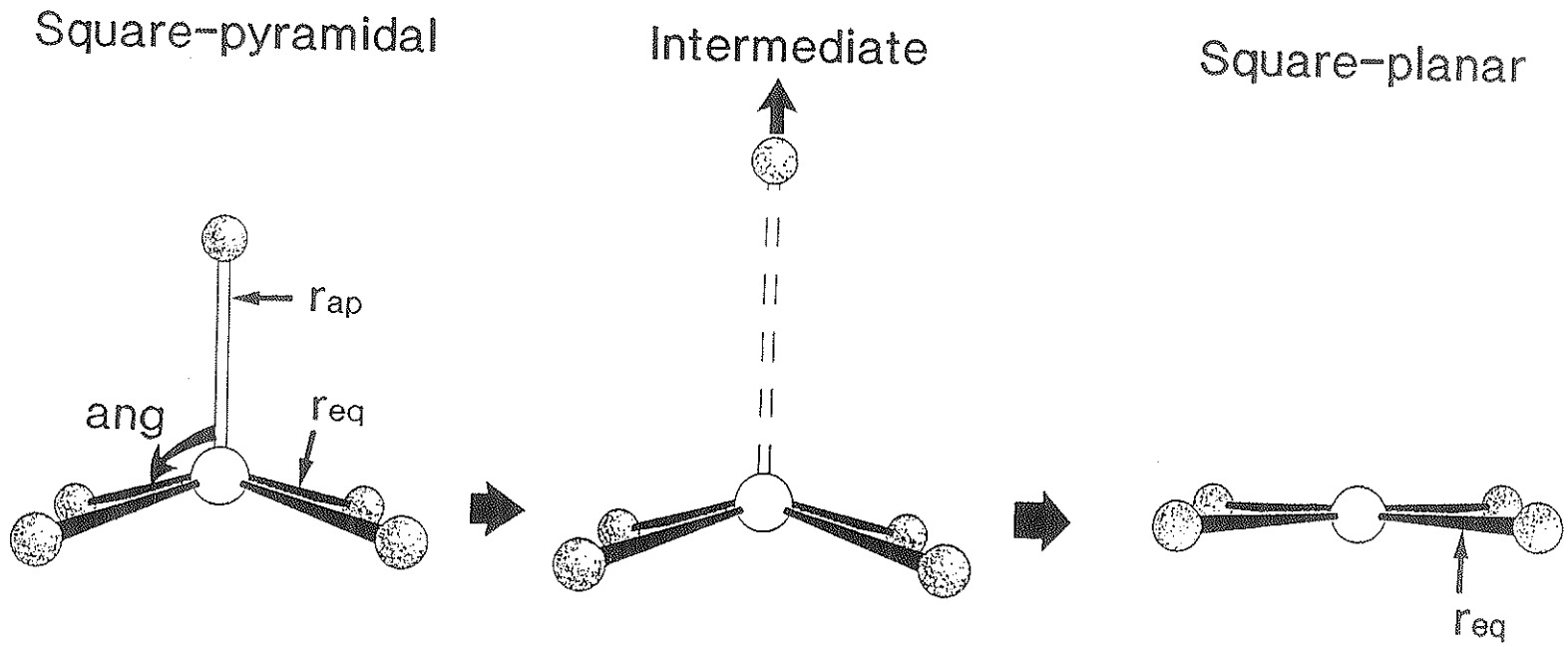

Figure 8.5. The square-pyramidal to square-planar transition. The copper atoms are open circles and the oxygen atoms are shaded with a random-dot pattern.

8.2.5 Square-Pyramidal <---> Triangular-Bipyramidal

The elongated square-pyramid may be derived from the compressed triangular-bipyramid by ϕ-Cu-ϕ adjustments and small changes in Cu-ϕ bond-lengths (Fig. 8.6). Due to the simple structural pathway between these two coordination geometries, examples of intermediates might be expected in minerals. However, Eby and Hawthorne (1990) did not find the complete range of transitional intermediates in Cu^{2+} oxysalt minerals, although they do occur in synthetic compounds (Effenberger, 1988a).

8.2.6 Triangular-Bipyramidal <---> Square-Planar

Removal of an equatorial ligand from the triangular-bipyramid allows the remaining $Cu^{2+}\phi_4$ group to rearrange into square-planar geometry (Fig. 8.7). Examination of $Cu^{2+}\phi_5$ triangular-bipyramids in Cu^{2+} oxysalt minerals (Table 7.1) shows that there is a considerable range of Cu-ϕ_{eq} bond-lengths, and there are examples (i.e., stoiberite) which have one Cu-ϕ_{eq} bond considerably longer than the other two bonds. These triangular-bipyramids *may* belong to a triangular-bipyramidal to square-planar structural pathway, but there are too few examples to be certain.

8.3 *Ab Initio* Hartree-Fock Molecular-Orbital Examination of Structural Pathways Between $Cu^{2+}\phi_n$ Coordination Geometries.

Molecular-orbital calculations for $Cu^{2+}\phi_n$ clusters with geometries that map the structural pathways between various $Cu^{2+}\phi_n$ coordination geometries will provide both optimized geometries and the energetics of the structural pathways.

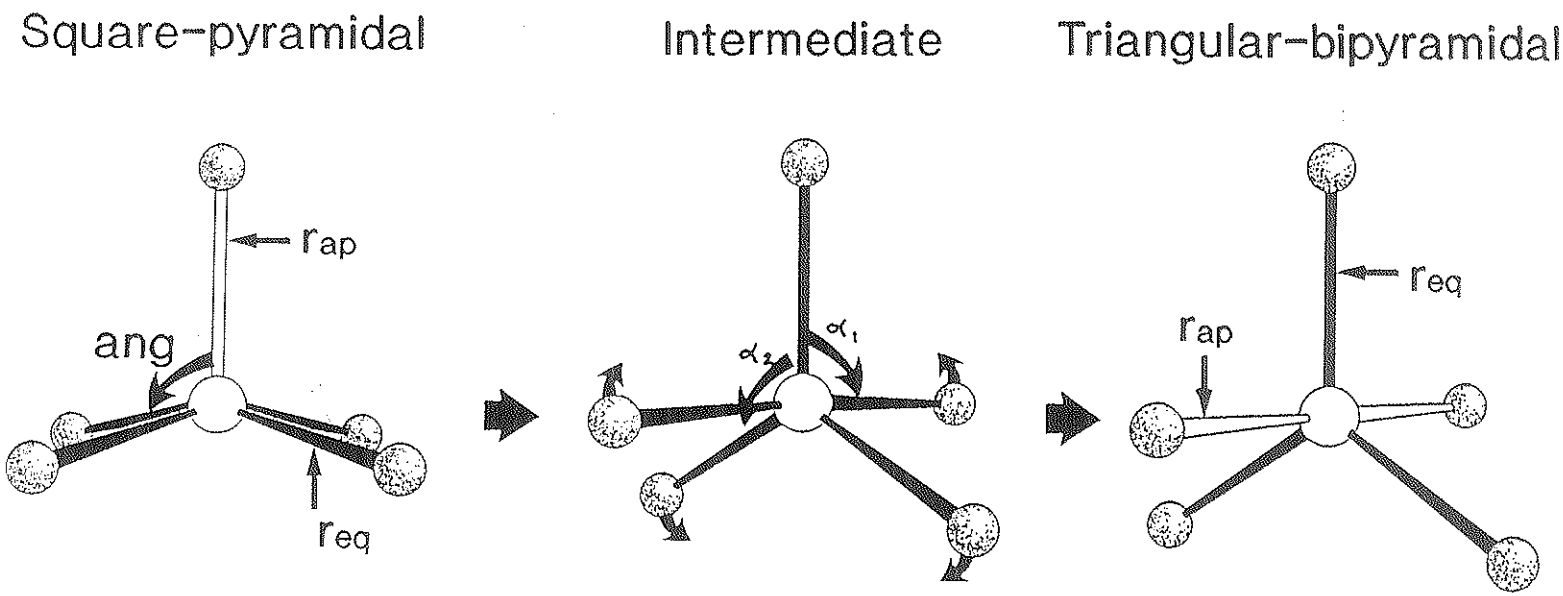

Figure 8.6. The square-pyramidal to triangular-bipyramidal transition. The copper atoms are open circles and the oxygen atoms are shaded with a random-dot pattern.

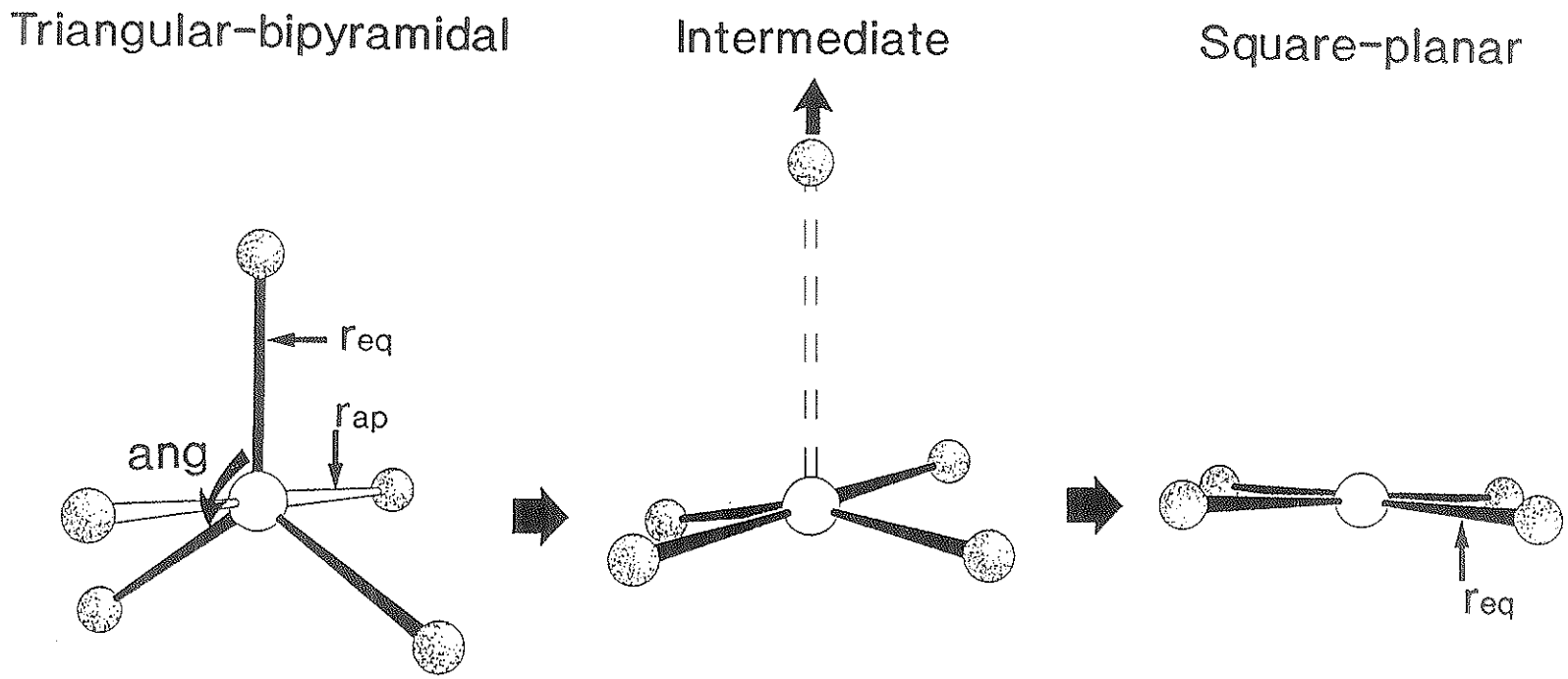

Figure 8.7. The triangular-bipyramidal to square-planar transition. The copper atoms are open circles and the oxygen atoms are shaded with a random-dot pattern.

The following calculations were done with Gaussian 86 (Frisch et al., 1984) and Gaussian 92 (Frisch et al., 1992). UHF calculations were done using the STO-3G* basis-set, and no spin contamination was observed in the final wavefunctions. Where cluster geometries were optimized, convergence criteria were the same as for the $Cu^{2+}\phi_5$ calculations (see Chapter 7); all Cu-O-H bond-angles were fixed at 110° and H-O bond-lengths at 0.98 Å.

Hartree-Fock calculations sometimes tend to give poor descriptions of systems when bond breaking occurs (Chapter 3). The use of UHF (spin unrestricted) calculations result in better performance for such systems than do closed-shell calculations. However, the lack of a proper treatment of electron correlation, particularly of the bonding electrons, may result in poorly estimated energies. In order to test the validity of the Hartree-Fock calculations reported here for $Cu^{2+}\phi_n$ structural pathways, partial configuration interaction (CID) and Møller-Plesset (MP2 and MP3) calculations (Chapter 3) were done for a selection of points along some of the structural pathways. Although the absolute values of the energies are different, the electron-correlation calculations give similar trends (Tables 8.5 and 8.6), and do not alter the conclusions drawn from the UHF calculations.

8.3.1 (4+2)-Octahedral <---> Square-Pyramidal

The starting point for examination of this pathway was the $[Cu^{2+}(OH)_6]^{4-}$ cluster [(4+2)-distorted octahedron] with Cu-ϕ bond-lengths obtained from Hartree-Fock calculations with the STO-3G* basis-set (Chapter 4). The structural pathway was modelled by increasing one of the Cu-ϕ_{ap} bond-lengths in a stepwise fashion, such that the apical ligand is

moved away from the copper ion in a direction perpendicular to the equatorial plane (Fig. 8.2). For each step, the Cu-ϕ_{ap} bond-length was fixed and the rest of the cluster geometry was reoptimized using Hartree-Fock calculations. Included in the reoptimization were the four Cu-ϕ_{eq} bond-lengths (constrained to be equivalent), the remaining Cu-ϕ_{ap} bond-length, and the four ϕ_{ap}-Cu-ϕ_{eq} angles (constrained to be equivalent) (labelled r_{eq}, r_{ap} and ang in Fig. 8.2). The optimized geometries and cluster energies are given in Table 8.3 and Figures 8.8 and 8.9.

These calculations show that as the apical oxygen moves away from its equilibrium position at 2.427 Å from the copper cation, the remaining atoms rapidly rearrange towards square-pyramidal geometry (Fig. 8.8). Most of the rearrangement occurs before the apical oxygen is 3.0 Å from the copper cation, and it is virtually complete before the oxygen is 3.5 Å from the copper cation. *There is no energy barrier along this pathway* (Fig. 8.9). These results support the proposed structural pathway between (4+2)-distorted octahedral and square-pyramidal geometries in Cu^{2+} oxysalt minerals, as suggested by the presence of (4+1+1)-distorted octahedral geometries.

8.3.2 (4+2)-Octahedral <---> Triangular-Bipyramidal

The starting point for examination of the (4+2)-distorted octahedral to triangular-bipyramidal structural pathway was the $[Cu^{2+}(OH)_6]^{4-}$ cluster with optimized (4+2)-distorted octahedral Cu-ϕ bond-lengths from Hartree-Fock calculations with the STO-3G* basis-set (Chapter 4). The structural pathway was modelled by extending one Cu-ϕ_{eq} bond in a stepwise fashion while reoptimizing the remaining cluster geometry using Hartree-Fock

Table 8.3 Reoptimized $[Cu^{2+}(OH)_6]^{4-}$ cluster geometries along the structural pathway from (4+2)-distorted octahedral to square-pyramidal.

		Optimized*			
Step	r_{ap}(fixed)	r_{eq} (Å)	r_{ap} (Å)	ang (°)	Energy (Hartrees**)
(4+2)-Octahedron	2.427 Å	2.081	2.427	90°+	-2066.5750
1	2.50	2.076	2.401	90.41	-2066.5750
2	2.60	2.070	2.373	90.93	-2066.5749
3	2.70	2.063	2.350	91.42	-2066.5752
4	2.85	2.055	2.322	92.12	-2066.5769
5	3.00	2.047	2.298	92.76	-2066.5804
6	3.20	2.040	2.274	93.49	-2066.5880
7	3.50	2.033	2.248	94.37	-2066.6042
8	5.00	2.026	2.187	96.87	-2066.6935
9	7.00	2.027	2.155	98.52	-2066.7693
10	8.00	2.028	2.146	98.99	-2066.7947
Square Pyramid		2.040	2.112	101.15	

* Refer to Figure 8.2 for an explanation of optimized parameters.
** 1 Hartree = 2625.4997 kJ/mole
\+ Held fixed at 90° for the (4+2)-octahedron optimization

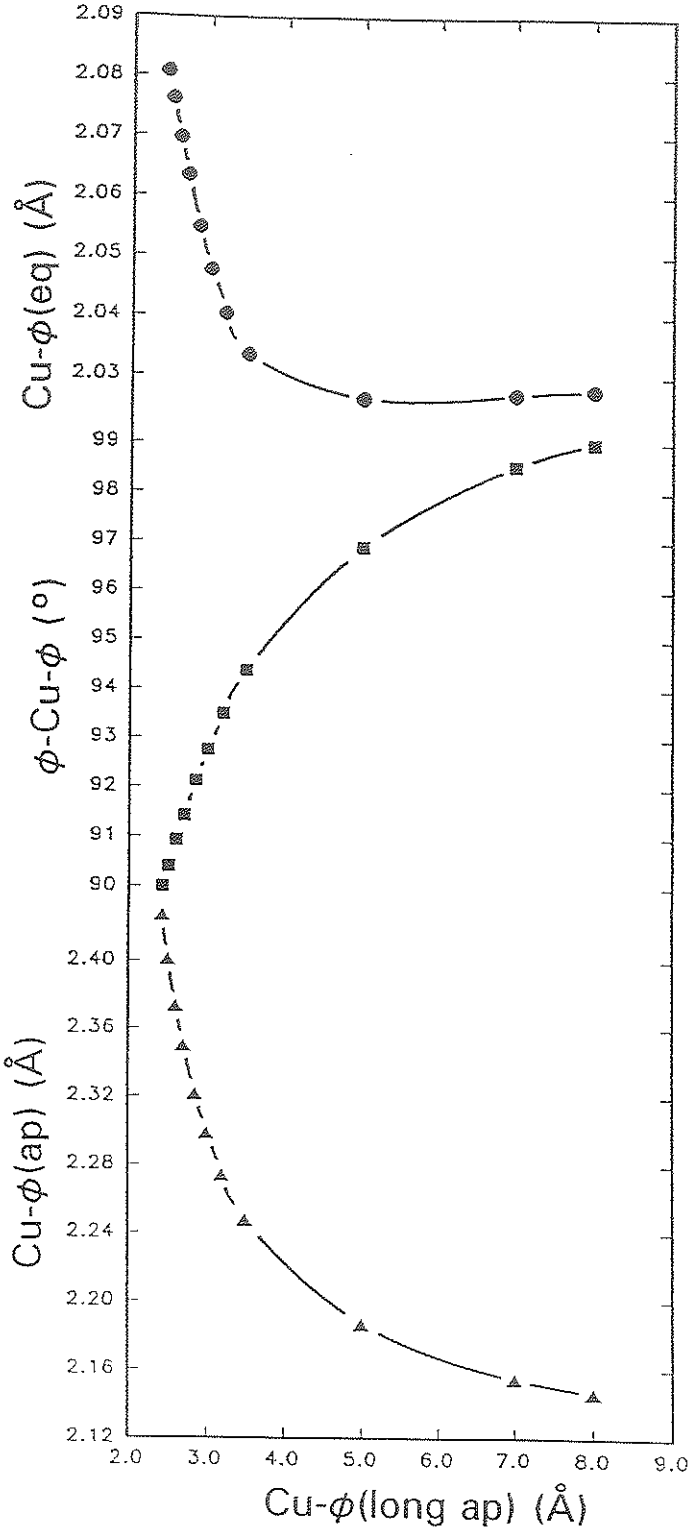

Figure 8.8. Optimized geometries along the structural pathway from (4+2)-distorted octahedral to square-pyramidal. The parameters are defined in Figure 8.2.

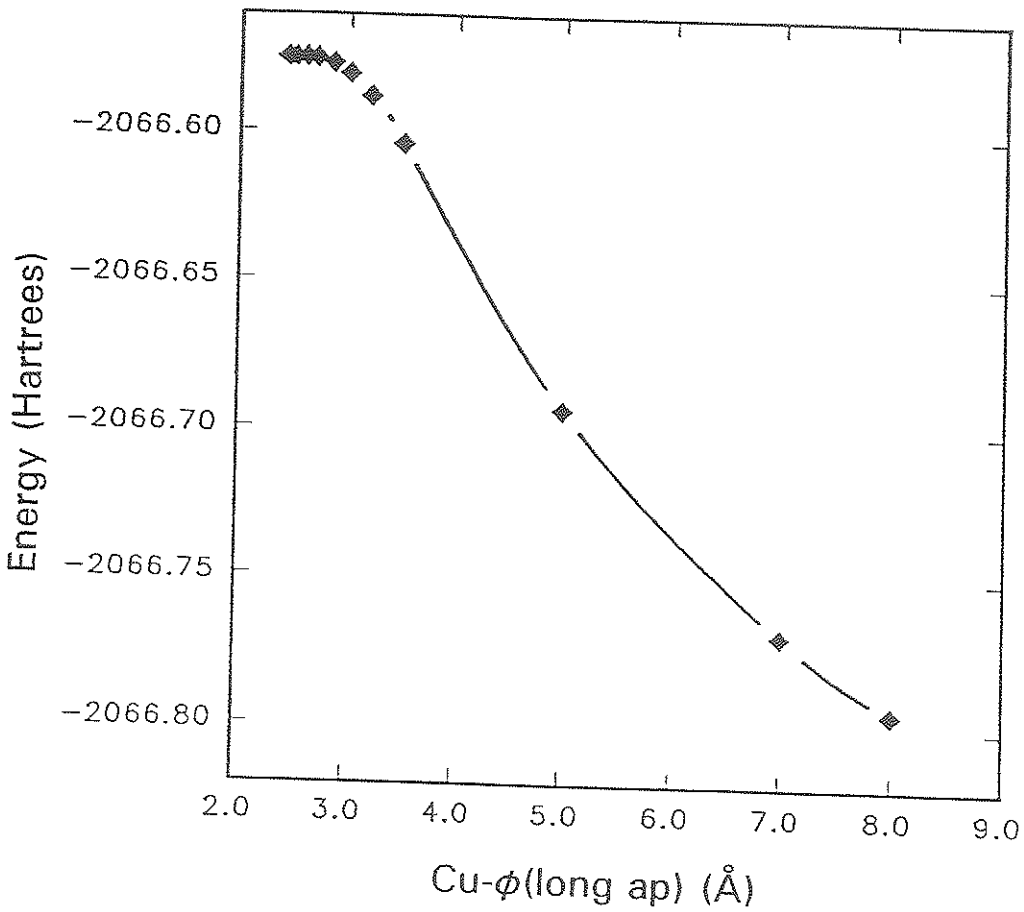

Figure 8.9. Cluster energies along the structural pathway from (4+2)-distorted octahedral to square-pyramidal. 1 Hartree = 2625.4997 kJ/mole.

theory. Included in the reoptimization were the remaining Cu-ϕ_{eq} bond-lengths (constrained to be equivalent), the Cu-ϕ_{ap} bond-lengths (constrained to be equivalent), and the ϕ_{eq}-Cu-ϕ_{eq} angles (labelled r_{eq}, r_{ap} and ang in Fig. 8.3). The optimized geometries and cluster energies are given in Table 8.4 and Figures 8.10 and 8.11.

As the Cu-ϕ_{eq} distance increases, the remaining cluster geometry distorts towards a triangular-bipyramidal arrangement (Fig. 8.10). However, this pathway has a steep energy barrier (Fig. 8.11), which explains why the complete range of transitional geometries are not observed in Cu^{2+} oxysalt minerals.

8.3.3 (4+2)-Octahedral <---> Square-Planar

The starting point for examination of the structural pathway between (4+2)-distorted octahedral and square-planar geometries was the $[Cu^{2+}(OH)_6]^{4-}$ cluster with optimized (4+2)-distorted octahedral bond-lengths from Hartree-Fock calculations with the STO-3G* basis-set (Chapter 4). The pathway was modelled by increasing both Cu-ϕ_{ap} bond-lengths in a stepwise fashion and reoptimizing the Cu-ϕ_{eq} bond-lengths for each step (Fig. 8.4). The optimized geometries and cluster energies are given in Table 8.5 and in Figure 8.12.

The remaining atoms rearrange towards a square-planar arrangement as the apical oxygens move away from the copper ion (Fig. 8.12). The majority of the transformation to the (contracted) square-planar arrangement occurs before Cu-ϕ_{ap} = 3.0 Å. The calculations indicate that there is a shallow energy barrier along the (4+2)-distorted octahedral to square-planar structural pathway (Fig. 8.12) which reaches a maximum at

Table 8.4 Reoptimized $[Cu^{2+}(OH)_6]^{4-}$ cluster geometries along the structural pathway from (4+2)-distorted octahedral to triangular-bipyramidal.

		Optimized+			
Step	r_{eq}(fixed)	r_{eq} (Å)	r_{ap} (Å)	ang (°)	Energy (Hartrees**)
(4+2)-Octahedron	2.081 Å	2.081	2.427	90*	-2066.5750
1	2.30	2.088	2.314	91.42	-2066.5704
2	2.50	2.065	2.189	91.84	-2066.5694
3	2.70	2.065	2.158	93.27	-2066.5671
4	2.90	2.060	2.136	94.75	-2066.5676
5	3.10	2.055	2.118	96.25	-2066.5718
Triangular Bipyramidal		2.079	2.017	120.0	

+ refer to Figure 8.3 for an explanation of optimized parameters
* Held fixed at 90° for the (4+2)-octahedral optimization.
** 1 Hartree = 2625.4997 kJ/mole

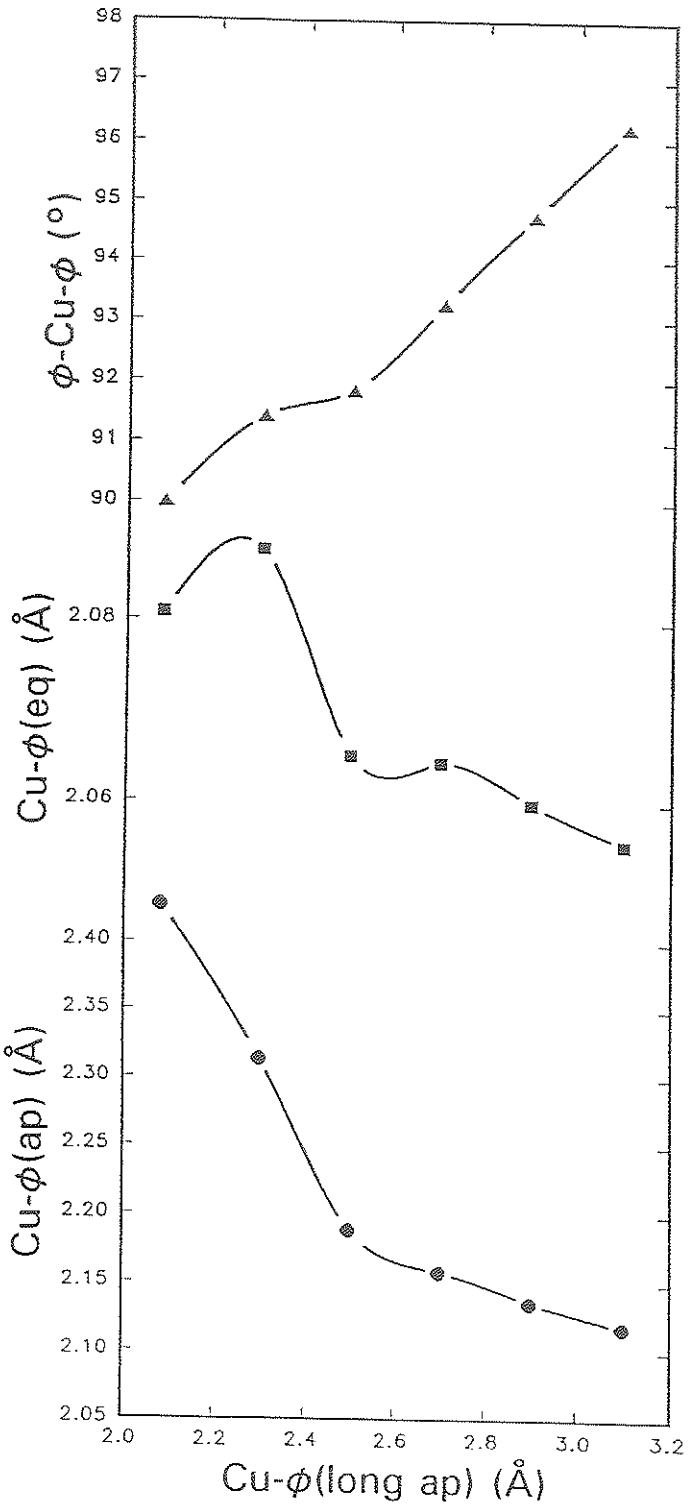

Figure 8.10. Optimized geometries along the structural pathway from (4+2)-distorted octahedral to triangular-bipyramidal. The parameters are defined in Figure 8.3.

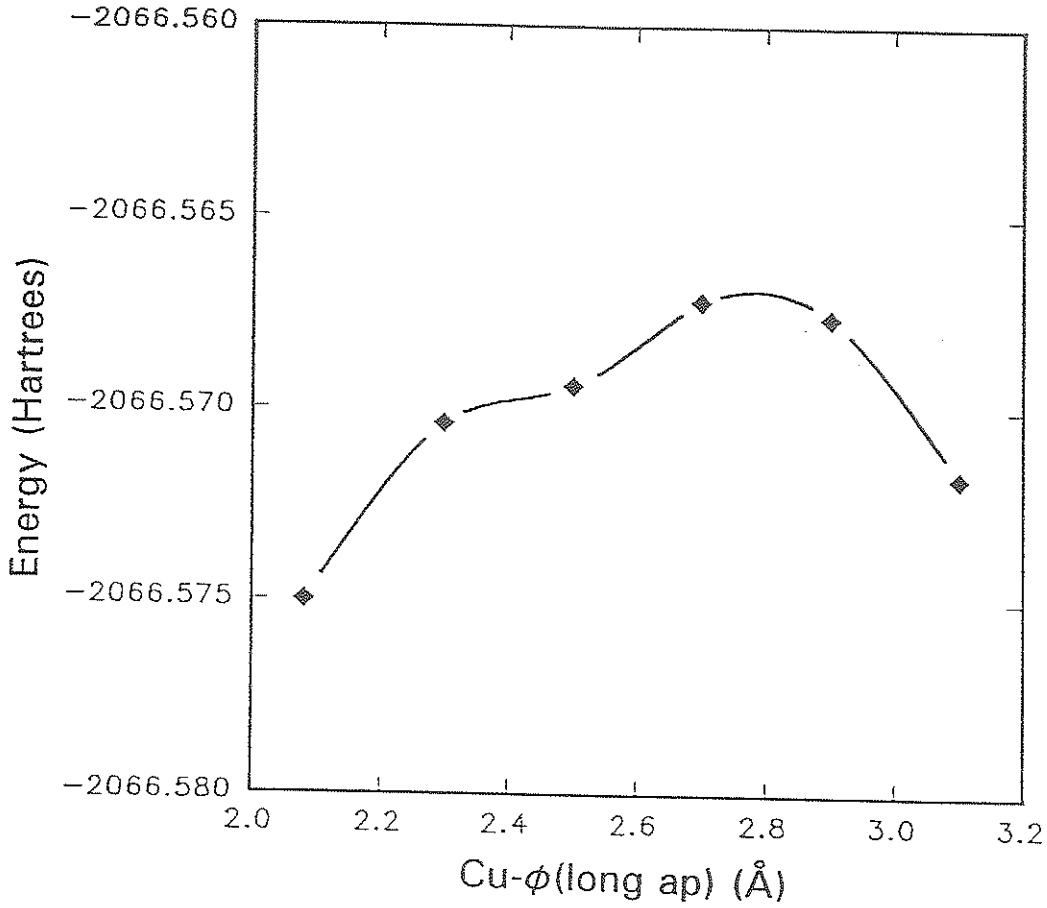

Figure 8.11. Cluster energies along the structural pathway from (4+2)-distorted octahedral to triangular-bipyramidal. 1 Hartree = 2625.4997 kJ/mole.

Table 8.5 Reoptimized $[Cu^{2+}(OH)_6]^{4-}$ cluster geometries* along the structural pathway from (4+2)-distorted octahedral to square-planar.

Step	r_{ap} (Å)	r_{eq}(optimized, Å)	E(SCF, Hartrees**)
1	2.00	2.283	-2066.5234
2	2.10	2.164	-2066.5621
3	2.20	2.134	-2066.5699
4	2.30	2.109	-2066.5737
5	2.40	2.086	-2066.5750
(4+2)-Octahedron	2.427	2.081	-2066.5750
6	2.50	2.067	-2066.5748
7	2.60	2.050	-2066.5740
8	2.70	2.034	-2066.5735
9	2.80	2.021	-2066.5736
10	2.90	2.009	-2066.5748
11	3.00	1.999	-2066.5773
12	3.10	1.990	-2066.5812
13	3.20	1.983	-2066.5865
14	3.30	1.976	-2066.5931
15	3.40	1.971	-2066.6008
Square-planar		1.931	

Electron-Correlation Calculations

Step	E(UHF)	E(CID)	E(MP2)	E(MP3)
6	-2066.57477	-2066.90120	-2066.90285	-2066.92818
11	-2066.57732	-2066.90549	-2066.91045	-2066.93161
15	-2066.60076	-2066.93065	-2066.93733	-2066.95672

* Refer to Figure 8.4 for an explanation of the optimized parameters.
** 1 Hartree = 2625.4997 kJ/mole

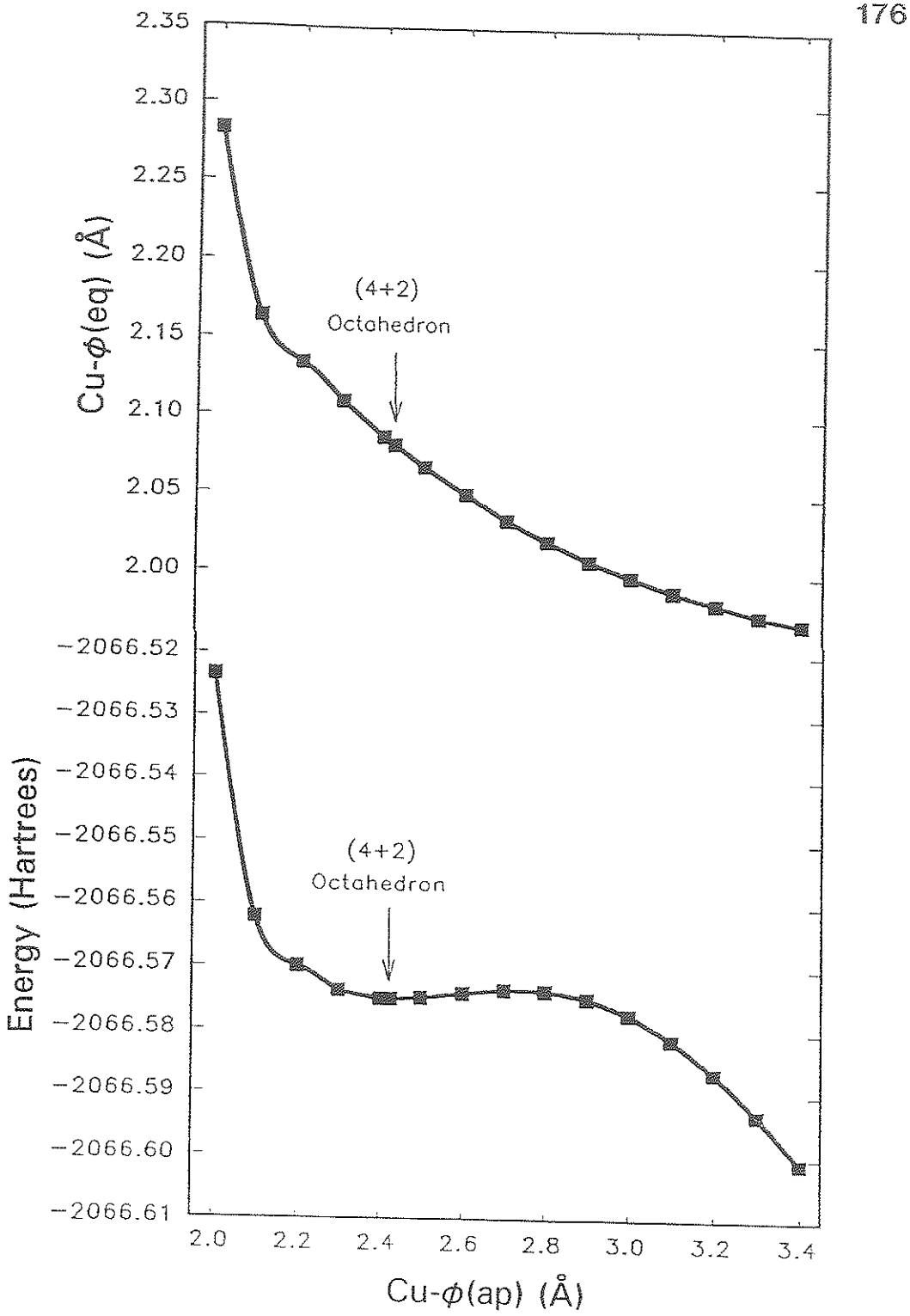

Figure 8.12. Optimized geometries and cluster energies along the structural pathway from (4+2)-distorted octahedral to square-planar. The parameters are defined in Figure 8.4. 1 Hartree = 2625.4997 kJ/mole.

about Cu-ϕ_{ap} = 2.70 Å, where the energy of the cluster is 0.0016 Hartrees greater than the energy of the (4+2)-distorted octahedron. Examination of Cu-ϕ bond-lengths in Cu^{2+} oxysalt minerals (Fig. 2.10) shows that they do seem to reflect the presence of this energy barrier. The apical bond-lengths show a bimodal distribution with maxima at 2.45 Å and 2.75 Å, and a minimum at ~2.65 Å. This minimum presumably reflects the small energy barrier along the structural pathway between the (4+2)-distorted octahedral (with identical apical bond-lengths) to square-planar geometry.

The continuous range of Cu-ϕ_{ap} distances from 2.2 to 3.1 Å suggests a continuous path from (4+2)-octahedral to square-planar geometry. However, the bimodal nature of the distribution (Fig. 2.10) indicates that geometries with <u>both</u> Cu-ϕ_{ap} distances at ~2.65 Å are avoided, in line with the (small) energy barrier found for this specific conformation. This suggests that a (4+2)-octahedral to square-planar structural pathway prefers a (4+1+1)-octahedral intermediate. Note that this is in line with the lack of energy barriers in the pathways from (4+2)-octahedral to square-pyramidal and (shown in the next section) square-pyramidal to square-planar.

8.3.4 Square-Pyramidal <---> Square-Planar

The starting point was the $[Cu^{2+}(OH)_5]^{3-}$ cluster with optimized square-pyramidal geometry from Hartree-Fock calculations with the STO-3G* basis-set (Chapter 7). The pathway was modelled by extending the Cu-ϕ_{ap} bond-length in a stepwise fashion and reoptimizing the remaining cluster geometry. The Cu-ϕ_{eq} bond-lengths (constrained to be equivalent) and ϕ_{ap}-Cu-ϕ_{eq} angles (constrained to be equivalent) were included in the

optimization (shown as r_{eq} and ang in Fig. 8.5). The optimized geometries and cluster energies are given in Table 8.6 and Figure 8.13.

The remaining atoms gradually rearrange towards square-planar geometry while the apical ligand is removed (Fig. 8.13), and there is no energy barrier along this structural pathway (Fig. 8.13). These calculations support the idea that *the square-pyramidal geometries observed in Cu^{2+} oxysalt minerals (Table 7.1), in at least some cases, belong to this structural pathway.*

8.3.5 Square-Pyramidal <---> Triangular-Bipyramidal

This structural pathway was modelled using the optimized geometries for the $[Cu^{2+}(OH)_5]^{3-}$ cluster from Hartree-Fock calculations with the STO-3G* basis-set (Chapter 7). The UHF (spin-unrestricted) Hartree-Fock energies were calculated for nine equally spaced steps along the most direct geometrical pathway between the two coordination geometries (Table 8.7, Fig. 8.14). The calculated Hartree-Fock SCF energies for each step along the structural pathway show that *there is no energy barrier between the two $Cu^{2+}\phi_5$ geometries.*

8.3.6 Triangular-Bipyramidal <---> Square-Planar

The starting point was the $[Cu^{2+}(OH)_5]^{3-}$ cluster with optimized triangular-bipyramidal geometry from Hartree-Fock calculations with the STO-3G* basis-set (Chapter 7). The pathway was modelled by extending one of the Cu-ϕ_{eq} bond-lengths in a stepwise fashion and reoptimizing the remaining cluster geometry. The remaining Cu-ϕ_{eq} bond-lengths (constrained to be equivalent), the Cu-ϕ_{ap} bond-lengths (constrained to be

Table 8.6 Reoptimized $[Cu^{2+}(OH)_5]^{3-}$ cluster geometries along the structural pathway from square-pyramidal to square-planar.

		Optimized+		
Step	r_{ap} (fixed)	r_{eq} (Å)	ang (°)	Energy (Hartrees*)
Square-Pyramidal	2.112 Å	2.040	101.14	-1992.9160
1	2.20	2.033	100.79	-1992.9149
2	2.30	2.027	100.39	-1992.9115
3	2.40	2.021	99.99	-1992.9066
4	2.50	2.015	99.59	-1992.9009
5	2.60	2.009	99.19	-1992.8949
6	2.70	2.003	98.79	-1992.8891
7	2.80	1.998	98.38	-1992.8838
8	2.90	1.993	97.99	-1992.8792
9	3.00	1.988	97.61	-1992.8756
10	3.20	1.978	96.86	-1992.8715
11	3.40	1.973	96.23	-1992.8714
Square-Planar		1.931	90.00	

Electron-Correlation Calculations

Step	E(UHF)	E(CID)	E(MP2)	E(MP3)
1	-1992.9149	-1993.2292	-1993.2345	-1993.2528
7	-1992.8838	-1993.1976	-1993.2058	-1993.2211
11	-1992.8714	-1993.1835	-1993.1922	-1993.2056

+ Refer to Figure 8.5 for an explanation of the optimized parameters.
* 1 Hartree = 2625.4997 kJ/mole

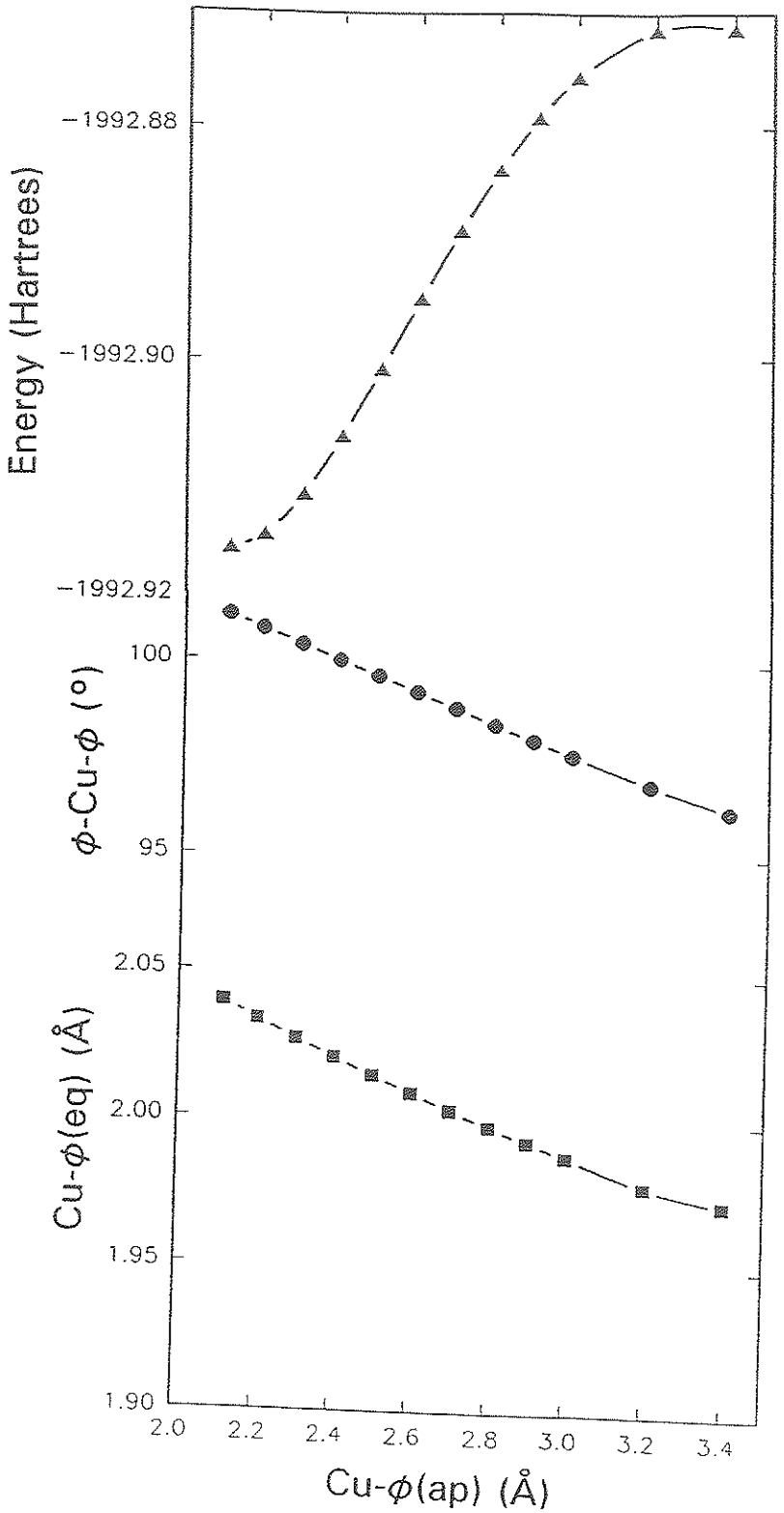

Figure 8.13. Optimized geometries and cluster energies along the structural pathway from square-pyramidal to square-planar. The parameters are defined in Figure 8.5. 1 Hartree = 2625.4997 kJ/mole.

Table 8.7 Hartree-Fock energies of cluster geometries transitional between compressed triangular-bipyramidal and elongated square-pyramidal coordinations.

	Geometry*					
Step	Cu-O1	Cu-O2	Cu-O3	α_1(°)	α_2(°)	Energy (Hartrees**)
Triangular Bipyramid	2.079	2.017	2.079	90	120	-1992.9203
1	2.082	2.019	2.075	91.11	118.11	-1992.9196
2	2.086	2.021	2.071	92.23	116.23	-1992.9190
3	2.089	2.024	2.067	93.34	114.34	-1992.9185
4	2.092	2.026	2.063	94.46	112.46	-1992.9179
5	2.096	2.028	2.059	95.57	110.57	-1992.9173
6	2.099	2.030	2.055	96.68	108.68	-1992.9169
7	2.102	2.033	2.051	97.80	106.80	-1992.9165
8	2.106	2.035	2.047	98.91	104.91	-1992.9163
9	2.109	2.037	2.044	100.03	103.03	-1992.9161
Square Pyramid	2.112	2.040	2.040	101.14	101.14	-1992.9160

* Fig. 8.6 gives the structural pathway geometries used for these calculations, distances in Å
** 1 Hartree = 2625.4997 kJ/mole

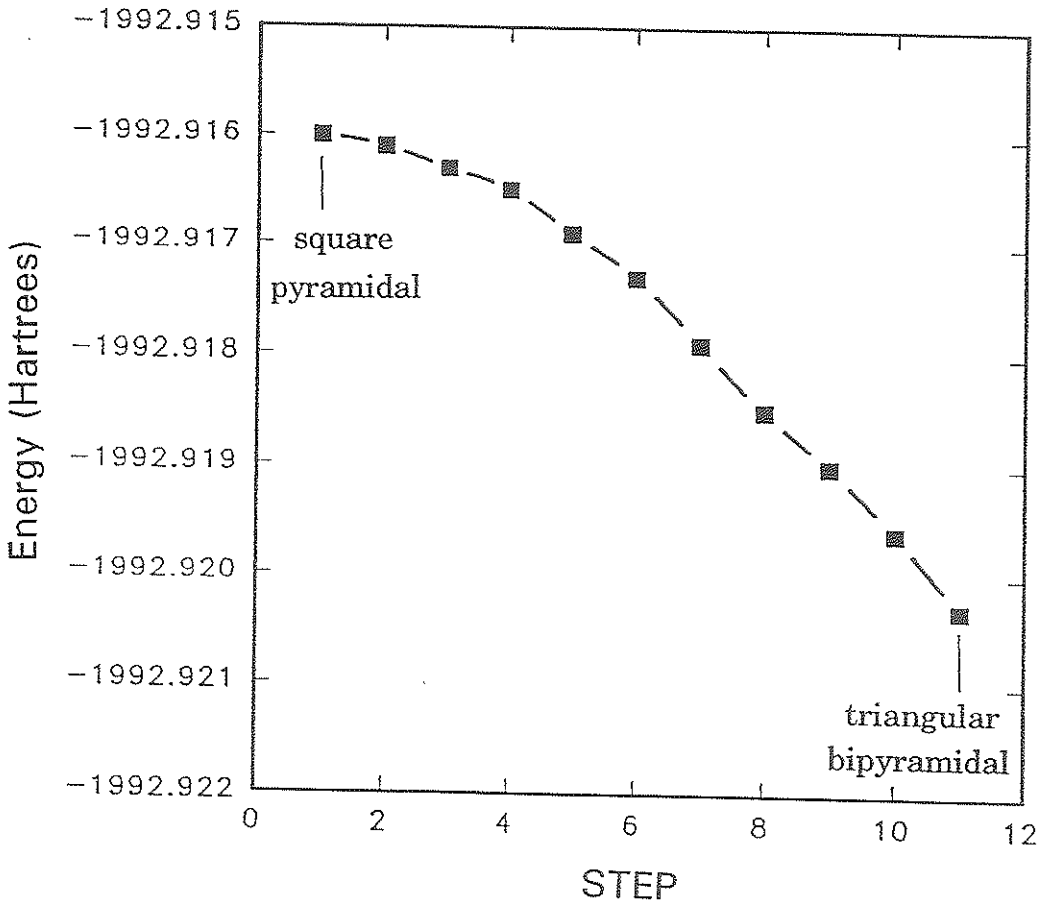

Figure 8.14. Cluster energies for the transition from square-pyramidal to triangular-bipyramidal along the most direct geometric pathway. 1 Hartree = 2625.4997 kJ/mole.

equivalent) and the ϕ_{eq}-Cu-ϕ_{eq} bond-angles (constrained to be equivalent) were included in the optimization (shown as r_{eq}, r_{ap} and ang in Fig. 8.7). The optimized geometries and cluster energies are given in Table 8.8 and Figure 8.15.

The remaining cluster gradually distorts towards square-planar geometry as the equatorial ligand is removed (Fig. 8.15), and there is no energy barrier along this pathway. Thus, it is probable that the triangular-bipyramidal to square-planar structural pathway occurs in Cu^{2+} oxysalt minerals.

8.4 Discussion

The Hartree-Fock calculations reported here indicate that there is no energy barrier between the square-pyramidal and triangular-bipyramidal $Cu^{2+}\phi_5$ geometries. It remains unclear as to why representative geometries of the square-pyramidal to triangular-bipyramidal structural pathway have not been observed in Cu^{2+} oxysalt minerals; this may be due to the relatively small number of examples found so far, as the fact that a complete range is found in synthetic compounds indicates that there are no intrinsic restrictions from the topological/energetic aspects of the overall structural arrangements.

A summary of the MO investigations of $Cu^{2+}\phi_n$ structural pathways is given in Figure 8.16, where arrows indicate continuous pathways as indicated by the calculations, and broken lines indicate energy barriers. Of the possible structural pathways indicated, representatives of the (4+2)-octahedral to square-pyramidal, (4+2)-octahedral to square-planar [with (4+1+1) intermediates] and square-pyramidal to square-planar pathways

Table 8.8 Reoptimized $[Cu^{2+}(OH)_5]^{3-}$ cluster geometries along the structural pathway from triangular-bipyramidal to square-pyramidal

		Optimized+			
Step	r_{eq}(fixed)	r_{eq}(Å)	r_{ap}(Å)	ang(°)	Energy (Hartrees*)
Triangular bipyramidal	2.079 Å	2.079	2.017	120	-1992.9203
1	2.30	2.066	2.000	118.34	-1992.9134
2	2.40	2.056	1.996	116.13	-1992.9077
3	2.50	2.046	1.993	114.20	-1992.9014
4	2.60	2.039	1.988	112.62	-1992.8948
5	2.70	2.030	1.985	111.37	-1992.8885
6	2.80	2.023	1.980	110.12	-1992.8827
7	2.90	2.016	1.976	109.10	-1992.8776
8	3.00	2.011	1.973	108.26	-1992.8735
9	3.25	1.998	1.965	106.09	-1992.8678
10	3.50	1.987	1.959	104.52	-1992.8684
Square planar		1.931	1.931	90	

+ Refer to Figure 8.7 for an explanation of the optimized parameters

* 1 Hartree = 2625.4997 kJ/mole

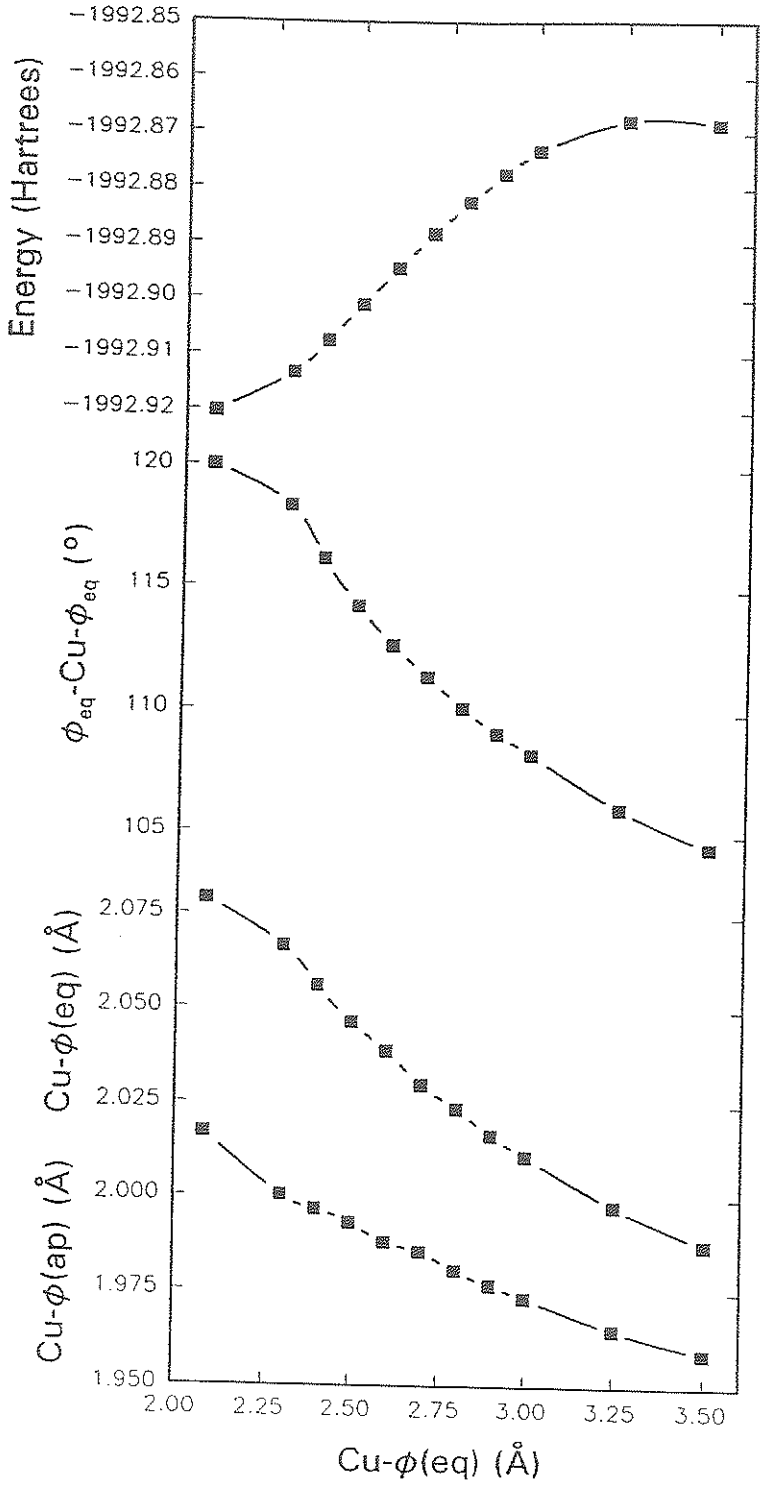

Figure 8.15. Optimized geometries and cluster energies along the structural pathway from triangular-bipyramidal to square-planar. The parameters are defined in Figure 8.7. 1 Hartree = 2625.4997 kJ/mole.

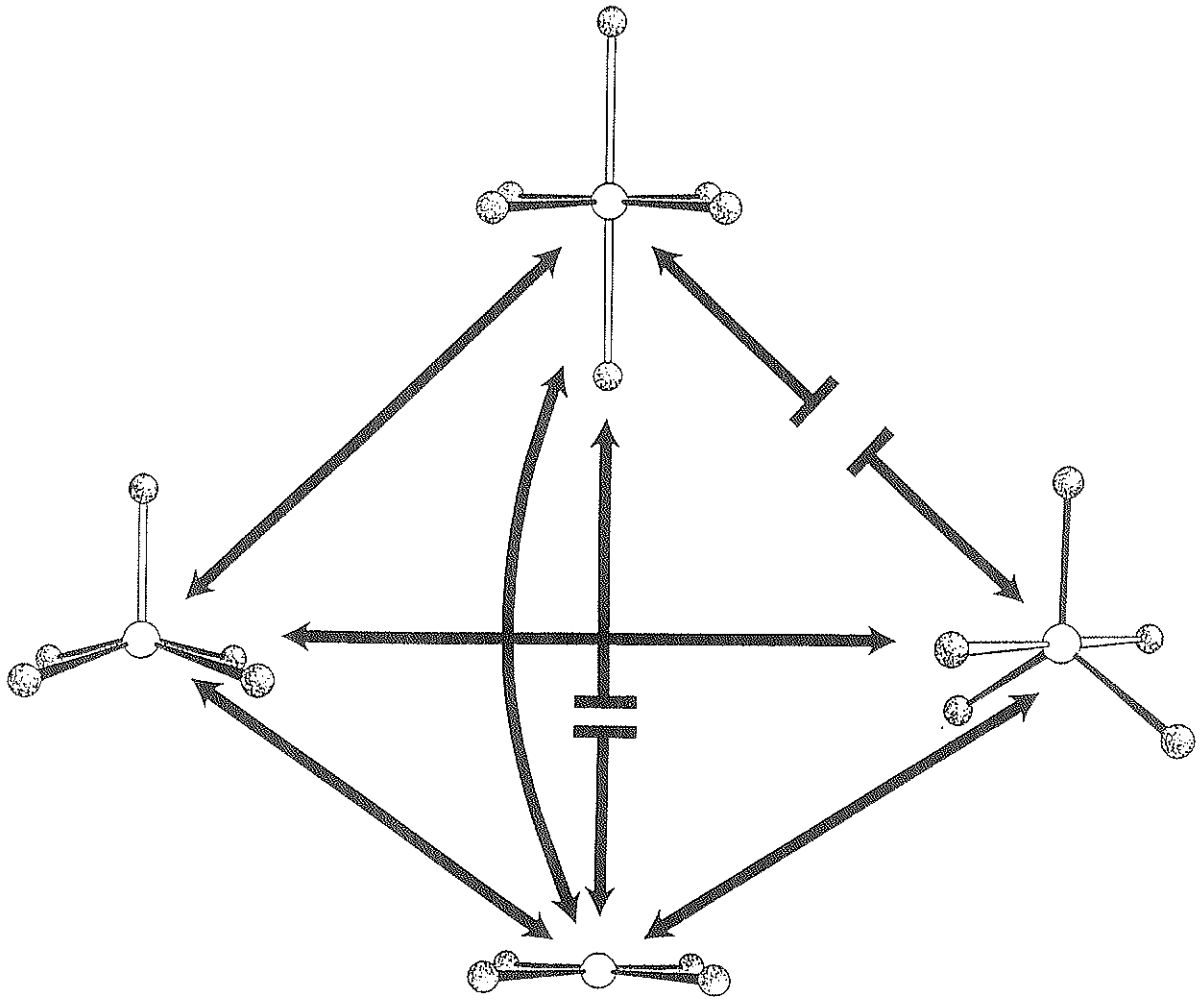

Figure 8.16. Structural pathways between copper polyhedra as indicated by Hartree-Fock MO calculations. Energy barriers are represented by breaks in the lines.

have thus far been observed in Cu^{2+} oxysalt minerals. Note, however, that Effenberger (1988a) notes that there are intermediates between square-pyramidal and triangular-bipyramidal $Cu^{2+}\phi_5$ geometries in synthetic Cu^{2+} oxysalts.

Many Cu^{2+} oxysalt minerals contain $Cu^{2+}\phi_n$ coordination polyhedra that are members of one of the structural pathways shown in Figure 8.16, rather than one of the principal coordination types. In past studies of Cu^{2+} oxysalt minerals, these structural pathways have not been explicitly recognized, and considerable confusion has arisen concerning the naming of these intermediate coordination geometries. This work suggests that Cu^{2+} coordination geometries should be described out to perhaps 3.2 Å (without necessarily implying that a specific long interaction is significant), and interpreted according to the idea of structural pathways before necessarily assigning a specific coordination number.

Chapter 9

Mixed-Ligand $Cu^{2+}\Phi_6$ Octahedra in Minerals

9.1 Mixed-Ligand $Cu^{2+}\Phi_6$ Octahedra.

Many Cu^{2+} oxysalt minerals contain $Cu^{2+}\phi_6$ with $\phi = O^{2-}$, OH^- and H_2O only. Such octahedra are almost invariably distorted into a (4+2) arrangement, due to the Jahn-Teller effect (Chapter 2). The previous chapters of this thesis have considered such Cu^{2+} minerals in detail, and have shown that the octahedral bond-length distribution can be quantitatively rationalized *via* the Jahn-Teller effect alone. Comparison of such coordination geometries, as well as the application of the Jahn-Teller theory, are facilitated by the similarity of each of the six coordinating ligands.

Many Cu^{2+} oxysalt minerals contain $Cu^{2+}\Phi_6$ octahedra where $\Phi = O^{2-}$, OH^-, H_2O and 1, 2 or 4 Cl ligands. Due to the mixture of ligands in these octahedra, the Cu^{2+} ion cannot achieve a holosymmetric environment, and the Jahn-Teller arguments are not directly applicable to such polyhedra. However, a near-degenerate electronic state may occur, and distortion of the octahedron may lead to a significant net stabilization of the mixed-ligand octahedron. This effect is referred to as a *pseudo-Jahn-Teller effect* (Hathaway, 1984). In $Cu^{2+}\Phi_6$ octahedra with mixed ligands, the bond-length variations are less straight forward to interpret than in the case of oxygen ligands ($\phi = O^{2-}$, OH^-, H_2O), as there is also an intrinsic contribution to bond-length variations that arises from the difference in size of the (O^{2-}, OH, H_2O) [$r \approx 1.36$ Å] and Cl^- [$r \approx 1.67$ Å] anions.

9.2 Rietveld Refinement of the Crystal Structure of Tolbachite, $Cu^{2+}Cl_2$.

Tolbachite, $Cu^{2+}Cl_2$, occurs as encrustations on basaltic magma flows from the Tolbachin eruption of 1975-1976, and was described as a new mineral by Bergasova and Filatov (1984). It is hygroscopic and hydrates rapidly to eriochalcite ($Cu^{2+}Cl_2.2H_2O$) on continued contact with air. This feature, along with the general lack of good crystals, presents special problems during structure characterization. The crystal structure of synthetic $Cu^{2+}Cl_2$ was determined by Wells (1947), but due to the aforementioned problems, was not refined. The unit-cell parameters and space group given by Wells (1947) and Bergosova and Filatov (1984) indicate that tolbachite is isostructural with synthetic $Cu^{2+}Cl_2$.

Tolbachite is the only mineral that is known to contain $Cu^{2+}Cl_6$ octahedra, and is thus of considerable interest as it will give the bond-length information, in combination with synthetic compounds, needed to evaluate Jahn-Teller relaxation in $Cu^{2+}Cl_6$ and $Cu^{2+}\Phi_6$ mixed-ligand octahedra.

9.2.1 Experimental

Synthetic tolbachite was prepared by heating $Cu^{2+}Cl_2.2H_2O$ in air at 105°C for a week. The resulting powder was gently back-pressed into an aluminum holder and the upper surface was serrated with a razor blade to reduce preferred orientation effects during data collection. After sample preparation, the aluminum holder containing the powder was heated to 105°C for 1 hour to dehydrate any $Cu^{2+}Cl_2.2H_2O$ that may have formed during sample preparation.

Tolbachite is extremely hygroscopic and quickly hydrates in air. Nitrogen was used to provide an inert atmosphere during data collection. The diffractometer sample chamber was modified to provide spaces for inlet and outlet pipes. Nitrogen was dried by pumping through a Leco rotometer, with the gas passing through concentrated sulphuric acid, ascarite and magnesium perchlorate before entering the sample chamber. Scans before and after data collection showed no detectable $Cu^{2+}Cl_2.2H_2O$.

The diffraction data for Rietveld refinement were collected at 25°C on a Philips PW1710 X-ray powder diffractometer with Bragg-Brentano geometry using CuKα X-radiation, fixed 1/2° slits and a diffracted-beam monochromator. Data were collected over the range ($14 < 2\theta < 130°$) with a step interval of 0.05°2θ and a count time of 5 s per step.

9.2.2 Structure Refinement

The Rietveld (Rietveld, 1969, 1967) structure refinement was done using the program LHPM1 (Howard and Hill, 1986; a modified version of the program by Wiles and Young, 1981). Refinement was initiated in the space group C2/m with the structural parameters of Wells (1947) as the starting model. The refinement included all of the data over the range ($14 < 2\theta < 130°$). Scattering factors for neutral atoms were taken from the International Tables For X-Ray Crystallography (1974). Peaks were modelled using a pseudo-Voigt profile function which was corrected for asymmetry to 30°2θ. The pattern background was modelled using a refinable fourth-order polynomial. Individual isotropic-displacement factors were unstable during the final cycles of refinement, and were fixed at typical single-crystal values; an overall displacement factor was refined.

The final R-indices were R_B = 2.4%, R_P = 3.5%, R_{WP} = 4.8% with R_{WP}(expected) = 3.2%; refined structural parameters are given in Table 9.1 and the observed powder pattern is compared to the pattern calculated using the refined structure parameters in Figure 9.1. The observed step-scan data is given in Appendix A.

9.2.3 Structure Description

Tolbachite contains $Cu^{2+}Cl_6$ octahedra distorted such that there are four Cu-Cl equatorial bond-lengths [2.263(6) Å] and two much longer Cu-Cl apical bond-lengths [2.991(6) Å], a (4+2)-distortion; this distorted environment is a result of the Jahn-Teller effect (Chapter 2). Each $Cu^{2+}Cl_6$ octahedron shares two Cu-Cl_{eq} edges with adjacent octahedra, and each of its apical Cl ions are equatorial ligands for adjacent octahedra. This linkage results in corrugated sheets (Fig. 9.2) of composition $Cu^{2+}Cl_2$ parallel to (001). Each sheet is electrostatically neutral, and linkage between adjacent sheets is *via* Van der Waals forces, explaining why tolbachite quickly hydrates in air.

9.2.4 Synthetic Compounds Containing $Cu^{2+}Cl_6$ Octahedra.

Crystal-structure data is available for several non-mineral inorganic compounds containing $Cu^{2+}Cl_6$ octahedra (Table 9.2). All $Cu^{2+}Cl_6$ octahedra show distorted (4+2)-geometries, with Cu-Cl_{eq} ranging from 2.234 to 2.381 Å (mean = 2.297 Å) and Cu-Cl_{ap} ranging from 2.706 to 3.19 Å (mean = 2.918 Å). The Cu-Cl bond-lengths obtained for tolbachite (Table 9.1) are in these ranges.

Table 9.1 Final structure parameters, R-indices, bond-lengths (Å) and bond-angles (°) in tolbachite, $Cu^{2+}Cl_2$.

Space Group		C2/m		
Cell	a (Å)	6.9038(9)	R-indices*	
	b	3.2995(4)		
	c	6.824(1)	R_B	2.4
	β (°)	122.197(8)	R_P	3.5
	V (Å^3)	131.54(5)	R_{WP}	4.8
	Z	2	R_{WP}(exp.)	3.2

Positional parameters

	x	y	z
Cu	0	0	0
Cl	0.5048(8)	0	0.2294(9)

Bond Distances		Bond Angles	
Cu-Cl x2	2.991(6)	Cl-Cu-Cla x4	87.6(2)
Cu-Cla x4	2.263(6)	Clb-Cu-Clc x4	92.4(2)
<Cu-Cl>	2.506	Cla-Cu-Cld x2	86.4(2)
		Clc-Cu-Cld x2	93.6(2)
		<Cl-Cu-Cl>	90.0

a = ½ - x, y - ½, -z; b = -x, y, -z; c = x - ½, y + ½, z; d = ½ - x, y + ½, -z

* R_B = Rietveld Bragg-agreement index
R_P = Rietveld profile-agreement index
R_{WP} = Rietveld weighted profile-agreement index
R_{WP}(exp) = expected (i.e., optimal) value for R_{WP}

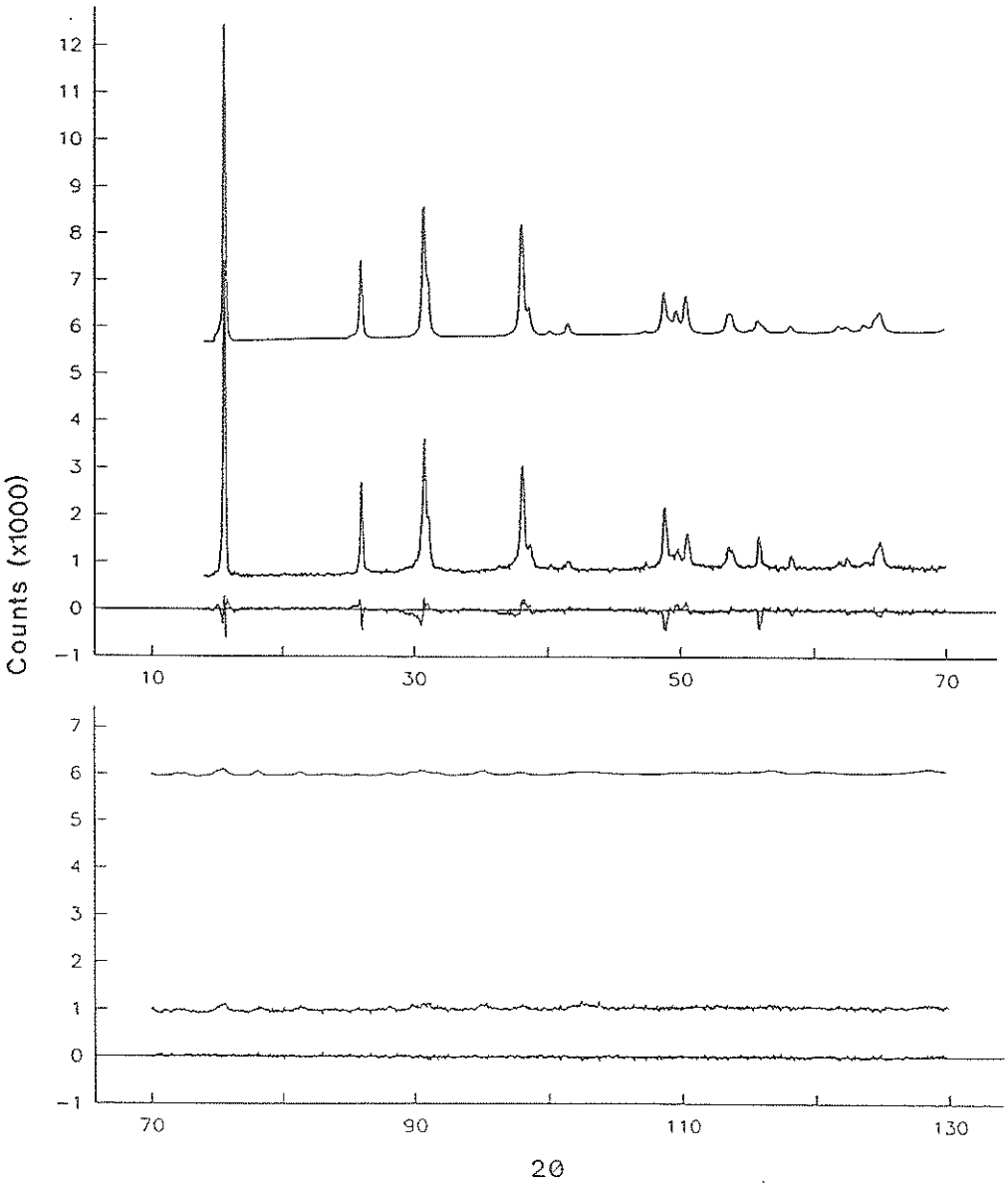

Figure 9.1. The observed (middle) and calculated (top) powder patterns for tolbachite; bottom: residual ($I_{calc.}$-$I_{obs.}$).

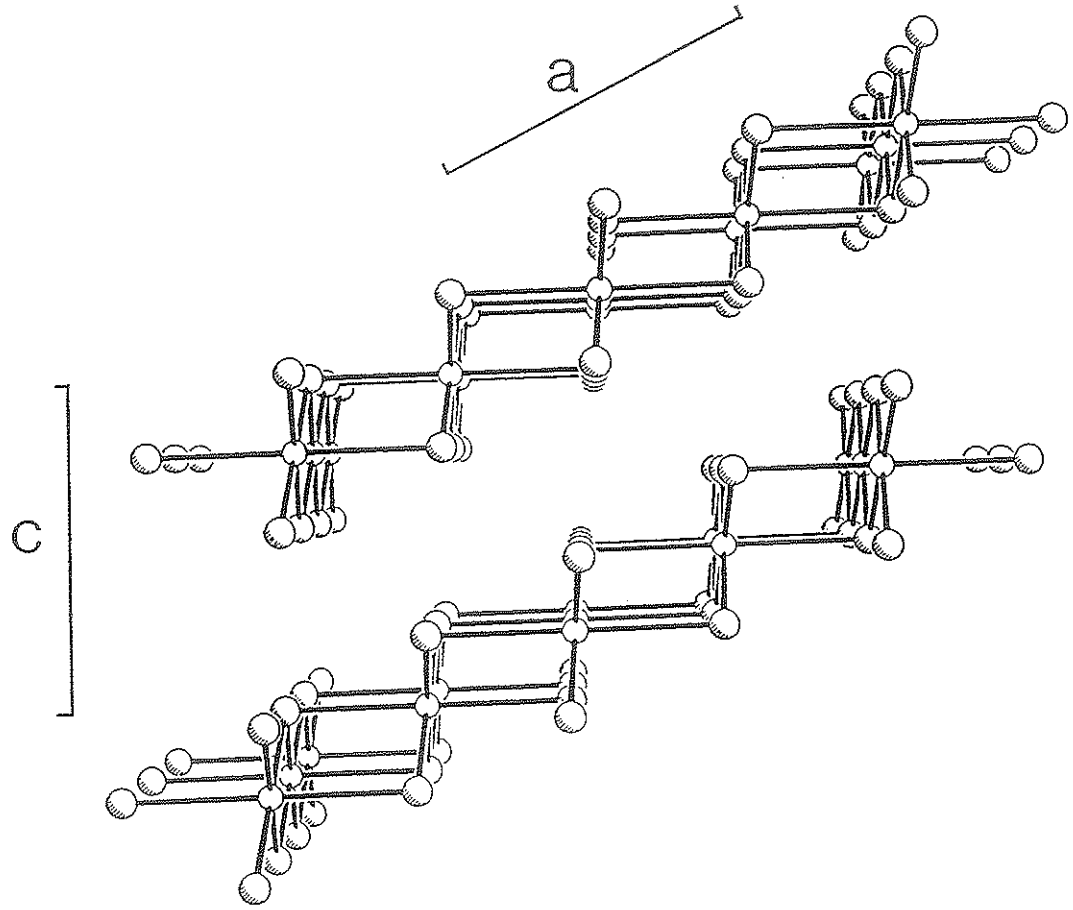

Figure 9.2. The tolbachite structure projected along [010]. Copper atoms are small open circles, chlorine atoms are larger open circles with shading in the lower left corners.

Table 9.2 $Cu^{2+}Cl_6$ octahedral geometries in inorganic compounds

	R_{eq} (Å)				R_{ap} (Å)		Ref.
$CsCu^{2+}Cl_3$	2.28	2.28	2.35	2.35	2.78	2.78	1
$Cu^{2+}Al_2Cl_8$	2.29	2.29	2.30	2.30	2.96	2.96	2
$Rb_3Cu_2^{2+}Cl_7$	2.234	2.234	2.325	2.381	2.870	2.870	3
$KCu^{2+}Cl_3$	2.248	2.267	2.314	2.322	2.941	3.113	4
$NH_4Cu^{2+}Cl_3$	2.25	2.26	2.32	2.32	2.99	3.19	4
$RbCu^{2+}Cl_3$	2.307	2.307	2.369	2.369	2.706	2.706	5
Tolbachite	2.263	2.263	2.263	2.263	2.991	2.991	
Mean		2.297				2.918	

References: 1: Schlueter et al. (1966); 2: Schäfer et al. (1980); 3: Crama (1981b); 4: Willett et al. (1963); 5: Crama (1981a).

An estimate of the Cu-Cl bond-length in an undistorted $Cu^{2+}Cl_6$ octahedron may be obtained by plotting <Cu-Cl> versus Δ (equation 2.1) for the octahedra. The intercept of the best-fit line at $\Delta = 0.0$ (Figure 9.3) gives <Cu-Cl> = 2.43 Å for the undistorted octahedron.

9.3 Mixed-Ligand $Cu^{2+}\Phi_6$ Octahedra in Minerals.

In the case of $Cu^{2+}\Phi_6$ octahedra with mixed ligands, either an elongation [(4+2)-distortion] or a compression [(2+4)-distortion] of the pseudo-octahedral environment will remove the near-degenerate electronic state and will result in a net stabilization of the octahedron.

The Cu-O and Cu-Cl bond-lengths expected for mixed-ligand $Cu^{2+}\Phi_6$ octahedra that have not been distorted by the pseudo-Jahn-Teller effect may be estimated by summing the respective ionic radii. This approach gives Cu^{2+}-O^{2-} = 2.09 Å and Cu^{2+}-Cl^- = 2.40 Å [Cu^{2+} = 0.73 Å, O^{2-} = 1.36 Å (Shannon, 1975); Cl^- = 1.67 Å (estimated by Whittaker and Muntus, 1970)]. Independent estimates of expected <Cu^{2+}-O^{2-}, OH^-, H_2O> and <Cu^{2+}-Cl^-> bond-lengths for undistorted octahedra are 2.083 Å and 2.43 Å, respectively, as obtained by extrapolating Δ (octahedral distortion) - <Cu-ϕ> relationships to zero distortion (Sections 2.5.2 and 9.2.4). These bond-lengths, as well as expected Cu-Cl bond-lengths for (4+2)-distorted octahedra obtained from the tolbachite structure refinement (Section 9.2), allow the identification and classification of distortion geometries in mixed-ligand $Cu^{2+}\Phi_6$ octahedra.

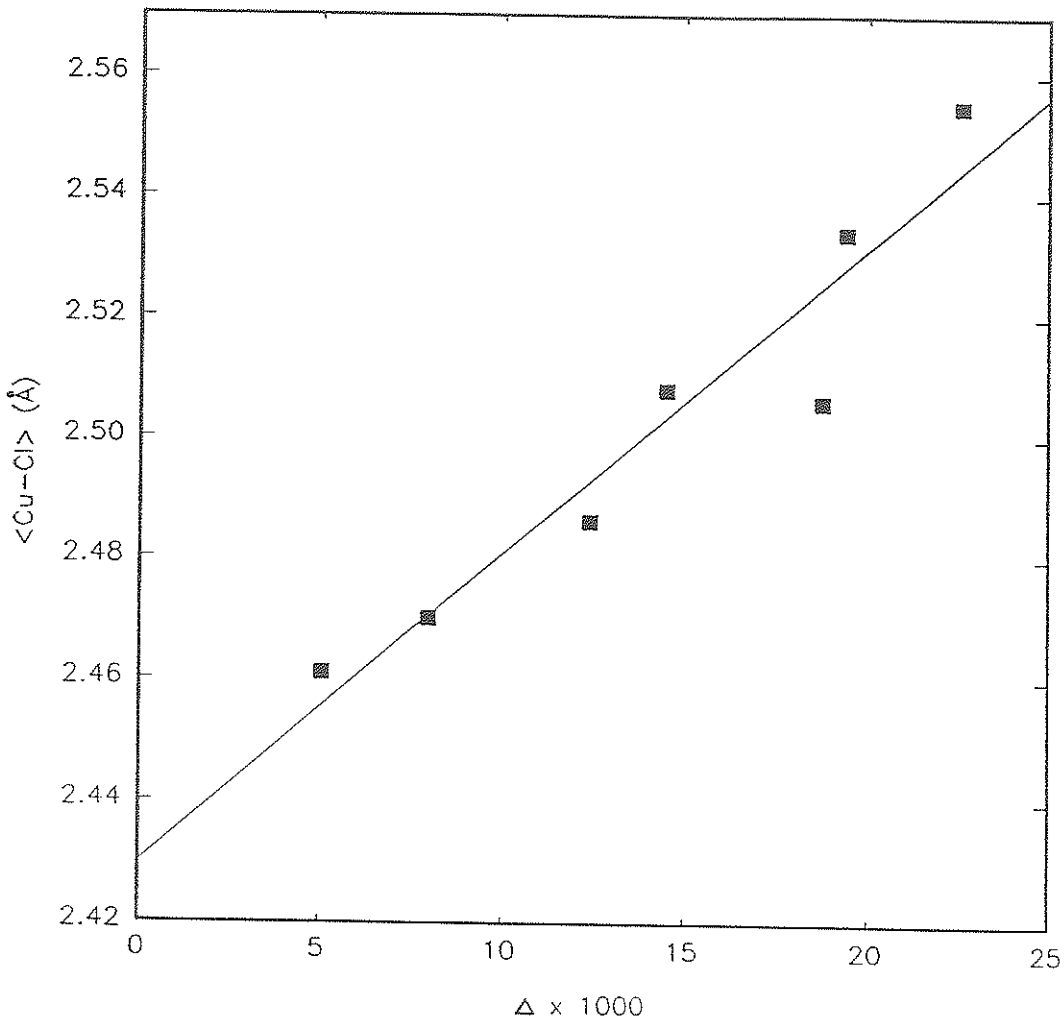

Figure 9.3. Mean Cu-Cl bond-lengths versus octahedral distortion for $Cu^{2+}Cl_6$ octahedra in tolbachite and various inorganic compounds. The least-squares line intercept is at <Cu-Cl> = 2.43 Å.

9.3.1 $Cu^{2+}\Phi_6$ With $\Phi = 4(O^{2-}, OH^-, H_2O)$ and 2 Cl.

The most common mixed-ligand $Cu^{2+}\Phi_6$ octahedral arrangement in Cu^{2+} oxysalt minerals involves $\Phi = 4(O^{2-}, OH^-, H_2O)$ and 2 Cl (Table 9.3). Comparison of these geometries with the (4+2)-distorted $Cu^{2+}Cl_6$ octahedra observed in tolbachite (Table 9.1), (4+2)-distorted $Cu^{2+}\phi_6$ octahedra ($\phi = O^{2-}$, OH^-, H_2O; Chapter 2), and undistorted octahedral bond-lengths derived from ionic radii sums (previous section) show that each of these mixed-ligand octahedra are (4+2)-distorted. In each case, the equatorial positions are occupied by the $4(O^{2-}, OH^-, H_2O)$ ligands and the two Cl ligands occur at the apical positions (Table 9.3). As was the case with $Cu^{2+}\phi_6$ octahedra, these mixed-ligand octahedra show considerable variability in distortion, particularly in the apical Cu-Cl bond-lengths, which range from 2.55 to 3.21 Å. Variation of the equatorial Cu-Φ distances is more restricted, with an observed range of 1.90 to 2.11 Å. The lower limit of the apical Cu-Cl bond-lengths (2.55 Å in nabokoite) is close to the expected Cu-Cl undistorted octahedral bond-length (2.43 Å). However, the equatorial octahedral Cu-Φ bond-lengths in nabokoite (1.971 Å) indicate that the octahedron is (4+2)-distorted.

9.3.2 $Cu^{2+}\Phi_6$ With $\Phi = 5(O^{2-}, OH^-, H_2O)$ and 1 Cl.

Six Cu^{2+} oxysalt minerals contain $Cu^{2+}\Phi_6$ octahedra with $\Phi = 5(O^{2-}$, OH^-, $H_2O)$ and 1 Cl (Table 9.4). Comparison of these mixed-ligand geometries with the (4+2)-distorted $Cu^{2+}Cl_6$ octahedral bond-lengths in tolbachite (Table 9.1), (4+2)-distorted $Cu^{2+}\phi_6$ octahedra with $\phi = (O^{2-}$, OH^-, $H_2O)$ (Chapter 2), and undistorted Cu-Φ octahedral bond-lengths derived from ionic radii sums (section 9.3) indicate that the mixed-ligand octahedra

Table 9.3 Mixed-ligand $Cu^{2+}\Phi_6$ octahedra in Cu^{2+} oxysalt minerals with $\Phi = 4(O^{2-}, OH^-, H_2O) + 2Cl$.

		O^{2-}, OH^-, H_2O (Å)				Cl (Å)		Ref.
Cumengéite	Cu(1)	1.99	1.96	1.95	1.95	2.993	2.855	1
	Cu(2)	1.96	1.96	1.96	1.96	2.75	2.75	
Botallackite	Cu(2)	1.920	1.920	2.001	2.001	2.789	2.789	2
Atacamite	Cu(1)	1.940	1.940	2.017	2.017	2.776	2.776	3
Chloroxiphite	Cu	1.98	1.98	1.99	1.99	2.97	2.97	4
Bandylite	Cu	1.98	1.98	1.98	1.98	2.80	2.80	5
Diaboleite	Cu	2.05	2.05	2.05	2.05	2.55	2.95	6
Nabokoite	Cu(2)	1.971	1.971	1.971	1.971	2.553	2.553	7
Francisite	Cu(1)	1.917	1.917	1.96	1.96	3.078	3.078	8
	Cu(2)	1.96	1.96	1.98	1.98	3.206	3.206	
Boleite	Cu	1.90	1.90	2.11	2.11	2.85	2.91	9
Paratacamite	Cu(3)	1.93	1.97	1.98	2.00	2.770	2.818	10
	Cu(4)	1.93	1.99	1.99	2.07	2.753	2.778	
Buttgenbachite	Cu(2)	1.949	1.949	1.974	1.974	2.968	2.968	11

References: 1: Hawthorne and Groat (1986); 2: Hawthorne (1985a); 3: Parse and Hyde (1986); 4: Finney et al. (1977); 5: Collin (1951); 6: Rouse (1971); 7: Pertlik and Zemann (1988); 8: Pring et al. (1990); 9: Rouse (1973); 10: Fleet (1975); 11: Fanfani et al. (1973).

Table 9.4 Mixed-ligand $Cu^{2+}\Phi_6$ octahedra in Cu^{2+} oxysalt minerals with $\Phi = 5(O^{2-}, OH^-, H_2O) + Cl$.

		O^{2-}, OH^-, H_2O (Å)				Cl (Å)		Ref.
Atacamite	Cu(2)	1.993	1.993	2.010	2.020	2.358	2.750	1
Botallackite	Cu(1)	1.995	1.995	1.998	1.998	2.367	2.732	2
Spangolite	Cu	1.935	1.958	1.979	1.979	2.425	2.835	3
Kamchatkite	Cu(1)	1.928	1.929	2.080	2.37	2.31	2.388	4
	Cu(2)	1.921	1.940	2.069	2.35	2.36	2.401	
Nabokoite	Cu(1)	1.935	1.988	1.998	2.002	2.200	2.769	5
Buttgenbachite	Cu(4)	1.963	1.963	1.983	1.983	2.912	2.801	6

References: 1: Parse and Hyde (1986); 2: Hawthorne (1985a); 3: Hawthorne et al. (1993); 4: Varaksina et al. (1990); 5: Pertlik and Zemann (1988); 6: Fanfani et al. (1973).

in atacamite, botallackite, spangolite, buttgenbachite and nabokoite are (4+2)-distorted with the lone Cl in an apical position. These minerals show equatorial Cu-(O^{2-}, OH^-, H_2O) bond-lengths from 1.935 to 1.998 Å, typical values for Cu^{2+} oxysalt minerals (Chapter 3). The single apical Cu - (O^{2-}, OH^-, H_2O) bond-length ranges from 2.200 to 2.367 Å (excluding the bond-length of 2.912 Å in buttgenbachite), values that are long enough to be identified as apical ligands, but that are generally shorter than average Cu-ϕ apical bond-lengths in non-mixed-ligand $Cu^{2+}\phi_6$ octahedra. Apical Cu-Cl bond-lengths range from 2.732 to 2.835 Å in these five minerals, values that are within the range observed in the previous group of mixed-ligand Cu^{2+} oxysalt minerals (Section 9.3.1).

All mixed-ligand $Cu^{2+}\Phi_6$ octahedra with Φ = 4(O^{2-}, OH^-, H_2O) and 2 Cl have the two Cl ligands at apical positions in a (4+2)-distorted octahedron (Table 9.3). Furthermore, five of these six minerals have the single Cl located at the apical position of the (4+2)-distorted octahedron. However, the two mixed-ligand $Cu^{2+}\Phi_6$ octahedra in kamchatkite do not follow the pattern observed in the rest of the mixed-ligand copper octahedra (Table 9.4): Here, the single Cl ligands are at equatorial positions in the (4+2)-distorted $Cu^{2+}\Phi_6$ octahedra. In both of these octahedra, three equatorial Cu-Φ bonds involve O^{2-}, OH^-, H_2O, with bond-lengths from 1.921 to 2.080 Å. The fourth equatorial ligand in each of these octahedra is Cl, with Cu-Cl_{eq} distances of 2.388 and 2.401 Å. Finally, the apical ligands are O^{2-}, OH^-, H_2O, with Cu-Φ_{ap} distances from 2.31 to 2.37 Å, values in the range of Cu-ϕ_{ap} (ϕ = O^{2-}, OH^-, H_2O) distances in non-mixed-ligand $Cu^{2+}\phi_6$ octahedra (Chapter 2).

The Cu(1) and Cu(2) octahedra in kamchatkite (Fig. 9.4) each have the two shortest Cu-O equatorial bonds in a *trans* arrangement. The longer Cu-O equatorial bonds [2.080 Å in Cu(1) and 2.069 Å in Cu(2)] are in a *trans* arrangement with the equatorial Cl ligands. Also, the two equatorial Cu-Cl bonds [2.388 Å in Cu(1) and 2.401 Å in Cu(2)] are considerably longer that the average Cu-Cl_{eq} bonds in $Cu^{2+}Cl_6$ octahedra (2.297 Å). These two octahedra may therefore be classified as (2+2+2)-distorted, and the possibility of a dynamic distortion must be addressed (i.e., similar to those observed in cyanochroite and bayldonite, Chapter 2). However, anisotropic-displacement parameters are not available for kamchatkite, so there is no way to assess the possibility of dynamic distortion in the Cu(1) and Cu(2) mixed-ligand octahedra.

9.3.3 $Cu^{2+}\Phi_6$ With $\Phi = 2(O^{2-}, OH^-, H_2O)$ and 4 Cl.

Only two Cu^{2+} oxysalt minerals contain $Cu^{2+}\Phi_6$ octahedra with $\Phi = 2(O^{2-}, OH^-, H_2O)$ and 4 Cl: eriochalcite and chlorothionite (Table 9.5) both contain (4+2)-distorted $Cu^{2+}\Phi_6$ octahedra. In each case, the $2(O^{2-}, OH^-, H_2O)$ ligands are in a *trans* arrangement in the equatorial positions of the distorted octahedra; the remaining equatorial positions, as well as the apical positions, are occupied by Cl. Equatorial Cu-(O^{2-}, OH^-, H_2O) and Cu-Cl distances are in the ranges observed in other mixed-ligand octahedra, as are the apical Cu-Cl bond-lengths (Table 9.5).

9.4 Discussion

Mixed-ligand $Cu^{2+}\Phi_6$ octahedra with 1, 2 or 4 Cl ligands occur in minerals, and octahedra with 3 or 5 Cl are conspicuously absent. For

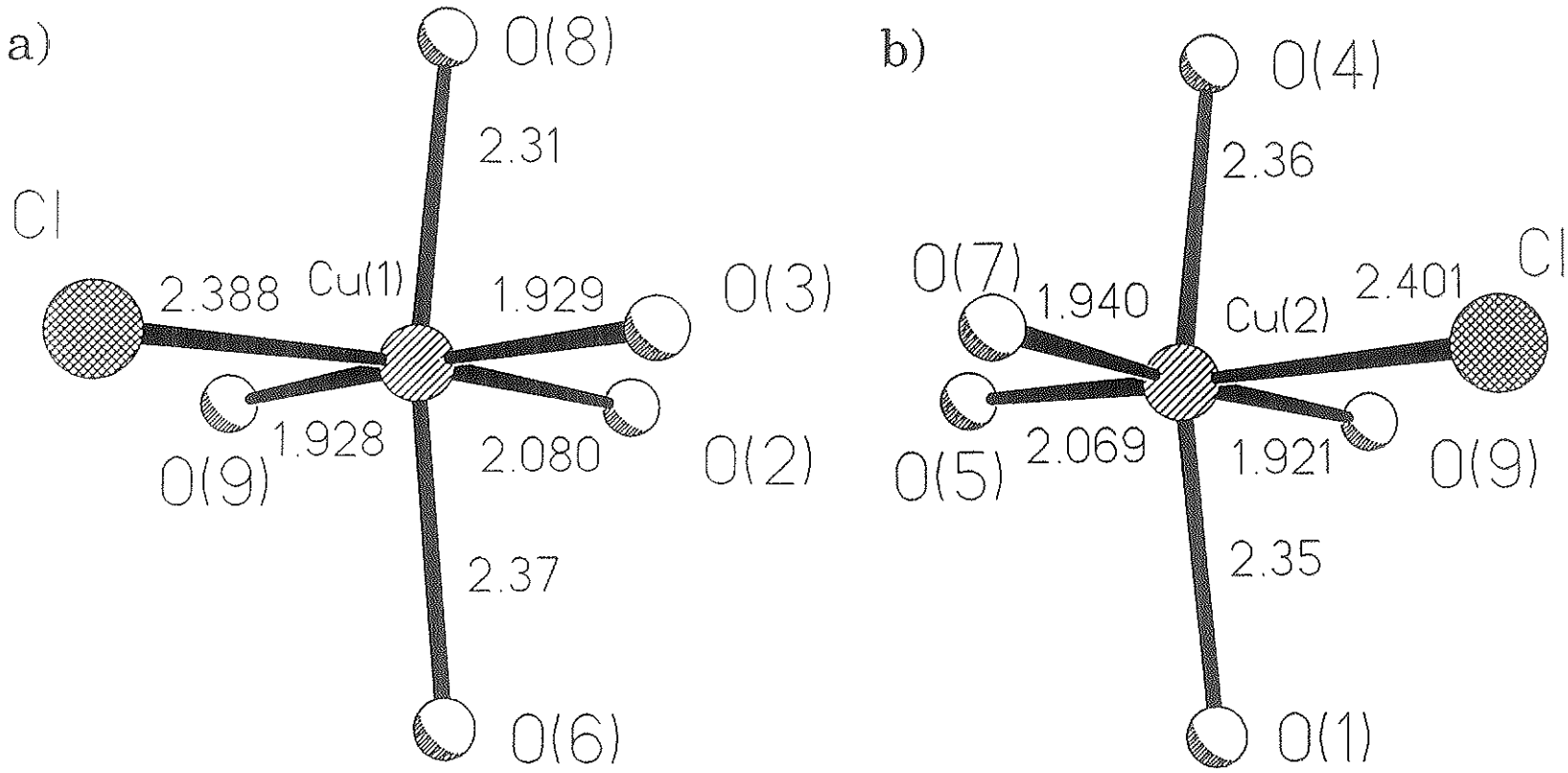

Figure 9.4. The $Cu^{2+}\Phi_6$ octahedra in kamchatkite. a) $Cu(1)\Phi_6$; b) $Cu(2)\Phi_6$; distances in Å.

Table 9.5 Mixed-ligand $Cu^{2+}\Phi_6$ octahedra in Cu^{2+} oxysalt minerals with $\Phi = 2(O^{2-}, OH^-, H_2O) + 4Cl$.

		O^{2-}, OH^-, H_2O (Å)			Cl (Å)			Ref.
Eriochalcite	Cu	1.925	1.925	2.275	2.275	2.938	2.938	1
Chlorothionite	Cu	2.019	2.001	2.252	2.237	3.047	3.047	2

References: 1: Engberg (1970); 2: Giacovazzo et al. (1976).

$Cu^{2+}\Phi_6$ octahedra with $\Phi = 4(O^{2-}, OH^-, H_2O) + 2(Cl)$, the Cl ligands are always located at the apical positions of (4+2)-distorted octahedra. There are no examples of octahedra with one or both Cl ligands at an equatorial position. Furthermore, there are no examples of (2+4)-distorted $Cu^{2+}\Phi_6$ octahedra with $\Phi = 4(O^{2-}, OH^-, H_2O) + 2(Cl)$.

In $Cu^{2+}\Phi_6$ octahedra with $\Phi = 5(O^{2-}, OH^-, H_2O) + 1(Cl)$, the single Cl ligand occurs at an apical position of the (4+2)-distorted octahedron; the other apical ligand is (O^{2-}, OH^-, H_2O), and the Cu-Φ_{ap} bond-length is usually considerably shorter than the average in $Cu^{2+}\phi_6$ octahedra. As in the case for mixed-ligand $Cu^{2+}\Phi_6$ octahedra with two Cl ligands, (2+4)-distorted octahedra do not occur. Kamchatkite shows two mixed-ligand (2+2+2)-distorted $Cu^{2+}\Phi_6$ octahedra with $\Phi = 5(O^{2-}, OH^-, H_2O)$ and 1(Cl) that do not conform to these rules, but these octahedra may result from a dynamic Jahn-Teller effect.

Cu^{2+} minerals containing $Cu^{2+}\Phi_6$ with $\Phi = 2(O^{2-}, OH^-, H_2O) + 4(Cl)$ are rare, only two examples are known. Both minerals contain $Cu^{2+}\Phi_6$ octahedra with Cl ligands at the apical positions and at two *trans* equatorial positions.

Examination of mixed-ligand $Cu^{2+}\Phi_6$ octahedral geometries in Cu^{2+} minerals has again illustrated the influence of the Jahn-Teller effect on the detailed stereochemistry of Cu^{2+} minerals. Every mixed-ligand $Cu^{2+}\Phi_6$ octahedron in minerals shows a strong pseudo-Jahn-Teller distortion, although this observation is somewhat masked by the complex nature of these octahedra. Also notable is the very strong preferences of Cl ligands for the apical positions of (4+2)-distorted octahedra. With the exception of

the octahedra in kamchatkite, Cl ligands are located at the apical positions whenever possible.

Chapter 10

Ab Initio Molecular-Orbital Studies of $Cu^{2+}\Phi_6$ Mixed-Ligand Octahedra

10.1 Introduction

Molecular-orbital calculations designed to study the Jahn-Teller distortion of $Cu^{2+}\phi_6$ ($\phi = O^{2-}$, OH^-, H_2O) octahedra are quite successful in predicting the general $Cu^{2+}\phi_6$ geometries observed in minerals (Chapter 4). Hartree-Fock calculations for the $[Cu^{2+}(OH)_6]^{4-}$ cluster done using the STO-3G* basis-set provided a potential-energy surface for the octahedron that included Jahn-Teller effects. This potential surface was then used to derive a potential-energy function designed to describe the energetics of a $Cu^{2+}\phi_6$ octahedron embedded in a crystal. The potential proved effective in the calculation of Cu^{2+} oxysalt mineral structures (Chapter 6). In the MO calculations, each of the octahedral ligands were equivalent and the Jahn-Teller theory was applicable to these systems.

Mixed-ligand $Cu^{2+}\Phi_6$ ($\Phi = O^{2-}$, OH^-, H_2O and a least 1 Cl) octahedra are the subject of this chapter. As the ligands in these octahedra are generally not equivalent, a strictly holosymmetric octahedral coordination about Cu^{2+} cannot occur, and Jahn-Teller theory is not directly applicable to these systems. However, the near-degenerate electronic state present in $Cu^{2+}\Phi_6$ octahedra may cause significant distortion of octahedral geometries, with the effect referred to as the pseudo-Jahn-Teller effect. The mixed-ligand nature of these octahedra makes identification of the distortion types rather tricky. However, comparison with ideal undistorted octahedral bond-lengths and the (4+2)-distorted $Cu^{2+}Cl_6$ octahedral bond-lengths in

tolbachite has allowed identification of the distortion types of all mixed-ligand $Cu^{2+}\Phi_6$ geometries occurring in minerals (Chapter 9).

10.2 Molecular-Orbital Studies of Mixed-Ligand $Cu^{2+}\Phi_6$ Octahedra

Hartree-Fock MO calculations were done for various clusters and basis-set combinations designed to model $Cu^{2+}\Phi_6$ mixed-ligand octahedra in minerals. The purpose of these calculations is to:

(1) Determine if Hartree-Fock MO calculations are able to predict the distortion geometries observed for $Cu^{2+}\Phi_6$ mixed-ligand octahedra in minerals.

(2) Determine the relative energetics of the various possible distortion geometries of $Cu^{2+}\Phi_6$ octahedra.

(3) Calculate potential-energy surfaces for $Cu^{2+}\Phi_6$ octahedra. These surfaces may later be used to derive potential functions for these octahedra, allowing the calculation of mixed-ligand $Cu^{2+}\Phi_6$ structures.

All calculations reported in this chapter were done with Gaussian 86 (Frisch et al., 1984) and Gaussian 92 (Frisch et al., 1992). The Hartree-Fock calculations reported are all UHF (spin-unrestricted) calculations with no spin contamination present in the final wavefunction. Convergence criteria for optimized geometries were the same as previously reported (Chapters 4 and 7); the basis-sets used in these calculations are described in Chapter 3.

10.2.1 Molecular-Orbital Calculations for $Cu^{2+}\Phi_6$ Mixed-ligand Octahedra with $\Phi = 4(O^{2-}, OH^-, H_2O) + 2(Cl)$.

Several Hartree-Fock calculations were done for clusters designed to model $Cu^{2+}\Phi_6$ with $\Phi = 4(O^{2-}, OH^-, H_2O) + 2(Cl)$. As this combination is the most common type of $Cu^{2+}\Phi_6$ mixed-ligand octahedron in minerals, considerable effort was expended in order to find the cluster and basis-set combination that best predicts the geometries of these octahedra.

The first cluster chosen was the neutral $[Cu^{2+}(H_2O)_4Cl_2]$ cluster (Fig. 10.1). Geometry optimizations for this cluster were done with the constraint that both Cu-Cl apical bond-lengths be equivalent, and that each Cu-(H_2O) equatorial bond-length be equivalent. The H-O-H bond-angles were fixed at 104.5° and the H-O bond-lengths at 0.957 Å. Optimized geometries (Table 10.1) were obtained using various basis-set combinations: STO-3G* on all atoms; 3-21G* on all atoms; STD-SET(1) on Cu^{2+} and 3-21G* on all other atoms; DZC-SET(1) on Cu^{2+} and 3-21G* on all the other atoms.

The optimized geometries for the $[Cu^{2+}(H_2O)_4Cl_2]$ cluster are compared to $Cu^{2+}\Phi_6$ [$\Phi = 4(O^{2-}, OH^-, H_2O) + 2(Cl)$] octahedral geometries in minerals in Table 10.1. With the exception of the calculation done using the 3-21G* basis-set on all atoms, all geometries have Cu-Cl distances that are shorter than the range observed in minerals. The STO-3G* basis-set performs the poorest in this regard, giving a Cu-Cl distance 0.57 Å shorter than the corresponding average distance observed in minerals. Geometries obtained using the STO-3G* basis-set, the STD-SET(1) and 3-21G* basis-set combination, and the DZC-SET(1) and 3-21G* basis-set combination all have Cu-(H_2O) distances within the range observed in minerals (Table 10.1).

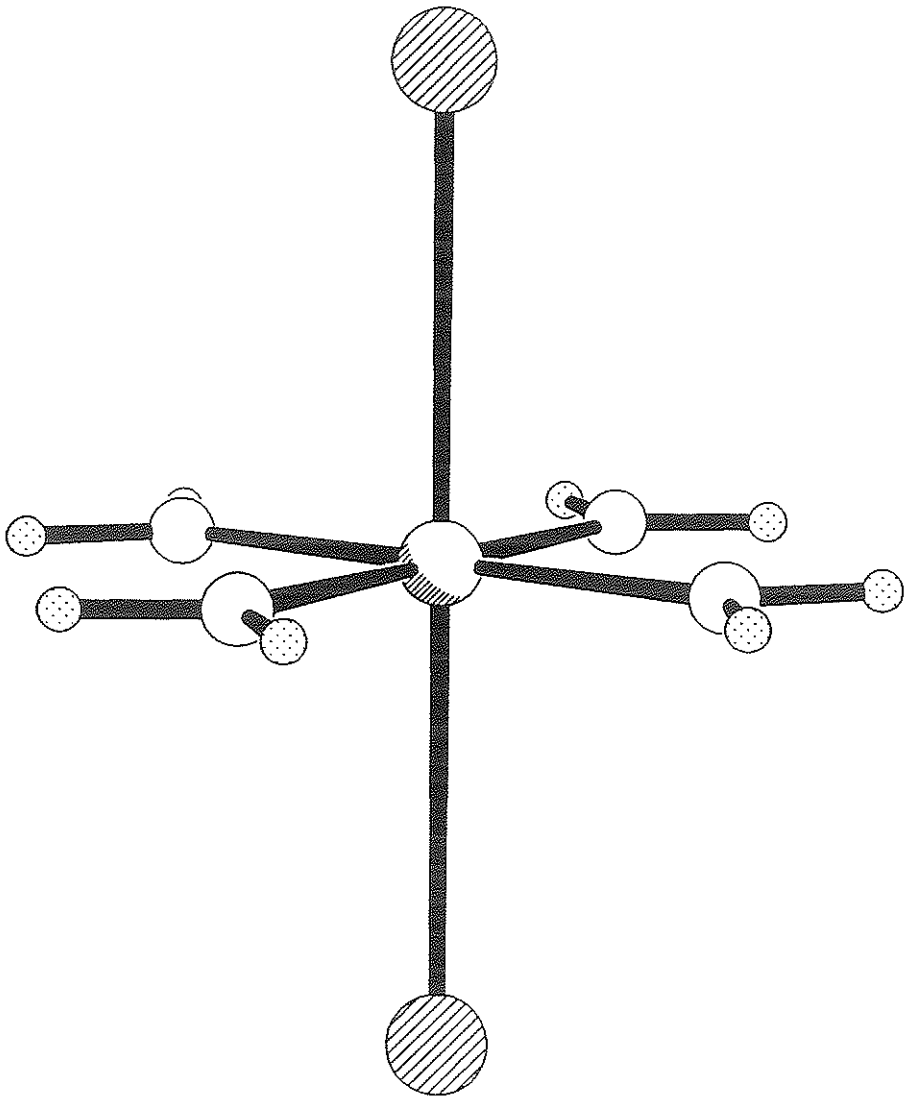

Figure 10.1. The $[Cu^{2+}(H_2O)_4Cl_2]$ cluster. Chlorine atoms are shaded with parallel lines, oxygen atoms are open circles, hydrogen atoms are shaded with a regular dot pattern and the copper atom is an open circle with shading in the lower left corner.

Table 10.1 Optimized geomtries for $Cu^{2+}\Phi_6$ mixed-ligand octahedra with $\Phi = 4(O^{2-}, OH^-, H_2O) + 2(Cl)$.

$[Cu^{2+}(H_2O)_4(Cl)_2]$ Cluster			
Basis Set	Cu-O	Cu-Cl	Energy (Hartrees+)
STO-3G*	2.055 (Å)	2.287 (Å)	-2831.1590
3-21G*	2.192	2.955	-2848.2710
STD-SET(1) (Cu^{2+}) 3-21G* (Cl^-, O^{2-}, H^+)	2.025	2.516	-2848.0676
DZC-SET(1) (Cu^{2+}) 3-21G* (Cl^-, O^{2-}, H^+)	2.053	2.495	-2848.6847

$[Cu^{2+}(H_2O)_4(ClH)_2]^{2+}$ Cluster			
Basis Set	Cu-O	Cu-Cl	Energy (Hartrees)
STO-3G*	1.951	2.600	-2831.9120
3-21G*	1.895	3.023	-2848.0344
STD-SET(1) (Cu^{2+}) 3-21G* (Cl^-, O^{2-}, H^+)	1.904	2.985	-2848.7160
LANL1DZ	2.023	3.120	

Mineral Data		
	Cu-O	Cu-Cl
Range	1.90-2.11	2.553-3.206
Average	1.978	2.857
1σ	0.045	0.170

+ 1 Hartree = 2625.4997 kJ/mole

Calculations using the 3-21G* basis-set result in a reasonable description of the Cu-Cl bond-lengths, but fail to give Cu-(H_2O) distances within the range observed in minerals (Table 10.1). Thus, *none* of the calculations for the $[Cu^{2+}(H_2O)_4Cl_2]$ cluster result in geometries compatible with those observed in mineral structures.

The inadequacy of the $[Cu^{2+}(H_2O)_4Cl_2]$ cluster for describing $Cu^{2+}\Phi_6$ mixed-ligand octahedral geometries may be rationalized on the basis of bond strengths. The equatorial ligands are H_2O groups, and the oxygen atoms must contribute about 0.8 valence units to each H atom. This leaves only about 0.4 valence units for the Cu-O bond. However, the apical Cl ligands may contribute up to a full valence unit to the Cu-Cl bond. The calculations for this cluster result in shorter Cu-Cl and longer Cu-O distances than expected, in response to the unbalanced bond-strengths associated with each Cu-ligand pair. This inadequacy in the model can be, at least partially, removed by attaching H to the Cl ligands, effectively lowering the valence units associated with the Cu-Cl bonds and simulating interactions that occur when the polyhedron is embedded in the structure.

Hartree-Fock MO calculations were done for the $[Cu^{2+}(H_2O)_4(ClH)_2]^{2+}$ cluster (Fig. 10.2). Geometry optimizations were done using the same constraints as for the $[Cu^{2+}(H_2O)_4(Cl)_2]$ cluster, with optimization including the Cl-H bond-lengths and the Cu-Cl-H angles. Optimized geometries (Table 10.1) were obtained using the following basis-set combinations: STO-3G* on all atoms; 3-21G* on all atoms; STD-SET(1) on Cu^{2+} and 3-21G* on the other atoms; the LANL1DZ Los Alamos National Laboratory effective core potential and valence double-zeta basis-set.

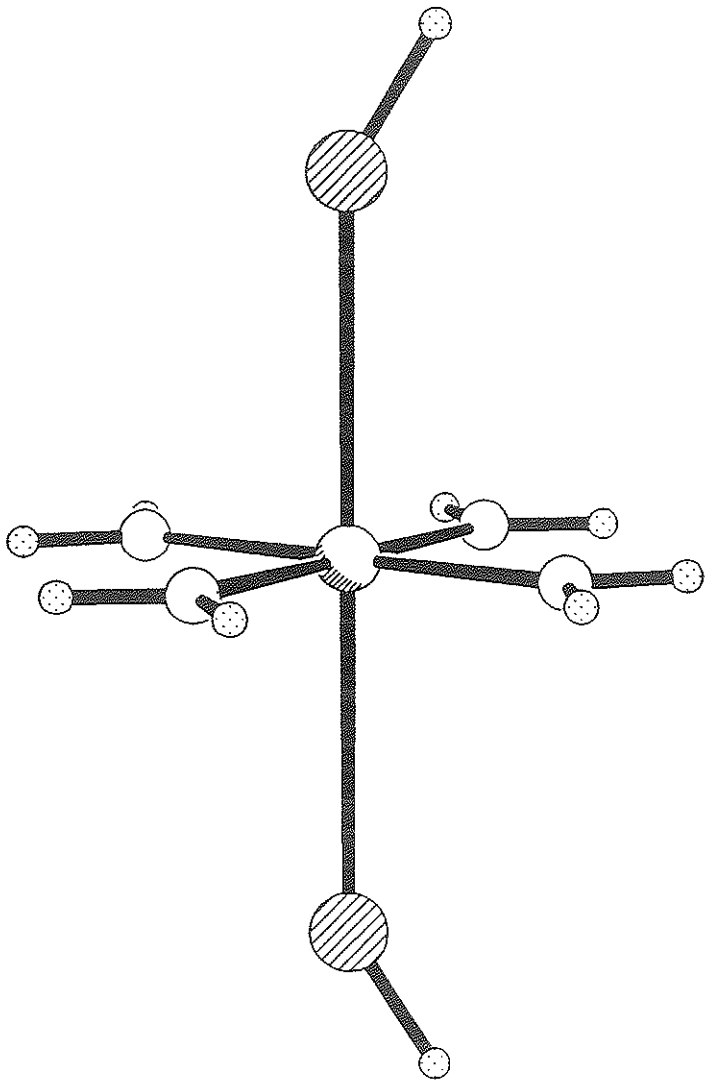

Figure 10.2. The $[Cu^{2+}(H_2O)_4(ClH)_2]^{2+}$ cluster. Legend as in Fig. 10.1.

Optimized geometries for the $[Cu^{2+}(H_2O)_4(ClH)_2]^{2+}$ cluster are compared to $Cu^{2+}\Phi_6$ octahedral geometries observed in minerals in Table 10.1. Each basis-set combination resulted in optimized Cu-O and Cu-Cl bond-lengths that fall within the range observed in minerals. Considerable variability in the calculated bond-lengths occurs, with the Cu-O distances ranging from 1.895 Å (3-21G*) to 2.023 Å (LANL1DZ) and Cu-Cl bond-lengths from 2.600 Å (STO-3G*) to 3.120 Å (LANL1DZ) (Table 10.1). The STO-3G* basis-set calculations gave Cu-O bond-lengths that agree with the average Cu-O bond-length in $Cu^{2+}\Phi_6$ [Φ = 4(O^{2-}, OH^-, H_2O) and 2(Cl)] octahedra in minerals, but the Cu-Cl distance is 0.257 Å shorter than the average observed for minerals. The LANL1DZ basis-set resulted in Cu-O and Cu-Cl bond-lengths that are consistently longer than those observed in minerals. The calculations using the 3-21G* basis-set on all atoms, and the calculation using the STD-SET(1) basis-set on Cu^{2+} with the 3-21G* basis-set on the other atoms lead to similar optimized geometries. The calculated Cu-Cl bond-lengths are close to the average observed in $Cu^{2+}\Phi_6$ [Φ = 4(O^{2-}, OH^-, H_2O) and 2(Cl)] octahedra in minerals, but the calculated Cu-O distances are somewhat shorter than the average observed in minerals. Based upon the mean absolute deviation of calculated octahedral bond-lengths from the average observed in $Cu^{2+}\Phi_6$ [Φ = 4(O^{2-}, OH^-, H_2O) and 2(Cl)] octahedra in minerals, it may be concluded that the combination of the STD-SET(1) basis-set on Cu^{2+} and 3-21G* basis-set on the rest of the atoms results in the best geometry. Furthermore, the lowest cluster energy is obtained when this basis-set combination is used.

Each of the optimized geometries obtained using Hartree-Fock calculations for the $[Cu^{2+}(H_2O)_4(ClH)_2]^{2+}$ cluster include pseudo-Jahn-Teller

distortions, as they are all-electron MO calculations. The bond-lengths expected for a $Cu^{2+}\Phi_6$ [Φ = 4(O^{2-}, OH^-, H_2O) + 2(Cl)] octahedron that is not distorted by a pseudo-Jahn-Teller effect are <Cu^{2+}-(O^{2-}, OH^-, H_2O)> = 2.083 Å (Chapter 2) and <Cu-Cl> = 2.43 Å (Chapter 9). Comparison of these bond-lengths and those of the optimized clusters (Table 10.1) shows that all of the optimized cluster geometries are (4+2)-distorted octahedra. Searches were conducted for a second energy minimum, corresponding to a (2+4)-distorted octahedron, but none was found.

A potential-energy surface was calculated for the $[Cu^{2+}(H_2O)_4(ClH)_2]^{2+}$ cluster using Hartree-Fock theory and the STD-SET(1) basis-set on Cu^{2+} and the 3-21G* basis-set on the other atoms (Fig. 10.3). The potential surface was calculated for a Cu-(H_2O) - Cu-Cl bond-length grid containing 160 points, with Cu-(H_2O) distances ranging from 1.80 to 2.15 Å and Cu-Cl distances ranging from 2.35 to 3.30 Å. Only one energy minimum, corresponding to a (4+2)-distorted octahedron, occurs on the potential-energy surface (Fig. 10.3). The potential has a much stronger curvature parallel to the Cu-(H_2O) equatorial axis than parallel to the apical axis. This is in line with the narrow range of Cu-(O^{2-}, OH^-, H_2O) equatorial bond-lengths compared to the broad range of Cu-Cl apical bond-lengths observed in $Cu^{2+}\Phi_6$ [Φ = 4(O^{2-}, OH^-, H_2O) + 2(Cl)] in minerals.

The potential-energy surface for the $[Cu^{2+}(H_2O)_4(ClH)_2]^{2+}$ cluster may be compared to the potential-energy surface reported earlier for the $[Cu^{2+}(OH)_6]^{4-}$ cluster (Fig. 5.1). Most notably, the minimum corresponding to a (2+4)-distorted octahedron and the saddle axis separating the (4+2) and (2+4)-octahedral-distortion minima in the $[Cu^{2+}(OH)_6]^{4-}$ potential are absent in the $[Cu^{2+}(H_2O)_4(ClH)_2]^{2+}$ potential surface. Both potential surfaces have

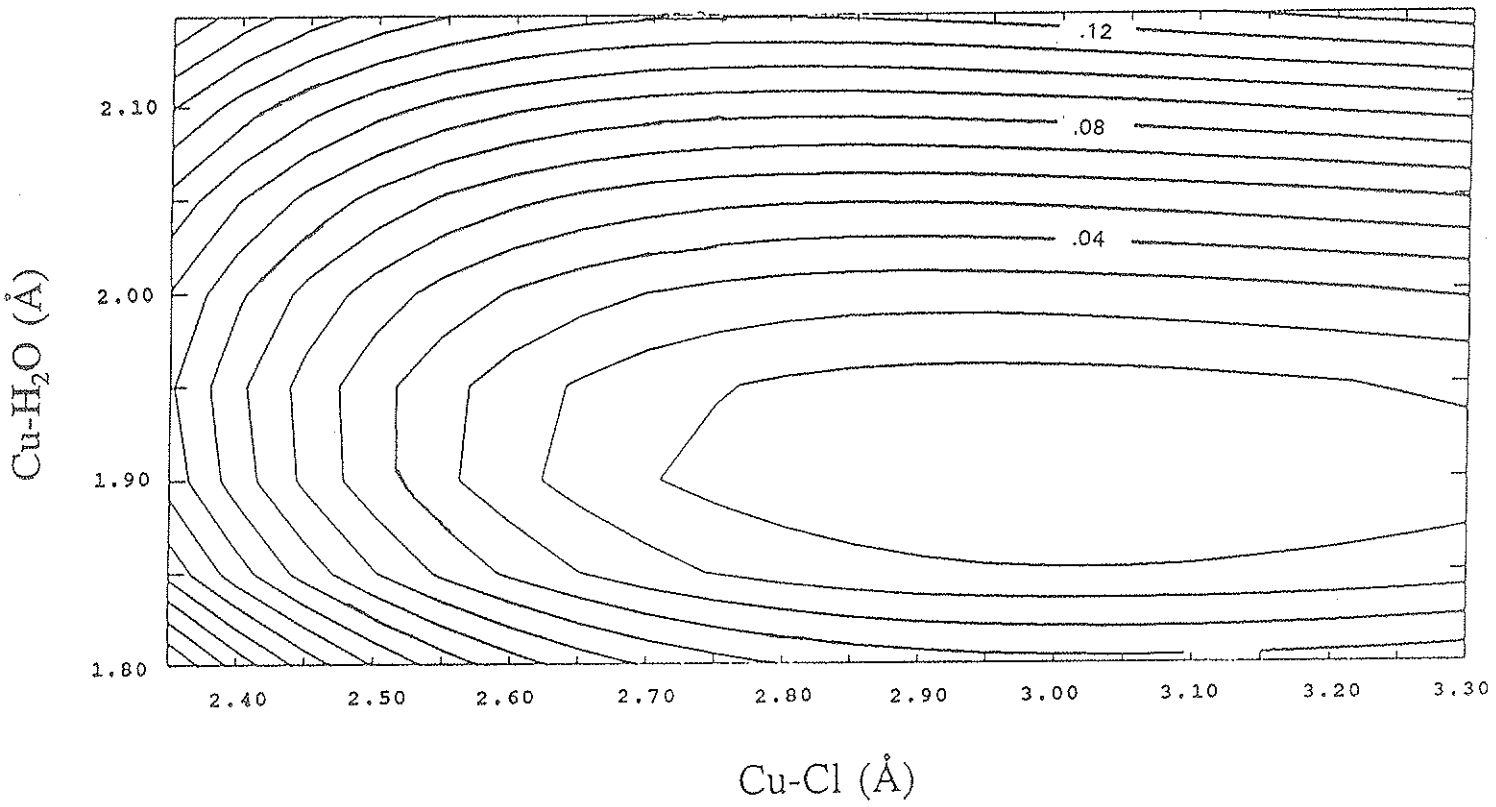

Figure 10.3. The potential-energy surface calculated for the $[Cu^{2+}(H_2O)_4(ClH)_2]^{2+}$ cluster using the STD-SET(1) basis set on copper and the 3-21G* basis-set on oxygen, chlorine and hydrogen. The contour interval is 0.01 Hartrees. 1 Hartree = 2625.4997 KJ/mole.

similar shapes in the area of the (4+2)-distortion minimum. However, the (4+2) minimum in the $[Cu^{2+}(H_2O)_4(ClH)_2]^{2+}$ potential surface occurs at considerably shorter equatorial and longer apical bond-lengths than the (4+2) minimum in the $[Cu^{2+}(OH)_6]^{4-}$ potential surface. The longer apical bond-lengths correspond to Cu-Cl bonds, compared to Cu-OH bonds in the $[Cu^{2+}(OH)_6]^{4-}$ cluster. However, it is not clear why the equatorial Cu-(H_2O) bond-lengths in the $[Cu^{2+}(H_2O)_4(ClH)_2]^{2+}$ cluster are significantly shorter than the equatorial Cu-OH bond-lengths in the $[Cu^{2+}(OH)_6]^{4-}$ cluster. It seems probable that the discrepancy results from a combination of basis-set differences and cluster-charge variation. The negative charge on the $[Cu^{2+}(OH)_6]^{4-}$ cluster is expected to result in somewhat longer octahedral bond-lengths than would a neutral cluster.

The calculations for the $[Cu^{2+}(H_2O)_4(ClH)_2]^{2+}$ cluster were done in part to examine the relative stabilities of various octahedral-distortion geometries. As already noted, there is no (2+4)-distorted octahedral energy-minimum in the potential surface, and searches to find such a minimum were unsuccessful. Calculations were also done in search of a minimum corresponding to a (4+2)-distorted geometry with H_2O groups in the apical positions, with equatorial positions occupied by two *trans* Cl ligands and two *trans* H_2O ligands. The calculations found no such minimum, and geometry optimization of the trial structures resulted in the same (4+2)-distorted octahedra with apical Cl ligands as reported earlier (Table 10.1).

10.2.2 Molecular-Orbital Calculations for $Cu^{2+}\Phi_6$ Mixed-Ligand Octahedra with $\Phi = 5(O^{2-}, OH^-, H_2O) + 1(Cl)$.

Hartree-Fock MO calculations were done for the $[Cu^{2+}(H_2O)_5(ClH)]^{2+}$ cluster (Fig. 10.4) using the STD-SET(1) basis-set on Cu^{2+} and the 3-21G* basis-set on the other atoms, and also with the 3-21G* basis-set on all atoms. These calculations were done in an attempt to find a model that would give optimized geometries similar to $Cu^{2+}\Phi_6$ [$\Phi = 5(O^{2-}, OH^-, H_2O) + 1(Cl)$] octahedra in minerals (Table 9.4). Geometry optimizations were done with the requirement that all four of the equatorial Cu-(H_2O) bond-lengths be equivalent. The H-O-H angles were fixed at 104.5° and the H-O bond-lengths at 0.957 Å. The Cl-H bond-length and Cu-Cl-H angle were included in the optimization.

The optimized geometries for the $[Cu^{2+}(H_2O)_5(ClH)]^{2+}$ cluster are compared to the $Cu^{2+}\Phi_6$ [$\Phi = 5(O^{2-}, OH^-, H_2O) + 1(Cl)$] octahedra in minerals in Table 10.2. Both of these calculations give results that are fairly consistent with observed $Cu^{2+}\Phi_6$ [$\Phi = 5(O^{2-}, OH^-, H_2O) + 1(Cl)$] geometries in minerals (Table 10.2). The clusters optimized to (4+2)-distorted octahedra, and the Cl ligand is at the apical position in each case. The optimized Cu-O_{eq} distances fall well below the average distance in minerals, but the optimized distances are within that range observed in minerals. The optimized Cu-O_{ap} distances are considerably shorter than the average observed in minerals and they fall below that range. However, the short Cu-O_{ap} distances predicted by the calculations are in line with the observation that the Cu-O_{ap} distances in $Cu^{2+}\Phi_6$ [$\Phi = 5(O^{2-}, OH^-, H_2O) + 1(Cl)$] octahedra tend to be shorter than those observed in $Cu^{2+}\phi_6$ octahedra (Chapter 9). Calculated Cu-Cl bond-lengths are close to, but outside, the

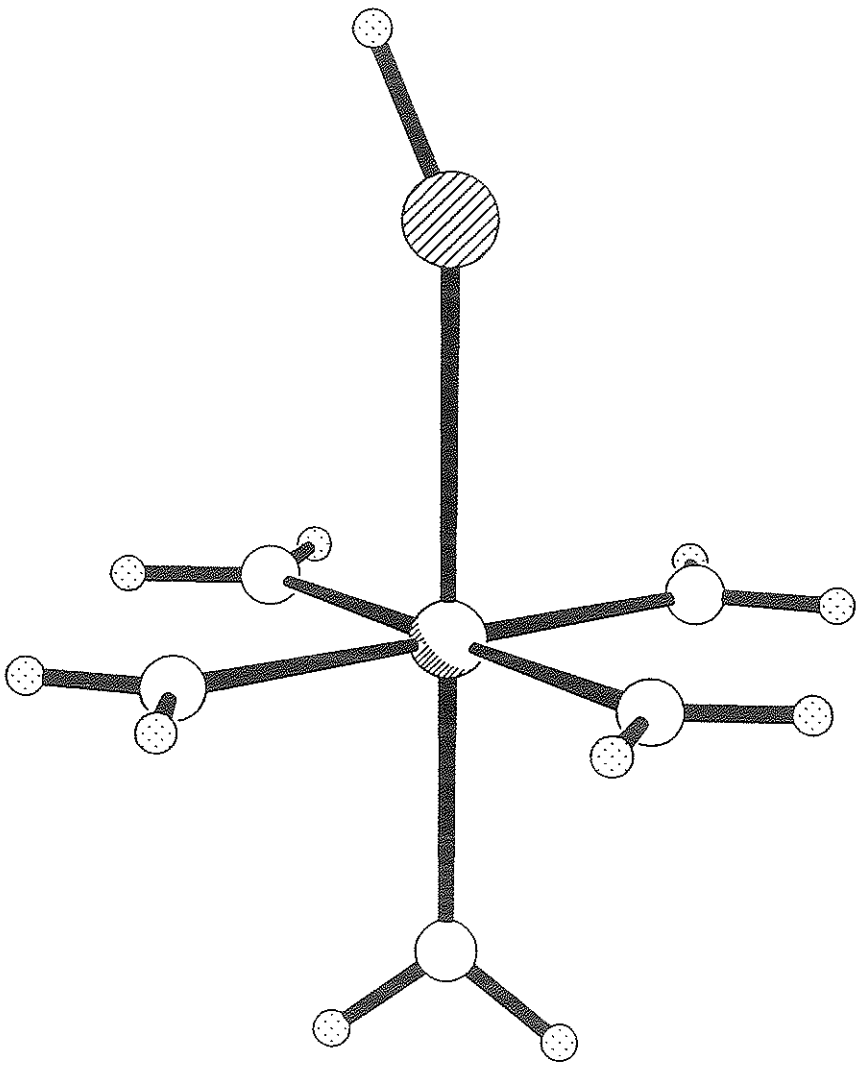

Figure 10.4. The $[Cu^{2+}(H_2O)_5(ClH)]^{2+}$ cluster. Legend as in Fig. 10.1.

Table 10.2 Optimized geometries for $Cu^{2+}\Phi_6$ mixed-ligand octahedra with $\Phi = 5(O^{2-}, OH^-, H_2O) + 1(Cl)$

$[Cu^{2+}(H_2O)_5(ClH)]^{2+}$				
Basis Set	$Cu\text{-}O_{eq}$	$Cu\text{-}O_{ap}$	Cu-Cl	Energy (Hartrees+)
STD-SET(1) (Cu^{2+}) 3-21G* (Cl^-, O^{2-}, H^+)	1.933 (Å)	2.130 (Å)	2.851	-2466.0795
3-21G*	1.921	2.117	3.056	-2465.4004
Range in Minerals++	1.92-2.20	2.20-2.91	2.732-2.835	
Average++	1.982	2.452	2.777	

+ 1 Hartree = 2625.4997 kJ/mole
++ Excluding the octahedra in kamchatkite

range observed in minerals. The optimized Cu-Cl distances obtained using the STD-SET(1) basis-set on Cu^{2+} and the 3-21G* basis-set on Cl, O^{2-}, H^{+} are quite similar to the values observed in minerals. Also, the cluster energy obtained using this basis-set combination is considerably lower than that obtained using the 3-21G* basis-set on all atoms (Table 10.2).

As was the case with the $Cu^{2+}\Phi_6$ [Φ = 4(O^{2-}, OH^{-}, H_2O) + 2(Cl)] calculations, these calculations indicate that there is no energy minimum corresponding to a (2+4)-distorted $Cu^{2+}\Phi_6$ [Φ = 5(O^{2-}, OH^{-}, H_2O) + 1(Cl)] octahedron. Searches for such a minimum were unsuccessful, and geometry optimization commencing from various starting geometries all resulted in a (4+2)-distorted octahedral geometry. Attempts to optimize the geometry for a cluster having the Cl ligand at an equatorial position were also unsuccessful.

A three-dimensional potential-energy surface was calculated for the $[Cu^{2+}(H_2O)_5(ClH)]^{2+}$ cluster using the STD-SET(1) basis-set on Cu^{2+} and the 3-21G* basis-set on the other atoms. The Hartree-Fock energies were calculated for 520 combinations of Cu-O_{eq}, Cu-O_{ap} and Cu-Cl. Slices of constant Cu-Cl through the three-dimensional potential are given in Figure 10.5. The potential-energy minimum is strongly anisotropic, with considerable elongation along the Cu-O_{ap} direction. This elongation is consistent with the range of Cu-O_{ap} bond-lengths in $Cu^{2+}\Phi_6$ [Φ = 5(O^{2-}, OH^{-}, H_2O) + 1(Cl)] octahedra in minerals. The relatively steep potential shape in the Cu-O_{eq} bond direction is also consistent with the relatively narrow range of these bond-lengths in $Cu^{2+}\Phi_6$ [Φ = 5(O^{2-}, OH^{-}, H_2O) + 1(Cl)] octahedra in minerals.

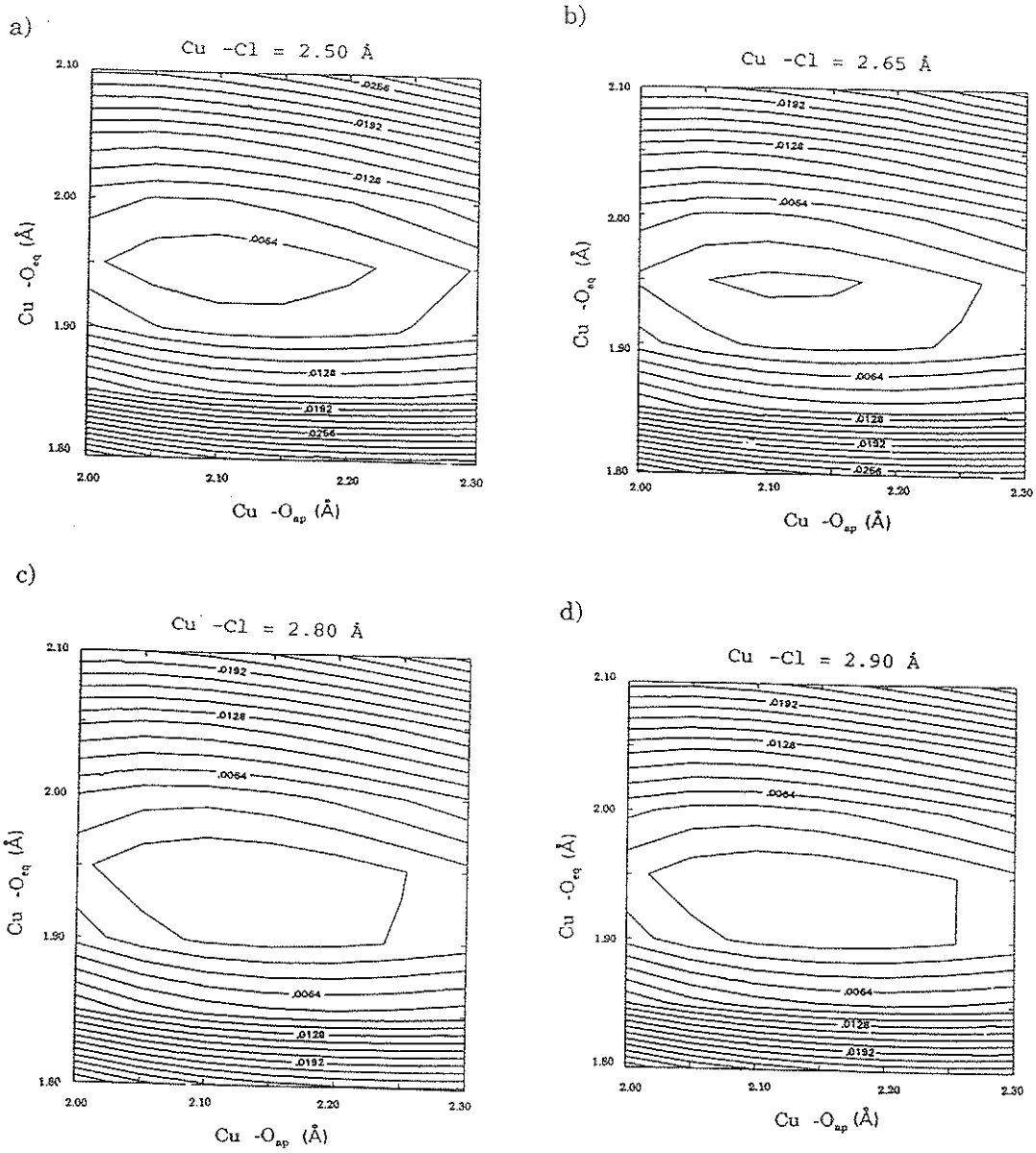

Figure 10.5 Slices of the potential-energy surface calculated for the $[Cu^{2+}(H_2O)_5(ClH)]^{2+}$ cluster using the STD-SET(1) basis-set on copper and the 3-21G* basis-set on oxygen, chlorine and hydrogen. The slices are for constant Cu-Cl distances: a) Cu-Cl = 2.50 Å; b) Cu-Cl = 2.65 Å; c) Cu-Cl = 2.80 Å; d) Cu-Cl = 2.90 Å. The contour interval is 0.0016 Hartrees. 1 Hartree = 2625.4997 KJ/mole.

10.3 Discussion

The MO calculations reported here show that the Hartree-Fock treatment predicts mixed-ligand $Cu^{2+}\Phi_6$ geometries consistent with those observed in minerals. The pseudo-Jahn-Teller effect has generally been appropriately described by these calculations, and the calculated potential surfaces agree well with the $Cu^{2+}\Phi_6$ octahedral geometry trends observed in minerals.

All the MO calculations for mixed-ligand octahedra indicate that there is no energy minimum corresponding to a (2+4)-distortion, unlike the calculations for $Cu^{2+}\phi_6$ octahedra (Chapter 4) which predicted potential minima corresponding to both (4+2)- and (2+4)-distorted geometries.

Chapter 11

Solid-Solution in Cu^{2+} Oxysalt Minerals

11.1 Introduction

Substitutional solid-solution is common in minerals, and is largely dependent upon the ionic radii of the ions involved. The solid-solution may be complete if the substituents have radii within 15% of each other. This being the case, substitution of Mg^{2+}, Ni^{2+} and Zn^{2+} for Cu^{2+} in oxysalt minerals is predicted; Each of these cations is divalent and the radii are similar to that of Cu^{2+} [Mg^{2+} = -1.4%, Ni^{2+} = -5.8%, Zn^{2+} = +1.4%; Shannon (1976)]. However, examination of chemical analyses and structure refinements available in the literature shows that such extensive solid-solution is *not* evident in Cu^{2+} oxysalt minerals. With a few conspicuous exceptions, Cu^{2+} oxysalt minerals do *not* show significant substitutional solid-solution involving the Cu^{2+} site.

None of the Mg^{2+}, Ni^{2+} (high spin) or Zn^{2+} cations have an energetically degenerate electronic ground state in an octahedral field, and thus the Jahn-Teller theorem does not apply. In the absence of steric effects, these cations will occur in regular octahedral environments, in contrast with the strongly (4+2)-distorted octahedral environment typical of Cu^{2+}. It is this difference in octahedral geometries that leads to the lack of substitutional solid-solution in Cu^{2+} oxysalt minerals.

The structural relationship between a Cu^{2+} oxysalt and its non-Cu^{2+} analogue will dictate the amount of substitutional solid-solution that may occur. There are four possibilities:

Type (I) Structures: The Cu^{2+} oxysalt structure is strictly isostructural with the non-Cu^{2+} analogue. This may occur for one of two reasons (Eby, 1988):

(a) The bonding within the structures is sufficiently flexible to allow considerable octahedral-site geometry variability.

(b) The non-Cu^{2+} structure contains a (4+2)-distorted octahedron due to bond-valence effects.

In either case, complete or nearly complete solid-solution involving the Cu^{2+} site may occur.

Type (II) Structures: The Cu^{2+} oxysalt structure is a lower-symmetry distortion of the non-Cu^{2+} structure, and the connectivity of the structures is identical. In this case, the structural connectivity is compatible with either a regular or (4+2)-distorted octahedral environment, but the lower symmetry of the Cu^{2+} phase is required to accommodate the (4+2)-distorted octahedron. Substitutional solid-solution involving the Cu^{2+} site may occur, and a second-order phase transition must occur at some point in the series.

Type (III) Structures: The Cu^{2+} structure shows a different connectivity than the non-Cu^{2+} analogue. Regular and (4+2)-distorted octahedra are not compatible with the same structural connectivity. Thus, substitutional solid-solution involving the Cu^{2+} site will be limited or absent.

Type (IV) Structures: The Cu^{2+} structure shows a different connectivity than the non-Cu^{2+} analogue, but the connectivity allows some (but not all) of the octahedral sites to be either (4+2)-distorted or more regular. More extensive (but limited) solid-solution may occur, until such flexible octahedral sites are filled with the substituent ion.

11.2 The Substitution $M^{2+} \leftrightarrow Cu^{2+}$ in Cu^{2+} Oxysalt Minerals.

The substitution $M^{2+} \leftrightarrow Cu^{2+}$ (M^{2+} = divalent cation) has been observed in a small number of Cu^{2+} oxysalt minerals. The substitution $Zn \leftrightarrow Cu^{2+}$ is by far the most common, and constitutes the only cases of $M^{2+} \leftrightarrow Cu^{2+}$ substitution in Cu^{2+} oxysalt minerals that have been verified by a crystal-structure refinement. Other possible examples of solid-solution in Cu^{2+} oxysalt minerals involve $M^{2+} = Fe^{2+}$, Ni and Mg.

11.2.1 M^{2+} = Zn

Perhaps the best documented example of $Zn \leftrightarrow Cu^{2+}$ substitution is in the descloizite [$PbZn(OH)VO_4$] - mottramite [$PbCu^{2+}(OH)VO_4$] series, in which the solid-solution seems to be complete (Van der Westhuizen et al., 1986). Only the crystal structure of descloizite has been refined, but X-ray data indicates that the end members are isostructural (Van der Westhuizen et al., 1986), and thus they are type (I) structures.

Kipushite, $(Cu^{2+},Zn)_6(PO_4)_2(OH)_6{\cdot}H_2O$, shows a range of Cu^{2+}:Zn ratios from 2.6:1 to 1.1:1 (Piret et al., 1985). The structure contains a sheet of tetrahedra of composition $[Zn(PO_4)OH]_n^{2n-}$, and two mixed sheets of $[(Cu^{2+},Zn)_5(OH)_5(H_2O)PO_4]_n^{2n-}$ composition which contain five $Cu^{2+}\phi_6$

octahedra and one tetrahedrally coordinated P (Piret et al., 1985). The chemical analyses gave an excess of Zn over what is required to fill the tetrahedral site, and a deficiency in the amount of Cu^{2+} needed to fill the octahedral sites. The excess Zn must occur at the octahedral sites, and there is partial ordering at three of the possible five sites (Piret et al., 1985). The Zn analogue of kipushite is not known; presumably this is an example of a type (IV) structure.

Philipsburgite, $(Cu^{2+},Zn)_6(AsO_4,PO_4)_2(OH)_6 \cdot H_2O$, is isostructural with kipushite, and also contains Zn in excess of the tetrahedral-site requirements (Peacor et al., 1985). The additional Zn must substitute at the Cu^{2+} octahedral sites, but the structure has not been refined. Again, philipsburgite is presumably a type (IV) structure.

Veszelyite, $(Cu^{2+}_{1.77}Zn_{0.24})ZnPO_4(OH)_3 \cdot 2H_2O$, is structurally related to kipushite and philipsburgite. It also contains Zn in excess of the amount required to fill the single tetrahedral site, and the excess Zn substitutes for Cu^{2+} in octahedral coordination; structure refinement showed that the excess Zn is distributed equally over the octahedral sites (Ghose et al., 1974).

The sulfates serpierite, ktenasite and ramsbeckite all show considerable $Zn \leftrightarrow Cu^{2+}$ substitution. The Zn analogues are not known for any of these minerals, suggesting that they all have type (IV) structures. Sabelli and Zanazzi (1968) determined the structure of serpierite with composition $Ca(Cu^{2+}_{0.66}Zn_{0.34})_4(OH)_6(SO_4)_2 \cdot 3H_2O$. Serpierite contains octahedrally coordinated cations which share six edges with adjacent octahedra, forming close-packed sheets. Cation ordering is significant: one octahedral site contains only Zn, and the remaining Zn is distributed over

the other four octahedral sites, possibly in a partially ordered arrangement (Sabelli and Zanazzi, 1968). The ktenasite structure (Mellini and Merlino, 1978) was solved for a crystal with composition $Zn_2(Cu^{2+}_{5.2}Zn_{2.8})(SO_4)_4(OH)_{12}\cdot 12H_2O$. It is made up of corrugated sheets of Cu^{2+} octahedra linked to SO_4 tetrahedra by corner sharing. Isolated $Zn\phi_6$ octahedra are sandwiched between these corrugated composite layers. There is also Zn substitution at the two octahedral Cu^{2+} sites, with ordering of Zn at the Cu(1) site suggested by the observed bond-lengths (Mellini and Merlino, 1978). The structure of ramsbeckite, $(Cu^{2+},Zn)_{15}(OH)_{22}(SO_4)_4\cdot 6H_2O$ with Cu:Zn = 2.9:1 was solved by Effenberger (1988b). The structure contains eight octahedral sites connected by edge sharing to form sheets, which in turn are interconnected through SO_4 tetrahedra and hydrogen bonding. Of the eight octahedral sites, bond-length considerations show that four contain Cu^{2+}, two contain only Zn, and the other two contain both Cu^{2+} and Zn.

Published chemical analyses indicate that a number of additional Cu^{2+} oxysalt minerals show $Zn \leftrightarrow Cu^{2+}$ substitution, but none of these analyses are accompanied by structural data, and it is not possible to be sure of the extent of $Zn \leftrightarrow Cu^{2+}$ substitution at any site in the structure. Examples include clareite $[(Cu^{2+}_{2.56}Zn_{0.38}Mn_{0.06})CO_3(OH)_4\cdot 4H_2O]$ (Walenta and Dunn, 1982), orthoserpierite $[Ca(Cu^{2+}_{3.54}Zn_{0.58})(SO_4)_2(OH)_6\cdot 3H_2O]$ (Sarp, 1985), namuwite $[(Zn_{2.50}Cu^{2+}_{1.49})SO_4(OH)_6\cdot 4H_2O]$, which is isostructural with $Zn_4SO_4(OH)_6\cdot 4H_2O$ (Bevins et al., 1982), and aurichalcite $[(Cu^{2+},Zn)_5(CO_3)_2(OH)_6$, Cu:Zn = 2.4:1] (Jambor and Pouliot, 1965), which is structurally related to, but not isostructural with, hydrozincite.

11.2.2 M^{2+} = Fe^{2+}, Ni and Mg

The only example of $Fe^{2+} \leftrightarrow Cu^{2+}$ substitution in a Cu^{2+} oxysalt mineral occurs in poitevinite, with composition $(Cu^{2+},Fe^{2+},Zn)SO_4 \cdot H_2O$ and Cu:Fe:Zn = 100:92:17 (Jambor et al., 1963). Poitevinite has the kieserite structure, and is an example of a type (I) structure (although the structure has not yet been refined).

The substitution $Ni \leftrightarrow Cu^{2+}$ is extensive in glaukosphaerite $[(Cu^{2+},Ni)_2(OH)_2CO_3]$ in which Cu:Ni ratios vary from 4:1 to 3:2 (Pryce and Just, 1974). The structure has not yet been refined, but it is probably isostructural with malachite, making it a type (I) structure.

Mcguinessite, $(Mg,Cu^{2+})_2(CO_3)(OH)_2$, with Mg:Cu = 54:46, 57:43 and 46:54 (Erd et al., 1981) is the only mineral that shows $Mg \leftrightarrow Cu^{2+}$ substitution. Mcguinessite is isostructural with rosasite, but the structure has not been refined.

11.3 Synthetic Cu^{2+}-Bearing Solid Solutions

Substitutional solid-solution in Cu^{2+} oxysalt minerals may be indirectly studied using synthetic Cu^{2+}-bearing compounds, and the solid-solution stability fields may thus be established. Many experimental techniques that are applied to minerals are plagued by a lack of material. The examination of synthetic Cu^{2+} compounds has the advantage that they may be synthesized in large quantities; however, the products tend to be fine grained, precluding studies which require single crystals. It is for this reason that structure refinements have not yet been reported for any synthetic solid-solution series involving Cu^{2+}.

Studies of Cu^{2+}-bearing series have been done for types (I), (II) and (III) structures. Type (I) structures give an isomorphous series, such as observed in $(Zn_{1-x}Cu_x^{2+})(OH)_3NO_3$ (Markov et al., 1990) and $K_2(Zn_{1-x}Cu_x^{2+})F_4$ (Jamet et al., 1987). Cu^{2+}-bearing solid-solution series of type (II) structures have a phase transition at some value $x=x_c$, such as in the series $(Zn_{1-x}Cu_x^{2+})WO_4$ (Schofield and Redform, 1992), $La_2(Ni_{1-x}Cu_x^{2+})O_4$ (Ramanujachary and Swamy, 1985), $K(Mg_{1-x}Cu_x^{2+})F_3$, $K(Zn_{1-x}Cu_x^{2+})F_3$, $(Mg_{1-x}Cu_x^{2+})F_2$ and $(Zn_{1-x}Cu_x^{2+})F_2$ (Schmitz-Dumont and Grimm, 1967). Cu^{2+}-bearing solid-solution series of type (III) [or type (IV)] structures do not form complete series; typical examples are α-$(Mg_{2-x}Cu_x^{2+})P_2O_7$ with the limits $0 \leq x \leq 0.70$ (Nord et al., 1990), $(Mg_{3-x}Cu_x^{2+})(PO_4)_2$ where values of $0 \leq x \leq 1.70$ give the $Mg_3(PO_4)_2$ structure, $2.30 \leq x \leq 3.00$ gives the $Cu_3^{2+}(PO_4)_2$ structure, and $1.70 \leq x \leq 2.30$ gives two phases (Moqine et al., 1987), and $(Ni_{1-x}Cu_x^{2+})O$ with limits $0.65 \leq x \leq 1.00$ (Davies, 1986).

The interaction of Jahn-Teller distortion centres within a crystal structure, such that the distortions act in a collective manner, is termed the cooperative Jahn-Teller effect (Chapter 2). This effect is apparent in Cu^{2+}-bearing solid-solutions of type (II) structures, in which the cooperative Jahn-Teller effect links the distortions of independent Cu^{2+} octahedra, leading to a phase transition at $x=x_c$. To date, there has only been one detailed study of such a system. A total of 21 samples in the series $(Zn_{1-x}Cu_x^{2+})WO_4$ (sanmartinite-cuproscheelite) were reported by Schofield and Redfern (1992). X-ray powder-diffraction studies showed that a phase transition from the space group P2/c (sanmartinite structure) to $P\bar{1}$ (cuproscheelite structure) occurs at $x_c \approx 0.22$. The phase transition was modelled in terms of a second-order Landau-type phenomenological

potential. However, no structural studies were done for series intermediates and the precise nature of the transition remains obscure.

The following chapters in this thesis report detailed synthesis work for the type (II)-structure series $(M_{1-x}Cu_x^{2+})F_2$ and $K(M_{1-x}Cu_x^{2+})F_3$ (M = divalent cation). X-ray powder-diffraction data and the Rietveld technique were used to refine the crystal structures of series intermediates in order to characterize the phase transition in each series.

Chapter 12

Jahn-Teller Driven Phase-Transitions: The MF_2 Rutile-Type Structure.

12.1 Introduction and Previous Work.

The crystal structure of $Cu^{2+}F_2$ is a monoclinic derivative of the tetragonal MF_2 (M = Zn, Ni, Fe^{2+}, Co, Mg) rutile-type structure (Fig. 1.4). The tetragonal MF_2 structure has metal ions in fairly regular octahedral coordination, whereas the $Cu^{2+}F_6$ octahedron in the monoclinic $Cu^{2+}F_2$ structure is (4+2)-distorted (Fig. 12.1), as expected for Cu^{2+} in octahedral coordination. The connectivities of the tetragonal MF_2 and monoclinic $Cu^{2+}F_2$ structures are identical, suggesting that the series $(M_{1-x}Cu_x^{2+})F_2$ should exist and that it will undergo a tetragonal-to-monoclinic phase transition at some value $x=x_c$ along the solid-solution series.

The tetragonal MF_2 structure contains two crystallographically distinct M-F bond-lengths that are usually of approximately the same length. In monoclinic $Cu^{2+}F_2$, the bond connectivity of the rutile structure-type is maintained but the decrease in symmetry results in three crystallographically distinct bond-lengths. In principle, the (4+2)-distortion of the $Cu^{2+}F_6$ octahedron could occur in the tetragonal structure, as there is one symmetrically equivalent set of four distances and another symmetrically equivalent set of two distances, allowing the usual (4+2)-distortion shown by octahedrally coordinated Cu^{2+}. However, what actually happens is rather different. The $Cu^{2+}F_2$ structure is monoclinic, and although the local distortion around the Cu^{2+} ion shows the usual (4+2) arrangement, this does not conform to the constraints of tetragonal

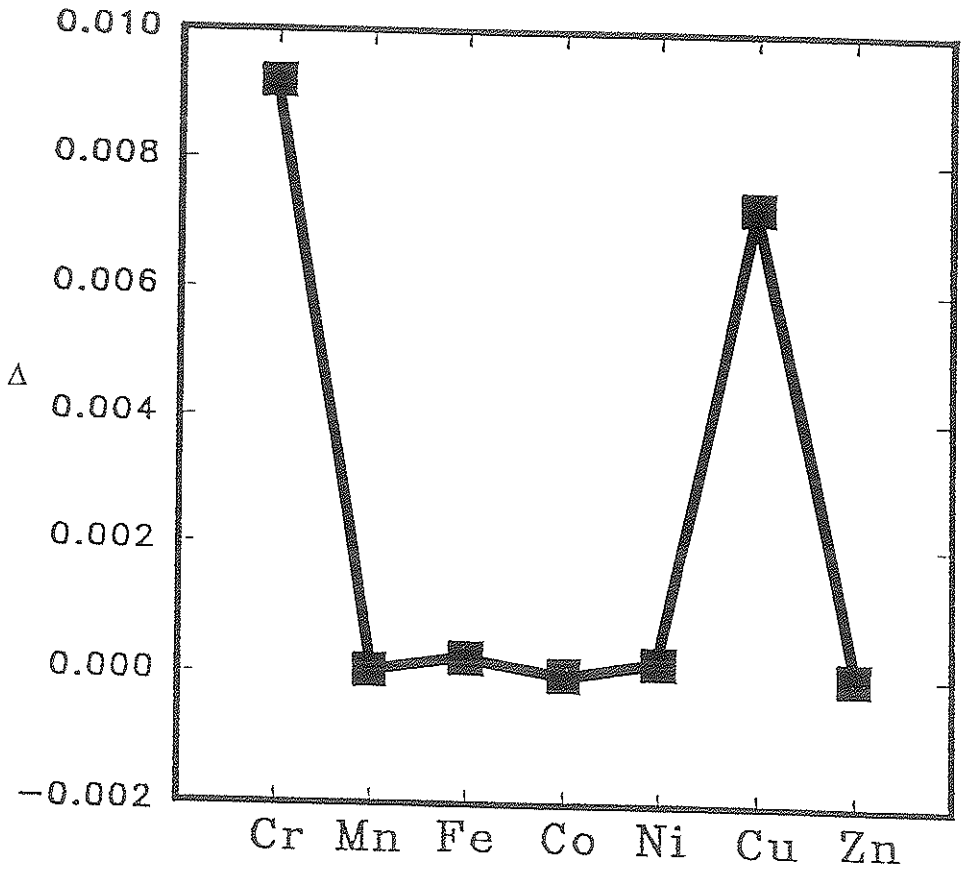

Figure 12.1. Octahedral distortion (Δ, Equation 2.1) in $M^{2+}F_2$ rutile-type structures.

symmetry. The pair of elongated Cu-F bonds in the monoclinic structure corresponds to two of the four bonds equivalent in the tetragonal structure, and not to the set of two equivalent bonds. Calculations show that approximately the same (4+2) distortion of the octahedral environment in the tetragonal rutile structure is obtained by distorting the unit-cell to a = 5.45, c = 2.45 Å (Cu-F_{ap} = 2.34, Cu-F_{eq} = 1.95 Å). However, this distortion of the tetragonal cell results in a Cu-Cu separation of only 2.45 Å, whereas the Cu-Cu distance in monoclinic $Cu^{2+}F_2$ is 3.30 Å. Evidently the connectivity of the structure does not allow strong (4+2)-distortion in the direction required by tetragonal symmetry, thus causing the change to monoclinic symmetry.

Substitution of Cu^{2+} into the $(M_{1-x}Cu_x^{2+})F_2$ structure for small values of x should not cause a phase transition, as the low concentrations of independent Jahn-Teller distorted $Cu^{2+}F_6$ octahedra embedded in the tetragonal MF_2 structure will not interact constructively. It is proposed that a critical concentration of distortion centres is reached ($x=x_c$), where the distortions of independent $Cu^{2+}\phi_6$ octahedra will couple via a phonon, leading to a tetragonal-to-monoclinic phase transition.

Previous work was done on the systems $(Mg_{1-x}Cu_x^{2+})F_2$ and $(Zn_{1-x}Cu_x^{2+})F_2$ by Schmitz-Dumont and Grimm (1967). They synthesized only five samples in each series. More detailed synthesis work will lead to a better understanding of how Cu^{2+} distortion centres interact in a crystal structure.

12.2 Synthesis of $(Mg_{1-x}Cu_x^{2+})F_2$, $(Zn_{1-x}Cu_x^{2+})F_2$ and $(Ni_{1-x}Cu_x^{2+})F_2$

The $(Mg_{1-x}Cu_x^{2+})F_2$, $(Zn_{1-x}Cu_x^{2+})F_2$ and $(Ni_{1-x}Cu_x^{2+})F_2$ series were synthesized using analytical grade CuF_2 (98% pure), ZnF_2 (99% pure), NiF_2

(99% pure) and MgF_2 (99.9% pure) supplied by the Aldrich Chemical Company. Powders were dried at 100°C, carefully weighed to ± 0.0002 grams for each synthesis run, mixed and thoroughly ground (dry) in an agate mortar, and then remixed and ground again.

Powders were gently pressed into pellets and placed in platinum foil baskets. Each pellet was annealed in a vertical tubular furnace, at atmospheric pressure in an inert atmosphere provided by a steady flow of argon from the bottom of the furnace. The temperature of the furnace (at the sample location) was monitored using a Pt-Rh thermocouple prior to each run. The series $(Mg_{1-x}Cu_x^{2+})F_2$ was heated at 765-818°C for 2 hours, $(Zn_{1-x}Cu_x^{2+})F_2$ at 750-755°C for 15 minutes, and $(Ni_{1-x}Cu_x^{2+})F_2$ at 735-737°C for 15 minutes. Samples were quenched in air. X-ray powder-diffraction patterns (Section 12.3) indicate that reactions were complete and that a single phase was present, with the exception of minor impurities of tenorite and cuprite which were present in about the same amounts (~ 5%) in all products.

12.3 Characterization of $(Mg_{1-x}Cu_x^{2+})F_2$, $(Zn_{1-x}Cu_x^{2+})F_2$ and $(Ni_{1-x}Cu_x^{2+})F_2$.

Powders of $(Mg_{1-x}Cu_x^{2+})F_2$, $(Zn_{1-x}Cu_x^{2+})F_2$ and $(Ni_{1-x}Cu_x^{2+})F_2$ were ground in an agate mortar and front-loaded into brass sample holders for X-ray examination. X-ray powder-diffraction patterns were collected at 25°C using a Philips PW1710 automated X-ray powder diffractometer with Bragg-Brentano geometry, CuKα X-radiation (40 kV and 40 mA), fixed 1° slits and a diffracted-beam monochromator over the range 10-100°2θ. A scan speed of 1.8°2θ/min. and an integration time of 1s were used. The diffractometer

was standardized using a silicon standard (National Bureau of Standards SRM 640b, a = 5.430940 ± 0.000035 Å); to avoid contamination of the samples, no internal standard was used.

Visual examination of the X-ray diffraction patterns revealed the locations of the tetragonal to monoclinic phase transition in each series. The powder patterns were indexed using the JCPDS cards for MgF_2, ZnF_2, NiF_2 and $Cu^{2+}F_2$. The unit-cell dimensions of each member of the series were refined using Appleman and Evans (1973) cell-refinement program (as modified by Burns and Trembath). The refined cell dimensions for each series are given in Tables 12.1, 12.2 and 12.3 and shown in Figures 12.2, 12.3 and 12.4.

12.4 Phase Transitions in $(Mg_{1-x}Cu_x^{2+})F_2$, $(Zn_{1-x}Cu_x^{2+})F_2$ and $(Ni_{1-x}Cu_x^{2+})F_2$.

Figures 12.2, 12.3 and 12.4 show phase transitions in $(Mg_{1-x}Cu_x^{2+})F_2$, $(Zn_{1-x}Cu_x^{2+})F_2$ and $(Ni_{1-x}Cu_x^{2+})F_2$ at $x=x_c$. The onset of the monoclinic structure is indicated by an abrupt departure of β from 90° and comparison of β shows that each series has a different $x=x_c$ (Fig. 12.5). The onset of the monoclinic structure occurs at $x_c \approx 0.45$ for the $(Zn_{1-x}Cu_x^{2+})F_2$ series, $x_c \approx 0.475$ for the $(Mg_{1-x}Cu_x^{2+})F_2$ series and $x_c \approx 0.50$ for the $(Ni_{1-x}Cu_x^{2+})F_2$ series. The ionic radii of Zn, Mg and Ni in octahedral coordination are 0.740, 0.720 and 0.690 Å, respectively (Shannon, 1976); the small variation of x_c for these three series is apparently a function of the ionic radius of the M ion.

The X-ray powder-diffraction study verifies that a single homogeneous (to X-rays) phase was synthesized in each of the synthesis

Table 12.1 Unit-cell parameters from least-squares refinement of powder data* for the series $(Mg_{1-x}Cu_x^{2+})F_2$.

x	T(°)	t(m)	a(Å)	b(Å)	c(Å)	β(°)	V(Å^3)
0.000	-	-	3.0516(3)	4.6215(3)	4.6215(3)	90	65.18(1)
0.250	844	120	3.0837(9)	4.6122(4)	4.6122(4)	90	65.60(2)
0.275	785	120	3.0932(6)	4.6092(4)	4.6092(4)	90	65.71(1)
0.300	785	120	3.0982(9)	4.6067(7)	4.6067(7)	90	65.75(2)
0.325	785	120	3.1024(9)	4.6051(7)	4.6051(7)	90	65.79(2)
0.350	785	120	3.1070(8)	4.6039(7)	4.6039(7)	90	65.85(2)
0.375	785	120	3.111(1)	4.6019(9)	4.6019(9)	90	65.89(3)
0.400	785	120	3.1179(8)	4.6022(6)	4.6022(6)	90	66.04(2)
0.425	785	120	3.122(1)	4.6015(3)	4.6015(3)	90	66.10(3)
0.450	785	120	3.1273(6)	4.5994(2)	4.5994(2)	90	66.15(1)
0.475	785	135	3.134(1)	4.597(2)	4.597(2)	89.68(7)	66.23(3)
0.500	818	120	3.1433(4)	4.5969(6)	4.5975(6)	88.33(1)	66.40(1)
0.525	785	120	3.1465(7)	4.594(1)	4.596(1)	88.08(2)	66.40(2)
0.550	818	120	3.1530(4)	4.5947(9)	4.597(1)	87.85(1)	66.55(1)
0.575	785	120	3.1576(8)	4.590(2)	4.594(2)	87.54(2)	66.52(2)
0.600	818	120	3.1651(4)	4.5924(7)	4.5976(8)	87.41(1)	66.76(1)
0.625	785	120	3.1745(4)	4.5907(6)	4.5990(9)	87.06(1)	66.93(1)
0.650	818	120	3.1782(3)	4.5890(6)	4.5968(7)	86.92(1)	66.95(1)
0.675	775	120	3.1882(8)	4.583(1)	4.591(1)	86.60(2)	66.96(2)
0.700	785	120	3.190(1)	4.582(2)	4.580(3)	86.35(5)	66.81(4)
0.725	775	120	3.2013(6)	4.5782(9)	4.5939(5)	86.09(1)	67.17(1)
0.750	765	120	3.2093(5)	4.5786(9)	4.5934(7)	85.86(1)	67.32(1)
0.775	775	120	3.212(1)	4.581(2)	4.596(2)	85.60(5)	67.42(3)
0.800	765	120	3.2268(6)	4.5741(9)	4.5958(7)	85.39(1)	67.61(2)
0.825	769	120	3.2334(7)	4.5688(8)	4.5934(9)	85.16(2)	67.61(2)
0.850	769	120	3.2449(7)	4.5709(8)	4.5986(9)	84.94(2)	67.94(2)
0.875	769	120	3.2577(9)	4.564(2)	4.597(1)	84.72(3)	68.07(3)
0.900	771	140	3.2595(5)	4.5665(6)	4.5999(6)	84.53(1)	68.16(1)
0.925	765	120	3.2727(7)	4.5584(6)	4.6003(6)	84.22(1)	68.28(1)
0.950	785	120	3.2792(6)	4.555(1)	4.598(1)	84.02(2)	68.31(2)
1.000	-	-	3.291(2)	4.543(3)	4.595(3)	83.37(6)	68.23(5)

* Powder-diffraction patterns are given in Appendix B.
+ Unit-cell dimensions of the tetragonal-structure materials have been transformed by the matrix (0,0,1; 1,0,0; 0,1,0) to give correspondence with the monoclinic cell.

Table 12.2 Unit-cell parameters from least-squares refinement of powder data* for the series $(Zn_{1-x}Cu_x^{2+})F_2$.

x	T(°)	t(m)	a(Å)	b(Å)	c(Å)	β(°)	V(Å^3)
0.000	-	-	3.1248(8)	4.7078(7)	4.7078(7)	90	69.26(2)
0.250	753	15	3.1568(7)	4.6697(6)	4.6697(6)	90	68.84(2)
0.275	753	15	3.1610(7)	4.6650(7)	4.6650(7)	90	68.79(2)
0.300	753	15	3.1640(6)	4.6609(6)	4.6609(6)	90	68.74(2)
0.325	753	15	3.1678(5)	4.6572(5)	4.6572(5)	90	68.71(2)
0.350	753	15	3.1708(7)	4.6528(7)	4.6528(7)	90	68.64(2)
0.375	753	15	3.1758(7)	4.6487(7)	4.6487(7)	90	86.63(2)
0.400	753	15	3.1783(7)	4.6479(6)	4.6469(6)	90	68.63(2)
0.425	753	15	3.1822(7)	4.6423(7)	4.6423(7)	90	68.58(2)
0.450	753	15	3.1859(9)	4.6380(6)	4.6380(6)	90	68.53(2)
0.475	753	15	3.1919(7)	4.631(1)	4.632(1)	88.26(3)	68.43(2)
0.500	753	15	3.1957(6)	4.6294(8)	4.632(1)	87.94(2)	68.48(2)
0.525	753	15	3.2018(5)	4.623(1)	4.6308(7)	87.67(1)	68.48(2)
0.550	753	15	3.2047(7)	4.6232(8)	4.624(1)	87.42(2)	68.44(2)
0.575	753	15	3.2102(5)	4.6185(9)	4.6219(9)	87.09(1)	68.44(2)
0.600	753	15	3.2138(5)	4.6146(9)	4.6227(9)	86.86(2)	68.45(1)
0.625	753	15	3.2194(4)	4.6108(8)	4.6191(9)	86.61(1)	68.45(1)
0.650	753	15	3.2246(4)	4.6072(9)	4.6185(8)	86.41(1)	68.48(1)
0.675	753	15	3.2294(4)	4.6034(8)	4.6164(8)	86.18(1)	68.48(1)
0.700	753	15	3.2339(5)	4.5997(9)	4.6139(8)	85.90(1)	68.46(2)
0.725	753	15	3.2395(4)	4.5952(8)	4.6116(5)	85.71(1)	68.46(1)
0.750	753	15	3.244(1)	4.590(1)	4.609(1)	85.49(2)	68.42(2)
0.775	753	15	3.2523(7)	4.5860(9)	4.6078(7)	85.29(2)	68.49(1)
0.800	753	15	3.257(2)	4.579(3)	4.609(1)	85.01(3)	68.49(3)
0.825	753	15	3.2576(4)	4.5775(5)	4.6065(4)	84.82(1)	68.41(1)
0.850	753	15	3.2672(9)	4.5735(7)	4.6041(7)	84.63(1)	68.50(2)
1.000	-	-	3.291(2)	4.543(3)	4.595(3)	83.37(6)	68.23(5)

* Powder-diffraction patterns are given in Appendix C.
+ Unit-cell dimensions of the tetragonal-structure materials have been transformed by the matrix (0,0,1; 1,0,0; 0,1,0) to give correspondence with the monoclinic cell.

Table 12.3 Unit-cell parameters from least-squares refinement of powder data* for the series $(Ni_{1-x}Cu_x^{2+})F_2$.

x	T(°)	t(m)	a(Å)	b(Å)	c(Å)	β(°)	V(Å^3)
0.000	-	-	3.0801(2)	4.6622(9)	4.6622(9)	90	66.95(4)
0.250	735	15	3.100(2)	4.6379(9)	4.6379(9)	90	66.69(4)
0.275	735	15	3.1131(9)	4.6356(6)	4.6356(6)	90	66.90(2)
0.300	735	15	3.117(1)	4.6308(8)	4.6308(8)	90	66.83(3)
0.325	735	15	3.122(1)	4.6275(9)	4.6275(9)	90	66.86(3)
0.350	735	15	3.1259(9)	4.6261(7)	4.6261(7)	90	66.90(2)
0.375	735	15	3.127(1)	4.6265(8)	4.6265(8)	90	66.93(5)
0.400	735	16	3.1298(8)	4.6247(6)	4.6247(6)	90	66.94(3)
0.425	735	15	3.1380(9)	4.6217(5)	4.6217(5)	90	67.03(4)
0.450	735	15	3.1410(8)	4.6188(6)	4.6188(6)	90	67.01(4)
0.475	735	15	3.1458(6)	4.6134(5)	4.6134(5)	90	66.95(2)
0.500	735	15	3.1460(9)	4.6120(7)	4.6120(7)	90	66.92(4)
0.525	735	15	3.1632(6)	4.6064(9)	4.6120(7)	88.22(3)	67.17(4)
0.550	735	15	3.166(1)	4.612(2)	4.609(2)	87.98(4)	67.26(9)
0.575	735	15	3.1740(5)	4.6067(9)	4.6082(7)	87.75(1)	67.33(4)
0.600	735	15	3.1740(6)	4.6034(7)	4.613(1)	87.71(2)	67.35(4)
0.625	735	15	3.1856(8)	4.5991(6)	4.6116(6)	87.26(2)	67.49(4)
0.650	735	15	3.1953(6)	4.5939(6)	4.605(1)	86.80(1)	67.49(2)
0.675	735	15	3.1969(8)	4.5942(9)	4.6030(6)	86.75(2)	67.50(4)
0.700	735	15	3.205(1)	4.588(1)	4.605(1)	86.42(3)	67.58(5)
0.725	735	15	3.220(1)	4.5815(7)	4.602(1)	85.93(2)	67.72(5)
0.750	735	15	3.2216(6)	4.5828(8)	4.6007(7)	85.85(1)	67.75(4)
0.775	735	15	3.230(3)	4.577(3)	4.595(4)	85.50(7)	67.7(2)
0.800	735	15	3.2434(9)	4.575(1)	4.602(1)	85.13(3)	68.04(5)
0.825	735	15	3.2456(6)	4.5685(8)	4.5988(6)	84.97(1)	67.93(4)
0.850	735	17	3.260(2)	4.567(2)	4.599(2)	84.70(4)	68.2(1)
0.875	735	16	3.2662(9)	4.5635(9)	4.6020(8)	84.42(2)	68.27(4)
0.900	735	17	3.2791(9)	4.5603(5)	4.6021(6)	84.07(2)	68.45(4)
0.925	735	15	3.2872(7)	4.5588(4)	4.604(1)	83.93(2)	68.61(4)
0.950	735	16	3.2927(5)	4.5543(5)	4.6017(7)	83.74(1)	68.60(3)
0.975	735	15	3.3004(5)	4.5503(8)	4.6016(8)	83.56(1)	68.67(3)
1.000	-	-	3.291(2)	4.543(3)	4.595(3)	83.37(6)	68.23(5)

* Powder-diffraction patterns are given in Appendix D.
+ Unit-cell dimensions of the tetragonal-structure materials have been transformed by the matrix (0,0,1; 1,0,0; 0,1,0) to give correspondence with the monoclinic cell.

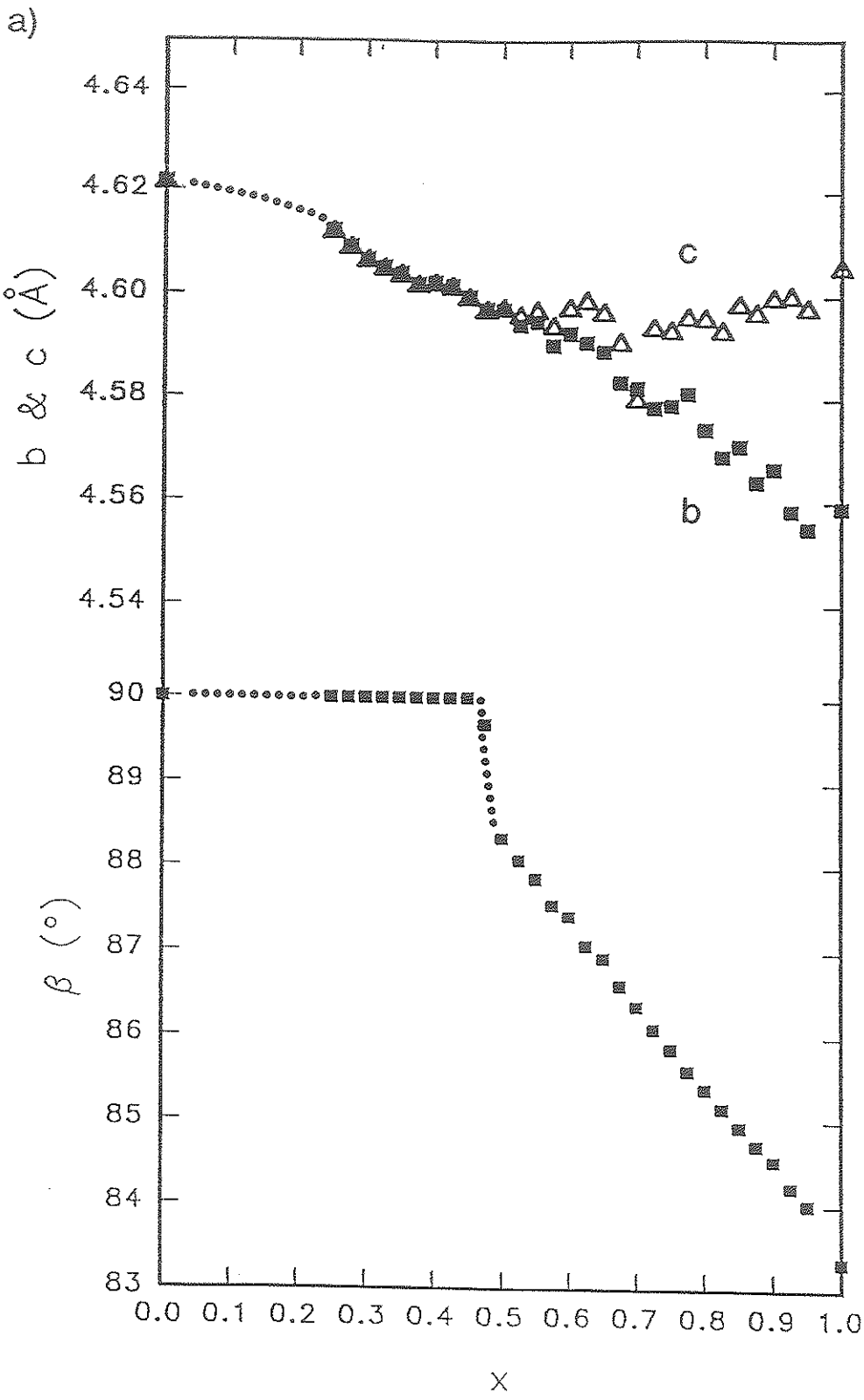

Figure 12.2. Unit-cell parameters for the $(Mg_{1-x}Cu_x^{2+})F_2$ series. a) β, *b* and *c*; b) *a*; standard deviations (Table 12.1) are smaller than the symbols.

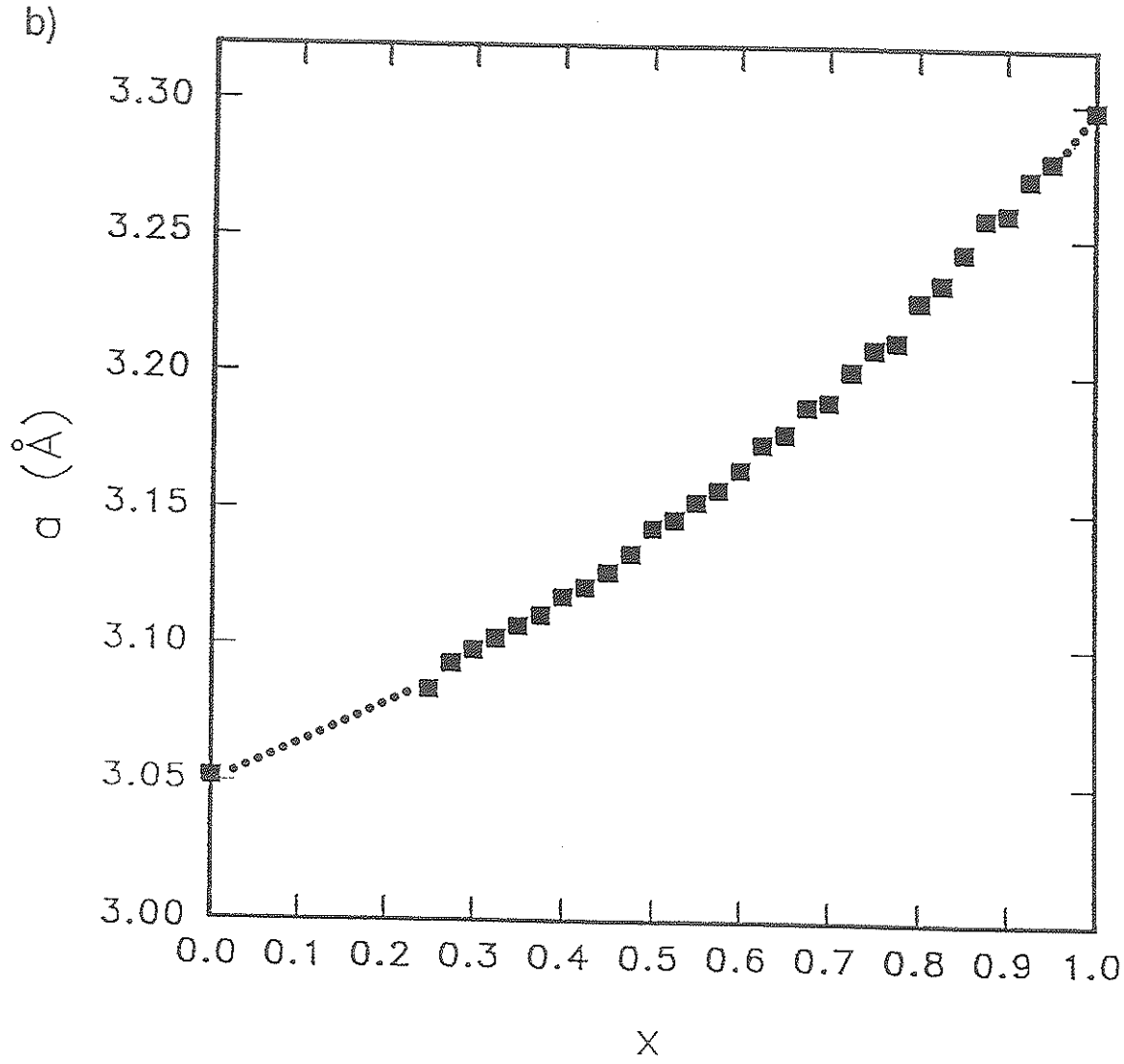

Figure 12.2. Continued

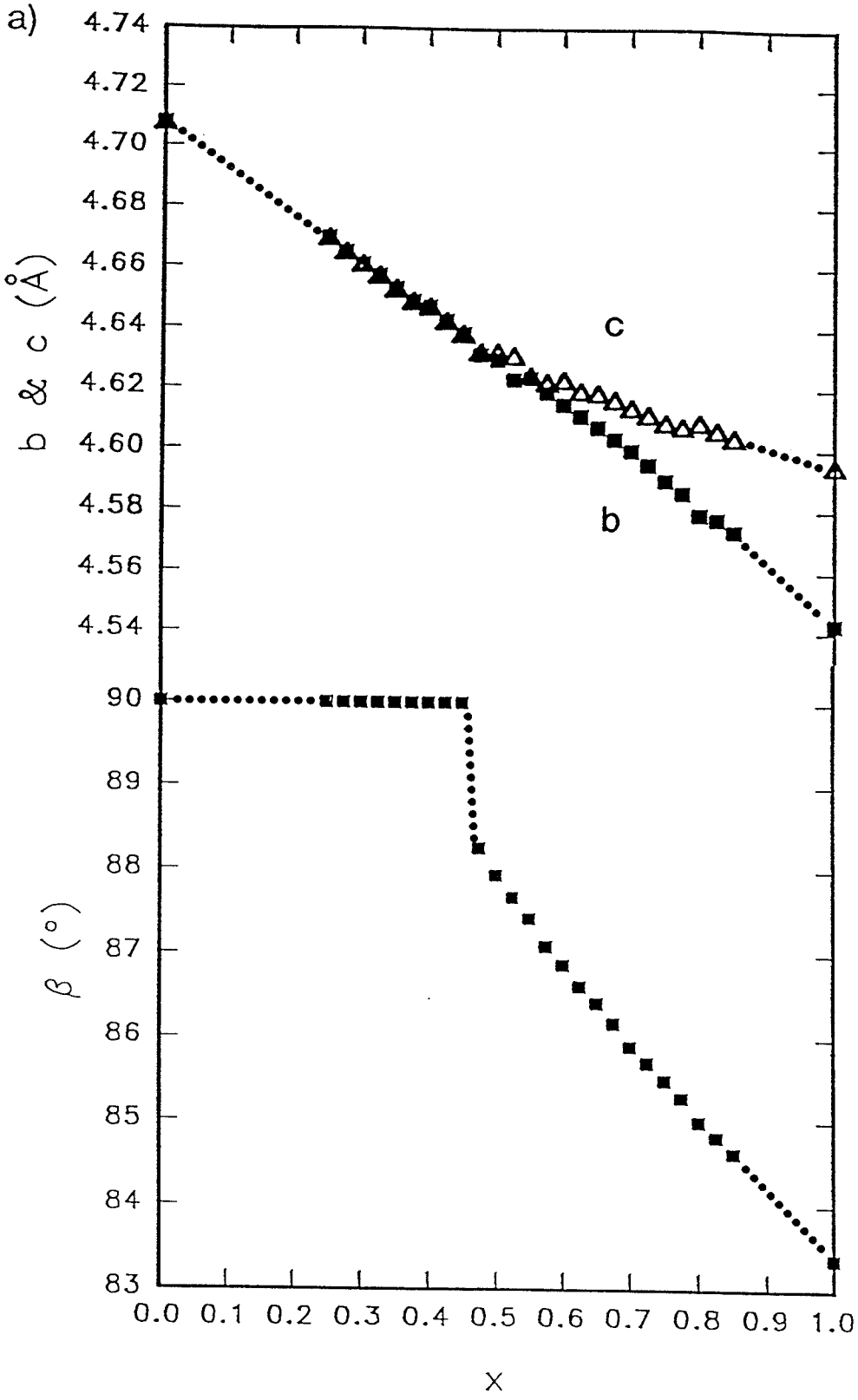

Figure 12.3. Unit-cell parameters for the $(Zn_{1-x}Cu_x^{2+})F_2$ series. a) β, *b* and *c*; b) *a*; standard deviations (Table 12.2) are smaller than the symbols.

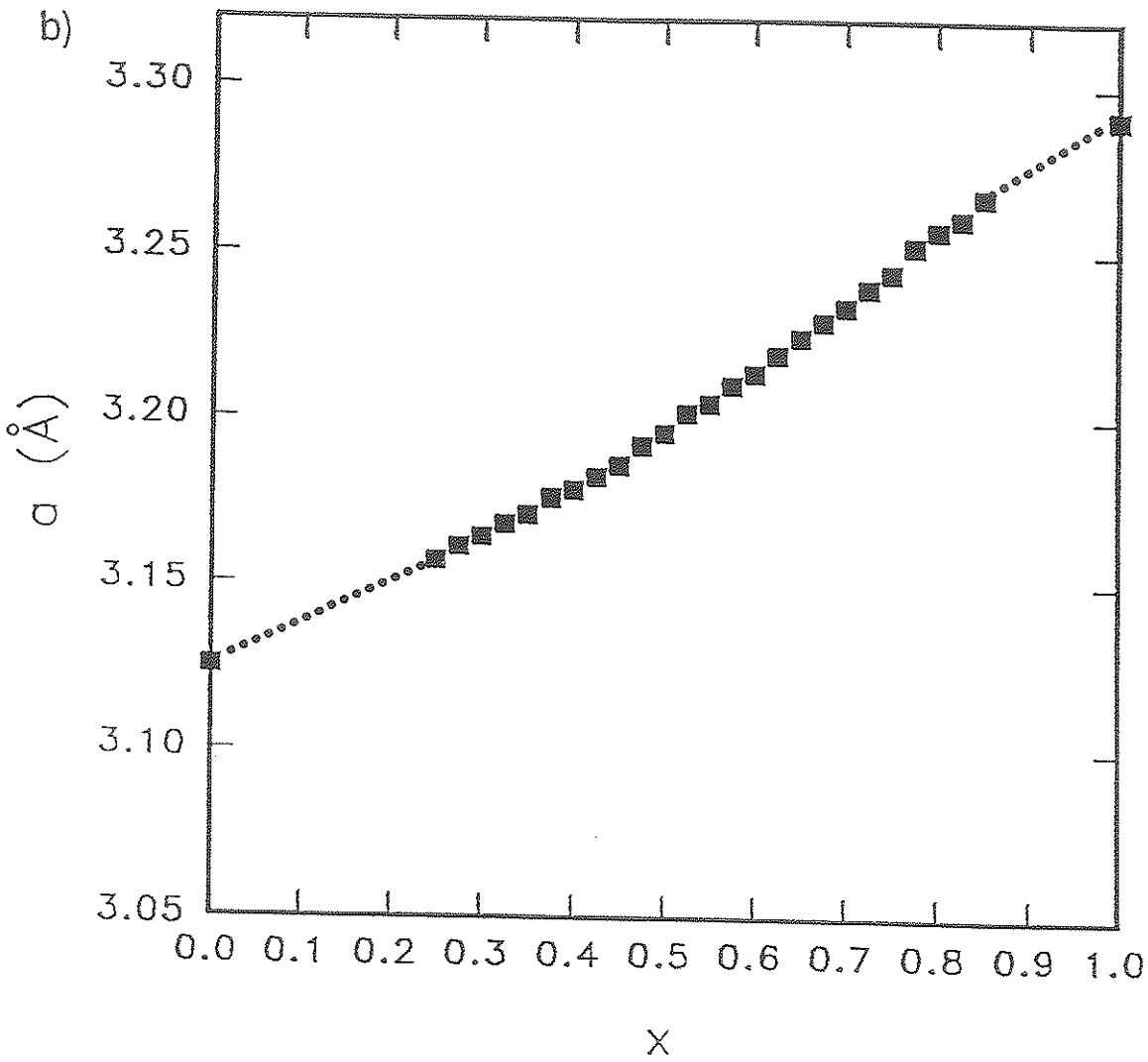

Figure 12.3. Continued

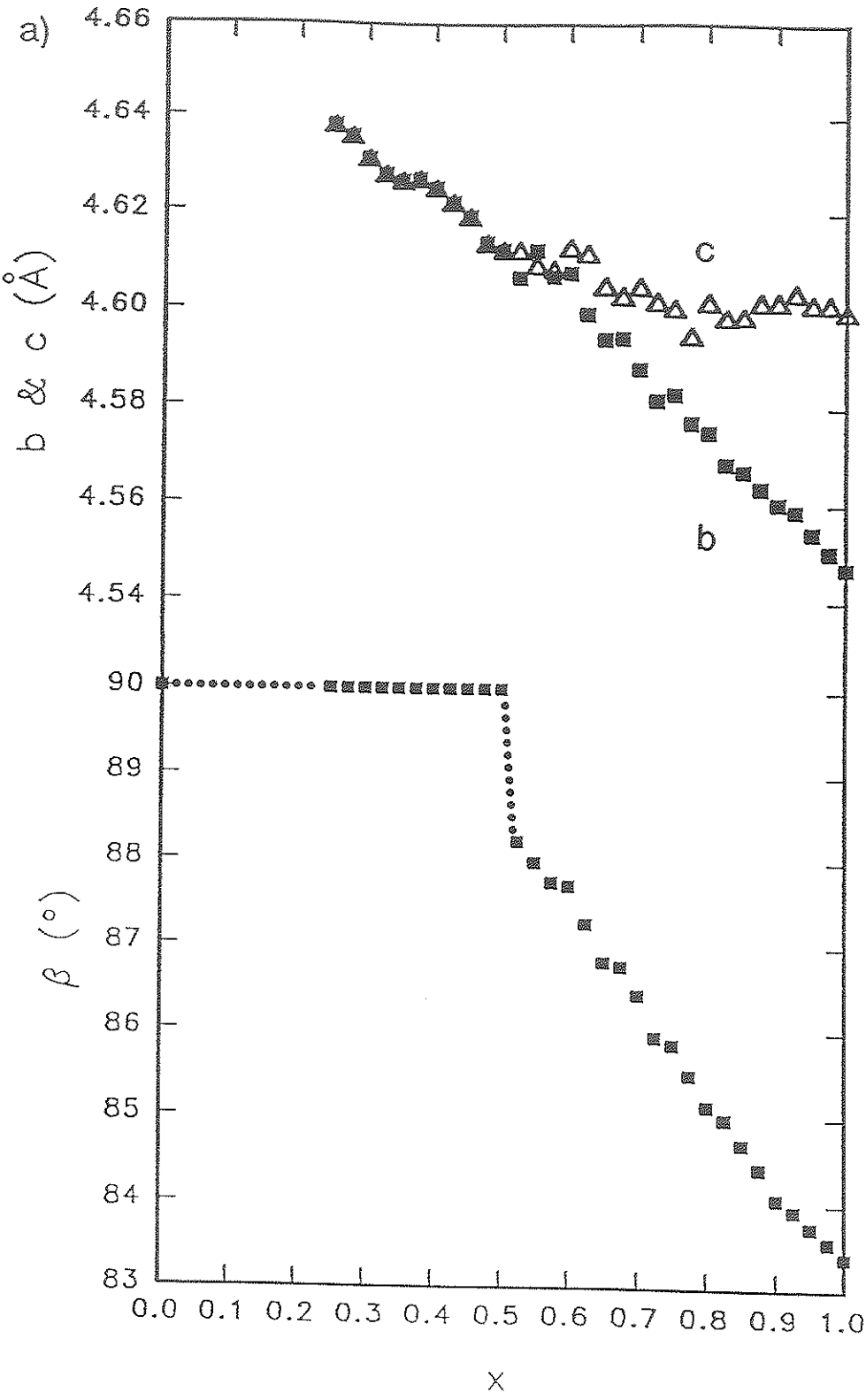

Figure 12.4. Unit-cell parameters for the $(Ni_{1-x}Cu_x^{2+})F_2$ series. a) β, *b* and *c*; b) *a*; standard deviations (Table 12.3) are smaller than the symbols.

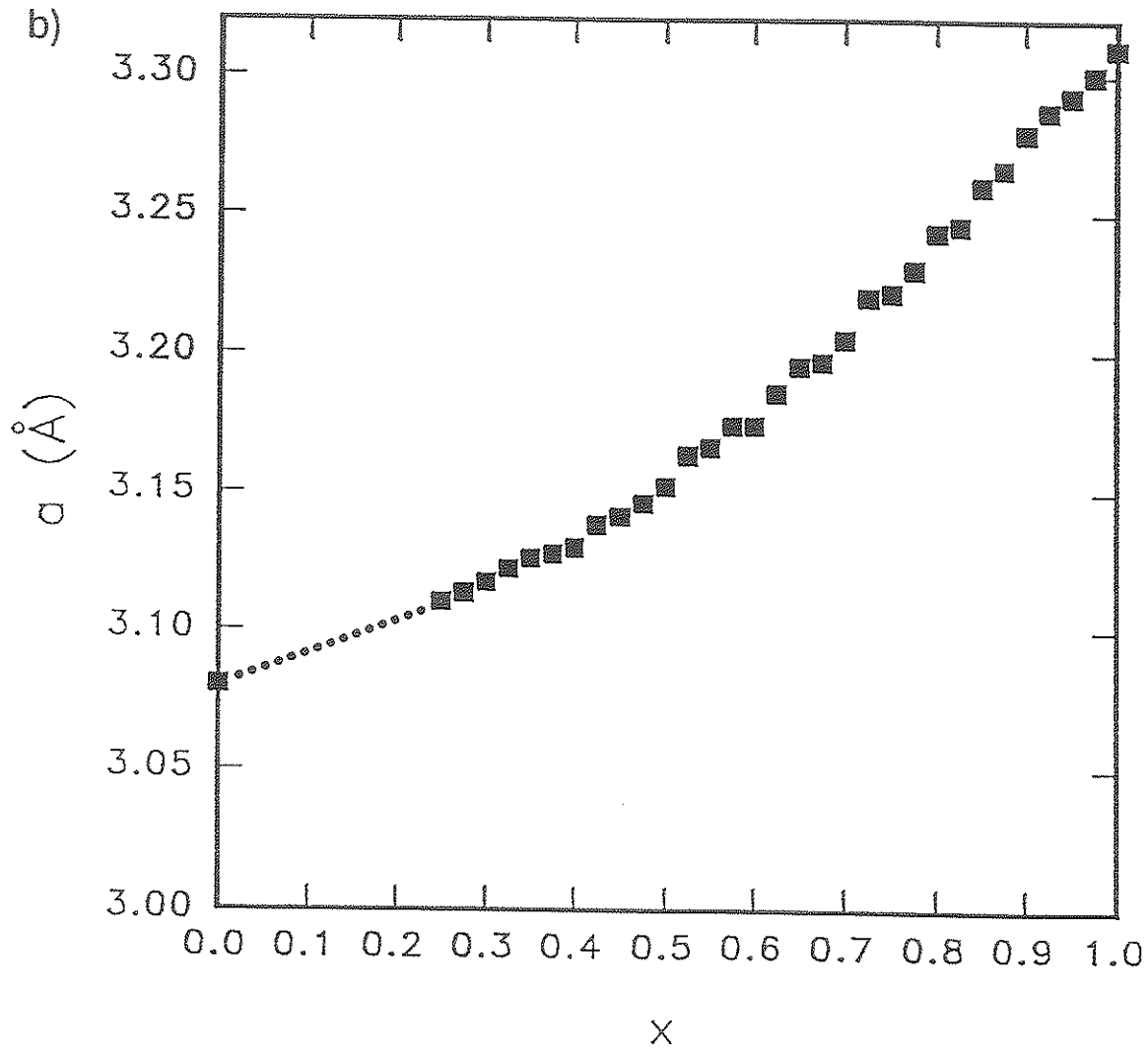

Figure 12.4. Continued

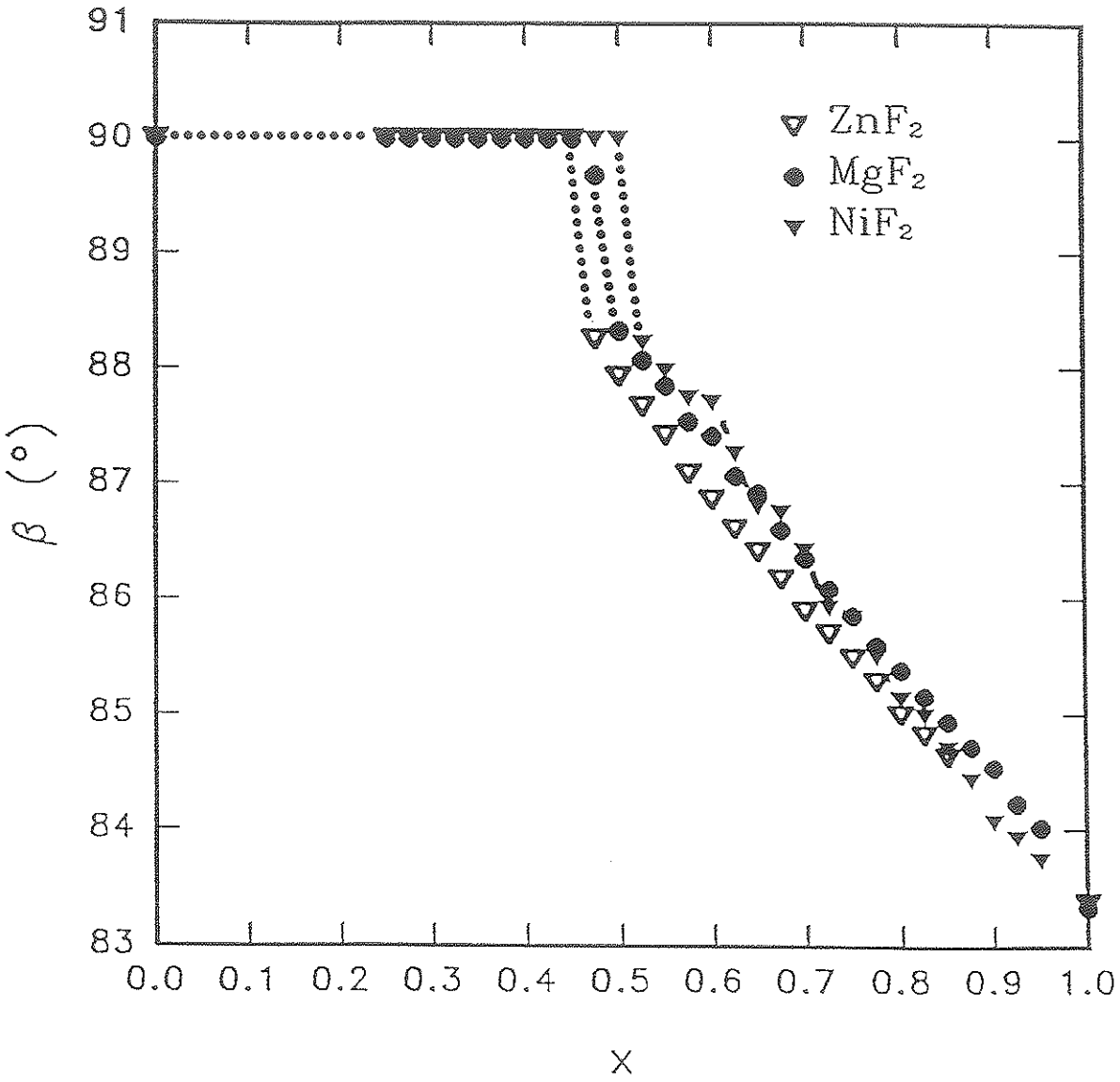

Figure 12.5. The β unit-cell parameter for the $(Mg_{1-x}Cu_x^{2+})F_2$, $(Zn_{1-x}Cu_x^{2+})F_2$ and $(Ni_{1-x}Cu_x^{2+})F_2$ series. Standard deviations are smaller than the symbols.

runs. Examples of selected diffraction patterns near the phase transition in the $(Zn_{1-x}Cu_x^{2+})F_2$ series are given in Figure 12.6.

12.5 Rietveld Structure Refinements for $(Mg_{1-x}Cu_x^{2+})F_2$ and $(Zn_{1-x}Cu_x^{2+})F_2$.

In order to obtain details of the crystal structures of selected members of the series $(Mg_{1-x}Cu_x^{2+})F_2$ and $(Zn_{1-x}Cu_x^{2+})F_2$, Rietveld structure refinements were done using X-ray powder-diffraction data. Samples were gently back-pressed into aluminum holders for X-ray study. The surface of each sample was serrated with a razor blade to reduce preferred orientation effects. Data were collected at 25°C with a Philips PW1710 X-ray powder diffractometer with Bragg-Brentano geometry using CuKα X-radiation (40 kV and 40 mA), fixed 1° slits and a diffracted-beam monochromator. Data were collected over the range 20-125°2θ with a step interval of 0.05°2θ and a count time of 5s per step.

Each Rietveld structure refinement was done using the program LHPM1 (Howard and Hill, 1986, a modified version of the program by Wiles and Young, 1981).

12.5.1 Rietveld Refinements of MgF_2, ZnF_2 and NiF_2

The crystal structures of MgF_2 (Baur, 1976), ZnF_2 and NiF_2 (Baur and Khan, 1971) were refined using single-crystal X-ray diffraction data. The structures of each of these compounds have been refined here using the Rietveld technique to obtain starting sets of profile parameters for the Rietveld structure refinements of the $(M_{1-x}Cu_x^{2+})F_2$ series. This work also

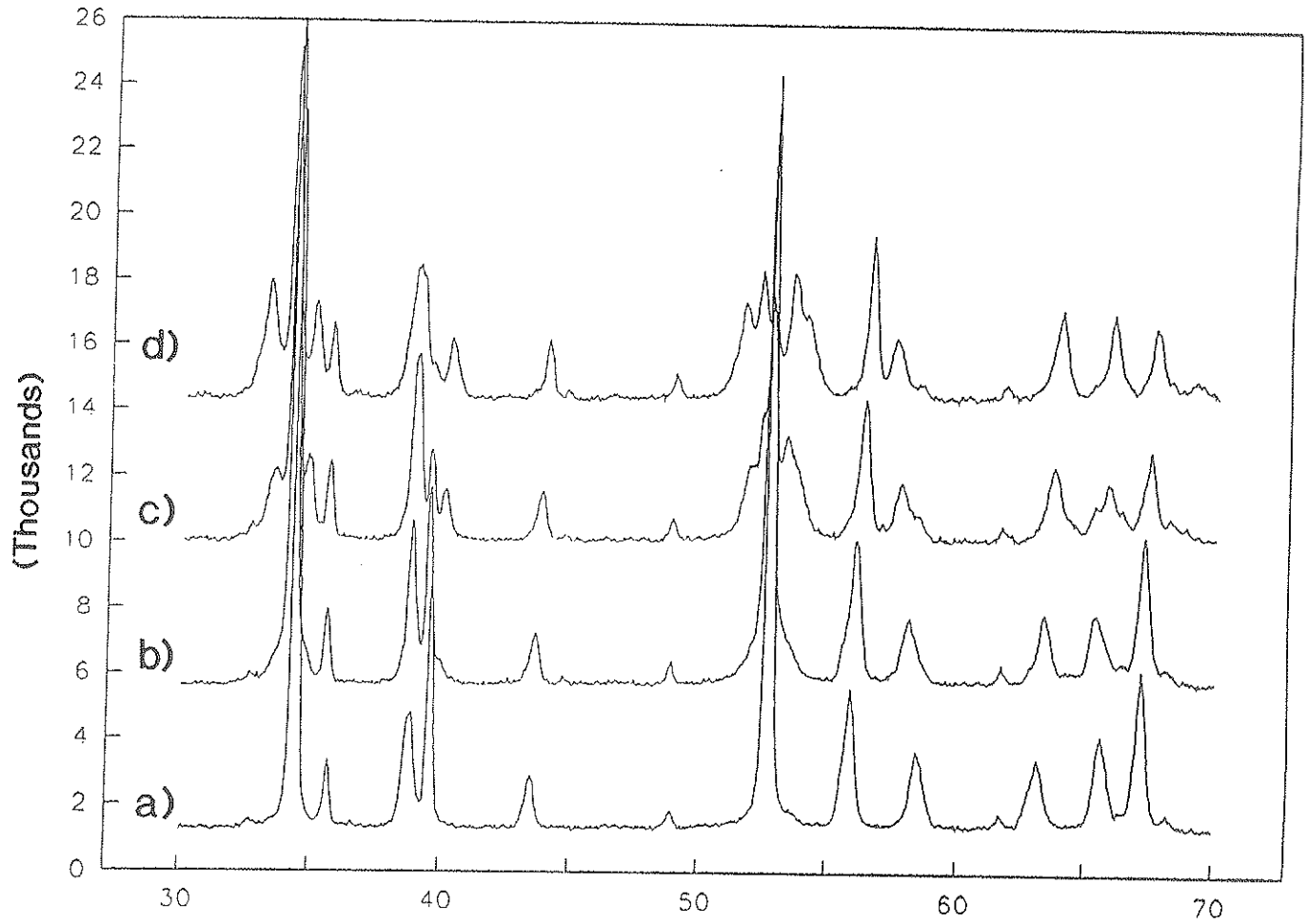

Figure 12.6. Selected regions of the X-ray powder-diffraction patterns for the $(Zn_{1-x}Cu^{2+}_{x})F_2$ series. a) $(Zn_{0.4}Cu^{2+}_{0.6})F_2$; b) $(Zn_{0.5}Cu^{2+}_{0.5})F_2$; c) $(Zn_{0.6}Cu^{2+}_{0.4})F_2$; d) $(Zn_{0.7}Cu^{2+}_{0.3})F_2$.

provides the opportunity to compare the results obtained using the Rietveld method to the structures previously reported using single-crystal methods.

Each refinement was done in the space group $P4_2/mnm$ with the structure parameters of MgF_2 (Baur, 1976) as starting parameters. Scattering factors for Mg^{2+}, Ni^{2+}, Zn^{2+} and F^{1-} were taken from the *International Tables for X-ray Crystallography* (1974). Peaks were modelled using a pseudo-Voigt profile function which was corrected for peak asymmetry to 30°2θ. Isotropic-displacement models were used, and all three refinements converged to the structures and R-indices given in Tables 12.4, 12.5 and 12.6. Observed and calculated powder patterns are in good agreement (Figures 12.7, 12.8 and 12.9). Observed step-scan patterns are given in Appendices F, G and H.

12.5.2 Standard Deviations and Rietveld Structure Refinement

It is well known that positive serial correlation of adjacent least-squares residuals during structure refinement of Rietveld data may lead to an underestimation of parameter standard deviations (Bérar and Lenann, 1991; Hill and Madsen, 1986). The Durbin-Watson d-statistic is a measure of the serial correlation of adjacent least-squares residuals and has a value of ~ 2.0 if no serial correlation of adjacent least-squares residuals is present (Hill and Madsen, 1986). Values of the Durbin-Watson d-statistic near 2.0 are in practice seldom encountered, due to the presence of systematic errors in the observed data, and to the systematically incorrect simulation of peak profiles. Reducing 2θ step widths and increasing the counting time per step will increase the apparent precision of the data; however, it will also increase the significance of any systematic errors present in the observed

Table 12.4 Refined structure parameters#, R-indices and bond-lengths for MgF_2 compared to single-crystal refinement results reported by Baur (1976).

Space group	$P4_2/mnm$		Z	2
	This Study		Baur (1976)	
Cell parameters				
a (Å)		4.6207(2)	4.6213(1)	
c		3.0512(1)	3.0519(1)	
V (Å^3)		65.146(8)	65.18(1)	
Atomic parameters				
Mg:	x	0	0	
	y	0	0	
	z	0	0	
	B (Å^2)	0.32(6)	anisotropic	
F:	x	0.3035(4)	0.30293(6)	
	y	0.3035(4)	0.30293(6)	
	z	0	0	
	B (Å^2)	0.58(8)	anisotropic	
Bond-lengths (Å)				
Mg-F x4		1.994(4)	1.9968(1)	
Mg-F_a x2		1.983(4)	1.9798(2)	
<Mg-F>		1.990	1.991	
R-indices* (%)				
R_B	2.16	R_P	7.07	
R_{WP}	11.08	R_{WP}(exp.)	3.60	
D-W	0.791	N-P	1983	

σs have been corrected using equation 12.1
* R_B = Rietveld Bragg-agreement index
R_P = Rietveld profile-agreement index
R_{WP} = Rietveld weighted profile-agreement index
D-W = Durbin-Watson d-statistic
N-P = Number of data points

Table 12.5 Refined structure parameters#, R-indices and bond-lengths for NiF_2 compared to single-crystal refinement results reported by Baur and Kahn (1971).

Space group	$P4_2/mnm$	Z	2
	This Study		Baur and Kahn (1971)
Cell parameters			
a (Å)		4.6622(5)	4.6498(3)
c		3.0801(5)	3.0838(1)
V (Å^3)		66.95(2)	66.67(1)
Atomic parameters			
Ni:	x	0	0
	y	0	0
	z	0	0
	B (Å^2)	0.17(7)	anisotropic
F:	x	0.3015(5)	0.3012(13)
	y	0.3015(5)	0.3012(13)
	z	0	0
	B (Å^2)	0.6(2)	anisotropic
Bond-lengths (Å)			
Ni-F x4		2.021(4)	2.022(6)
Ni-F_a x2		1.988(4)	1.981(9)
<Ni-F>		2.010	2.008

R-indices* (%)

R_B	0.92	R_P	3.42
R_{WP}	4.37	R_{WP}(exp.)	2.56
D-W	0.514	N-P	1983

σs have been corrected using equation 12.1
* R_B = Rietveld Bragg-agreement index
R_P = Rietveld profile-agreement index
R_{WP} = Rietveld weighted profile-agreement index
D-W = Durbin-Watson d-statistic
N-P = Number of data points

Table 12.6 Refined structure parameters#, R-indices and bond-lengths for ZnF_2 compared to single-crystal refinement results reported by Baur and Kahn (1971).

Space group	$P4_2/mnm$	Z	2
This Study		Baur and Kahn (1971)	
Cell parameters			
a (Å)		4.7125(2)	4.7048(1)
c		3.1277(2)	3.1338(2)
V (Å^3)		69.459(9)	69.37(1)
Atomic parameters			
Zn:	x	0	0
	y	0	0
	z	0	0
	B (Å^2)	0.29(5)	anisotropic
F:	x	0.3024(7)	0.3024(16)
	y	0.3024(7)	0.3024(16)
	z	0	0
	B (Å^2)	0.6(2)	anisotropic
Bond-lengths (Å)			
Zn-F x4		2.045(7)	2.046(7)
Zn-F_a x2		2.015(7)	2.012(10)
<Zn-F>		2.035	2.035
R-indices* (%)			
R_B	1.62	R_P	5.67
R_{WP}	7.76	R_{WP}(exp.)	2.98
D-W	0.488	N-P	1983

σs have been corrected using equation 12.1
* R_B = Rietveld Bragg-agreement index
R_P = Rietveld profile-agreement index
R_{WP} = Rietveld weighted profile-agreement index
D-W = Durbin-Watson d-statistic
N-P = Number of data points

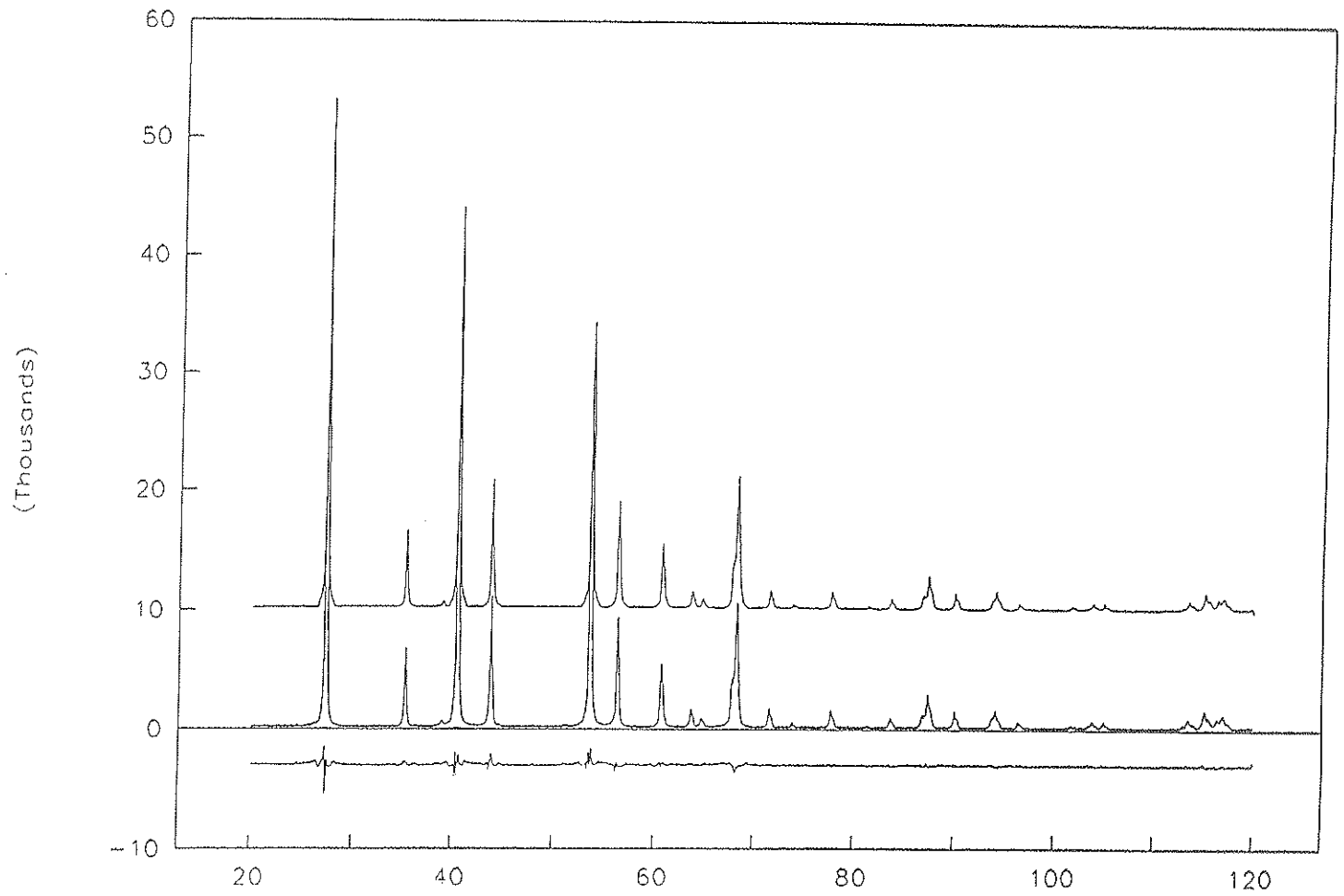

Figure 12.7. The observed (middle) and calculated (top) powder pattern for MgF_2; bottom: residual (I_{calc}-I_{obs}).

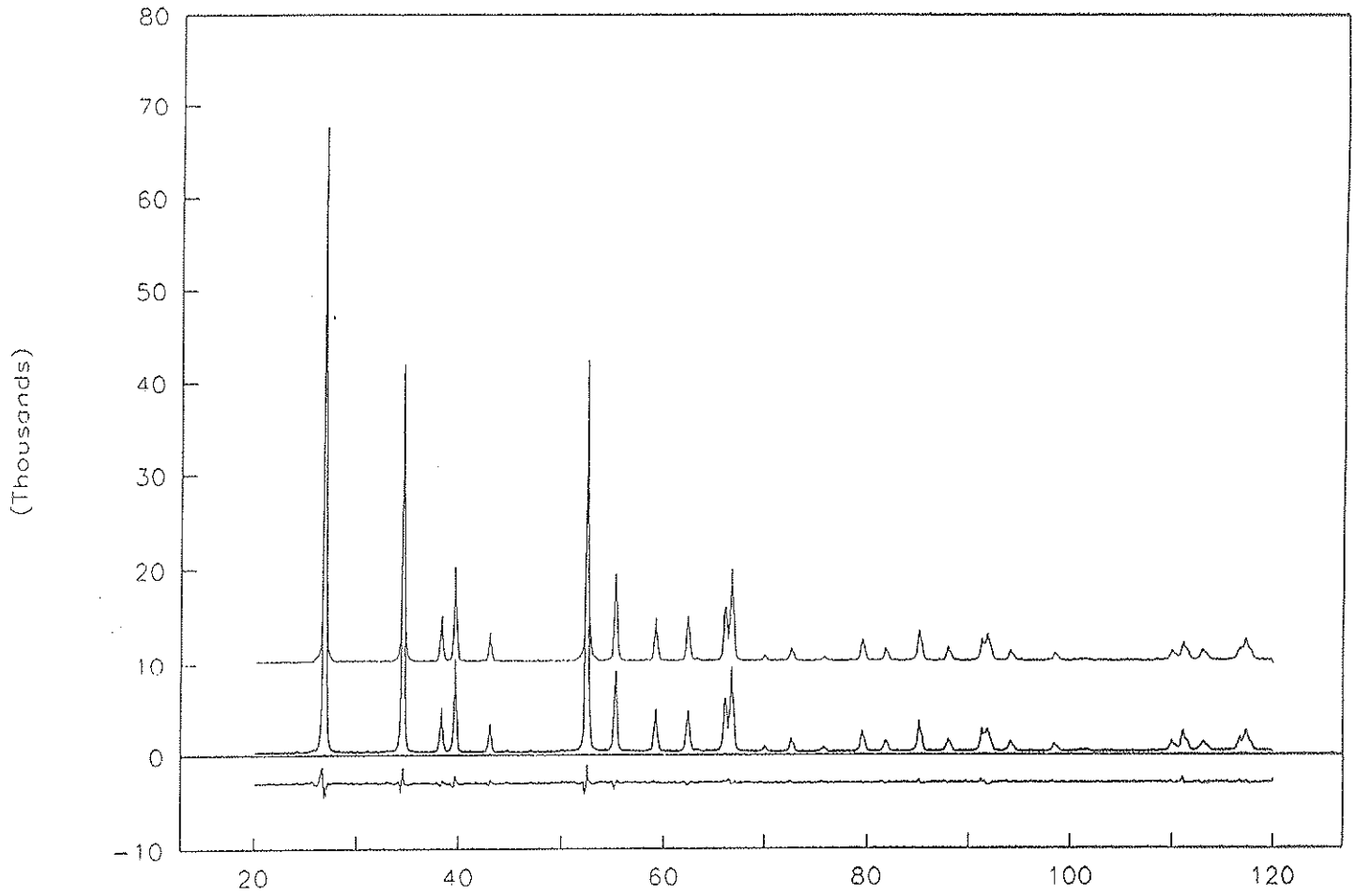

Figure 12.8. The observed (middle) and calculated (top) powder pattern for ZnF_2; bottom: residual (I_{calc}-I_{obs}).

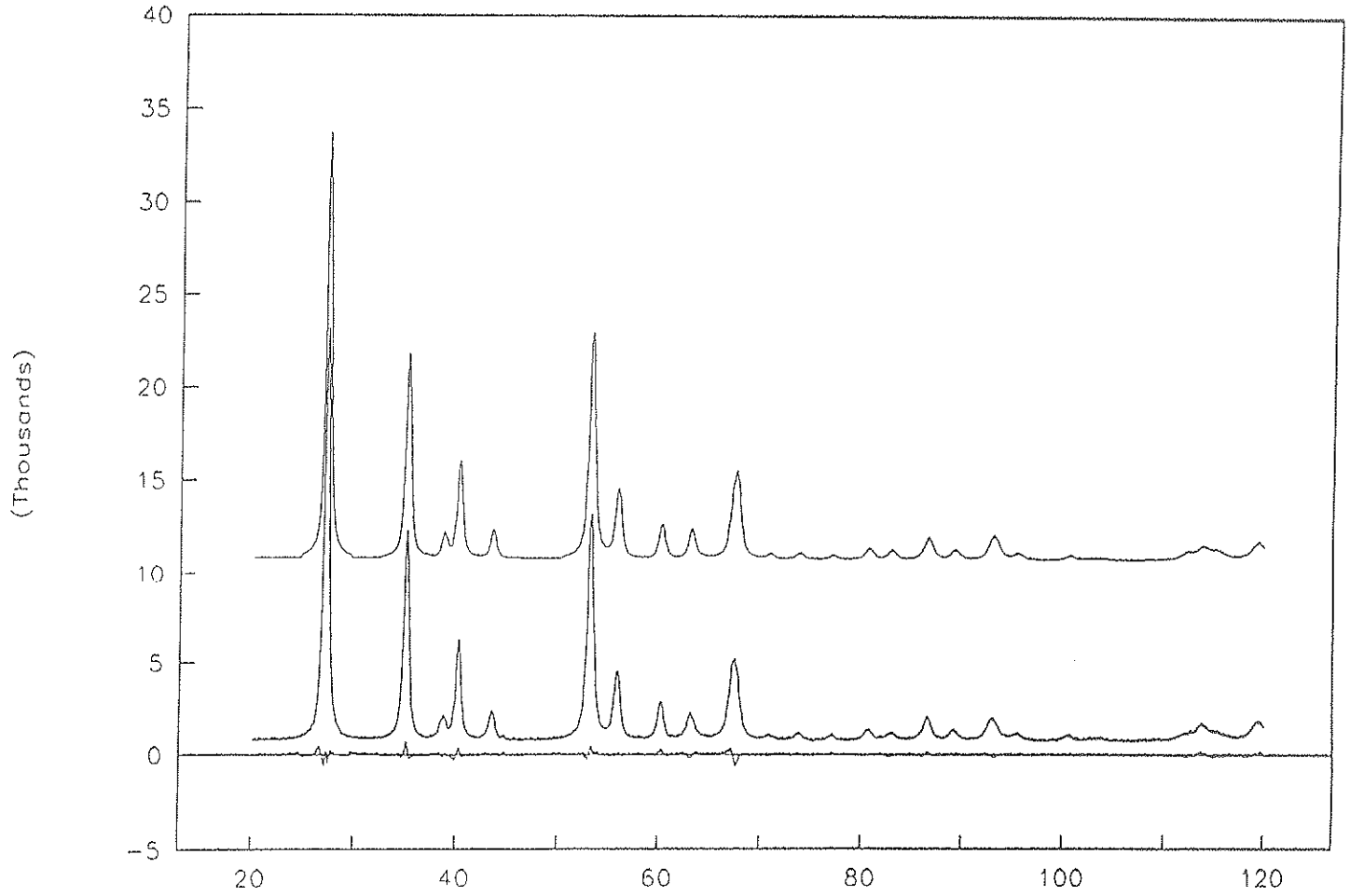

Figure 12.9. The observed (middle) and calculated (top) powder pattern for NiF_2; bottom: residual (I_{calc}-I_{obs}).

data or in the model, thus leading to underestimation of parameter standard deviations (Bérar and Lenann, 1991) and a Durbin-Watson d-statistic < 2.0.

Refinements of the structures of MgF_2, NiF_2 and ZnF_2 were done for data collected with a 0.05°2θ step width and 5s spent counting per step. The Durbin-Watson d-statistics obtained from these refinements are reported in Tables 12.4, 12.5 and 12.6 and are considerably lower than the optimal value of 2.0. There is significant positive serial correlation of adjacent least-squares residuals, and the parameter E.S.D.s are probably underestimated.

The serial correlation of adjacent residuals may be reduced by increasing the 2θ step width or by reducing the time spent counting at each step (Hill and Madsen, 1986). However, this approach amounts to omitting data that is useful during the refinement of accurate structural parameters in order to get realistic E.S.D.s for the refined parameters.

Another approach is to complete the Rietveld refinement using a high-quality data set, with an appropriate correction of the E.S.D.s to account for the serial correlation of adjacent least-squares residuals as indicated by the Durbin-Watson d-statistic. A relationship between the E.S.D.s and the Durbin-Watson d-statistic for a given structure type and set of experimental conditions may be derived. Using this relationship, the appropriate correction of the E.S.D.s may be estimated regardless of the amount of serial correlation of adjacent least-squares residuals.

The X-ray powder-diffraction data for MgF_2 was collected using a step width of 0.01°θ and 5s spent counting per step. A series of Rietveld refinements were done for subsets of this data at different step intervals,

giving a range of Durbin-Watson d-statistics from 0.084 to 1.951. The relationship between the Durbin-Watson d-statistic and the E.S.D.s for various structural parameters is given in Figure 12.10, in which it has been assumed that the E.S.D.s are unaffected by the serial correlation of adjacent least-squares residuals when the Durbin-Watson d-statistic is 1.951 (~ 2.0).

There is an approximately linear relationship (R = 0.975) between the structure-parameter E.S.D.s and the Durbin-Watson d-statistic (Fig. 12.10) for the MgF_2 refinements, and this relationship is largely independent of the identity of the structure parameters. The best-fit line is:

$$y = 0.3442x + 0.2529 \qquad (12.1)$$

where x is the Durbin-Watson d-statistic for the refinement. The E.S.D.s derived from the refinement may be scaled by 1/y to obtain an estimate of the E.S.D.s in the absence of serial correlation of adjacent least-squares residuals.

The E.S.D.s obtained for MgF_2, NiF_2 and ZnF_2 (Tables 12.4, 12.5 and 12.6) have been corrected using equation 12.1, giving more reasonable estimates of the precision of the refined structure parameters.

The Rietveld results for the MgF_2 structure are compared to the single-crystal refinement results reported by Baur (1976) in Table 12.5. The unit-cell dimensions and atomic positional parameters obtained using the two methods are identical within 3σ and 1.5σ, respectively. The bond-lengths obtained using each method are identical within 1σ.

The unit-cell parameters obtained using the Rietveld technique for NiF_2 and ZnF_2 are in poor agreement with those reported by Baur and

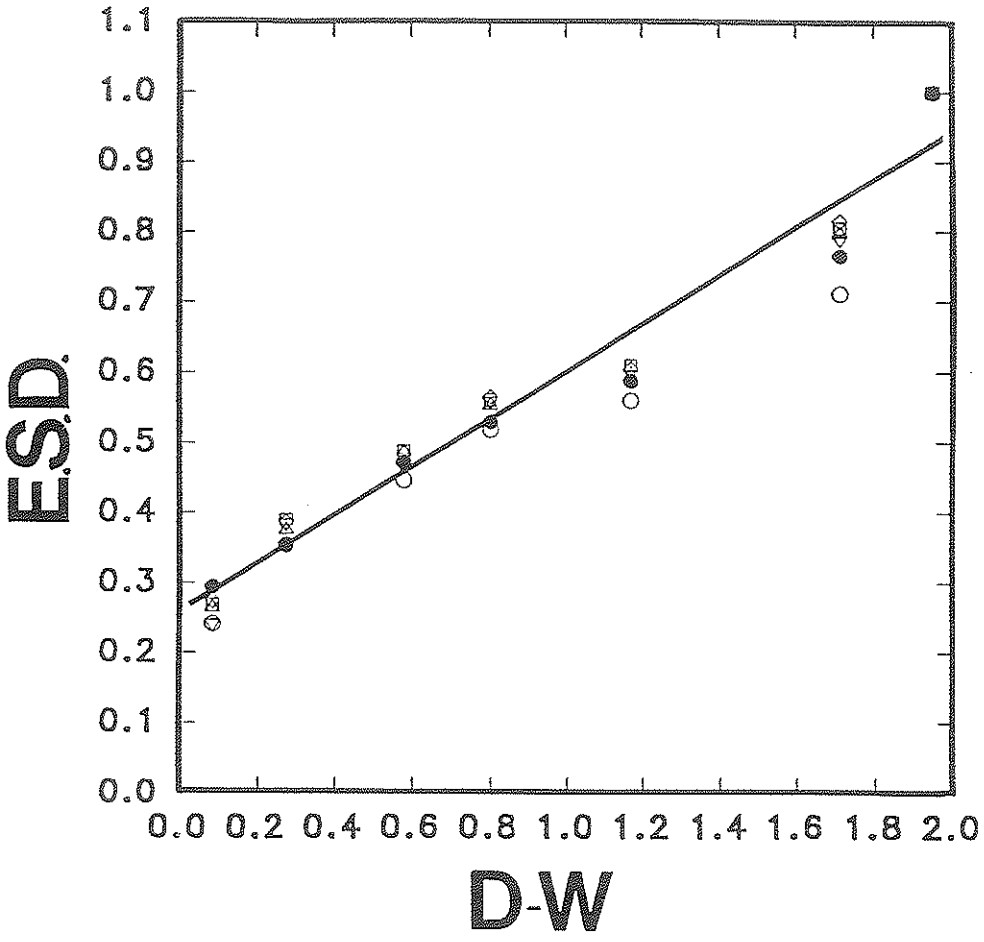

Figure 12.10. The relationship between the Rietveld estimated standard deviations (E.S.D.s) and the refinement Durbin-Watson d-statistic (D-W) for MgF_2. The straight line is y = 0.3442x + 0.2529. The *a* and *b* unit-cell parameter E.S.D.s are open circles and open downward-pointing triangles, respectively; the F positional parameter E.S.D.s are open upward-pointing triangles; isotropic-displacement parameter E.S.D.s for Mg and F are open squares and open diamonds, respectively; the occupancy factor E.S.D.s for the Mg site are closed circles.

Khan (1971) as derived from single-crystal data (Tables 12.5 and 12.6). It is unlikely, in view of the excellent agreement of the unit-cell parameters derived by the two methods for MgF_2, and considering that the single-crystal refinement for MgF_2 is more recent (Baur, 1976), that the unit-cell dimensions for NiF_2 and ZnF_2 reported by Baur and Khan (1971) are accurate. The atomic positional parameters and M-F bond-lengths obtained from the Rietveld refinement are more precise than those reported by Baur and Khan (1971) and the parameters derived by each method are identical within 1σ.

It is apparent from these results that the Rietveld method of crystal-structure refinement gives results comparable to single-crystal studies for MgF_2, ZnF_2 and NiF_2. It is therefore appropriate to use the method to study the details of structural changes in the $(M_{1-x}Cu^{2+}_x)F_2$ series.

12.5.3 $Cu^{2+}F_2$.

Refinement of the $Cu^{2+}F_2$ structure was initiated in the space group $P2_1/n$ with the structural parameters of Billy and Haendler (1956) as starting values. Scattering factors for Cu^{2+} and F^{1-} were taken from the *International Tables for X-ray Crystallography* (1974). Peaks were modelled using a pseudo-Voigt profile function which was corrected for peak asymmetry to 30°2θ. Refinement of the structure converged to the structure parameters given in Table 12.7. An anisotropic-displacement model was attempted, but resulted in a general instability of the refinement. The final observed and calculated patterns are given in Figure 12.11. The observed step-scan pattern is given in Appendix E.

Table 12.7 Refined structure parameters[#], R-indices and bond-lengths for $Cu^{2+}F_2$.

Space group	$P2_1/n$	
Cell parameters		
a (Å)	3.2973(4)	
b	4.5624(6)	
c	4.6157(6)	
β (°)	83.293(6)	
V (Å^3)	68.96(4)	
Z	2	
Atomic parameters		
Cu:	x	0
	y	0
	z	0
	B (Å^2)	0.52(4)
F:	x	-0.042(1)
	y	0.2941(9)
	z	0.2941(9)
	B (Å^2)	0.5(2)

Bond-lengths (Å)	
Cu-F x2	1.902(6)
Cu-F_a x2	1.932(6)
Cu-F_b x2	2.318(6)
<Cu-F>	2.051
R-indices[*] (%)	
R_B	0.97
R_P	1.99
R_{WP}	2.71
R_{WP}(exp.)	1.46
D-W	0.611
N-P	1999

σs have been corrected using equation 12.1
* R_B = Rietveld Bragg-agreement index
R_P = Rietveld profile-agreement index
R_{WP} = Rietveld weighted profile-agreement index
D-W = Durbin-Watson d-statistic
N-P = Number of data points

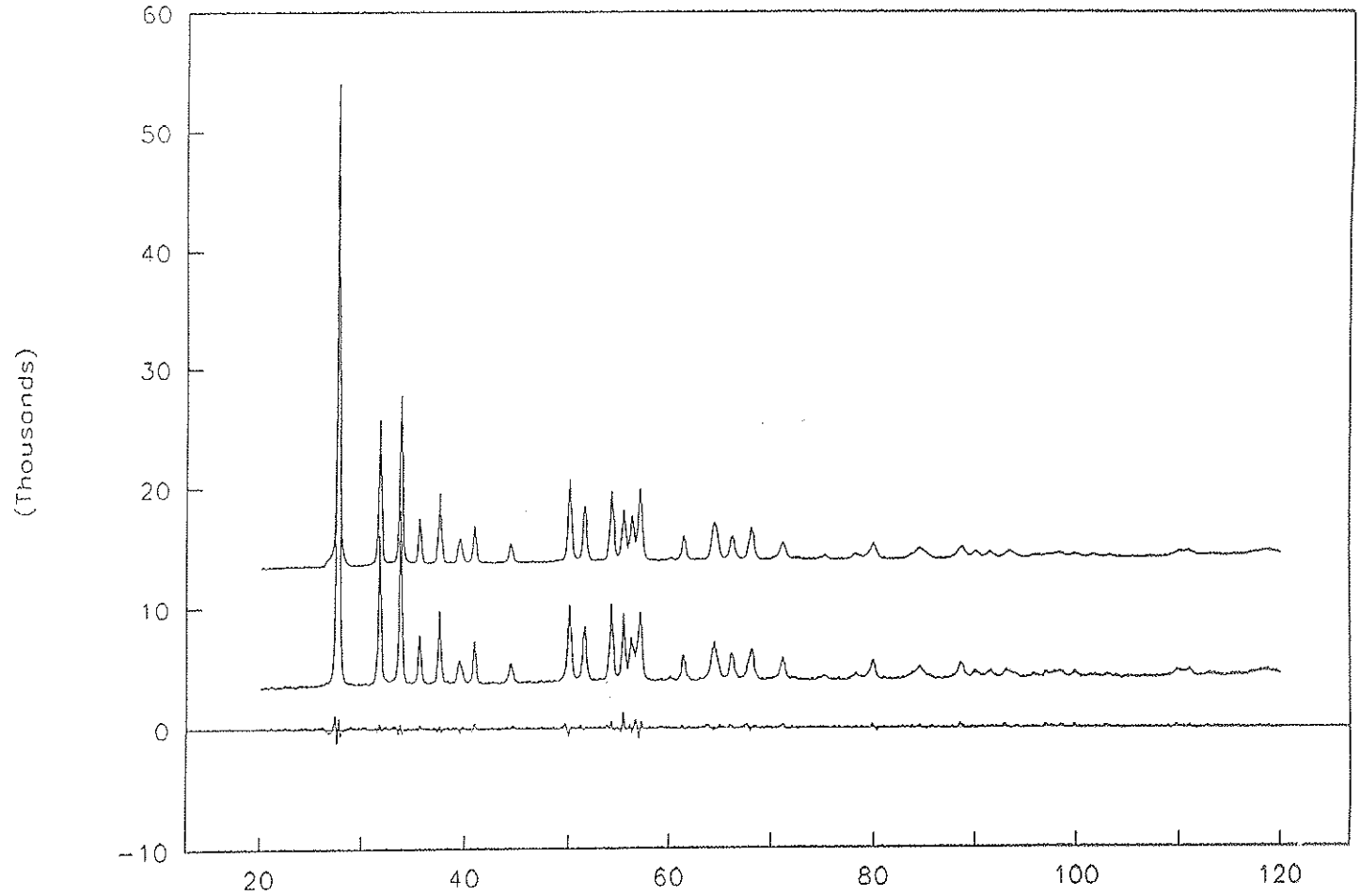

Figure 12.11. The observed (middle) and calculated (top) powder pattern for $Cu^{2+}F_2$; bottom: residual (I_{calc}-I_{obs}).

As expected, the Rietveld refinement of the $Cu^{2+}F_2$ structure indicates that the $Cu^{2+}F_6$ octahedron is in a (4+2)-distorted arrangement, with Cu-F x2 = 1.902(6), Cu-F_a x2 = 1.932(6) and Cu-F_b x2 = 2.318(6) Å.

12.5.4 The $(Zn_{1-x}Cu_x^{2+})F_2$ Series.

Variation of the octahedral geometry in the series $(Zn_{1-x}Cu_x^{2+})F_2$ with increasing x, caused by the Jahn-Teller effect, drives the tetragonal to monoclinic phase transition. Rietveld structure refinements were done for $0 \leq x \leq 1$ to obtain octahedral M-F distances.

Rietveld refinements for the monoclinic-structure samples ($x > 0.475$) were done in the space group $P2_1/n$ (the space group of $Cu^{2+}F_2$) using the refined $Cu^{2+}F_2$ structure parameters reported in section 12.5.2 as starting parameters. Refinement of tetragonal samples ($x< 0.475$) were done in the space group $P4_2/mnm$ (the space group of ZnF_2) with the refined structure parameters of ZnF_2 (Section 12.5.1) as the starting model. Other refinement procedures were as for the end members of the series (Section 12.5.1 and 12.5.2). The observed step-scan patterns for this series are given in Appendix I.

The $(Zn_{1-x}Cu_x^{2+})F_2$ series did not display crystal quality as high as the commercial $Cu^{2+}F_2$ and ZnF_2 materials, as reflected by considerably higher refinement R-indices (Table 12.8). The structure refinements were not as stable as the end-member refinements, as indicated by relatively slow convergence and unrealistic isotropic-displacement parameters. Final refinements were therefore done with the isotropic-displacement parameters fixed at the values obtained for $Cu^{2+}F_2$ and ZnF_2, with an overall

Table 12.8 Refined structure parameters[#] and R-indices[*] (%) for the $(Zn_{1-x}Cu_x^{2+})F_2$ series.

x	a(Å)	b(Å)	c(Å)	β(°)	Vol(Å^3)
0.00	4.7125(2)	4.7125(2)	3.1277(2)	90	69.459(9)
0.10	4.6976(3)	4.6976(3)	3.1396(3)	90	69.28(2)
0.20	4.6825(5)	4.6825(5)	3.1509(5)	90	69.09(3)
0.30	4.6676(8)	4.6676(8)	3.1636(6)	90	68.92(3)
0.40	4.652(1)	4.652(1)	3.1775(8)	90	68.75(6)
0.50	3.196(3)	4.627(3)	4.640(6)	87.98(6)	68.6(2)
0.60	3.212(1)	4.612(3)	4.629(3)	86.95(3)	68.5(1)
0.70	3.235(1)	4.599(3)	4.617(3)	85.76(3)	68.5(1)
0.80	3.261(1)	4.582(2)	4.616(2)	84.86(2)	68.69(8)
0.90	3.2835(5)	4.565(1)	4.608(1)	84.12(1)	68.71(5)
1.00	3.2973(4)	4.5624(6)	4.6157(6)	83.293(6)	68.96(4)

x	S.G.	R_B	R_P	R_{WP}	R_{WP}(exp.)	D-W	$B_{overall}$
0.00	$P4_2/mnm$	1.62	5.67	7.76	2.98	0.488	----
0.10	$P4_2/mnm$	4.18	7.01	10.30	2.64	0.357	-0.2(1)
0.20	$P4_2/mnm$	2.97	5.82	9.08	2.35	0.345	-0.4(1)
0.30	$P4_2/mnm$	4.08	5.46	9.08	2.35	0.290	-0.6(2)
0.40	$P4_2/mnm$	2.28	5.56	8.03	2.05	0.296	-0.8(3)
0.50	$P2_1/n$	6.23	6.44	10.98	1.92	0.160	-0.5(4)
0.60	$P2_1/n$	3.63	4.39	6.97	1.81	0.200	-0.7(3)
0.70	$P2_1/n$	3.56	3.84	6.43	1.75	0.198	-0.6(3)
0.80	$P2_1/n$	2.82	3.63	6.13	1.65	0.342	-0.3(3)
0.90	$P2_1/n$	1.79	2.99	5.10	1.56	0.381	-0.2(3)
1.00	$P2_1/n$	0.97	1.99	2.71	1.46	0.611	----

x	F(x)	F(y)	F(z)
0.00	0.3024(7)	0.302(4)	0
0.10	0.302(1)	0.302(1)	0
0.20	0.304(1)	0.304(1)	0
0.30	0.302(1)	0.302(1)	0
0.40	0.304(2)	0.304(2)	0
0.50	0.008(9)	0.305(6)	0.305(6)
0.60	-0.007(6)	0.303(3)	0.303(3)
0.70	-0.010(6)	0.300(3)	0.300(3)
0.80	-0.012(5)	0.300(2)	0.300(2)
0.90	-0.019(1)	0.2971(8)	0.2971(8)
1.00	-0.042(1)	0.2941(9)	0.2941(9)

σs have been corrected using equation 12.1
* R_B = Rietveld Bragg-agreement index; R_P = Rietveld profile-agreement index; R_{WP} = Rietveld weighted profile-agreement index; D-W = Durbin-Watson d-statistic

displacement factor refined. The refined structure parameters are listed in Table 12.8 and the M-F bond-lengths in Table 12.9.

Unit-cell parameters obtained for the $(Zn_{1-x}Cu_x^{2+})F_2$ series by Rietveld refinement are in good agreement with those derived by least-squares refinement of peak-positional data reported in section 12.3 (Table 12.8, Figure 12.12). The M-F bond-lengths obtained by Rietveld refinement for the series (Table 12.9) are shown in Figure 12.13.

For values of $x < 0.50$, the structure is tetragonal with two sets of unique M-F bond-lengths (Fig. 12.13). A small increase in the four equivalent M-F distances, coupled with a small decrease of the two equivalent M-F bond-lengths occurs with increasing x in the tetragonal structure material. For values of $x > 0.50$, the structure has three sets of equivalent M-F bond-lengths, two of which decrease while the other set increases in length with increasing x, giving a (4+2)-distorted octahedral coordination of ligands around the metal cation for values of $x > 0.50$. The (4+2)-distortion is obtained by decreasing two and increasing two of the bond-lengths of the four M-F bonds that were equivalent in the tetragonal structure (Fig. 12.13).

12.5.5 The $(Mg_{1-x}Cu_x^{2+})F_2$ Series.

Rietveld structure refinements were done for selected values of x in the series $(Mg_{1-x}Cu_x^{2+})F_2$ to verify that the M-F octahedral bond-lengths vary in the same fashion as observed in the $(Zn_{1-x}Cu_x^{2+})F_2$ series (Section 12.5.3). The Rietveld refinements were done as for the $(Zn_{1-x}Cu_x^{2+})F_2$ series (Section 12.5.3); observed step-scan patterns are given in Appendix J.

Table 12.9 Bond-lengths (Å) for the $(Zn_{1-x}Cu_x^{2+})F_2$ series.

x	M-F x2	MF_a x2	$M\text{-}F_b$ x2
0.00	2.015(7)	2.045(7)	2.045(7)
0.10	2.01(1)	2.05(1)	2.05(1)
0.20	2.01(2)	2.04(2)	2.04(2)
0.30	1.99(2)	2.05(2)	2.05(2)
0.40	2.00(2)	2.05(2)	2.05(2)
0.50	2.00(6)	2.04(6)	2.05(6)
0.60	1.98(3)	2.00(3)	2.11(3)
0.70	1.96(3)	2.00(3)	2.15(2)
0.80	1.95(2)	1.99(2)	2.18(2)
0.90	1.92(2)	1.98(2)	2.23(2)
1.00	1.902(6)	1.932(6)	2.318(6)

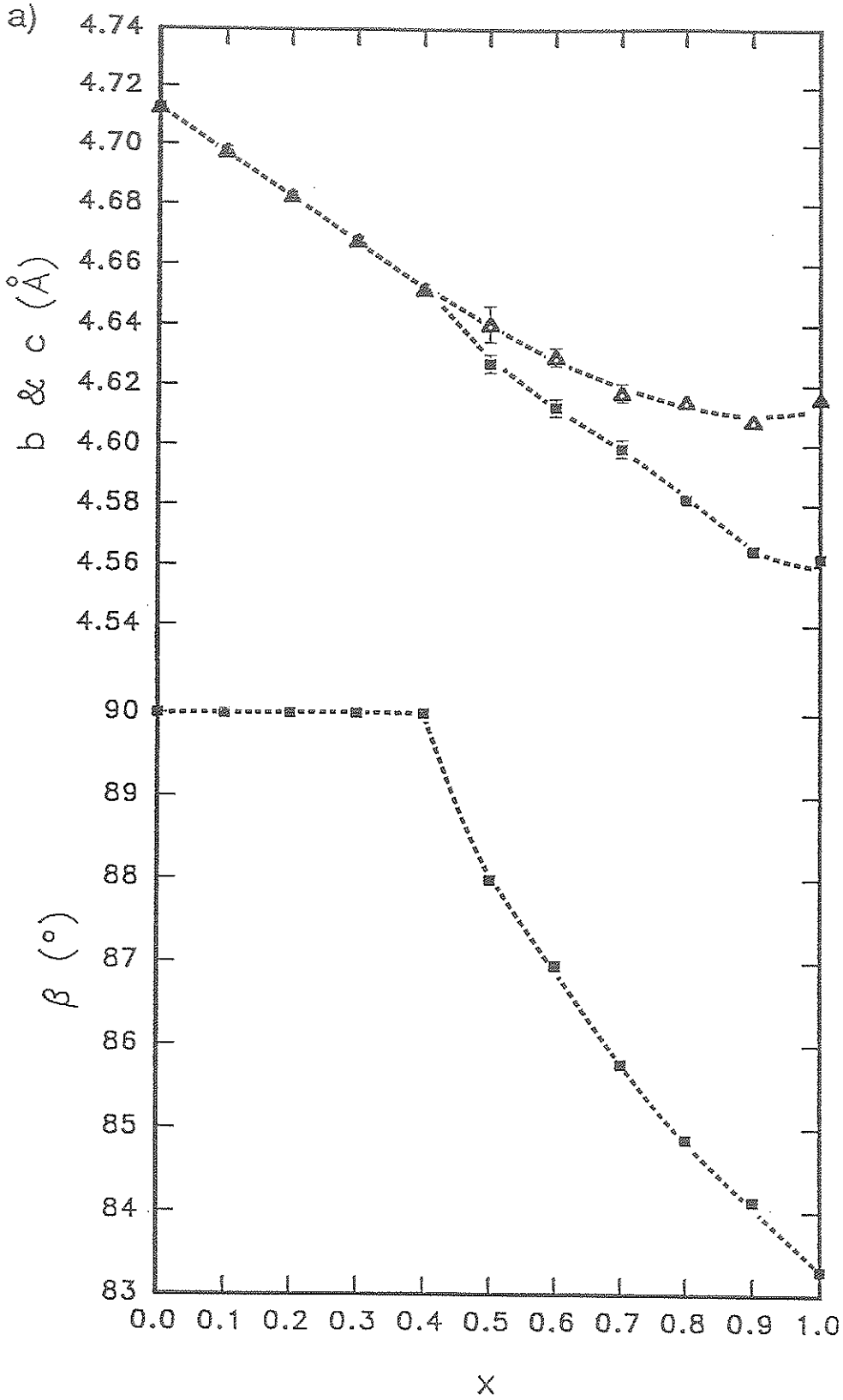

Figure 12.12. Rietveld unit-cell parameters for the $(Zn_{1-x}Cu_x^{2+})F_2$ series. a) β, *b* and *c*; b) *a* and *V*.

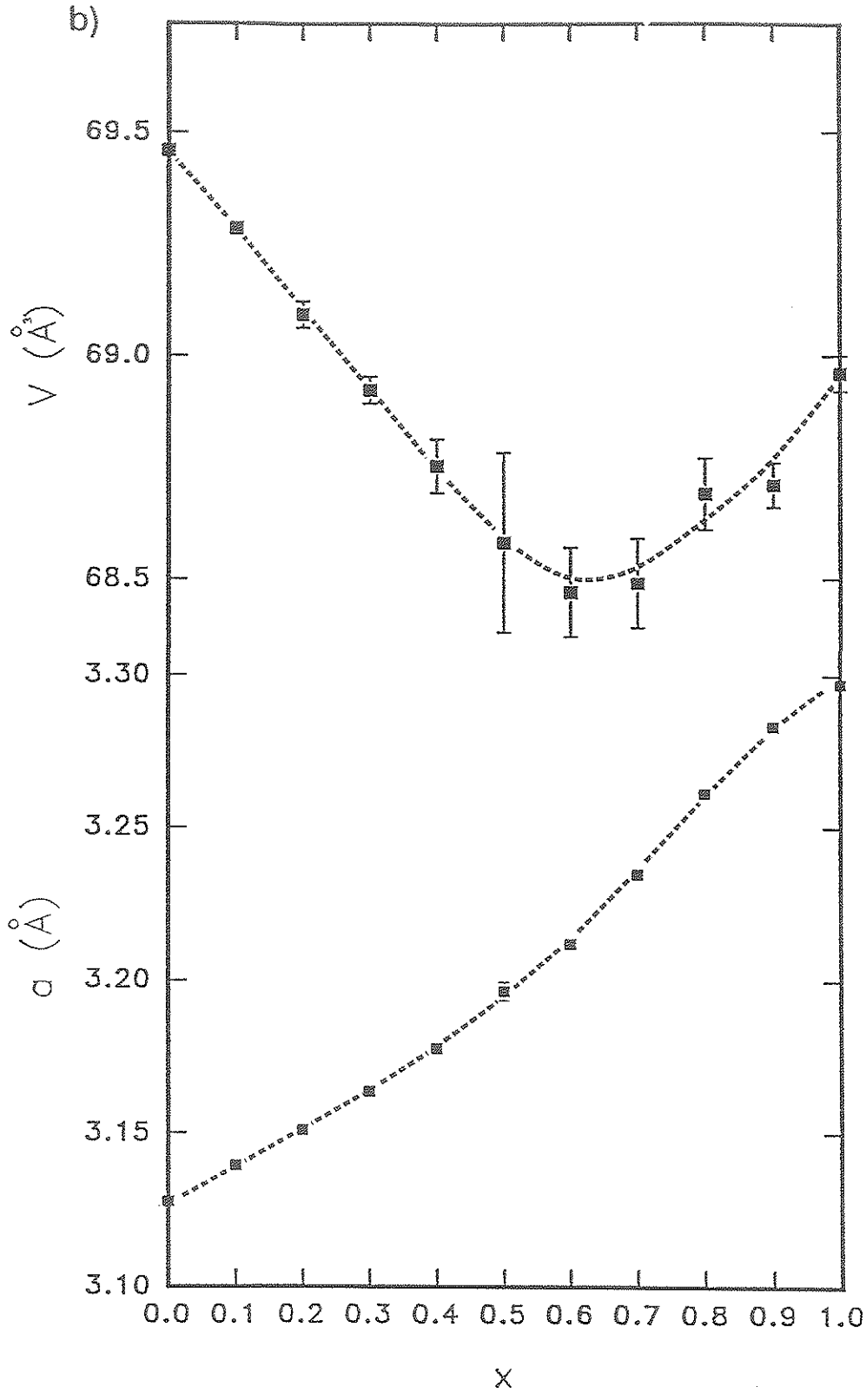

Figure 12.12 Continued

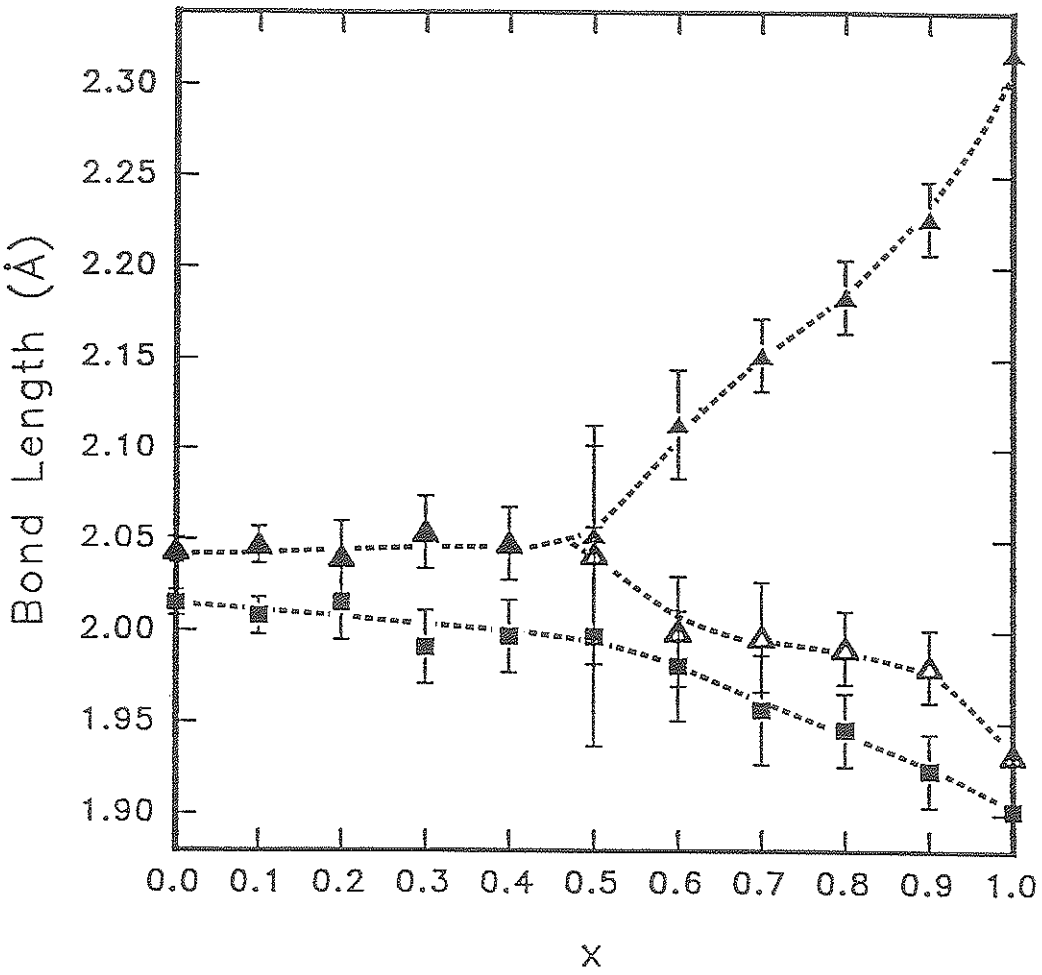

Figure 12.13. Octahedral bond-lengths for the $(Zn_{1-x}Cu_x^{2+})F_2$ series.

The synthesized powders of $(Mg_{1-x}Cu_x^{2+})F_2$ composition were of good quality as indicated by low R-indices (Table 12.10). Unlike the refinements for the $(Zn_{1-x}Cu_x^{2+})F_2$ series, isotropic-displacement parameters were well behaved, and are reported along with the other refined parameters in Table 12.10. The X-ray scattering powers of Mg^{2+} and Cu^{2+} are quite different, and so the site occupancies of each sample were refined. The refined occupancies agreed with the nominal occupancies within 3σ. The unit-cell parameters from the Rietveld refinements are in good agreement with those derived by least-squares refinement of peak-positional data (Section 12.3, Table 12.10, Figure 12.14). The M-F bond-lengths obtained from the refined structure parameters are given in Table 12.11 and Figure 12.15.

12.6 Mechanisms of the Phase Transition in the $(M_{1-x}Cu_x^{2+})F_2$ Series.

Jahn-Teller distortion of the octahedral-ligand arrangement around Cu^{2+} results in a phase transition in the $(Zn_{1-x}Cu_x^{2+})F_2$ and $(Mg_{1-x}Cu_x^{2+})F_2$ series. Electron spin resonance (ESR) spectroscopy shows that dilute concentrations of octahedrally coordinated Cu^{2+} in a host structure show distortions of their octahedral geometries, acting as distortion centres in the host structure (i.e., Rubins and Drumheller, 1987). At low concentrations of Cu^{2+} in $(Zn_{1-x}Cu_x^{2+})F_2$ and $(Mg_{1-x}Cu_x^{2+})F_2$, the local $Cu^{2+}F_6$ octahedral distortions do not interact. However, at $x=x_c$ in each series, the independent $Cu^{2+}F_6$ octahedral distortions couple to a phonon, resulting in a tetragonal-to-monoclinic phase transition.

The four equivalent M-F bond-lengths of the tetragonal $(Zn_{1-x}Cu_x^{2+})F_2$ and $(Mg_{1-x}Cu_x^{2+})F_2$ structures increase with x (Figs. 12.13 and 12.15). This increase is offset by a decrease of the bond-lengths of the pair of equivalent

Table 12.10 Structure parameters[#] and R-indices[*] (%) for the $(Mg_{1-x}Cu_x^{2+})F_2$ series.

x	a(Å)	b(Å)	c(Å)	β(°)	Vol(Å^3)
0.00	4.6207(2)	4.6207(2)	3.0512(1)	90	65.146(8)
0.30	4.6092(5)	4.6092(5)	3.1011(2)	90	65.88(2)
0.40	4.6042(4)	4.6042(4)	3.1212(2)	90	66.17(2)
0.50	3.1462(4)	4.5973(7)	4.6038(7)	88.41(1)	66.14(3)
0.60	3.1676(1)	4.5903(4)	4.5974(4)	87.288(5)	66.77(1)
0.80	3.2252(3)	4.5781(8)	4.5978(8)	85.475(9)	67.68(3)
0.90	3.2592(3)	4.5628(4)	4.5972(4)	84.497(6)	68.05(1)
1.00	3.2973(4)	4.5624(6)	4.6157(6)	83.293(6)	68.96(4)

x	S.G.	R_B	R_P	R_{WP}	$R_{(WP)}$(exp.)	D-W
0.00	$P4_2/mnm$	2.16	7.07	11.08	3.60	0.791
0.30	$P4_2/mnm$	1.36	2.67	4.30	1.63	0.430
0.40	$P4_2/mnm$	1.83	2.49	3.56	1.59	0.820
0.50	$P2_1/n$	2.68	2.95	4.44	1.55	1.274
0.60	$P2_1/n$	2.42	2.61	3.75	1.48	1.656
0.80	$P2_1/n$	2.37	2.89	4.44	1.47	1.099
0.90	$P2_1/n$	1.49	2.46	3.54	1.47	1.308
1.00	$P2_1/n$	0.97	1.99	2.71	1.46	0.611

x	F(x)	F(y)	F(z)
0.00	0.3035(4)	0.3035(4)	0
0.30	0.3009(7)	0.3009(7)	0
0.40	0.3011(6)	0.3011(6)	0
0.50	-0.001(2)	0.3001(7)	0.3001(7)
0.60	-0.014(1)	0.3013(5)	0.3013(5)
0.80	-0.018(2)	0.2996(9)	0.2996(9)
0.90	-0.030(1)	0.2970(7)	0.2970(7)
1.00	-0.042(1)	0.2941(9)	0.2941(9)

x	B(M)	B(F)
0.00	0.32(6)	0.58(8)
0.30	0.5(1)	0.5(2)
0.40	0.2(1)	0.7(2)
0.50	0.4(1)	0.5(3)
0.60	0.53(7)	0.8(2)
0.80	0.4(1)	0.9(5)
0.90	0.2(9)	0.9(5)
1.00	0.52(2)	0.48(7)

σs have been corrected using equation 12.1; * R_B = Rietveld Bragg-agreement index; R_P = Rietveld profile-agreement index; R_{WP} = Rietveld weighted profile-agreement index; D-W = Durbin-Watson d-statistic.

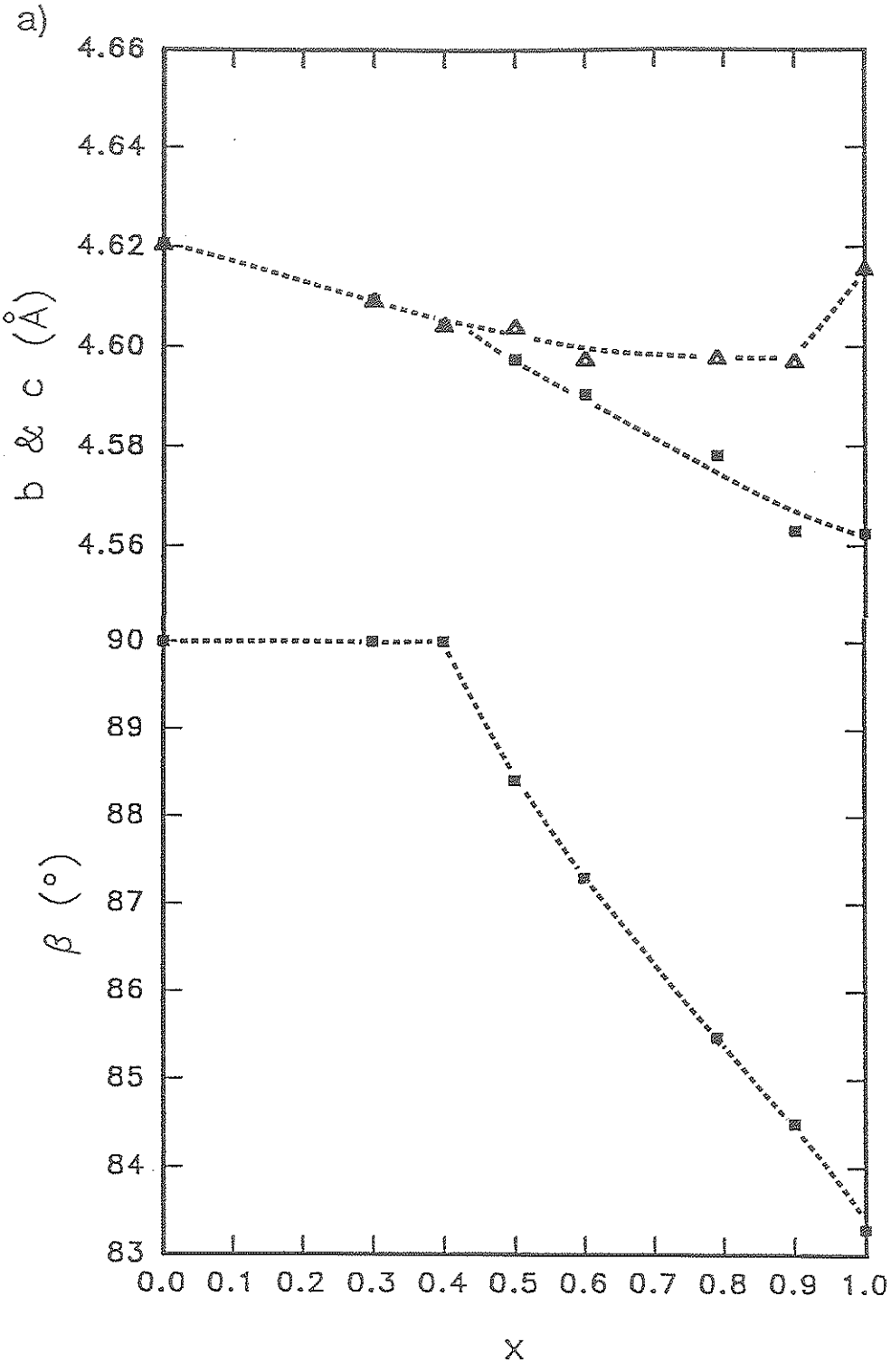

Figure 12.14. Rietveld unit-cell parameters for the $(Mg_{1-x}Cu_x^{2+})F_2$ series. a) β, *b* and *c*; b) *a* and *V*.

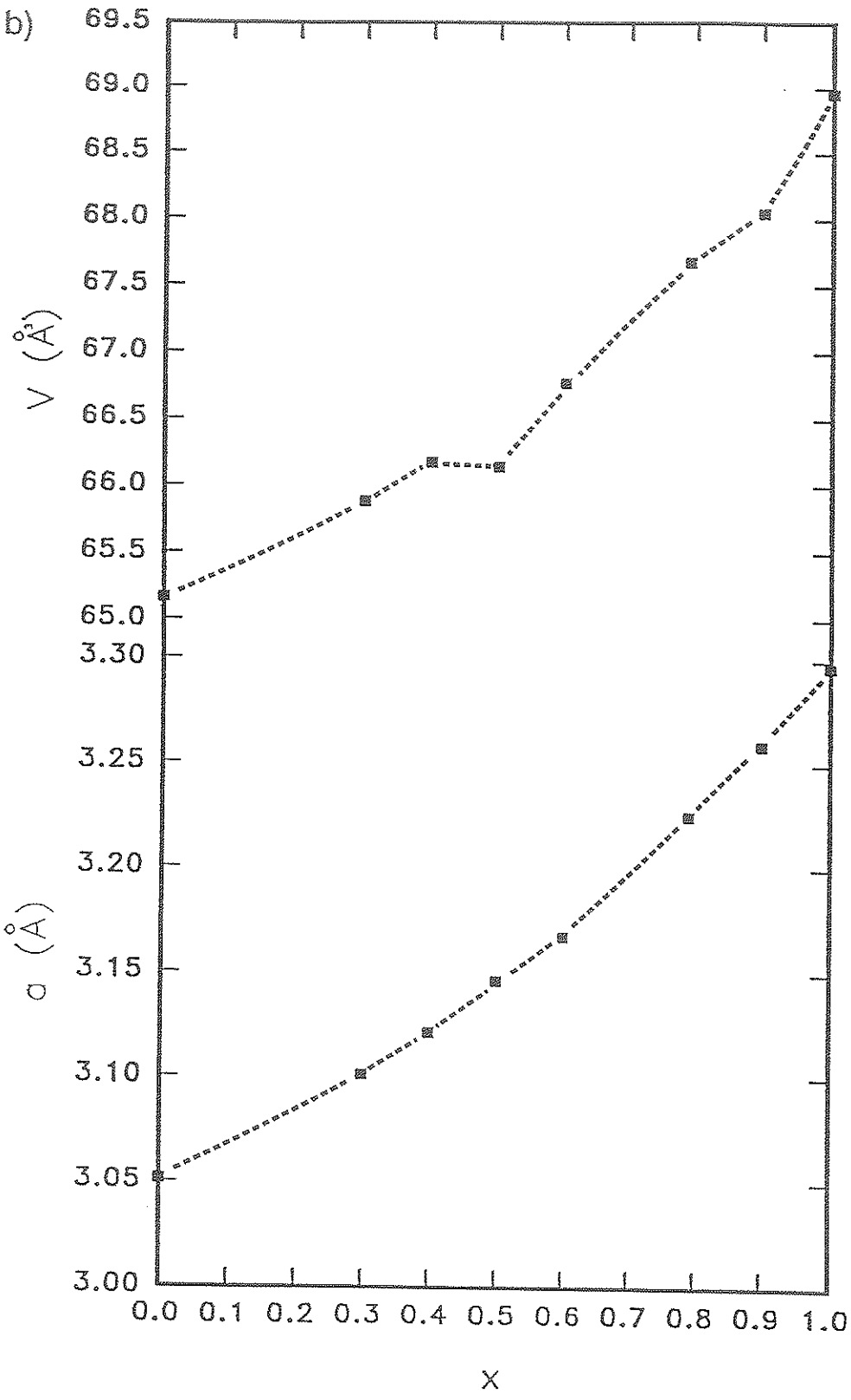

Figure 12.14. Continued

Table 12.11 Bond-lengths (Å) for the $(Mg_{1-x}Cu_x^{2+})F_2$ series.

x	M-F x2	$M-F_a$ x2	$M-F_b$ x2
0.00	1.983(4)	1.994(4)	1.994(4)
0.30	1.962(7)	2.022(7)	2.022(7)
0.40	1.961(6)	2.028(6)	2.028(6)
0.50	1.952(7)	2.018(7)	2.064(7)
0.60	1.957(6)	1.976(6)	2.111(6)
0.80	1.947(9)	1.970(9)	2.174(9)
0.90	1.920(7)	1.950(7)	2.241(7)
1.00	1.902(6)	1.932(6)	2.318(6)

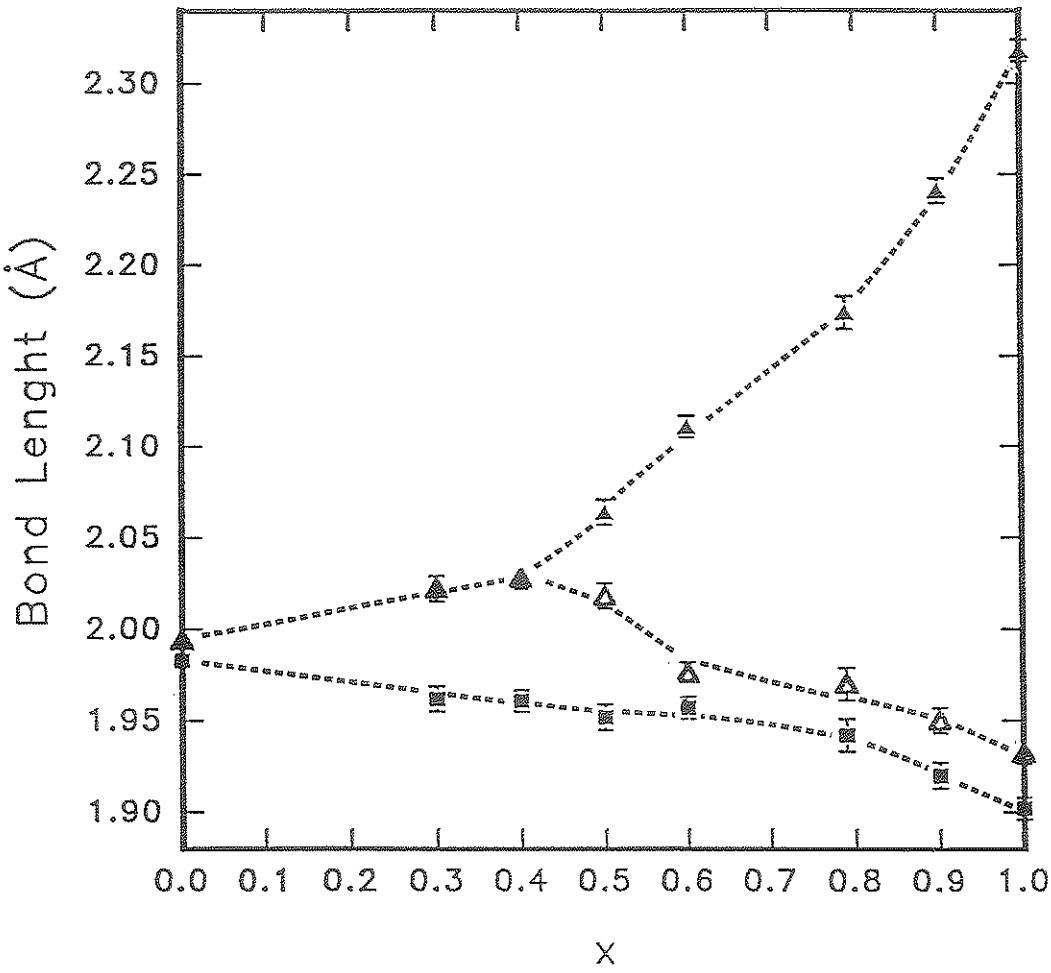

Figure 12.15. Octahedral bond-lengths for $(Mg_{1-x}Cu_x^{2+})F_2$ series.

M-F bond-lengths with increasing x. Examination of the M-F bond-lengths for $0 < x < x_c$ in the $(Zn_{1-x}Cu_x^{2+})F_2$ and $(Mg_{1-x}Cu_x^{2+})F_2$ series (Figs. 12.13 and 12.15) shows that the octahedral site is (2+4)-distorted. This result is unexpected as Cu^{2+} compounds seldom show a (2+4)-distorted static octahedron (Chapter 2).

Of the three principal axes of the $Cu^{2+}F_6$ octahedron in the tetragonal structure, there are only two symmetrically unique directions. Vibrational interaction with the energetically degenerate electronic state leads to a warped Mexican-hat potential (as discussed in Chapter 2, Fig. 2.4). If the sign of the Jahn-Teller coupling term is negative, the minima in the potential-energy surface occur at $\phi = 0$, 120 and 240°, and correspond to (4+2)-distorted octahedra with the elongation direction of the octahedra pointing in one of the three directions in each well (Hathaway, 1984). The saddlepoints in the potential-energy surface correspond to (2+4)-distorted octahedral geometries. A circular cross-section through the potential-energy minimum contains three energy wells (Fig. 2.5), two of which are equivalent as required by tetragonal symmetry (Fig. 2.5b). The set of four equivalent M-F bond-lengths are the longest M-F bonds in the tetragonal $(Zn_{1-x}Cu_x^{2+})F_2$ and $(Mg_{1-x}Cu_x^{2+})F_2$ structures, suggesting that more $Cu^{2+}F_6$ octahedra are elongated in these directions than in the third direction. The two equivalent energy wells have a lower energy than the third well, as shown in Figure 2.5b.

For values of $x < x_c$, the $Cu^{2+}F_6$ octahedra in $(Zn_{1-x}Cu_x^{2+})F_2$ and $(Mg_{1-x}Cu_x^{2+})F_2$ are probably (4+2)-distorted, with equal populations of octahedra in each of the two symmetrically equivalent energy wells. This means that the $Cu^{2+}F_6$ octahedra embedded in the host structure may be

elongated in one or the other of the two directions that are equivalent by symmetry, with little or no elongation of octahedra in the third direction. Although the local $Cu^{2+}F_6$ octahedra are (4+2)-distorted, the distribution of the elongation directions over the two symmetrically equivalent directions is averaged to a (2+4)-distorted octahedron by X-ray scattering.

The distortion directions of $Cu^{2+}F_6$ octahedra in tetragonal $(Zn_{1-x}Cu_x^{2+})F_2$ and $(Mg_{1-x}Cu_x^{2+})F_2$ may be static if the thermal energy is less than the energy barrier between the two equivalent wells (labelled B in Fig. 2.5). Variable temperature ESR studies for Cu^{2+}-doped $ZnTiF_6.6H_2O$ (Rubins and Drumheller, 1987) and $MgSiF_6.6H_2O$ (Rubins et al., 1984) show that it is also possible that the thermal energy at room temperature is higher than the energy barrier between the wells (labelled B in Fig. 2.5). In this case, a continuous interchange of $Cu^{2+}F_6$ distortion directions would occur as the energy barrier is overcome. X-ray structure refinements will not resolve which of the two possibilities occur in these compounds.

At $x=x_c$, independent $Cu^{2+}F_6$ octahedra in the $(Zn_{1-x}Cu_x^{2+})F_2$ and $(Mg_{1-x}Cu_x^{2+})F_2$ structures are linked via a phonon, and this cooperative effect distorts the structure from tetragonal to monoclinic. The circular cross-section of the warped Mexican-hat potential surface corresponding to $Cu^{2+}F_6$ octahedra embedded in a monoclinic structure contains three energy wells corresponding to (4+2)-distorted octahedra (Fig. 2.5c). All three wells have a different energy, and the lowest well contains most or all of the octahedra. The lowest energy well is one of the two wells that were equivalent in tetragonal symmetry, as shown by bond-length relations (Figs. 12.13 and 12.15). Although the $Cu^{2+}F_6$ octahedron is (4+2)-distorted at all values of x

$> x_c$, the magnitude of the distortion increases steadily with increasing x (Figs. 12.13 and 12.15).

Chapter 13

Jahn-Teller Driven Phase Transitions: The KMF_3 Perovskite-Type Structure

13.1 Introduction and Previous Work.

The fluoride perovskite-type structures $KM^{2+}F_3$, M^{2+} = (Mg, Mn, Fe^{2+}, Co, Ni, Zn), crystallize in the space group Pm3m. The $KCu^{2+}F_3$ structure is a distorted derivative of the cubic perovskite structure. This is a direct result of the cooperative Jahn-Teller effect involving (4+2)-distorted $Cu^{2+}F_6$ octahedra. Two modifications of the $KCu^{2+}F_3$ structure are known (type a and type d; Okazaki, 1967a,b); the type-a structure (Fig. 13.1) is the more common (Tanaka et al., 1979), and is the only structure type encountered in this study. The type-a structure is tetragonal, space group I4/mcm. In this structure, the F(2) atom is located on an 8(h) position, such that it is displaced from the midpoint between two neighbouring Cu^{2+} atoms in the (001) plane, giving both short (equatorial) and long (apical) Cu-F(2) distances. The Cu-F(1) distance is intermediate between the short and the long Cu-F(2) distances, but it is much closer to the short distance; thus it is also designated as an equatorial Cu-F bond, completing the (4+2)-distorted $Cu^{2+}F_6$ octahedron. The direction of the F(2) atom displacements alternate along the c-axis, doubling the c period of the cubic perovskite structure.

This chapter reports the syntheses and structures of the series of compositions $K(Zn_{1-x}Cu_x^{2+})F_3$ and $K(Mg_{1-x}Cu_x^{2+})F_3$, $0 \le x \le 1$; these form complete solid-solutions at about 730°C. The room-temperature structures show a second-order phase transition, where the cooperative Jahn-Teller effect drives the cubic to tetragonal phase transition at $x = x_c$.

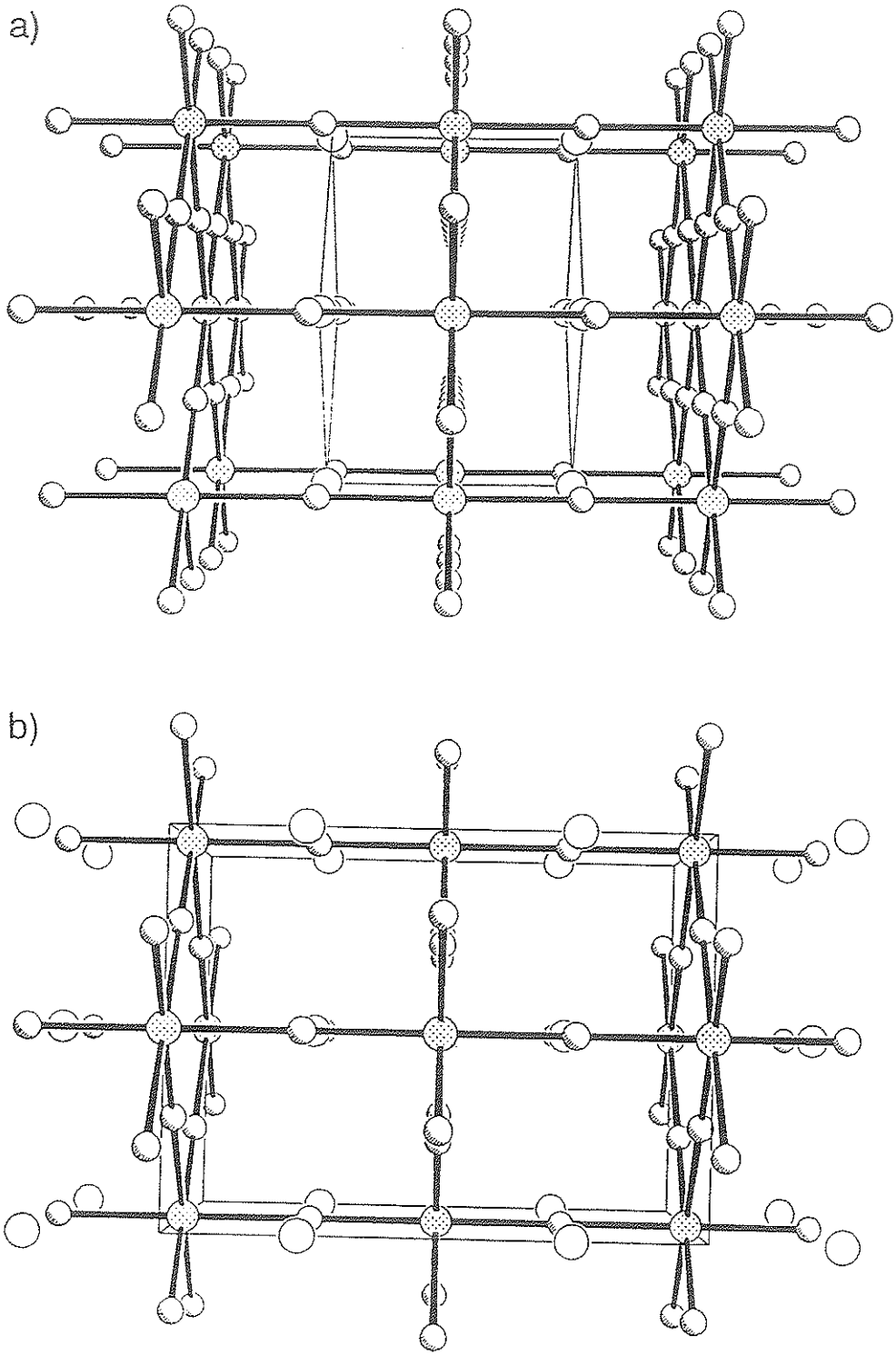

Figure 13.1. The perovskite-type structure. a) cubic, space group Pm3m; b) tetragonal, space group I4/mcm. The divalent-metal cations are circles shaded with a dot pattern, the potassium atoms are large open circles and the fluorine atoms are small circles with shading in the lower left corners.

The systems $K(Zn_{1-x}Cu_x^{2+})F_3$ and $K(Mg_{1-x}Cu_x^{2+})F_3$ were previously studied by Schmitz-Dumont and Grimm (1967) who reported optical absorption and X-ray powder patterns for five intermediate compositions in each series.

13.2 Synthesis of $K(Zn_{1-x}Cu_x^{2+})F_3$ and $K(Mg_{1-x}Cu_x^{2+})F_3$.

The $K(Zn_{1-x}Cu_x^{2+})F_3$ and $K(Mg_{1-x}Cu_x^{2+})F_3$ series were synthesized using ZnF_2 (99% pure), MgF_2 (99.9% pure) and $Cu^{2+}F_2$ (98% pure), and KF obtained by heating $KF.2H_2O$ (99.9% pure) at 350°C for 24 hours. The powders were weighed to ± 0.0002 grams and thoroughly mixed and ground together in an agate mortar prior to each synthesis run.

Powders were pressed into pellets and heated in platinum-foil baskets using a vertical drop furnace. A steady flow of argon from the bottom of the furnace provided an inert atmosphere. The furnace temperature was monitored using a Pt-Rh thermocouple. Each sample was annealed at 730-735°C for 15 minutes and then quenched in air.

13.3 X-Ray Powder-Diffraction Characterization.

Products of $K(Zn_{1-x}Cu_x^{2+})F_3$ and $K(Mg_{1-x}Cu_x^{2+})F_3$ compositions were ground in an agate mortar and front-loaded into brass sample holders for X-ray diffraction examination. X-ray powder diffractograms were collected at 25°C using a Philips PW1710 automated X-ray powder diffractometer with Bragg-Brentano geometry, CuKα X-radiation (40 kV and 40 mA), fixed 1° slits and a diffracted-beam monochromator. A scan speed of 1.8°2θ/minute and an integration time of 1 second were used over the range 10-100°2θ.

The powder patterns show $K(Zn_{1-x}Cu_x^{2+})F_3$ and $K(Mg_{1-x}Cu_x^{2+})F_3$ to be the major phase present in each product, with minor tenorite and/or cuprite present (~ 5%) in the copper-rich products as surface oxidation on the pellets. Unit-cell parameters were obtained using Appleman and Evans (1973) least-squares cell-refinement program (modified by Burns and Trembath). Peaks were indexed using the JCPDS cards for $KMgF_3$, $KZnF_3$ and $KCu^{2+}F_3$. Refined unit-cell parameters are reported in Tables 13.1 and 13.2. Variations of unit-cell dimensions with x for each series are shown in Figures 13.2 and 13.3. In each of these figures, the tetragonal unit-cell parameters are plotted as a_o and c_o to relate them to those of the cubic unit cell; $a_o = a/\sqrt{2}$, $c_o = c/2$.

The transition from the cubic perovskite structure to the $KCu^{2+}F_3$ structure occurs at $x_c \approx 0.55$ in the $K(Zn_{1-x}Cu_x^{2+})F_3$ series and $x_c \approx 0.65$ in the $K(Mg_{1-x}Cu_x^{2+})F_3$ series based upon diffraction peak splitting. The first synthesis product of $K(Mg_{1-x}Cu_x^{2+})F_3$ at this composition seemed dominantly cubic with distinct peak broadening, suggesting the presence of some tetragonal material. A second product synthesized at the same composition seems to contain both cubic and tetragonal material (dominantly tetragonal), suggesting that the phase transition occurs in $K(Mg_{1-x}Cu_x^{2+})F_3$ at $x_c \approx 0.65$. It is notable that the cubic to tetragonal phase transition in $K(M_{1-x}Cu_x^{2+})F_3$ perovskite-type structures occurs at higher values of $x = x_c$ than in the $(M_{1-x}Cu_x^{2+})F_2$ rutile-structure series (Chapter 12). Also, the phase transition in the series $(Zn_{1-x}Cu_x^{2+})F_2$ occurs at a lower $x = x_c$ than in $(Mg_{1-x}Cu_x^{2+})F_2$, concordant with the results for the $K(M_{1-x}Cu_x^{2+})F_3$ structures. This suggests that the location of the phase transition at room temperature is both structurally *and* compositionally dependent.

Table 13.1 Unit-cell parameters from least-squares refinement of powder data* for the $K(Zn_{1-x}Cu_x^{2+})F_3$ series.

x	T(°C)	t(m)	a(Å)	c(Å)	V(Å^3)
0.000	735	15	4.0520(5)	4.0520(5)	66.53(2)
0.100	735	15	4.0525(4)	4.0525(4)	66.55(2)
0.200	735	15	4.0515(5)	4.0515(5)	66.51(2)
0.300	735	15	4.0532(2)	4.0532(2)	66.59(1)
0.400	735	15	4.0532(3)	4.0532(3)	66.59(1)
0.525	735	15	4.0541(3)	4.0541(3)	66.63(1)
0.550	735	15	4.0529(5)	4.0529(5)	66.57(2)
0.575	735	15	5.746(4)	8.070(4)	266.5(2)
0.600	735	15	5.770(1)	8.010(4)	266.7(1)
0.650	735	15	5.781(1)	7.982(4)	266.84(1)
0.700	735	15	5.7970(4)	7.968(1)	267.76(4)
0.750	735	15	5.8034(7)	7.942(2)	267.44(8)
0.800	735	15	5.8162(4)	7.924(1)	268.04(4)
0.850	735	15	5.8250(5)	7.907(1)	268.28(4)
0.900	735	15	5.833(1)	7.885(2)	268.32(8)
0.950	735	15	5.8431(8)	7.858(2)	268.32(8)
1.000	735	15	5.850(1)	7.844(2)	268.4(1)

* Powder patterns for each sample are given in Appendix K.

Table 13.2 Unit-cell dimensions from least-squares refinement of powder data* for the $K(Mg_{1-x}Cu_x^{2+})F_3$ series.

x	T(°C)	t(m)	a(Å)	c(Å)	V(Å^3)
0.000	737	15	3.9859(7)	3.9859(7)	63.33(4)
0.100	737	15	3.9894(8)	3.9894(8)	63.49(4)
0.200	737	15	3.9978(3)	3.9978(3)	63.89(2)
0.300	737	15	3.9987(5)	3.9987(5)	63.94(2)
0.400	737	15	4.0068(7)	4.0068(7)	64.33(4)
0.500	737	15	4.0112(4)	4.0112(4)	64.54(2)
0.575	737	15	4.0148(9)	4.0148(9)	64.71(5)
0.650	737	15	4.0183(6)	4.0183(6)	64.88(3)
0.700	737	15	5.739(3)	7.914(6)	260.7(3)
0.750	737	15	5.753(3)	7.896(6)	261.3(3)
0.800	737	15	5.778(3)	7.892(4)	263.6(3)
0.850	737	15	5.791(1)	7.888(2)	264.6(2)
0.900	737	15	5.811(1)	7.879(2)	266.1(1)
0.950	737	15	5.829(1)	7.858(4)	267.0(2)
1.000	737	15	5.850(1)	7.842(2)	268.4(1)

* Powder patterns for each sample are given in Appendix L.

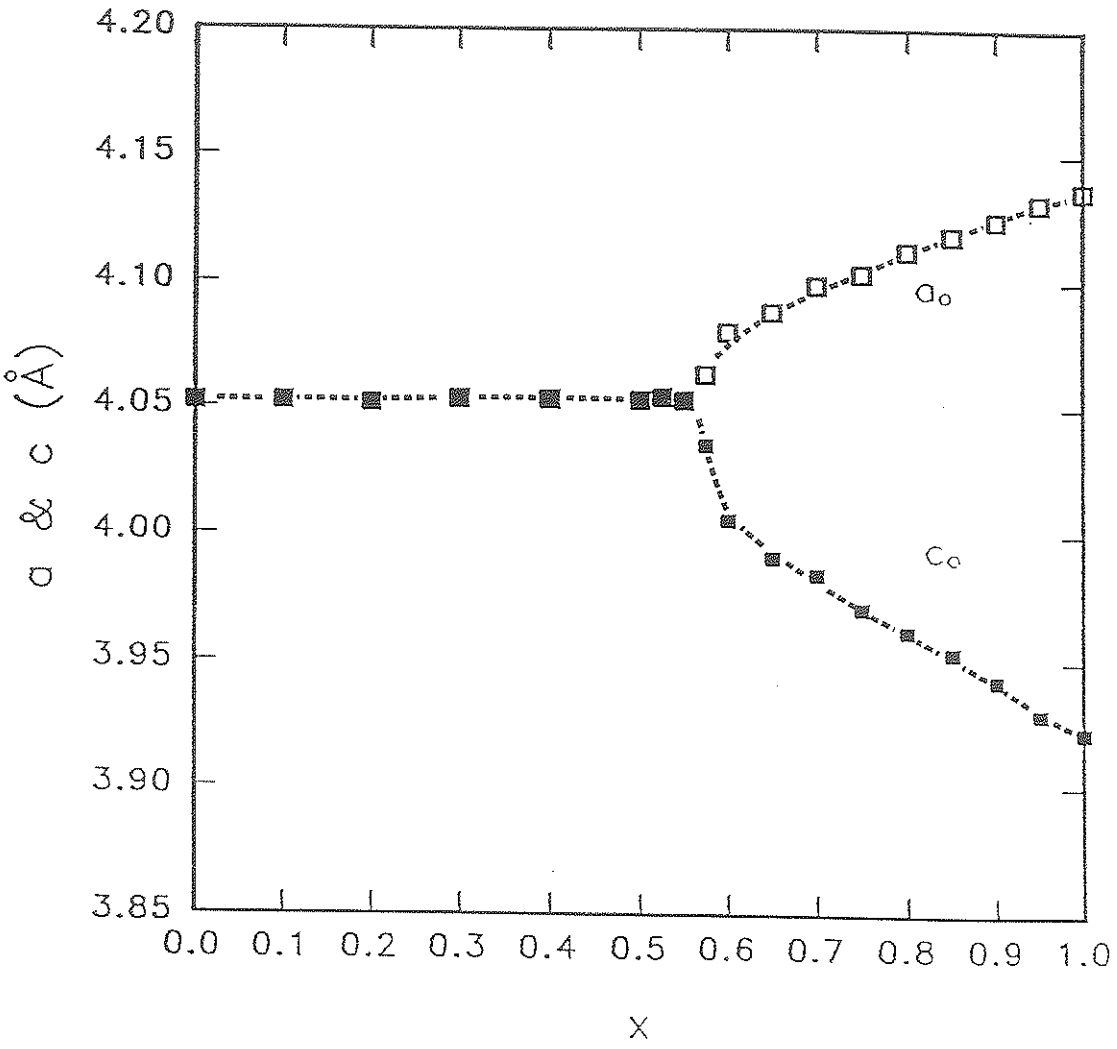

Figure 13.2. Unit-cell parameters for the $K(Zn_{1-x}Cu_x^{2+})F_3$ series. a_o and c_o are plotted for tetragonal structure mixed crystals; $a_o = a/\sqrt{2}$, $c_o = c/2$. Standard deviations (Table 13.1) are smaller than the symbols.

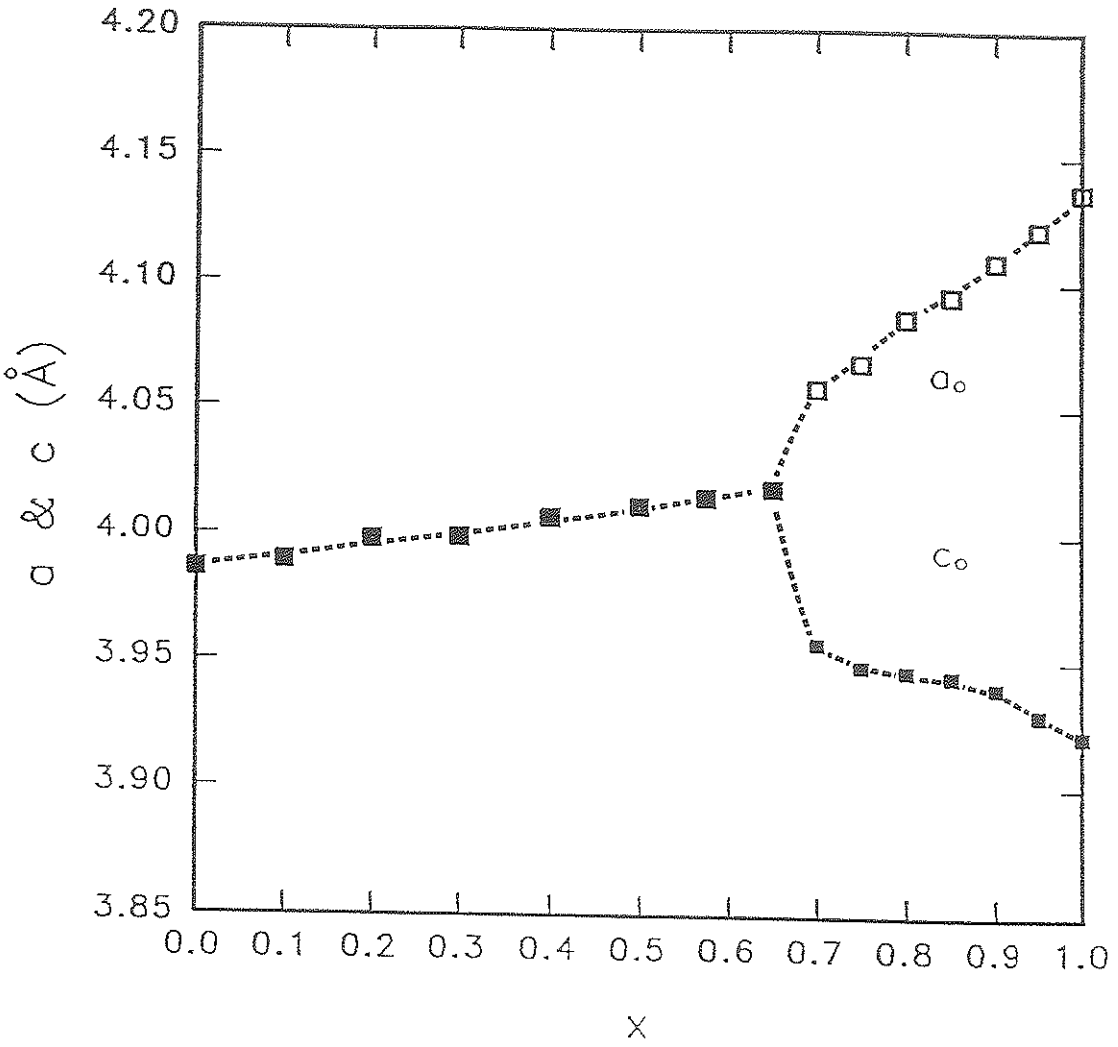

Figure 13.3. Unit-cell parameters for the $K(Mg_{1-x}Cu_x^{2+})F_3$ series. a_o and c_o are plotted for tetragonal structure mixed crystals; $a_o = a/\sqrt{2}$, $c_o = c/2$. Standard deviations (Table 13.2) are smaller than the symbols.

13.4 Rietveld Structure Refinement

The detailed octahedral geometries of each member of the series are needed to characterize the phase transition. In the case of the cubic perovskite structure, the metal cation is in a strictly holosymmetric octahedron, and only the unit-cell parameters affect the metal-fluorine distances. In the tetragonal $K(Cu^{2+},M^{2+})F_3$ series, it is necessary to refine the F(2) position to obtain the metal-fluorine bond-lengths. Rietveld structure refinements from X-ray powder data were done for $K(Mg_{1-x}Cu_x^{2+})F_3$ with $x \geq 0.575$ and $K(Zn_{1-x}Cu_x^{2+})F_3$ with $x \geq 0.60$ to obtain this information.

Samples were prepared for data collection by gently back-pressing the powders into an aluminum sample holder. The top surface of the sample was serrated with a razor blade to minimize preferred-orientation effects. Step-scan data were collected using the experimental conditions given in Section 13.3. A step size of 0.05°2θ and a count time of 5 seconds/step were used over the range 20-135°2θ.

All structure refinements were done using the program LHPM1 (Howard and Hill, 1986, a modified version of the program by Wiles and Young, 1981). Atomic scattering factors for Zn, Cu, Mg, F and K were taken from the *International Tables for X-Ray Crystallography* (1974).

The structures of the tetragonal members of each series were refined in the space group I4/mcm using the structural parameters of $KCu^{2+}F_3$ given by Tanaka et al. (1979) as the starting model. Cubic members of each series were refined in the space group Pm3m. Peaks were modelled using a pseudo-Voigt peak-profile function corrected for asymmetry to 30°2θ. Isotropic-displacement parameters were not stable during refinement; they

were fixed at single-crystal values and an overall-displacement parameter was refined.

Final R_{Bragg} indices ranged from 1.8 to 4.9% for $K(Mg_{1-x}Cu_x^{2+})F_3$ refinements and from 1.8 to 4.5% for $K(Zn_{1-x}Cu_x^{2+})F_3$ refinements. Refined structure parameters, unit-cell parameters and R-indices are given in Tables 13.3 and 13.4. Bond-lengths for members of each series are listed in Tables 13.5 and 13.6. Figures 13.4, 13.5, 13.6 and 13.7 show the unit-cell parameter and bond-length variations across each series. The observed powder pattern for $KCu^{2+}F_3$ is compared to the pattern calculated from the refined structure parameters in Figure 13.8. Observed step-scan patterns are given in Appendices M and N.

13.5 The Phase Transitions in $K(Mg_{1-x}Cu_x^{2+})F_3$ and $K(Zn_{1-x}Cu_x^{2+})F_3$

The (cubic) unit-cell parameters for $K(Mg_{1-x}Cu_x^{2+})F_3$ ($0 \leq x \leq 0.575$) and for $K(Zn_{1-x}Cu_x^{2+})F_3$ ($0 \leq x \leq 0.55$) show a steady but gentle linear increase with x (Figs. 13.4 and 13.6). At the cubic to tetragonal transition, located at $x \approx 0.65$ in the $K(Mg_{1-x}Cu_x^{2+})F_3$ series and $x \approx 0.55$ in the $K(Zn_{1-x}Cu_x^{2+})F_3$ series, the a_o and c_o parameters rapidly diverge in a non-linear fashion (Figs. 13.4 and 13.6). The unit-cell volume varies linearly with increasing x for the cubic $K(Mg_{1-x}Cu_x^{2+})F_3$ and $K(Zn_{1-x}Cu_x^{2+})F_3$ series, with a rapid change in the unit-cell volume occurring in the vicinity of the transition (Figs. 13.4 and 13.6).

The metal cation is in holosymmetrical octahedral coordination in cubic $K(M_{1-x}Cu_x^{2+})F_3$ (Figs. 13.5 and 13.7). At the phase transition, the F(2) atom, located at the 8(h) position in the space group I4/mcm, moves away from the midpoint between adjacent Cu atoms. This results in a steady

Table 13.3 Rietveld structures[#] and R-indices[*] (%) for the $K(Zn_{1-x}Cu_x^{2+})F_3$ series.

Space Group	I4/mcm	(Zn,Cu) at 0, ½, 0 K at 0, 0, ¼		F(1) at 0, ½, ¼ F(2) at u, u+½, 0		
x	R_B	R_P	R_{WP}	R_{WP}(exp.)	a(Å)	c(Å)	V(Å^3)	u	B(overall)
1.00	1.8	2.8	4.0	2.1	5.8613(6)	7.858(1)	270.0(1)	0.226(2)	-0.2(2)
0.90	3.1	3.2	4.8	2.1	5.8355(9)	7.894(1)	268.8(1)	0.227(2)	0.2(2)
0.80	3.1	3.9	5.8	2.2	5.814(1)	7.934(2)	268.2(2)	0.228(3)	-0.1(3)
0.70	4.5	4.5	7.0	2.4	5.791(1)	7.984(3)	267.7(3)	0.231(6)	-0.7(3)
0.60	3.3	4.7	7.1	2.5	5.755(1)	8.064(3)	267.1(3)	0.243(9)	-0.3(3)

Space Group	Pm3m	(Zn,Cu) at 0, 0, 0 K at ½, ½, ½	F at ½, 0, 0
x	a(Å)	V(Å^3)
0.525[+]	4.0541(3)	66.63(1)
0.40[+]	4.0532(3)	66.59(1)
0.30[+]	4.0532(2)	66.59(1)
0.20[+]	4.0515(5)	66.51(2)
0.10[+]	4.0520(4)	66.55(2)
0.00[+]	4.0520(5)	66.53(2)

σs have been corrected using equation 12.1. * R_B = Rietveld Bragg-agreement index R_P = Rietveld profile-agreement index. R_{WP} = Rietveld weighted profile-agreement index. + Rietveld structure refinements were not done for $0 \leq x \leq 0.50$; reported unit-cell parameters were obtained from powder data using Appleman and Evans (1973) cell refinement program.

Table 13.4. Rietveld structures[#] and R-indices[*] (%) for the $K(Mg_{1-x}Cu_x^{2+})F_3$ series

Space Group	I4/mcm	(Mg,Cu) at 0, ½, 0 K at 0, 0, ¼	F(1) at 0, ½, ¼ F(2) at u, u+½, 0						
x	R_B	R_P	R_{WP}	R_{WP}(exp.)	a(Å)	c(Å)	V(Å^3)	u	B(overall)	K[**]
1.000	1.8	2.8	4.0	2.1	5.8613(6)	7.858(1)	270.0(1)	0.226(2)	-0.2(2)	0.92(6)
0.950	4.3	4.5	6.8	2.1	5.856(1)	7.855(2)	269.4(2)	0.225(3)	-0.5(3)	0.90(3)
0.900	4.2	4.8	7.6	2.1	5.849(2)	7.858(3)	268.8(3)	0.225(3)	-0.5(3)	0.87(3)
0.850	3.1	5.6	8.7	2.1	5.842(3)	7.865(3)	268.4(3)	0.225(6)	-0.8(6)	0.82(6)
0.800	3.0	5.6	8.6	2.1	5.831(3)	7.875(6)	267.7(6)	0.228(6)	-0.7(6)	0.80(3)
0.750	3.7	6.6	10.3	2.2	5.815(6)	7.886(6)	266.7(6)	0.231(9)	-0.9(6)	0.75(6)
0.700	3.9	7.1	11.2	2.2	5.802(6)	7.901(9)	265.9(9)	0.237(9)	-0.9(6)	0.71(6)
0.650	4.9	7.7	12.6	2.3	5.775(3)	7.924(4)	264.4(9)	0.240(9)	-1.2(9)	0.60(6)

Space Group	Pm3m	(Mg,Cu) at 0, 0, 0 K at ½, ½, ½	F at ½, 0, 0			
x	R_B	R_P	R_{WP}	R_{WP}(exp.)	a(Å)	V(Å^3)	B(overall)	K[**]
0.575	1.4	5.1	8.2	2.4	4.023(1)	65.09(6)	-0.5(3)	0.52(3)
0.500[+]					4.0112(4)	64.54(2)		
0.400[+]					4.0068(7)	64.33(3)		
0.300[+]					3.9987(5)	63.94(2)		
0.200[+]					3.9978(3)	63.89(1)		
0.100[+]					3.9894(8)	63.49(4)		
0.000[+]					3.9859(8)	63.33(4)		

σs corrected using equation 12.1. * R_P = Rietveld profile-agreement index R_{WP} = weighted Rietveld profile-agreement index. R_B = Rietveld Bragg-agreement index. + Rietveld structure refinements were not done for $0 \leq x \leq 0.50$; reported unit-cell parameters were obtained from powder data using Appleman and Evans (1973) cell refinement program. ** Refined occupancy value.

Table 13.5. Selected bond-lengths (Å) for the $K(Zn_{1-x}Cu_x^{2+})F_3$ series

x	Cu-F(2) x2	Cu-F(1) x2	Cu-F(2a) x2	K-F(2) x8	K-F(1) x4
1.00+	1.873(4)	1.964(2)	2.27(1)	2.862(2)	2.931(1)
0.90+	1.87(1)	1.974(2)	2.25(2)	2.861(2)	2.918(1)
0.80+	1.87(2)	1.984(2)	2.24(2)	2.862(2)	2.907(1)
0.70+	1.89(5)	1.996(3)	2.20(5)	2.864(3)	2.895(1)
0.60+	1.97(13)	2.016(3)	2.09(7)	2.865(3)	2.877(1)

x	Cu-F x6	K-F x12
0.50*	2.027(1)	2.867(1)
0.40*	2.027(1)	2.866(1)
0.30*	2.027(1)	2.866(1)
0.20*	2.026(1)	2.865(1)
0.10*	2.026(1)	2.866(1)
0.00*	2.026(1)	2.865(1)

\+ Bond-lengths calculated using the structure parameters refined by the Rietveld method (Table 13.3).
* Bond-lengths calculated from the refined unit-cell dimensions (Table 13.1).

Table 13.6. Selected bond-lengths (Å) for the $K(Mg_{1-x}Cu_x^{2+})F_3$ series

x	Cu-F(2) x2	Cu-F(1) x2	Cu-F(2a) x2	K-F(2) x8	K-F(1) x4
1.000+	1.85(2)	1.963(2)	2.30(2)	2.863(2)	2.930(1)
0.950+	1.87(3)	1.964(3)	2.27(3)	2.861(3)	2.928(1)
0.900+	1.86(3)	1.965(3)	2.27(3)	2.860(3)	2.924(1)
0.850+	1.86(6)	1.966(3)	2.27(3)	2.859(3)	2.921(1)
0.800+	1.88(3)	1.969(3)	2.25(6)	2.857(6)	2.916(2)
0.750+	1.90(6)	1.972(3)	2.21(6)	2.853(6)	2.907(2)
0.700+	1.94(9)	1.975(6)	2.16(9)	2.850(3)	2.901(2)
0.650+	1.96(15)	1.981(3)	2.12(15)	2.846(3)	2.887(5)

x	Cu-F x6	K-F x12
0.575+	2.011(1)	2.844(1)
0.500*	2.006(1)	2.836(1)
0.400*	2.003(1)	2.833(1)
0.300*	1.999(1)	2.828(1)
0.200*	1.999(1)	2.827(1)
0.100*	1.995(1)	2.821(1)
0.000*	1.993(1)	2.818(1)

+ Bond-lengths calculated using the structure parameters refined by the Rietveld method (Table 13.4).
* Bond-lengths calculated from the refined unit-cell dimensions (Table 13.2).

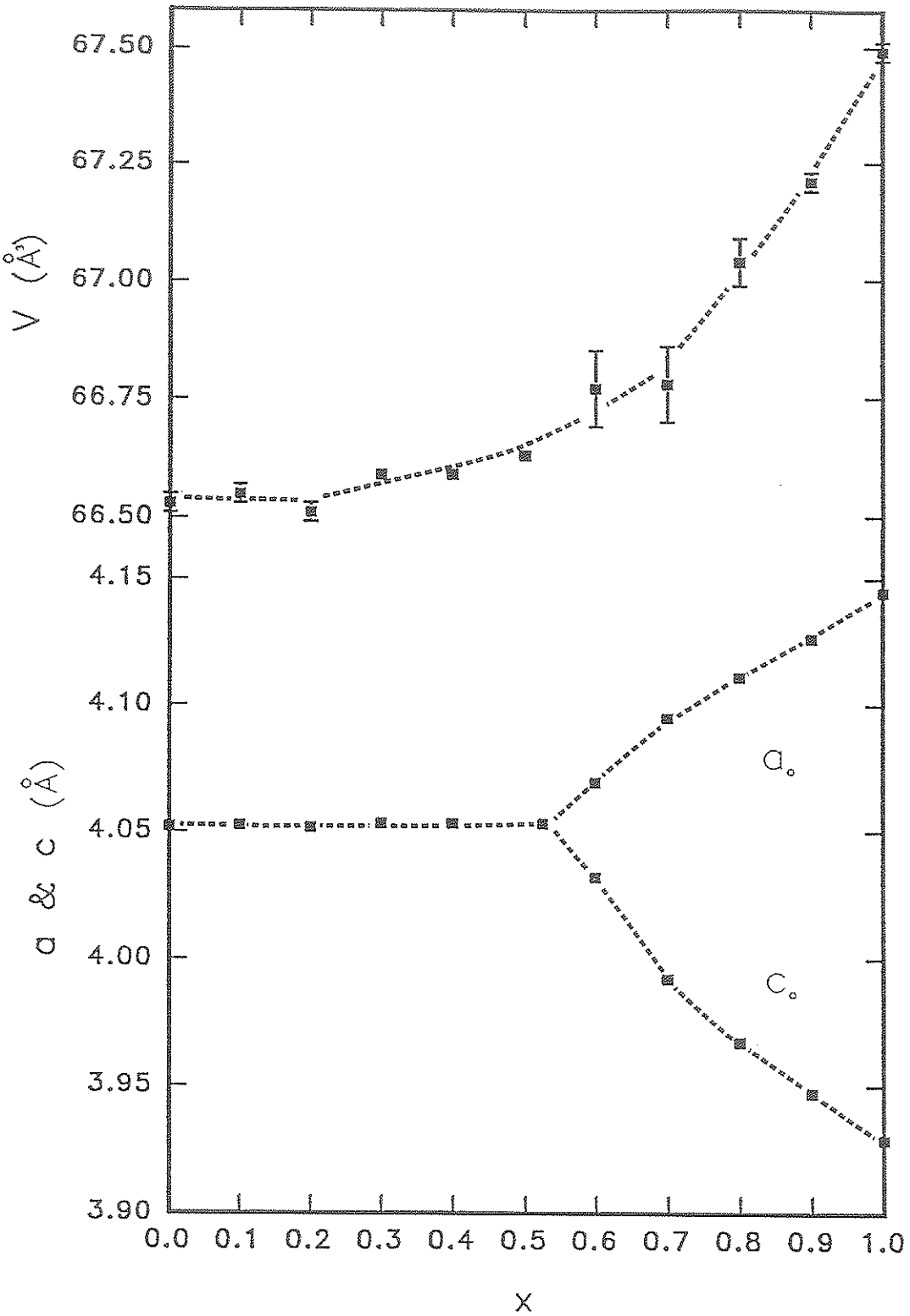

Figure 13.4. Rietveld unit-cell parameters for the $K(Zn_{1-x}Cu_x^{2+})F_3$ series. a_o and c_o are plotted for tetragonal structure mixed crystals; $a_o = a/\sqrt{2}$, $c_o = c/2$.

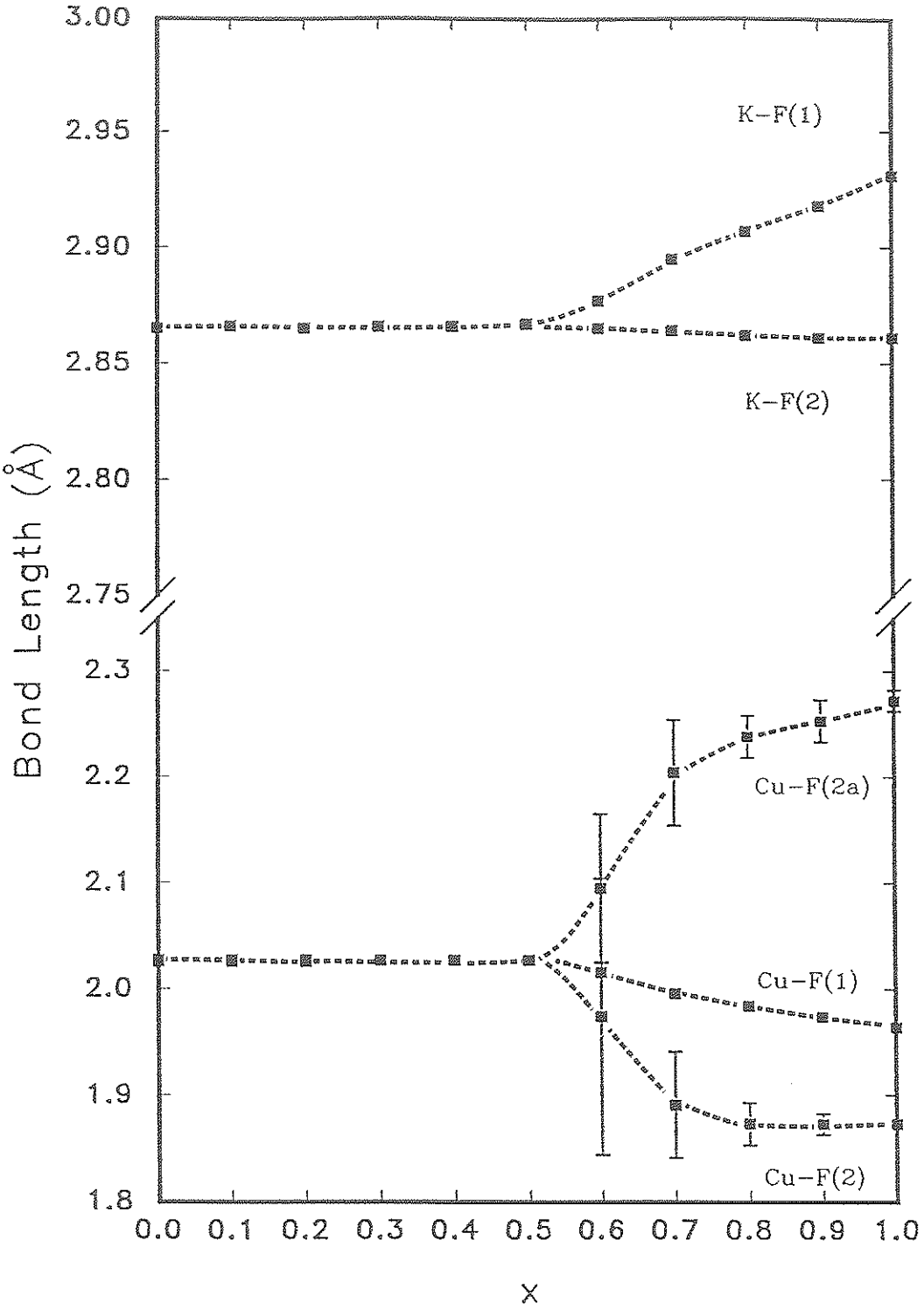

Figure 13.5. Bond-lengths for the $K(Zn_{1-x}Cu_x^{2+})F_3$ series.

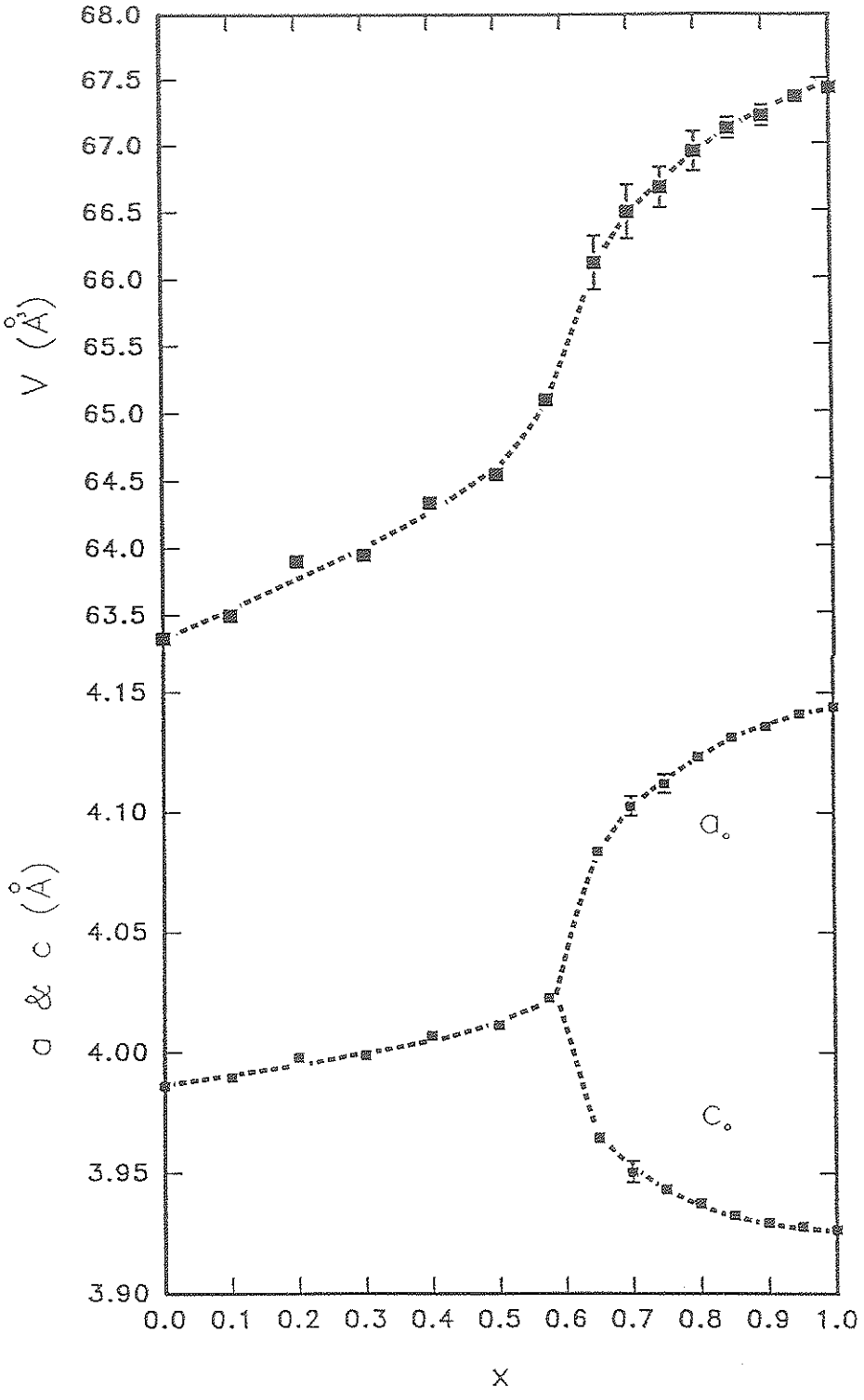

Figure 13.6. Rietveld unit-cell parameters for the $K(Mg_{1-x}Cu_x^{2+})F_3$ series. a_o and c_o are plotted for tetragonal structure mixed crystals; $a_o = a/\sqrt{2}$, $c_o = c/2$.

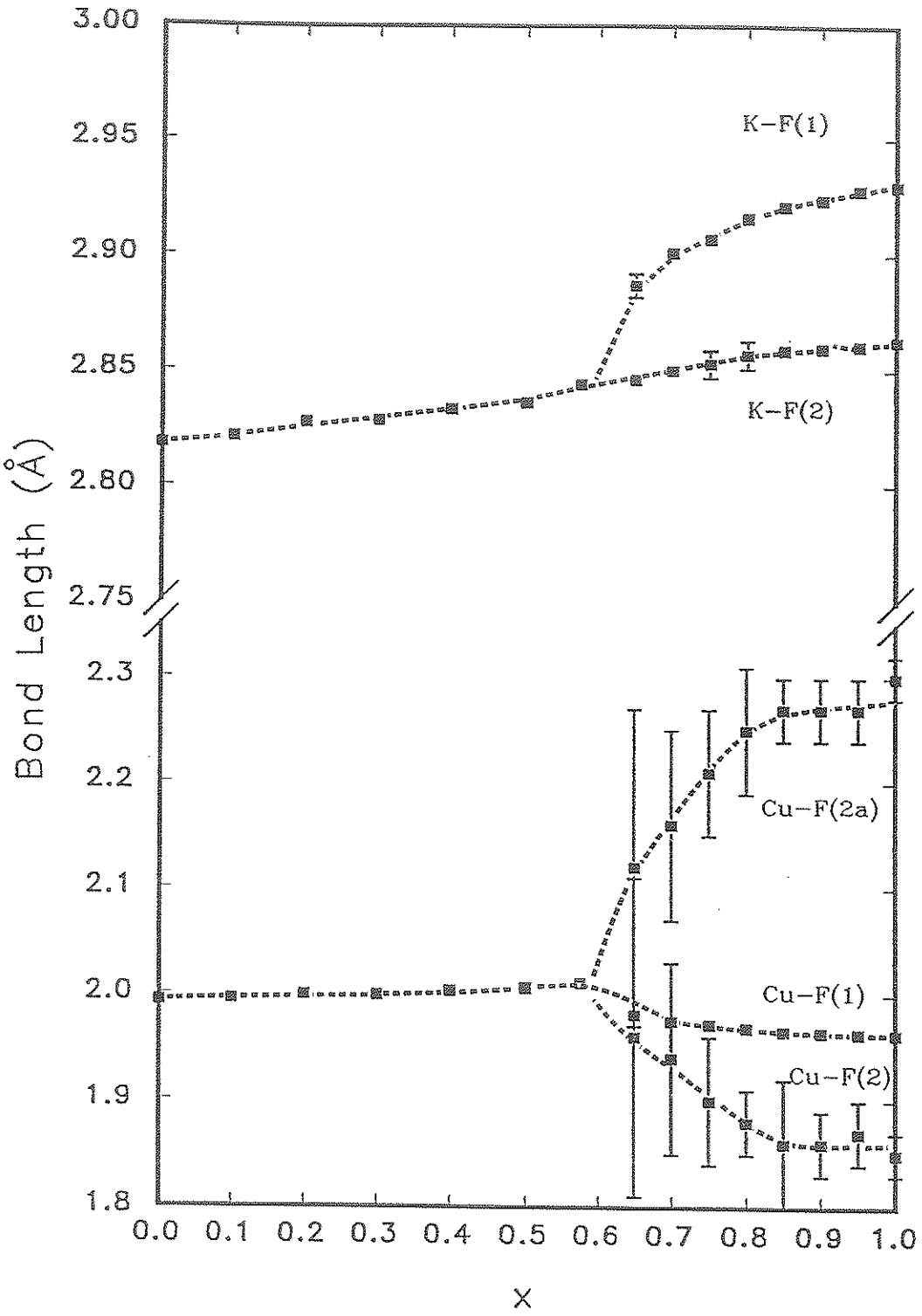

Figure 13.7. Bond-lengths for the $K(Mg_{1-x}Cu_x^{2+})F_3$ series.

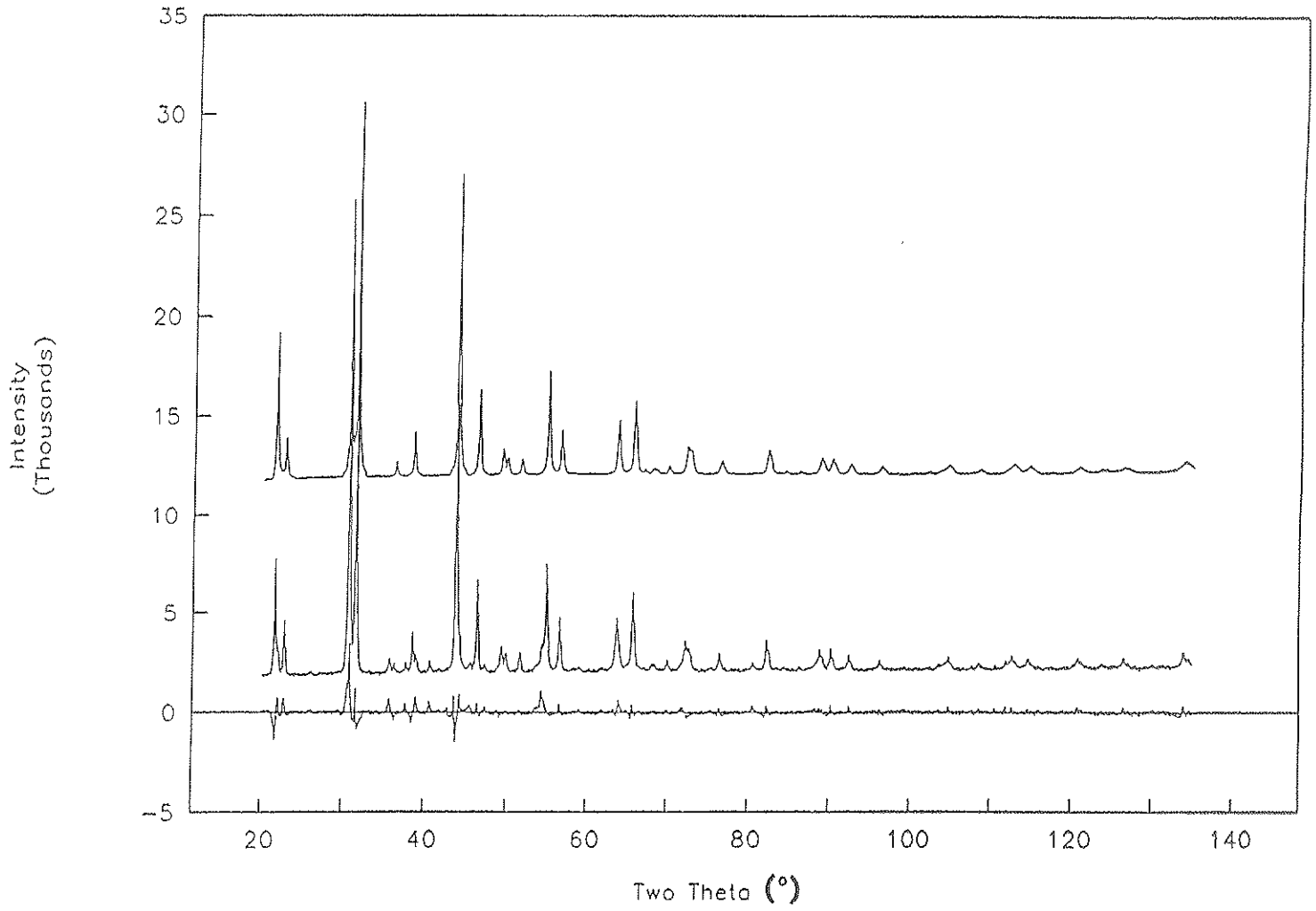

Figure 13.8. The observed (middle) and calculated (top) powder pattern for $KCu^{2+}F_3$; bottom: residual (I_{calc}-I_{obs}).

decrease in the Cu-F(2) bond-length, coupled with a sharp increase in the Cu-F(2a) bond-length. The Cu-F(1) bond-length decreases gradually after the phase transition (Figs. 13.5 and 13.7). These changing Cu-F bond-lengths lead to a (4+2)-distorted octahedral environment about the copper ion, as predicted on the basis of the Jahn-Teller instability associated with Cu^{2+} in an octahedral environment.

When a (4+2)-distorted $Cu^{2+}F_6$ octahedron is embedded in the cubic perovskite structure, the octahedron may be elongated in any of the three symmetrically equivalent octahedral directions in the cubic structure. For values of $x < x_c$, $K(M_{1-x}Cu_x^{2+})F_3$ series members are cubic, indicating that the $Cu^{2+}F_6$ (4+2)-distorted octahedra are randomly aligned, maintaining long-range cubic symmetry. At $x = x_c$, the (4+2)-distorted $Cu^{2+}F_6$ octahedra have reached a sufficient concentration to begin to interact via some phonon mode. The resulting cooperative Jahn-Teller effect propels the F(2) position away from the midpoint between adjacent Cu^{2+} ions, such that for all values of $x \geq x_c$, there is a significant long-range coupling between (4+2)-distorted $Cu^{2+}\phi_6$ octahedra. Increasing x above x_c results in a gradual increase in the average (4+2)-distortion of the $(Cu^{2+},M)F_6$ octahedron.